T2K 3.010×10^{20}-POT Joint 3-Flavour Oscillation Analysis

Costas Andreopoulos[a], Anselmo Cervera[d], Thomas Dealtry[a,b], Lorena Escudero Sánchez[d], Nick Grant[c], Michel Sorel[d], and Panagiotis Stamoulis[d]

[a] *Particle Physics Dept., Rutherford Appleton Laboratory, STFC*
Harwell Science and Innovation Campus
Oxfordshire OX11 0QX, UK
[b] *Subdepartment of Particle Physics, University of Oxford*
Denys Wilkinson Building, Keble Road
Oxfordshire OX1 3RH, UK
[c] *Physics Dept., Lancaster University*
Lancaster, LA1 4YB, UK
[d] *Instituto de Fisica Corpuscular*
CSIC and University of Valencia
Valencia, Spain

Abstract

We report the results of the *VaLOR* (Valencia-Lancaster-Oxford-Rutherford) joint 3-flavour oscillation analysis on the combined Run 1+2+3 dataset. This dataset corresponds to an integrated JPARC neutrino beam exposure of 3.020 $\times10^{20}$ POT.

In this analysis, the atmospheric squared-mass splitting $|\Delta m^2|$ (the Fogli-Lisi convention is used, see main text for details), the mixing angles $sin^2\theta_{23}$, $sin^2\theta_{13}$ and the CP-invariance violating phase δ_{CP}, are determined jointly through a simultaneous oscillation fit to the reconstructed energy spectrum of the SuperK single μ-like ring and single e-like ring event samples. The oscillation fit was performed in a 3-flavour framework including matter effects in constant density matter. Official T2K 2012 analysis inputs were used. All 83 systematics considered in this analysis were allowed to float in the fit.

The motivation for performing a joint 3-flavour oscillation fit is presented in detail and the results of this analysis are compared with the ones obtained by the stand-alone 3-flavour ν_e-appearance and ν_μ-disappearance analyses. The analysis reported here is the baseline *VaLOR* joint 3-flavour oscillation analysis, where possible, but currently unknown, correlations between the single μ-like ring and single e-like ring systematics related to FSI+SI and SK efficiencies were neglected. In the future those correlations will be used for the following Run1-4a joint oscillation analysis. If they were not available in time, then the potential effect of these correlations on our baseline analysis would be reported by the VaLOR group on a separate note.

Assuming normal hierachy (NH), the joint 3-flavour oscillation fit to the observed reconstructed energy spectrum of single μ-like ring and single e-like ring events of the combined Run 1+2+3 dataset, with all mixing angles constrained to the physical region, yields $|\Delta m^2|$ = 2.494$\times10^{-3}$ eV^2/c^4, $\sin^2\theta_{23}$ = 0.516, $\sin^2\theta_{13}$ = 0.029 and δ_{CP} = 2.086 as the best-fit values (p-value = 0.86). The corresponding results for inverted hierachy (IH) are $|\Delta m^2|$ = 2.468$\times10^{-3}$ eV^2/c^4, $\sin^2\theta_{23}$ = 0.516, $\sin^2\theta_{13}$ = 0.034 and δ_{CP} = 0.922 (p-value = 0.85). Both fits used 2012 PDG values for $\sin^2 2\theta_{12}$ and the solar squared-mass splitting δm^2 [24].

Confidence regions are constructed using the constant-$\Delta\chi^2$ method. For NH, the 90% (68%) CL allowed region for the four oscillation parameters can be summarized as 2.227$\times10^{-3}$ (2.332$\times10^{-3}$) $eV^2/c^4 < |\Delta m^2| <$ 2.773$\times10^{-3}$ (2.659$\times10^{-3}$) eV^2/c^4, 0.401 (0.433) $< sin^2\theta_{23} <$ 0.628 (0.596), 0.006 (0.012) $< sin^2\theta_{13} <$ 0.058 (0.048) and -π (-π) $< \delta_{CP} < \pi$ (π). For IH, the corresponding 90% (68%) CL allowed regions are 2.218 $\times10^{-3}$ (2.311$\times10^{-3}$) $eV^2/c^4 < |\Delta m^2| <$ 2.729 $\times10^{-3}$ (2.627$\times10^{-3}$) eV^2/c^4, 0.397 (0.433) $< sin^2\theta_{23} <$ 0.627 (0.596), 0.006 (0.013) $< sin^2\theta_{13} <$ 0.069 (0.054) and -π (-π) $< \delta_{CP} < \pi$ (π).

Contents

1 Introduction **27**

2 Motivation **27**

3 Choice of oscillation parameters **30**

4 Predictions of single μ-like ring and single e-like ring event reconstructed energy spectrum in SuperK **31**

5 Systematic effects in the prediction of the single μ-like ring and single e-like ring event reconstructed energy spectrum **38**

6 Neutrino oscillation fitting **47**
6.1 Minimization method . . . 47
6.2 Goodness-of-fit tests . . . 47
6.3 Toy-MC study of fitter performance . . . 48
6.4 Construction of confidence regions . . . 48

7 Results of the joint oscillation analysis with the Run 1+2+3 (3.010×10^{20} POT) dataset **49**
7.1 Best-fit oscillation parameters and systematic parameter pulls . . . 49
7.2 Goodness-of-fit tests . . . 49
7.3 Best-fit single e-like ring and single μ-like ring event reconstructed energy spectra . . . 49
7.4 Confidence regions . . . 50

8 Summary **69**

Appendices **71**

A Implementation of ν_e-appearance analysis in the *VaLOR* analysis framework **72**

B Fitter performance. Study of residuals. **75**
B.1 '4 + 0' fit . . . 75
B.2 '4 + 83' fit . . . 79

C 3.010$\times$10^{20} POT fake dataset fits **95**

D 3.010$\times$10^{20} POT sensitivity studies **128**

E Difference between $\sin^2\theta_{23}$ values for maximal mixing and maximal disappearance. **136**

F Study of the effect of 12-sector (solar) oscillation parameters in the joint oscillation analysis **139**

G Further studies for δ_{CP} **140**

H Comparison between results in the two mass hierarchies using the Fogli and Lisi convention $\left(|\Delta m^2|, \delta m^2\right)$ and the $\left(|\Delta m^2_{32}|, \Delta m^2_{21}\right)$ convention. **146**

I Coverage studies **148**
I.1 Coverage studies with statistical fluctuations only . . . 150
I.1.1 Coverage studies in 1D . . . 150
I.1.2 Coverage studies in 2D . . . 155
I.2 Coverage studies in 2D including systematic variations . . . 164
I.3 Coverage studies in 2D including the other oscillation parameters in the fit . . . 167

List of Figures

1 Examples of the effect of the interdependence between the oscillation parameters in the oscillation probabilities $P(\nu_\mu \to \nu_\mu)$(left) and $P(\nu_\mu \to \nu_e)$ (right). These probabilities are computed for different values of $\sin^2 2\theta_{13}$ (left) or $\sin^2 2\theta_{23}$ (right) with the other 3 parameters being fixed at $\sin^2 2\theta_{23}$ = 0.96, $|\Delta m^2_{32}|$ = 2.4×10^{-3} eV^2/c^4, δ_{CP} = 0 (left) or $\sin^2 2\theta_{13}$ = 0.1, $|\Delta m^2_{32}|$ = 2.4×10^{-3} eV^2/c^4, δ_{CP} = 0 (right). 28

2 Illustration of the effect of changing the assumed value of $\sin^2 2\theta_{23}$ in the ν_e-appearance contours for 7×10^{21} POT. Dashed lines are contours of the stand-alone ν_e-appearance analysis assuming maximal mixing ($\sin^2 2\theta_{23}$ = 1.0), and solid lines are contours of the stand-alone ν_e-appearance analysis assuming $\sin^2 2\theta_{23}$ = 0.96, the true value with which the toy experiment was created. The other parameters have the following values: $\sin^2 2\theta_{13}$ = 0.12, $|\Delta m^2_{32}|$ = 2.5×10^{-3} eV^2/c^4, and δ_{CP} = 0.5. The confidence regions were constructed using the constant-$\Delta\chi^2$ method, which is described in Sec. 6. 29

3 Plot of the same contours as in Fig. 2 rescaling the contours for maximal prior $\sin^2 2\theta_{23}$ = 1.0 with the cited replacement of $\sin^2 2\theta_{13}$ by $2\sin^2\theta_{23}\sin^2 2\theta_{13}$, using for θ_{23} the true value for the toy experiment. 29

4 $\sin^2\theta_{23}$ (appears in leading-order term of P($\nu_\mu \to \nu_e$) vs $\sin^2 2\theta_{23}$(appears in leading-order term of P($\nu_\mu \to \nu_\mu$). 30

5 Effects of changing the convention for the inputs of the mass-squared splitting parameters on P($\nu_\mu \to \nu_\mu$) (left) and P($\nu_\mu \to \nu_e$) (right): $|\Delta m^2_{32}|$ = 2.32×10^{-3} eV^2/c^4 (solid lines) and $|\Delta m^2|$ = 2.32×10^{-3} eV^2/c^4 (dashed lines) for the normal hierarchy (blue) and inverted hierarchy (red). The other oscillation parameters are $\sin^2 2\theta_{12}$ = 0.857, δm^2 = 7.5×10^{-5} eV^2/c^4, $\sin^2 2\theta_{13}$ = 0.098 (2012 PDG values), δ_{CP} = 0 and $\sin^2 2\theta_{23}$ = 0.9. 31

6 Predicted number of single μ-like ring events, as a function of $\sin^2\theta_{23}$ and $|\Delta m^2|$, for an exposure of 3.010×10^{20} POT. The number of events was calculated using the BANFF-tuned MC templates. 2012 PDG values are used for $\sin^2\theta_{13}$, $\sin^2\theta_{12}$ and δm^2 and δ_{CP}=0. The numbers shown were generated assuming the normal hierarchy. 33

7 Predicted number of single e-like ring events, as a function of $\sin^2\theta_{13}$ and δ_{CP}, for an exposure of 3.010×10^{20} POT. The number of events was calculated using the BANFF-tuned MC templates. 2012 PDG values are used for $\sin^2\theta_{12}$, $|\Delta m^2|$ and δm^2, while $\sin^2\theta_{23}$ was set to 0.5. The numbers shown were generated assuming the normal hierarchy. 33

8 Predicted number of single μ-like ring events, as a function of $\sin^2\theta_{13}$ and δ_{CP}, which are typically fixed to constant values by the stand-alone ν_μ-disappearance analysis, for an exposure of 3.010×10^{20} POT. The number of events was calculated using the BANFF-tuned MC templates. 2012 PDG values are used for $\sin^2\theta_{12}$, $|\Delta m^2|$ and δm^2, while $\sin^2\theta_{23}$ was set to 0.5. The numbers shown were generated assuming the normal hierarchy. . . 33

9 Predicted number of single e-like ring events, as a function of $\sin^2\theta_{23}$ and $|\Delta m^2|$, which are typically fixed to constant values by the stand-alone ν_e-appearance analysis, for an exposure of 3.010×10^{20} POT. The number of events was calculated using the BANFF-tuned MC templates. 2012 PDG values are used for $\sin^2\theta_{13}$, $\sin^2\theta_{12}$ and δm^2 and δ_{CP}=0. The numbers shown were generated assuming the normal hierarchy. 33

10 Predicted reconstructed-energy spectrum of single μ-like ring events, and contributions from various true neutrino reaction modes, for no oscillations and for an exposure of 3.010×10^{20} POT. The 28 components of the spectrum are calculated separately in the actual analysis, but, for this plot, are grouped into just 5 categories: ν_μ CCQE, ν_μ CCnonQE, $\bar{\nu}_\mu$ CC, $\nu_e/\bar{\nu}_e$ CC and NC. The spectrum was generated using the BANFF-tuned MC templates. 35

11 Predicted reconstructed-energy spectrum of single e-like ring events, and contributions from various true neutrino reaction modes, for no oscillations and for an exposure of 3.010×10^{20} POT. The 32 components of the spectrum are calculated separately in the actual analysis, but, for this plot, are grouped into just four categories: ν_μ+$\bar{\nu}_\mu$ CC, ν_μ+$\bar{\nu}_\mu$ NC, ν_e+$\bar{\nu}_e$ (intrinsic beam component) and oscillated ν_e. The spectrum was generated using the BANFF-tuned MC templates. 35

12 Predicted reconstructed-energy spectrum of single μ-like ring events, and contributions from various true neutrino reaction modes, for oscillations with $\sin^2\theta_{23}$=0.5 and $|\Delta m^2|$=2.4×10^{-3} eV^2/c^4 The spectrum was generated using the BANFF-tuned MC templates. 2012 PDG values are used for $\sin^2\theta_{13}$, $\sin^2\theta_{12}$ and δm^2, while δ_{CP}=0. The spectrum shown was generated assuming the normal hierarchy. Note that the vertical axis is zoomed in by a factor of 4 compared with Fig. 10. 35

13 Predicted reconstructed-energy spectrum of single e-like ring events, and contributions from various true neutrino reaction modes, for oscillations with $\sin^2\theta_{23}$=0.5, $|\Delta m^2|$=2.4×10^{-3} eV^2/c^4, $\sin^2\theta_{13}$=0.098 and for an exposure of 3.010×10^{20} POT. The spectrum was generated using the BANFF-tuned MC templates. 2012 PDG values are used for $\sin^2\theta_{12}$ and δm^2, while δ_{CP}=0. The spectrum shown was generated assuming the normal hierarchy. 35

14 Total error envelope of the single μ-like ring event reconstructed energy spectrum (top) and total error envelope of the single e-like ring event reconstructed energy spectrum (bottom), for oscillations with $|\Delta m^2|$=2.36$\times 10^{-3}$ eV^2/c^4. $\sin^2\theta_{23}$=0.5, $\sin^2\theta_{13}$=0.025, δ_{CP}=0. 2012 PDG values are used for the solar parameters and the normal mass hierarchy is assumed. The plot shown was calculated for an exposure of 3.010$\times 10^{20}$ POT and BANFF-tuned MC templates were used. 46
15 Systematic parameter pulls for the 83 systematics allowed to float in the Run 1+2+3 joint 3-flavour oscillation fit with Normal Hierarchy. 52
16 Systematic parameter pulls for the 83 systematics allowed to float in the Run 1+2+3 joint 3-flavour oscillation fit with Inverted Hierarchy. 53
17 Distribution of χ^2_{gof}, the goodness-of-fit (gof) χ^2, from 1k toy MC experiments generated at the Run 1+2+3 joint 3-flavour analysis best-fit oscillation point with Normal Hierarchy. The χ^2_{gof} value for the Run 1+2+3 data (χ^2_{data}) is highlighted. All χ^2_{gof} values were computed using the 5 (single μ-like ring) + 3 (single e-like ring) reconstructed energy binning scheme described in Sec. 6.2, ... 54
18 Distribution of χ^2_{gof} from 1k toy MC experiments generated at the Run 1+2+3 stand-alone 3-flavour ν_μ disappearance analysis best-fit oscillation point with Normal Hierarchy. The χ^2_{gof} value for the Run 1+2+3 data (χ^2_{data}) is highlighted. All χ^2_{gof} values were computed using the 5 (single μ-like ring) reconstructed energy binning scheme described in Sec. 6.2, ... 54
19 Distribution of χ^2_{gof} from 1k toy MC experiments generated at the Run 1+2+3 stand-alone 3-flavour ν_e appearance analysis best-fit oscillation point with Normal Hierarchy. The χ^2_{gof} value for the Run 1+2+3 data (χ^2_{data}) is highlighted. All χ^2_{gof} values were computed using the 3 (single e-like ring) reconstructed energy binning scheme as described in Sec. 6.2, ... 54
20 Distribution of χ^2_{gof}, the goodness-of-fit (gof) χ^2, from 1k toy MC experiments generated at the Run 1+2+3 joint 3-flavour analysis best-fit oscillation point with Inverted Hierarchy. The χ^2_{gof} value for the Run 1+2+3 data (χ^2_{data}) is highlighted. All χ^2_{gof} values were computed using the 5 (single μ-like ring) + 3 (single e-like ring) reconstructed energy binning scheme described in Sec. 6.2. 55
21 Distribution of χ^2_{gof} from 1k toy MC experiments generated at the Run 1+2+3 stand-alone 3-flavour ν_μ disappearance analysis best-fit oscillation point with Inverted Hierarchy. The χ^2_{gof} value for the Run 1+2+3 data (χ^2_{data}) is highlighted. All χ^2_{gof} values were computed using the 5 (single μ-like ring) reconstructed energy binning scheme described in Sec. 6.2. 55
22 Distribution of χ^2_{gof} from 1k toy MC experiments generated at the Run 1+2+3 stand-alone 3-flavour ν_e appearance analysis best-fit oscillation point with Inverted Hierarchy. The χ^2_{gof} value for the Run 1+2+3 data (χ^2_{data}) is highlighted. All χ^2_{gof} values were computed using the 3 (single e-like ring) reconstructed energy binning scheme as described in Sec. 6.2. 55
23 Run 1+2+3 best-fit single μ-like ring event reconstructed energy spectrum for the fit with Normal Hierarchy (black: joint 3-flavour oscillation analysis, blue: stand-alone ν_μ disappearance analysis). The distributions are shown with the binning used in the fit. 56
24 Run 1+2+3 best-fit single e-like ring event reconstructed energy spectrum for the fit with Normal Hierarchy (black: joint 3-flavour oscillation analysis, red: stand-alone ν_e disappearance analysis). The distributions are shown with the binning used in the fit. 56
25 Run 1+2+3 best-fit single μ-like ring event reconstructed energy spectrum for the fit with Inverted Hierarchy (black: joint 3-flavour oscillation analysis, blue: stand-alone ν_μ disappearance analysis). The distributions are shown with the binning used in the fit. 57
26 Run 1+2+3 best-fit single e-like ring event reconstructed energy spectrum for the fit with inverted Hierarchy (black: joint 3-flavour oscillation analysis, red: stand-alone ν_e disappearance analysis). The distributions are shown with the binning used in the fit. 57
27 Run 1+2+3 best-fit single μ-like ring event reconstructed energy spectrum for the fit with Normal Hierarchy (black: joint 3-flavour oscillation analysis, blue: stand-alone ν_μ disappearance analysis). The distributions are shown with the coarse binning defined in the main text. 58
28 Run 1+2+3 best-fit single e-like ring event reconstructed energy spectrum for the fit with Normal Hierarchy (black: joint 3-flavour oscillation analysis, red: stand-alone ν_e disappearance analysis). The distributions are shown with the coarse binning defined in the main text. 58
29 Run 1+2+3 best-fit single μ-like ring event reconstructed energy spectrum for the fit with Inverted Hierarchy (black: joint 3-flavour oscillation analysis, blue: stand-alone ν_μ disappearance analysis). The distributions are shown with the coarse binning defined in the main text. 59

30 Run 1+2+3 best-fit single e-like ring event reconstructed energy spectrum for the fit with inverted Hierarchy (black: joint 3-flavour oscillation analysis, red: stand-alone ν_e disappearance analysis). The distributions are shown with the coarse binning defined in the main text. 59
31 Ratio of the Run 1+2+3 best-fit single μ-like ring event reconstructed energy spectra obtained from the joint 3-flavour oscillation and the stand-alone ν_μ disappearance analyses (joint / stand-alone) with Normal Hierarchy. The distributions are shown with the binning used in the fit. 60
32 Ratio of the Run 1+2+3 best-fit single e-like ring event reconstructed energy spectra obtained from the joint 3-flavour oscillation and the stand-alone ν_e appearance analyses. (joint / stand-alone) with Normal Hierarchy. The distributions are shown with the binning used in the fit. 60
33 Ratio of the Run 1+2+3 best-fit single μ-like ring event reconstructed energy spectra obtained from the joint 3-flavour oscillation and the stand-alone ν_μ disappearance analyses (joint / stand-alone) with Inverted Hierarchy. The distributions are shown with the binning used in the fit. 61
34 Ratio of the Run 1+2+3 best-fit single e-like ring event reconstructed energy spectra obtained from the joint 3-flavour oscillation and the stand-alone ν_e appearance analyses. (joint / stand-alone) with Inverted Hierarchy. The distributions are shown with the binning used in the fit. 61
35 $\Delta\chi^2$ as function of $|\Delta m^2|$ from the analysis of the Run 1+2+3 dataset comparing the joint analysis (black) with the stand-alone ν_μ disappearance (blue) for Normal Hierarchy. At each point, χ^2 was minimized with respect to all oscillation parameters not shown (and not considered to be fixed) and all relevant nuisance parameters. . 62
36 $\Delta\chi^2$ as function of $sin^2\theta_{23}$ from the analysis of the Run 1+2+3 dataset comparing the joint analysis (black) with the stand-alone ν_μ disappearance (blue) for Normal Hierarchy. At each point, χ^2 was minimized with respect to all oscillation parameters not shown (and not considered to be fixed) and all relevant nuisance parameters. . 62
37 $\Delta\chi^2$ as function of $sin^2\theta_{13}$ from the analysis of the Run 1+2+3 dataset comparing the joint analysis (black) with the stand-alone ν_e appearance (red) for Normal Hierarchy. At each point, χ^2 was minimized with respect to all oscillation parameters not shown (and not considered to be fixed) and all relevant nuisance parameters. . 62
38 $\Delta\chi^2$ as function of δ_{CP} from the analysis of the Run 1+2+3 dataset for Normal Hierarchy. At each point, χ^2 was minimized with respect to all oscillation parameters not shown (and not considered to be fixed) and all relevant nuisance parameters. 62
39 68% (dashed lines) and 90% (solid lines) CL regions in ($sin^2\theta_{23}$, $|\Delta m^2|$) space from the analysis of the Run 1+2+3 dataset comparing the joint analysis (black) with the stand-alone ν_μ disappearance (blue) for Normal Hierarchy. At each point, χ^2 was minimized with respect to all oscillation parameters not shown (and not considered to be fixed) and all relevant nuisance parameters. 63
40 68% (dashed lines) and 90% (solid lines) CL regions in ($sin^2\theta_{13}$, δ_{CP}) space from the analysis of the Run 1+2+3 dataset comparing the joint analysis (black) with the stand-alone ν_e appearance (red) for Normal Hierarchy. At each point, χ^2 was minimized with respect to all oscillation parameters not shown (and not considered to be fixed) and all relevant nuisance parameters. Notice that different methods are used to construct confidence regions for the joint analysis (global minimum) and for the stand-alone appearance analysis (raster scan). Middle solid red line is the line of best-fit points from the raster scan in the stand-alone appearance analysis. . 63
41 68% (dashed lines) and 90% (solid lines) CL regions in ($sin^2\theta_{13}$, $|\Delta m^2|$) space from the analysis of the Run 1+2+3 dataset for Normal Hierarchy. At each point, χ^2 was minimized with respect to all oscillation parameters not shown (and not considered to be fixed) and all relevant nuisance parameters. 64
42 68% (dashed lines) and 90% (solid lines) CL regions in ($sin^2\theta_{23}$, $sin^2\theta_{13}$) space from the analysis of the Run 1+2+3 dataset for Normal Hierarchy. At each point, χ^2 was minimized with respect to all oscillation parameters not shown (and not considered to be fixed) and all relevant nuisance parameters. 64
43 $\Delta\chi^2$ as function of $|\Delta m^2|$ from the joint 3-flavour oscillation analysis of the Run 1+2+3 dataset. Comparing $\Delta\chi^2$ curves for Normal Hierarchy (black) and Inverted Hierarchy (azure). At each point, χ^2 was minimized with respect to all oscillation parameters not shown (and not considered to be fixed) and all relevant nuisance parameters. 65
44 $\Delta\chi^2$ as function of $sin^2\theta_{23}$ from the 3-flavour oscillation analysis of the Run 1+2+3 dataset. Comparing $\Delta\chi^2$ curves for Normal Hierarchy (black) and Inverted Hierarchy (azure). At each point, χ^2 was minimized with respect to all oscillation parameters not shown (and not considered to be fixed) and all relevant nuisance parameters. 65
45 $\Delta\chi^2$ as function of $sin^2\theta_{13}$ from the 3-flavour oscillation analysis of the Run 1+2+3 dataset. Comparing $\Delta\chi^2$ curves for Normal Hierarchy (black) and Inverted Hierarchy (azure). At each point, χ^2 was minimized with respect to all oscillation parameters not shown (and not considered to be fixed) and all relevant nuisance parameters. 65

46 $\Delta\chi^2$ as function of δ_{CP} from the 3-flavour oscillation analysis of the Run 1+2+3 dataset. Comparing $\Delta\chi^2$ curves for Normal Hierarchy (black) with Inverted Hierarchy (azure). At each point, χ^2 was minimized with respect to all oscillation parameters not shown (and not considered to be fixed) and all relevant nuisance parameters. . . . 65
47 90% CL regions in ($sin^2\theta_{23}$, $|\Delta m^2|$) space from the joint 3-flavour oscillation analysis of the Run 1+2+3 dataset, comparing contours for the Normal Hierarchy (black) and Inverted Hierarchy (azure). At each point, χ^2 was minimized with respect to all oscillation parameters not shown (and not considered to be fixed) and all relevant nuisance parameters. . . . 66
48 90% CL regions in ($sin^2\theta_{13}$, δ_{CP}) space from the joint 3-flavour oscillation analysis of the Run 1+2+3 dataset, comparing contours for the Normal Hierarchy (black) and Inverted Hierarchy (azure). At each point, χ^2 was minimized with respect to all oscillation parameters not shown (and not considered to be fixed) and all relevant nuisance parameters. . . . 66
49 90% CL regions in ($sin^2\theta_{13}$, $|\Delta m^2|$) space from the joint 3-flavour oscillation analysis of the Run 1+2+3 dataset, comparing contours for the Normal Hierarchy (black) and Inverted Hierarchy (azure). At each point, χ^2 was minimized with respect to all oscillation parameters not shown (and not considered to be fixed) and all relevant nuisance parameters. . . . 67
50 90% CL regions in ($sin^2\theta_{23}$, $sin^2\theta_{13}$) space from the joint 3-flavour oscillation analysis of the Run 1+2+3 dataset, comparing contours for the Normal Hierarchy (black) and Inverted Hierarchy (azure). At each point, χ^2 was minimized with respect to all oscillation parameters not shown (and not considered to be fixed) and all relevant nuisance parameters. . . . 67
51 68% (dashed lines) and 90% (solid lines) CL regions in ($sin^2\theta_{13}$, δ_{CP}) space from the analysis of the Run 1+2+3 dataset comparing the joint analysis (black) with the stand-alone ν_e appearance (red) for Normal Hierarchy, using the raster scan in both analyses. Middle solid black (red) line is the line of best-fit points from the raster scan in the joint (stand-alone appearance) analysis. . . . 68
52 68% (dashed lines) and 90% (solid lines) CL regions in ($sin^2\theta_{13}$, δ_{CP}) space from the analysis of the Run 1+2+3 dataset comparing the joint analysis (black) with the stand-alone ν_e appearance (red) for Inverted Hierarchy, using the raster scan in both analyses. Middle solid black (red) line is the line of best-fit points from the raster scan in the joint (stand-alone appearance) analysis. . . . 68
53 MC predicted reconstructed neutrino energy distribution (area-normalized) for $\nu_\mu \rightarrow \nu_e$ CC signal (red), intrinsic ν_e CC background (green) and NC background (blue) components obtained with *VaLOR* framework, using $sin^2(2\theta_{12}) = 0.8704$, $\Delta m^2_{21} = 7.6 \times 10^{-5}$, $sin^2(2\theta_{23}) = 1.0$, $|\Delta m^2_{32}| = 2.4 \times 10^{-3}$, $\delta_{CP} = 0$ and normal hierarchy. . . . 73
54 Distribution of predicted number of nu_e candidate events over 1×10^6 toy experiments with $sin^2(2\theta_{13}) = 0$, including statistical and systematic variations, for 3.010×10^{20} POT, $sin^2(2\theta_{12}) = 0.8704$, $\Delta m^2_{21} = 7.6 \times 10^{-5}$, $sin^2(2\theta_{23}) = 1.0$, $|\Delta m^2_{32}| = 2.4 \times 10^{-3}$, $\delta_{CP} = 0$ and normal hierarchy. . . . 73
55 $\Delta\chi^2$ distribution for the Run1+2+3 data fit assuming normal (left) and inverted (right) mass hierarchy, for 2012 *VaLOR* appearance analysis (dashed blue) and 2012 official results from Fig. 21 in [15] (solid black - digitalized). Fixed values used: $sin^2(2\theta_{12}) = 0.8704$, $\Delta m^2_{21} = 7.6 \times 10^{-5}$, $sin^2(2\theta_{23}) = 1.0$, $|\Delta m^2_{32}| = 2.4 \times 10^{-3}$ and $\delta_{CP} = 0$. . . . 74
56 Reconstructed energy spectrum at the best-fit point for Run1+2+3 data fit with the *VaLOR* appearance analysis, assuming $\delta_{CP} = 0$, $sin^2(2\theta_{12}) = 0.8704$, $\Delta m^2_{21} = 7.6 \times 10^{-5}$, $sin^2(2\theta_{23}) = 1.0$, $|\Delta m^2_{32}| = 2.4 \times 10^{-3}$ and normal hierarchy. . . . 74
57 Distribution of residuals of the four oscillation parameters in the '4 + 0' fit for oscillation point # 0. . . . 76
58 Distribution of residuals of the four oscillation parameters in the '4 + 0' fit for oscillation point # 9. . . . 76
59 Distribution of residuals of the four oscillation parameters in the '4 + 0' fit for oscillation point # 1. . . . 76
60 Distribution of residuals of the four oscillation parameters in the '4 + 0' fit for oscillation point # 2. . . . 76
61 Distribution of residuals of the four oscillation parameters in the '4 + 0' fit for oscillation point # 3. . . . 77
62 Distribution of residuals of the four oscillation parameters in the '4 + 0' fit for oscillation point # 4. . . . 77
63 Distribution of residuals of the four oscillation parameters in the '4 + 0' fit for oscillation point # 5. . . . 77
64 Distribution of residuals of the four oscillation parameters in the '4 + 0' fit for oscillation point # 6. . . . 77
65 Distribution of residuals of the four oscillation parameters in the '4 + 0' fit for oscillation point # 7. . . . 78
66 Distribution of residuals of the four oscillation parameters in the '4 + 0' fit for oscillation point # 8. . . . 78
67 Distribution of residuals for $sin^2(\theta_{23})$ in the '4 + 0' fit for oscillation point # 1 with 3.010×10^{22} POT. . . . 78
68 Distribution of residuals of the four oscillation parameters in the '4 + 83' fit for oscillation point # 0. . . . 81
69 Distribution of residuals of the four oscillation parameters in the '4 + 83' fit for oscillation point # 9. . . . 81
70 Distribution of residuals of the four oscillation parameters in the '4 + 83' fit for oscillation point # 1. . . . 81

71 Distribution of residuals of the four oscillation parameters in the '4 + 83' fit for oscillation point # 2. 81
72 Distribution of residuals of the four oscillation parameters in the '4 + 83' fit for oscillation point # 3. 82
73 Distribution of residuals of the four oscillation parameters in the '4 + 83' fit for oscillation point # 4. 82
74 Distribution of residuals of the four oscillation parameters in the '4 + 83' fit for oscillation point # 5. 82
75 Distribution of residuals of the four oscillation parameters in the '4 + 83' fit for oscillation point # 6. 82
76 Distribution of residuals of the four oscillation parameters in the '4 + 83' fit for oscillation point # 7. 83
77 Distribution of residuals of the four oscillation parameters in the '4 + 83' fit for oscillation point # 8. 83
78 Distribution of residuals of the BANFF (0-9) systematic parameters in the '4 + 83' fit for oscillation point # 0. 84
79 Distribution of residuals of the BANFF (10-19) systematic parameters in the '4 + 83' fit for oscillation point # 0. 85
80 Distribution of residuals of the BANFF (20-29) systematic parameters in the '4 + 83' fit for oscillation point # 0. 86
81 Distribution of residuals of the BANFF (30-32) and uncorrelated cross sections (I) systematic parameters in the '4 + 83' fit for oscillation point # 0. 87
82 Distribution of residuals of uncorrelated cross sections (II) systematic parameters in the '4 + 83' fit for oscillation point # 0. 88
83 Distribution of residuals of SK detector (I) systematic parameters in the '4 + 83' fit for oscillation point # 0. . . 89
84 Distribution of residuals of SK detector (II) systematic parameters in the '4 + 83' fit for oscillation point # 0. . 90
85 Distribution of residuals of FSI+SI (I) systematic parameters in the '4 + 83' fit for oscillation point # 0. 91
86 Distribution of residuals of FSI+SI (I) systematic parameters in the '4 + 83' fit for oscillation point # 0. 92
87 Summary of distribution of residuals of systematic parameters in the '4 + 83' fit for oscillation point # 0. . . . 93
88 Summary of distribution of residuals of systematic parameters in the '4 + 83' fit for oscillation point # 1. . . . 93
89 Summary of distribution of residuals of systematic parameters in the '4 + 83' fit for oscillation point # 2. . . . 93
90 Summary of distribution of residuals of systematic parameters in the '4 + 83' fit for oscillation point # 3. . . . 93
91 Summary of distribution of residuals of systematic parameters in the '4 + 83' fit for oscillation point # 4. . . . 94
92 Summary of distribution of residuals of systematic parameters in the '4 + 83' fit for oscillation point # 5. . . . 94
93 Summary of distribution of residuals of systematic parameters in the '4 + 83' fit for oscillation point # 6. . . . 94
94 Summary of distribution of residuals of systematic parameters in the '4 + 83' fit for oscillation point # 7. . . . 94
95 Summary of distribution of residuals of systematic parameters in the '4 + 83' fit for oscillation point # 8. . . . 94
96 Summary of distribution of residuals of systematic parameters in the '4 + 83' fit for oscillation point # 9. . . . 94
97 $\Delta\chi^2$ as function of $|\Delta m^2|$ for fake dataset #0. At each point, χ^2 was minimized with respect to $\sin^2\theta_{23}$, $\sin^2\theta_{13}$, δ_{CP} and all relevant nuisance parameters for the joint analysis (black) and with respect to $\sin^2\theta_{23}$ and all relevant nuisance parameters for the disappearance analysis (blue). 97
98 $\Delta\chi^2$ as function of $sin^2\theta_{23}$ for fake dataset #0. At each point, χ^2 was minimized with respect to $|\Delta m^2|$, $\sin^2\theta_{13}$, δ_{CP} and all relevant nuisance parameters for the joint analysis (black) and with respect to $\sin^2\theta_{23}$ and all relevant nuisance parameters for the disappearance analysis (blue). 97
99 $\Delta\chi^2$ as function of $sin^2\theta_{13}$ for fake dataset #0. At each point, χ^2 was minimized with respect to $\sin^2\theta_{23}$, $\sin^2\theta_{13}$, δ_{CP} and all relevant nuisance parameters for the joint analysis (black) and with respect to all relevant nuisance parameters (δ_{CP} is fixed to 0) for the appearance analysis (red). 97
100 $\Delta\chi^2$ as function of δ_{CP} for fake dataset #0. At each point, χ^2 was minimized with respect to all oscillation parameters not shown (and not considered to be fixed) and all relevant nuisance parameters. 97
101 68% and 90% CL regions in ($sin^2\theta_{23}$, $|\Delta m^2|$) space for fake dataset #0. At each point, χ^2 was minimized with respect to $\sin^2\theta_{13}$, δ_{CP} and all relevant nuisance parameters for the joint analysis (black) and with respect to all relevant nuisance parameters for the disappearance analysis (blue). 97
102 68% and 90% CL regions in ($sin^2\theta_{13}$, $|\Delta m^2|$) space for fake dataset #0. At each point, χ^2 was minimized with respect to all oscillation parameters not shown (and not considered to be fixed) and all relevant nuisance parameters. 97
103 68% and 90% CL regions in ($sin^2\theta_{13}$, δ_{CP}) space for fake dataset #0. At each point, χ^2 was minimized with respect to $|\Delta m^2|$, $\sin^2\theta_{23}$ and all relevant nuisance parameters for the joint analysis (black) and with respect to all relevant nuisance parameters for the appearance analysis (red). Notice that different methods are used to construct confidence regions for the joint analysis (global minimum) and for the stand-alone appearance analysis (raster scan). 97
104 68% and 90% CL regions in ($sin^2\theta_{23}$, $sin^2\theta_{13}$) space for fake dataset #0. At each point, χ^2 was minimized with respect to all oscillation parameters not shown (and not considered to be fixed) and all relevant nuisance parameters. 97
105 $\Delta\chi^2$ as function of $|\Delta m^2|$ for fake dataset #1. At each point, χ^2 was minimized with respect to $\sin^2\theta_{23}$, $\sin^2\theta_{13}$, δ_{CP} and all relevant nuisance parameters for the joint analysis (black) and with respect to $\sin^2\theta_{23}$ and all relevant nuisance parameters for the disappearance analysis (blue). 98

106 $\Delta\chi^2$ as function of $sin^2\theta_{23}$ for fake dataset #1. At each point, χ^2 was minimized with respect to $|\Delta m^2|$, $\sin^2\theta_{13}$, δ_{CP} and all relevant nuisance parameters for the joint analysis (black) and with respect to $\sin^2\theta_{23}$ and all relevant nuisance parameters for the disappearance analysis (blue). 98
107 $\Delta\chi^2$ as function of $sin^2\theta_{13}$ for fake dataset #1. At each point, χ^2 was minimized with respect to $\sin^2\theta_{23}$, $\sin^2\theta_{13}$, δ_{CP} and all relevant nuisance parameters for the joint analysis (black) and with respect to all relevant nuisance parameters (δ_{CP} is fixed to 0) for the appearance analysis (red). 98
108 $\Delta\chi^2$ as function of δ_{CP} for fake dataset #1. At each point, χ^2 was minimized with respect to all oscillation parameters not shown (and not considered to be fixed) and all relevant nuisance parameters. 98
109 68% and 90% CL regions in ($sin^2\theta_{23}$, $|\Delta m^2|$) space for fake dataset #1. At each point, χ^2 was minimized with respect to $\sin^2\theta_{13}$, δ_{CP} and all relevant nuisance parameters for the joint analysis (black) and with respect to all relevant nuisance parameters for the disappearance analysis (blue). 98
110 68% and 90% CL regions in ($sin^2\theta_{13}$, $|\Delta m^2|$) space for fake dataset #1. At each point, χ^2 was minimized with respect to all oscillation parameters not shown (and not considered to be fixed) and all relevant nuisance parameters. 98
111 68% and 90% CL regions in ($sin^2\theta_{13}$, δ_{CP}) space for fake dataset #1. At each point, χ^2 was minimized with respect to $|\Delta m^2|$, $\sin^2\theta_{23}$ and all relevant nuisance parameters for the joint analysis (black) and with respect to all relevant nuisance parameters for the appearance analysis (red). Notice that different methods are used to construct confidence regions for the joint analysis (global minimum) and for the stand-alone appearance analysis (raster scan). 98
112 68% and 90% CL regions in ($sin^2\theta_{23}$, $sin^2\theta_{13}$) space for fake dataset #1. At each point, χ^2 was minimized with respect to all oscillation parameters not shown (and not considered to be fixed) and all relevant nuisance parameters. 98
113 $\Delta\chi^2$ as function of $|\Delta m^2|$ for fake dataset #2. At each point, χ^2 was minimized with respect to $\sin^2\theta_{23}$, $\sin^2\theta_{13}$, δ_{CP} and all relevant nuisance parameters for the joint analysis (black) and with respect to $\sin^2\theta_{23}$ and all relevant nuisance parameters for the disappearance analysis (blue). 99
114 $\Delta\chi^2$ as function of $sin^2\theta_{23}$ for fake dataset #2. At each point, χ^2 was minimized with respect to $|\Delta m^2|$, $\sin^2\theta_{13}$, δ_{CP} and all relevant nuisance parameters for the joint analysis (black) and with respect to $\sin^2\theta_{23}$ and all relevant nuisance parameters for the disappearance analysis (blue). 99
115 $\Delta\chi^2$ as function of $sin^2\theta_{13}$ for fake dataset #2. At each point, χ^2 was minimized with respect to $\sin^2\theta_{23}$, $\sin^2\theta_{13}$, δ_{CP} and all relevant nuisance parameters for the joint analysis (black) and with respect to all relevant nuisance parameters (δ_{CP} is fixed to 0) for the appearance analysis (red). 99
116 $\Delta\chi^2$ as function of δ_{CP} for fake dataset #2. At each point, χ^2 was minimized with respect to all oscillation parameters not shown (and not considered to be fixed) and all relevant nuisance parameters. 99
117 68% and 90% CL regions in ($sin^2\theta_{23}$, $|\Delta m^2|$) space for fake dataset #2. At each point, χ^2 was minimized with respect to $\sin^2\theta_{13}$, δ_{CP} and all relevant nuisance parameters for the joint analysis (black) and with respect to all relevant nuisance parameters for the disappearance analysis (blue). 99
118 68% and 90% CL regions in ($sin^2\theta_{13}$, $|\Delta m^2|$) space for fake dataset #2. At each point, χ^2 was minimized with respect to all oscillation parameters not shown (and not considered to be fixed) and all relevant nuisance parameters. 99
119 68% and 90% CL regions in ($sin^2\theta_{13}$, δ_{CP}) space for fake dataset #2. At each point, χ^2 was minimized with respect to $|\Delta m^2|$, $\sin^2\theta_{23}$ and all relevant nuisance parameters for the joint analysis (black) and with respect to all relevant nuisance parameters for the appearance analysis (red). Notice that different methods are used to construct confidence regions for the joint analysis (global minimum) and for the stand-alone appearance analysis (raster scan). 99
120 68% and 90% CL regions in ($sin^2\theta_{23}$, $sin^2\theta_{13}$) space for fake dataset #2. At each point, χ^2 was minimized with respect to all oscillation parameters not shown (and not considered to be fixed) and all relevant nuisance parameters. 99
121 $\Delta\chi^2$ as function of $|\Delta m^2|$ for fake dataset #3. At each point, χ^2 was minimized with respect to $\sin^2\theta_{23}$, $\sin^2\theta_{13}$, δ_{CP} and all relevant nuisance parameters for the joint analysis (black) and with respect to $\sin^2\theta_{23}$ and all relevant nuisance parameters for the disappearance analysis (blue). 100
122 $\Delta\chi^2$ as function of $sin^2\theta_{23}$ for fake dataset #3. At each point, χ^2 was minimized with respect to $|\Delta m^2|$, $\sin^2\theta_{13}$, δ_{CP} and all relevant nuisance parameters for the joint analysis (black) and with respect to $\sin^2\theta_{23}$ and all relevant nuisance parameters for the disappearance analysis (blue). 100
123 $\Delta\chi^2$ as function of $sin^2\theta_{13}$ for fake dataset #3. At each point, χ^2 was minimized with respect to $\sin^2\theta_{23}$, $\sin^2\theta_{13}$, δ_{CP} and all relevant nuisance parameters for the joint analysis (black) and with respect to all relevant nuisance parameters (δ_{CP} is fixed to 0) for the appearance analysis (red). 100

124 $\Delta\chi^2$ as function of δ_{CP} for fake dataset #3. At each point, χ^2 was minimized with respect to all oscillation parameters not shown (and not considered to be fixed) and all relevant nuisance parameters. 100
125 68% and 90% CL regions in ($sin^2\theta_{23}$, $|\Delta m^2|$) space for fake dataset #3. At each point, χ^2 was minimized with respect to $\sin^2\theta_{13}$, δ_{CP} and all relevant nuisance parameters for the joint analysis (black) and with respect to all relevant nuisance parameters for the disappearance analysis (blue). 100
126 68% and 90% CL regions in ($sin^2\theta_{13}$, $|\Delta m^2|$) space for fake dataset #3. At each point, χ^2 was minimized with respect to all oscillation parameters not shown (and not considered to be fixed) and all relevant nuisance parameters. 100
127 68% and 90% CL regions in ($sin^2\theta_{13}$, δ_{CP}) space for fake dataset #3. At each point, χ^2 was minimized with respect to $|\Delta m^2|$, $\sin^2\theta_{23}$ and all relevant nuisance parameters for the joint analysis (black) and with respect to all relevant nuisance parameters for the appearance analysis (red). Notice that different methods are used to construct confidence regions for the joint analysis (global minimum) and for the stand-alone appearance analysis (raster scan). 100
128 68% and 90% CL regions in ($sin^2\theta_{23}$, $sin^2\theta_{13}$) space for fake dataset #3. At each point, χ^2 was minimized with respect to all oscillation parameters not shown (and not considered to be fixed) and all relevant nuisance parameters. 100
129 $\Delta\chi^2$ as function of $|\Delta m^2|$ for fake dataset #4. At each point, χ^2 was minimized with respect to $\sin^2\theta_{23}$, $\sin^2\theta_{13}$, δ_{CP} and all relevant nuisance parameters for the joint analysis (black) and with respect to $\sin^2\theta_{23}$ and all relevant nuisance parameters for the disappearance analysis (blue). 101
130 $\Delta\chi^2$ as function of $sin^2\theta_{23}$ for fake dataset #4. At each point, χ^2 was minimized with respect to $|\Delta m^2|$, $\sin^2\theta_{13}$, δ_{CP} and all relevant nuisance parameters for the joint analysis (black) and with respect to $\sin^2\theta_{23}$ and all relevant nuisance parameters for the disappearance analysis (blue). 101
131 $\Delta\chi^2$ as function of $sin^2\theta_{13}$ for fake dataset #4. At each point, χ^2 was minimized with respect to $\sin^2\theta_{23}$, $\sin^2\theta_{13}$, δ_{CP} and all relevant nuisance parameters for the joint analysis (black) and with respect to all relevant nuisance parameters (δ_{CP} is fixed to 0) for the appearance analysis (red). 101
132 $\Delta\chi^2$ as function of δ_{CP} for fake dataset #4. At each point, χ^2 was minimized with respect to all oscillation parameters not shown (and not considered to be fixed) and all relevant nuisance parameters. 101
133 68% and 90% CL regions in ($sin^2\theta_{23}$, $|\Delta m^2|$) space for fake dataset #4. At each point, χ^2 was minimized with respect to $\sin^2\theta_{13}$, δ_{CP} and all relevant nuisance parameters for the joint analysis (black) and with respect to all relevant nuisance parameters for the disappearance analysis (blue). 101
134 68% and 90% CL regions in ($sin^2\theta_{13}$, $|\Delta m^2|$) space for fake dataset #4. At each point, χ^2 was minimized with respect to all oscillation parameters not shown (and not considered to be fixed) and all relevant nuisance parameters. 101
135 68% and 90% CL regions in ($sin^2\theta_{13}$, δ_{CP}) space for fake dataset #4. At each point, χ^2 was minimized with respect to $|\Delta m^2|$, $\sin^2\theta_{23}$ and all relevant nuisance parameters for the joint analysis (black) and with respect to all relevant nuisance parameters for the appearance analysis (red). Notice that different methods are used to construct confidence regions for the joint analysis (global minimum) and for the stand-alone appearance analysis (raster scan). 101
136 68% and 90% CL regions in ($sin^2\theta_{23}$, $sin^2\theta_{13}$) space for fake dataset #4. At each point, χ^2 was minimized with respect to all oscillation parameters not shown (and not considered to be fixed) and all relevant nuisance parameters. 101
137 $\Delta\chi^2$ as function of $|\Delta m^2|$ for fake dataset #5. At each point, χ^2 was minimized with respect to $\sin^2\theta_{23}$, $\sin^2\theta_{13}$, δ_{CP} and all relevant nuisance parameters for the joint analysis (black) and with respect to $\sin^2\theta_{23}$ and all relevant nuisance parameters for the disappearance analysis (blue). 102
138 $\Delta\chi^2$ as function of $sin^2\theta_{23}$ for fake dataset #5. At each point, χ^2 was minimized with respect to $|\Delta m^2|$, $\sin^2\theta_{13}$, δ_{CP} and all relevant nuisance parameters for the joint analysis (black) and with respect to $\sin^2\theta_{23}$ and all relevant nuisance parameters for the disappearance analysis (blue). 102
139 $\Delta\chi^2$ as function of $sin^2\theta_{13}$ for fake dataset #5. At each point, χ^2 was minimized with respect to $\sin^2\theta_{23}$, $\sin^2\theta_{13}$, δ_{CP} and all relevant nuisance parameters for the joint analysis (black) and with respect to all relevant nuisance parameters (δ_{CP} is fixed to 0) for the appearance analysis (red). 102
140 $\Delta\chi^2$ as function of δ_{CP} for fake dataset #5. At each point, χ^2 was minimized with respect to all oscillation parameters not shown (and not considered to be fixed) and all relevant nuisance parameters. 102
141 68% and 90% CL regions in ($sin^2\theta_{23}$, $|\Delta m^2|$) space for fake dataset #5. At each point, χ^2 was minimized with respect to $\sin^2\theta_{13}$, δ_{CP} and all relevant nuisance parameters for the joint analysis (black) and with respect to all relevant nuisance parameters for the disappearance analysis (blue). 102

142 68% and 90% CL regions in ($sin^2\theta_{13}$, $|\Delta m^2|$) space for fake dataset #5. At each point, χ^2 was minimized with respect to all oscillation parameters not shown (and not considered to be fixed) and all relevant nuisance parameters. . . . 102
143 68% and 90% CL regions in ($sin^2\theta_{13}$, δ_{CP}) space for fake dataset #5. At each point, χ^2 was minimized with respect to $|\Delta m^2|$, $\sin^2\theta_{23}$ and all relevant nuisance parameters for the joint analysis (black) and with respect to all relevant nuisance parameters for the appearance analysis (red). Notice that different methods are used to construct confidence regions for the joint analysis (global minimum) and for the stand-alone appearance analysis (raster scan). . . . 102
144 68% and 90% CL regions in ($sin^2\theta_{23}$, $sin^2\theta_{13}$) space for fake dataset #5. At each point, χ^2 was minimized with respect to all oscillation parameters not shown (and not considered to be fixed) and all relevant nuisance parameters. . . . 102
145 Single μ-like ring event best-fit reconstructed energy spectrum to fake dataset #6. . . . 104
146 Single e-like ring event best-fit reconstructed energy spectrum to fake dataset #6. . . . 104
147 Systematic parameter pulls for the oscillation fit to fake dataset #6. . . . 104
148 Distribution of χ^2_{gof}, the goodness-of-fit (gof) χ^2, from 1k toy MC experiments generated at dataset #6 joint 3-flavour analysis best-fit oscillation point. The χ^2_{gof} value for the dataset #6 (χ^2_{data}) is highlighted. All χ^2_{gof} values were computed using the 5 (single μ-like ring) + 1 (single e-like ring) reconstructed energy binning scheme described in Sec. 6.2, . . . 105
149 Distribution of χ^2_{gof} from 1k toy MC experiments generated at the dataset #6 stand-alone 3-flavour ν_μ disappearance analysis best-fit oscillation point. The χ^2_{gof} value for the dataset #6 (χ^2_{data}) is highlighted. All χ^2_{gof} values were computed using the 5 (single μ-like ring) reconstructed energy binning scheme described in Sec. 6.2, . . . 105
150 Distribution of χ^2_{gof} from 1k toy MC experiments generated at the dataset #6 stand-alone 3-flavour ν_e appearance analysis best-fit oscillation point. The χ^2_{gof} value for the dataset #6 (χ^2_{data}) is highlighted. All χ^2_{gof} values were computed using a single reconstructed energy bin, as described in Sec. 6.2, . . . 105
151 $\Delta\chi^2$ as function of $|\Delta m^2|$ for fake dataset #6. At each point, χ^2 was minimized with respect to $\sin^2\theta_{23}$, $\sin^2\theta_{13}$, δ_{CP} and all relevant nuisance parameters for the joint analysis (black) and with respect to $\sin^2\theta_{23}$ and all relevant nuisance parameters for the disappearance analysis (blue). . . . 106
152 $\Delta\chi^2$ as function of $sin^2\theta_{23}$ for fake dataset #6. At each point, χ^2 was minimized with respect to $|\Delta m^2|$, $\sin^2\theta_{13}$, δ_{CP} and all relevant nuisance parameters for the joint analysis (black) and with respect to $\sin^2\theta_{23}$ and all relevant nuisance parameters for the disappearance analysis (blue). . . . 106
153 $\Delta\chi^2$ as function of $sin^2\theta_{13}$ for fake dataset #6. At each point, χ^2 was minimized with respect to $\sin^2\theta_{23}$, $\sin^2\theta_{13}$, δ_{CP} and all relevant nuisance parameters for the joint analysis (black) and with respect to all relevant nuisance parameters (δ_{CP} is fixed to 0) for the appearance analysis (red). . . . 106
154 $\Delta\chi^2$ as function of δ_{CP} for fake dataset #6. At each point, χ^2 was minimized with respect to all oscillation parameters not shown (and not considered to be fixed) and all relevant nuisance parameters. . . . 106
155 68% and 90% CL regions in ($sin^2\theta_{23}$, $|\Delta m^2|$) space for fake dataset #6. At each point, χ^2 was minimized with respect to $\sin^2\theta_{13}$, δ_{CP} and all relevant nuisance parameters for the joint analysis (black) and with respect to all relevant nuisance parameters for the disappearance analysis (blue). . . . 106
156 68% and 90% CL regions in ($sin^2\theta_{13}$, $|\Delta m^2|$) space for fake dataset #6. At each point, χ^2 was minimized with respect to all oscillation parameters not shown (and not considered to be fixed) and all relevant nuisance parameters. . . . 106
157 68% and 90% CL regions in ($sin^2\theta_{13}$, δ_{CP}) space for fake dataset #6. At each point, χ^2 was minimized with respect to $|\Delta m^2|$, $\sin^2\theta_{23}$ and all relevant nuisance parameters for the joint analysis (black) and with respect to all relevant nuisance parameters for the appearance analysis (red). Notice that different methods are used to construct confidence regions for the joint analysis (global minimum) and for the stand-alone appearance analysis (raster scan). . . . 106
158 68% and 90% CL regions in ($sin^2\theta_{23}$, $sin^2\theta_{13}$) space for fake dataset #6. At each point, χ^2 was minimized with respect to all oscillation parameters not shown (and not considered to be fixed) and all relevant nuisance parameters. . . . 106
159 Single μ-like ring event best-fit reconstructed energy spectrum to fake dataset #7. . . . 107
160 Single e-like ring event best-fit reconstructed energy spectrum to fake dataset #7. . . . 107
161 Systematic parameter pulls for the oscillation fit to fake dataset #7. . . . 107

162 Distribution of χ^2_{gof}, the goodness-of-fit (gof) χ^2, from 1k toy MC experiments generated at dataset #7 joint 3-flavour analysis best-fit oscillation point. The χ^2_{gof} value for the dataset #7 (χ^2_{data}) is highlighted. All χ^2_{gof} values were computed using the 5 (single μ-like ring) + 3 (single e-like ring) reconstructed energy binning scheme described in Sec. 6.2. . . . 108
163 Distribution of χ^2_{gof} from 1k toy MC experiments generated at the dataset #7 stand-alone 3-flavour ν_μ disappearance analysis best-fit oscillation point. The χ^2_{gof} value for the dataset #7 (χ^2_{data}) is highlighted. All χ^2_{gof} values were computed using the 5 (single μ-like ring) reconstructed energy binning scheme described in Sec. 6.2. . . . 108
164 Distribution of χ^2_{gof} from 1k toy MC experiments generated at the dataset #7 stand-alone 3-flavour ν_e appearance analysis best-fit oscillation point. The χ^2_{gof} value for the dataset #7 (χ^2_{data}) is highlighted. All χ^2_{gof} values were computed using the 3 (single e-like ring) reconstructed energy binning scheme as described in Sec. 6.2. . 108
165 $\Delta\chi^2$ as function of $|\Delta m^2|$ for fake dataset #7. At each point, χ^2 was minimized with respect to $\sin^2\theta_{23}$, $\sin^2\theta_{13}$, δ_{CP} and all relevant nuisance parameters for the joint analysis (black) and with respect to $\sin^2\theta_{23}$ and all relevant nuisance parameters for the disappearance analysis (blue). . . . 109
166 $\Delta\chi^2$ as function of $sin^2\theta_{23}$ for fake dataset #7. At each point, χ^2 was minimized with respect to $|\Delta m^2|$, $\sin^2\theta_{13}$, δ_{CP} and all relevant nuisance parameters for the joint analysis (black) and with respect to $\sin^2\theta_{23}$ and all relevant nuisance parameters for the disappearance analysis (blue). . . . 109
167 $\Delta\chi^2$ as function of $sin^2\theta_{13}$ for fake dataset #7. At each point, χ^2 was minimized with respect to $\sin^2\theta_{23}$, $\sin^2\theta_{13}$, δ_{CP} and all relevant nuisance parameters for the joint analysis (black) and with respect to all relevant nuisance parameters (δ_{CP} is fixed to 0) for the appearance analysis (red). . . . 109
168 $\Delta\chi^2$ as function of δ_{CP} for fake dataset #7. At each point, χ^2 was minimized with respect to all oscillation parameters not shown (and not considered to be fixed) and all relevant nuisance parameters. . . . 109
169 68% and 90% CL regions in ($sin^2\theta_{23}$, $|\Delta m^2|$) space for fake dataset #7. At each point, χ^2 was minimized with respect to $\sin^2\theta_{13}$, δ_{CP} and all relevant nuisance parameters for the joint analysis (black) and with respect to all relevant nuisance parameters for the disappearance analysis (blue). . . . 109
170 68% and 90% CL regions in ($sin^2\theta_{13}$, $|\Delta m^2|$) space for fake dataset #7. At each point, χ^2 was minimized with respect to all oscillation parameters not shown (and not considered to be fixed) and all relevant nuisance parameters. . . . 109
171 68% and 90% CL regions in ($sin^2\theta_{13}$, δ_{CP}) space for fake dataset #7. At each point, χ^2 was minimized with respect to $|\Delta m^2|$, $\sin^2\theta_{23}$ and all relevant nuisance parameters for the joint analysis (black) and with respect to all relevant nuisance parameters for the appearance analysis (red). Notice that different methods are used to construct confidence regions for the joint analysis (global minimum) and for the stand-alone appearance analysis (raster scan). . . . 109
172 68% and 90% CL regions in ($sin^2\theta_{23}$, $sin^2\theta_{13}$) space for fake dataset #7. At each point, χ^2 was minimized with respect to all oscillation parameters not shown (and not considered to be fixed) and all relevant nuisance parameters. . . . 109
173 Single μ-like ring event best-fit reconstructed energy spectrum to fake dataset #8. . . . 110
174 Single e-like ring event best-fit reconstructed energy spectrum to fake dataset #8. . . . 110
175 Systematic parameter pulls for the oscillation fit to fake dataset #8. . . . 110
176 Distribution of χ^2_{gof}, the goodness-of-fit (gof) χ^2, from 1k toy MC experiments generated at dataset #8 joint 3-flavour analysis best-fit oscillation point. The χ^2_{gof} value for the dataset #8 (χ^2_{data}) is highlighted. All χ^2_{gof} values were computed using the 5 (single μ-like ring) + 3 (single e-like ring) reconstructed energy binning scheme described in Sec. 6.2. . . . 111
177 Distribution of χ^2_{gof} from 1k toy MC experiments generated at the dataset #8 stand-alone 3-flavour ν_μ disappearance analysis best-fit oscillation point. The χ^2_{gof} value for the dataset #8 (χ^2_{data}) is highlighted. All χ^2_{gof} values were computed using the 5 (single μ-like ring) reconstructed energy binning scheme described in Sec. 6.2. . . . 111
178 Distribution of χ^2_{gof} from 1k toy MC experiments generated at the dataset #8 stand-alone 3-flavour ν_e appearance analysis best-fit oscillation point. The χ^2_{gof} value for the dataset #8 (χ^2_{data}) is highlighted. All χ^2_{gof} values were computed using the 3 (single e-like ring) reconstructed energy binning scheme as described in Sec. 6.2. . 111
179 $\Delta\chi^2$ as function of $|\Delta m^2|$ for fake dataset #8. At each point, χ^2 was minimized with respect to $\sin^2\theta_{23}$, $\sin^2\theta_{13}$, δ_{CP} and all relevant nuisance parameters for the joint analysis (black) and with respect to $\sin^2\theta_{23}$ and all relevant nuisance parameters for the disappearance analysis (blue). . . . 112
180 $\Delta\chi^2$ as function of $sin^2\theta_{23}$ for fake dataset #8. At each point, χ^2 was minimized with respect to $|\Delta m^2|$, $\sin^2\theta_{13}$, δ_{CP} and all relevant nuisance parameters for the joint analysis (black) and with respect to $\sin^2\theta_{23}$ and all relevant nuisance parameters for the disappearance analysis (blue). . . . 112

181 $\Delta\chi^2$ as function of $sin^2\theta_{13}$ for fake dataset #8. At each point, χ^2 was minimized with respect to $\sin^2\theta_{23}$, $\sin^2\theta_{13}$, δ_{CP} and all relevant nuisance parameters for the joint analysis (black) and with respect to all relevant nuisance parameters (δ_{CP} is fixed to 0) for the appearance analysis (red). 112
182 $\Delta\chi^2$ as function of δ_{CP} for fake dataset #8. At each point, χ^2 was minimized with respect to all oscillation parameters not shown (and not considered to be fixed) and all relevant nuisance parameters. 112
183 68% and 90% CL regions in ($sin^2\theta_{23}$, $|\Delta m^2|$) space for fake dataset #8. At each point, χ^2 was minimized with respect to $\sin^2\theta_{13}$, δ_{CP} and all relevant nuisance parameters for the joint analysis (black) and with respect to all relevant nuisance parameters for the disappearance analysis (blue). 112
184 68% and 90% CL regions in ($sin^2\theta_{13}$, $|\Delta m^2|$) space for fake dataset #8. At each point, χ^2 was minimized with respect to all oscillation parameters not shown (and not considered to be fixed) and all relevant nuisance parameters. 112
185 68% and 90% CL regions in ($sin^2\theta_{13}$, δ_{CP}) space for fake dataset #8. At each point, χ^2 was minimized with respect to $|\Delta m^2|$, $\sin^2\theta_{23}$ and all relevant nuisance parameters for the joint analysis (black) and with respect to all relevant nuisance parameters for the appearance analysis (red). Notice that different methods are used to construct confidence regions for the joint analysis (global minimum) and for the stand-alone appearance analysis (raster scan). 112
186 68% and 90% CL regions in ($sin^2\theta_{23}$, $sin^2\theta_{13}$) space for fake dataset #8. At each point, χ^2 was minimized with respect to all oscillation parameters not shown (and not considered to be fixed) and all relevant nuisance parameters. 112
187 Single μ-like ring event best-fit reconstructed energy spectrum to fake dataset #9. 113
188 Single e-like ring event best-fit reconstructed energy spectrum to fake dataset #9. 113
189 Systematic parameter pulls for the oscillation fit to fake dataset #9. 113
190 Distribution of χ^2_{gof}, the goodness-of-fit (gof) χ^2, from 1k toy MC experiments generated at dataset #9 joint 3-flavour analysis best-fit oscillation point. The χ^2_{gof} value for the dataset #9 (χ^2_{data}) is highlighted. All χ^2_{gof} values were computed using the 5 (single μ-like ring) + 3 (single e-like ring) reconstructed energy binning scheme described in Sec. 6.2. 114
191 Distribution of χ^2_{gof} from 1k toy MC experiments generated at the dataset #9 stand-alone 3-flavour ν_μ disappearance analysis best-fit oscillation point. The χ^2_{gof} value for the dataset #9 (χ^2_{data}) is highlighted. All χ^2_{gof} values were computed using the 5 (single μ-like ring) reconstructed energy binning scheme described in Sec. 6.2. 114
192 Distribution of χ^2_{gof} from 1k toy MC experiments generated at the dataset #9 stand-alone 3-flavour ν_e appearance analysis best-fit oscillation point. The χ^2_{gof} value for the dataset #9 (χ^2_{data}) is highlighted. All χ^2_{gof} values were computed using the 3 (single e-like ring) reconstructed energy binning scheme as described in Sec. 6.2. . 114
193 $\Delta\chi^2$ as function of $|\Delta m^2|$ for fake dataset #9. At each point, χ^2 was minimized with respect to $\sin^2\theta_{23}$, $\sin^2\theta_{13}$, δ_{CP} and all relevant nuisance parameters for the joint analysis (black) and with respect to $\sin^2\theta_{23}$ and all relevant nuisance parameters for the disappearance analysis (blue). 115
194 $\Delta\chi^2$ as function of $sin^2\theta_{23}$ for fake dataset #9. At each point, χ^2 was minimized with respect to $|\Delta m^2|$, $\sin^2\theta_{13}$, δ_{CP} and all relevant nuisance parameters for the joint analysis (black) and with respect to $\sin^2\theta_{23}$ and all relevant nuisance parameters for the disappearance analysis (blue). 115
195 $\Delta\chi^2$ as function of $sin^2\theta_{13}$ for fake dataset #9. At each point, χ^2 was minimized with respect to $\sin^2\theta_{23}$, $\sin^2\theta_{13}$, δ_{CP} and all relevant nuisance parameters for the joint analysis (black) and with respect to all relevant nuisance parameters (δ_{CP} is fixed to 0) for the appearance analysis (red). 115
196 $\Delta\chi^2$ as function of δ_{CP} for fake dataset #9. At each point, χ^2 was minimized with respect to all oscillation parameters not shown (and not considered to be fixed) and all relevant nuisance parameters. 115
197 68% and 90% CL regions in ($sin^2\theta_{23}$, $|\Delta m^2|$) space for fake dataset #9. At each point, χ^2 was minimized with respect to $\sin^2\theta_{13}$, δ_{CP} and all relevant nuisance parameters for the joint analysis (black) and with respect to all relevant nuisance parameters for the disappearance analysis (blue). 115
198 68% and 90% CL regions in ($sin^2\theta_{13}$, $|\Delta m^2|$) space for fake dataset #9. At each point, χ^2 was minimized with respect to all oscillation parameters not shown (and not considered to be fixed) and all relevant nuisance parameters. 115
199 68% and 90% CL regions in ($sin^2\theta_{13}$, δ_{CP}) space for fake dataset #9. At each point, χ^2 was minimized with respect to $|\Delta m^2|$, $\sin^2\theta_{23}$ and all relevant nuisance parameters for the joint analysis (black) and with respect to all relevant nuisance parameters for the appearance analysis (red). Notice that different methods are used to construct confidence regions for the joint analysis (global minimum) and for the stand-alone appearance analysis (raster scan). 115

200 68% and 90% CL regions in ($sin^2\theta_{23}$, $sin^2\theta_{13}$) space for fake dataset #9. At each point, χ^2 was minimized with respect to all oscillation parameters not shown (and not considered to be fixed) and all relevant nuisance parameters. . . . 115
201 Single μ-like ring event best-fit reconstructed energy spectrum to fake dataset #10. . . . 116
202 Single e-like ring event best-fit reconstructed energy spectrum to fake dataset #10. . . . 116
203 Systematic parameter pulls for the oscillation fit to fake dataset #10. . . . 116
204 Distribution of χ^2_{gof}, the goodness-of-fit (gof) χ^2, from 1k toy MC experiments generated at dataset #10 joint 3-flavour analysis best-fit oscillation point. The χ^2_{gof} value for the dataset #10 (χ^2_{data}) is highlighted. All χ^2_{gof} values were computed using the 5 (single μ-like ring) + 3 (single e-like ring) reconstructed energy binning scheme described in Sec. 6.2. . . . 117
205 Distribution of χ^2_{gof} from 1k toy MC experiments generated at the dataset #10 stand-alone 3-flavour ν_μ disappearance analysis best-fit oscillation point. The χ^2_{gof} value for the dataset #10 (χ^2_{data}) is highlighted. All χ^2_{gof} values were computed using the 5 (single μ-like ring) reconstructed energy binning scheme described in Sec. 6.2. . . . 117
206 Distribution of χ^2_{gof} from 1k toy MC experiments generated at the dataset #10 stand-alone 3-flavour ν_e appearance analysis best-fit oscillation point. The χ^2_{gof} value for the dataset #10 (χ^2_{data}) is highlighted. All χ^2_{gof} values were computed using the 3 (single e-like ring) reconstructed energy binning scheme as described in Sec. 6.2. . . . 117
207 $\Delta\chi^2$ as function of $|\Delta m^2|$ for fake dataset #10. At each point, χ^2 was minimized with respect to $\sin^2\theta_{23}$, $\sin^2\theta_{13}$, δ_{CP} and all relevant nuisance parameters for the joint analysis (black) and with respect to $\sin^2\theta_{23}$ and all relevant nuisance parameters for the disappearance analysis (blue). . . . 118
208 $\Delta\chi^2$ as function of $sin^2\theta_{23}$ for fake dataset #10. At each point, χ^2 was minimized with respect to $|\Delta m^2|$, $\sin^2\theta_{13}$, δ_{CP} and all relevant nuisance parameters for the joint analysis (black) and with respect to $\sin^2\theta_{23}$ and all relevant nuisance parameters for the disappearance analysis (blue). . . . 118
209 $\Delta\chi^2$ as function of $sin^2\theta_{13}$ for fake dataset #10. At each point, χ^2 was minimized with respect to $\sin^2\theta_{23}$, $\sin^2\theta_{13}$, δ_{CP} and all relevant nuisance parameters for the joint analysis (black) and with respect to all relevant nuisance parameters (δ_{CP} is fixed to 0) for the appearance analysis (red). . . . 118
210 $\Delta\chi^2$ as function of δ_{CP} for fake dataset #10. At each point, χ^2 was minimized with respect to all oscillation parameters not shown (and not considered to be fixed) and all relevant nuisance parameters. . . . 118
211 68% and 90% CL regions in ($sin^2\theta_{23}$, $|\Delta m^2|$) space for fake dataset #10. At each point, χ^2 was minimized with respect to $\sin^2\theta_{13}$, δ_{CP} and all relevant nuisance parameters for the joint analysis (black) and with respect to all relevant nuisance parameters for the disappearance analysis (blue). . . . 118
212 68% and 90% CL regions in ($sin^2\theta_{13}$, $|\Delta m^2|$) space for fake dataset #10. At each point, χ^2 was minimized with respect to all oscillation parameters not shown (and not considered to be fixed) and all relevant nuisance parameters. . . . 118
213 68% and 90% CL regions in ($sin^2\theta_{13}$, δ_{CP}) space for fake dataset #10. At each point, χ^2 was minimized with respect to $|\Delta m^2|$, $\sin^2\theta_{23}$ and all relevant nuisance parameters for the joint analysis (black) and with respect to all relevant nuisance parameters for the appearance analysis (red). Notice that different methods are used to construct confidence regions for the joint analysis (global minimum) and for the stand-alone appearance analysis (raster scan). . . . 118
214 68% and 90% CL regions in ($sin^2\theta_{23}$, $sin^2\theta_{13}$) space for fake dataset #10. At each point, χ^2 was minimized with respect to all oscillation parameters not shown (and not considered to be fixed) and all relevant nuisance parameters. . . . 118
215 Single μ-like ring event best-fit reconstructed energy spectrum to fake dataset #11. . . . 119
216 Single e-like ring event best-fit reconstructed energy spectrum to fake dataset #11. . . . 119
217 Systematic parameter pulls for the oscillation fit to fake dataset #11. . . . 119
218 Distribution of χ^2_{gof}, the goodness-of-fit (gof) χ^2, from 1k toy MC experiments generated at dataset #11 joint 3-flavour analysis best-fit oscillation point. The χ^2_{gof} value for the dataset #11 (χ^2_{data}) is highlighted. All χ^2_{gof} values were computed using the 5 (single μ-like ring) + 3 (single e-like ring) reconstructed energy binning scheme described in Sec. 6.2. . . . 120
219 Distribution of χ^2_{gof} from 1k toy MC experiments generated at the dataset #11 stand-alone 3-flavour ν_μ disappearance analysis best-fit oscillation point. The χ^2_{gof} value for the dataset #11 (χ^2_{data}) is highlighted. All χ^2_{gof} values were computed using the 5 (single μ-like ring) reconstructed energy binning scheme described in Sec. 6.2. . . . 120

220 Distribution of χ^2_{gof} from 1k toy MC experiments generated at the dataset #11 stand-alone 3-flavour ν_e appearance analysis best-fit oscillation point. The χ^2_{gof} value for the dataset #11 (χ^2_{data}) is highlighted. All χ^2_{gof} values were computed using the 3 (single e-like ring) reconstructed energy binning scheme as described in Sec. 6.2. . . . 120
221 $\Delta\chi^2$ as function of $|\Delta m^2|$ for fake dataset #11. At each point, χ^2 was minimized with respect to $\sin^2\theta_{23}$, $\sin^2\theta_{13}$, δ_{CP} and all relevant nuisance parameters for the joint analysis (black) and with respect to $\sin^2\theta_{23}$ and all relevant nuisance parameters for the disappearance analysis (blue). . . . 121
222 $\Delta\chi^2$ as function of $sin^2\theta_{23}$ for fake dataset #11. At each point, χ^2 was minimized with respect to $|\Delta m^2|$, $\sin^2\theta_{13}$, δ_{CP} and all relevant nuisance parameters for the joint analysis (black) and with respect to $\sin^2\theta_{23}$ and all relevant nuisance parameters for the disappearance analysis (blue). . . . 121
223 $\Delta\chi^2$ as function of $sin^2\theta_{13}$ for fake dataset #11. At each point, χ^2 was minimized with respect to $\sin^2\theta_{23}$, $\sin^2\theta_{13}$, δ_{CP} and all relevant nuisance parameters for the joint analysis (black) and with respect to all relevant nuisance parameters (δ_{CP} is fixed to 0) for the appearance analysis (red). . . . 121
224 $\Delta\chi^2$ as function of δ_{CP} for fake dataset #11. At each point, χ^2 was minimized with respect to all oscillation parameters not shown (and not considered to be fixed) and all relevant nuisance parameters. . . . 121
225 68% and 90% CL regions in ($sin^2\theta_{23}$, $|\Delta m^2|$) space for fake dataset #11. At each point, χ^2 was minimized with respect to $\sin^2\theta_{13}$, δ_{CP} and all relevant nuisance parameters for the joint analysis (black) and with respect to all relevant nuisance parameters for the disappearance analysis (blue). . . . 121
226 68% and 90% CL regions in ($sin^2\theta_{13}$, $|\Delta m^2|$) space for fake dataset #11. At each point, χ^2 was minimized with respect to all oscillation parameters not shown (and not considered to be fixed) and all relevant nuisance parameters. . . . 121
227 68% and 90% CL regions in ($sin^2\theta_{13}$, δ_{CP}) space for fake dataset #11. At each point, χ^2 was minimized with respect to $|\Delta m^2|$, $\sin^2\theta_{23}$ and all relevant nuisance parameters for the joint analysis (black) and with respect to all relevant nuisance parameters for the appearance analysis (red). Notice that different methods are used to construct confidence regions for the joint analysis (global minimum) and for the stand-alone appearance analysis (raster scan). . . . 121
228 68% and 90% CL regions in ($sin^2\theta_{23}$, $sin^2\theta_{13}$) space for fake dataset #11. At each point, χ^2 was minimized with respect to all oscillation parameters not shown (and not considered to be fixed) and all relevant nuisance parameters. . . . 121
229 Single μ-like ring event best-fit reconstructed energy spectrum to fake dataset #12. . . . 122
230 Single e-like ring event best-fit reconstructed energy spectrum to fake dataset #12. . . . 122
231 Systematic parameter pulls for the oscillation fit to fake dataset #12. . . . 122
232 Distribution of χ^2_{gof}, the goodness-of-fit (gof) χ^2, from 1k toy MC experiments generated at dataset #12 joint 3-flavour analysis best-fit oscillation point. The χ^2_{gof} value for the dataset #12 (χ^2_{data}) is highlighted. All χ^2_{gof} values were computed using the 5 (single μ-like ring) + 3 (single e-like ring) reconstructed energy binning scheme described in Sec. 6.2. . . . 123
233 Distribution of χ^2_{gof} from 1k toy MC experiments generated at the dataset #12 stand-alone 3-flavour ν_μ disappearance analysis best-fit oscillation point. The χ^2_{gof} value for the dataset #12 (χ^2_{data}) is highlighted. All χ^2_{gof} values were computed using the 5 (single μ-like ring) reconstructed energy binning scheme described in Sec. 6.2. . . . 123
234 Distribution of χ^2_{gof} from 1k toy MC experiments generated at the dataset #12 stand-alone 3-flavour ν_e appearance analysis best-fit oscillation point. The χ^2_{gof} value for the dataset #12 (χ^2_{data}) is highlighted. All χ^2_{gof} values were computed using the 3 (single e-like ring) reconstructed energy binning scheme as described in Sec. 6.2. . . . 123
235 $\Delta\chi^2$ as function of $|\Delta m^2|$ for fake dataset #12. At each point, χ^2 was minimized with respect to $\sin^2\theta_{23}$, $\sin^2\theta_{13}$, δ_{CP} and all relevant nuisance parameters for the joint analysis (black) and with respect to $\sin^2\theta_{23}$ and all relevant nuisance parameters for the disappearance analysis (blue). . . . 124
236 $\Delta\chi^2$ as function of $sin^2\theta_{23}$ for fake dataset #12. At each point, χ^2 was minimized with respect to $|\Delta m^2|$, $\sin^2\theta_{13}$, δ_{CP} and all relevant nuisance parameters for the joint analysis (black) and with respect to $\sin^2\theta_{23}$ and all relevant nuisance parameters for the disappearance analysis (blue). . . . 124
237 $\Delta\chi^2$ as function of $sin^2\theta_{13}$ for fake dataset #12. At each point, χ^2 was minimized with respect to $\sin^2\theta_{23}$, $\sin^2\theta_{13}$, δ_{CP} and all relevant nuisance parameters for the joint analysis (black) and with respect to all relevant nuisance parameters (δ_{CP} is fixed to 0) for the appearance analysis (red). . . . 124
238 $\Delta\chi^2$ as function of δ_{CP} for fake dataset #12. At each point, χ^2 was minimized with respect to all oscillation parameters not shown (and not considered to be fixed) and all relevant nuisance parameters. . . . 124

239 68% and 90% CL regions in ($sin^2\theta_{23}$, $|\Delta m^2|$) space for fake dataset #12. At each point, χ^2 was minimized with respect to $\sin^2\theta_{13}$, δ_{CP} and all relevant nuisance parameters for the joint analysis (black) and with respect to all relevant nuisance parameters for the disappearance analysis (blue). . . . 124
240 68% and 90% CL regions in ($sin^2\theta_{13}$, $|\Delta m^2|$) space for fake dataset #12. At each point, χ^2 was minimized with respect to all oscillation parameters not shown (and not considered to be fixed) and all relevant nuisance parameters. . . . 124
241 68% and 90% CL regions in ($sin^2\theta_{13}$, δ_{CP}) space for fake dataset #12. At each point, χ^2 was minimized with respect to $|\Delta m^2|$, $\sin^2\theta_{23}$ and all relevant nuisance parameters for the joint analysis (black) and with respect to all relevant nuisance parameters for the appearance analysis (red). Notice that different methods are used to construct confidence regions for the joint analysis (global minimum) and for the stand-alone appearance analysis (raster scan). . . . 124
242 68% and 90% CL regions in ($sin^2\theta_{23}$, $sin^2\theta_{13}$) space for fake dataset #12. At each point, χ^2 was minimized with respect to all oscillation parameters not shown (and not considered to be fixed) and all relevant nuisance parameters. . . . 124
243 Single μ-like ring event best-fit reconstructed energy spectrum to fake dataset #13. . . . 125
244 Single e-like ring event best-fit reconstructed energy spectrum to fake dataset #13. . . . 125
245 Systematic parameter pulls for the oscillation fit to fake dataset #13. . . . 125
246 Distribution of χ^2_{gof}, the goodness-of-fit (gof) χ^2, from 1k toy MC experiments generated at dataset #13 joint 3-flavour analysis best-fit oscillation point. The χ^2_{gof} value for the dataset #13 (χ^2_{data}) is highlighted. All χ^2_{gof} values were computed using the 5 (single μ-like ring) + 3 (single e-like ring) reconstructed energy binning scheme described in Sec. 6.2. . . . 126
247 Distribution of χ^2_{gof} from 1k toy MC experiments generated at the dataset #13 stand-alone 3-flavour ν_μ disappearance analysis best-fit oscillation point. The χ^2_{gof} value for the dataset #13 (χ^2_{data}) is highlighted. All χ^2_{gof} values were computed using the 5 (single μ-like ring) reconstructed energy binning scheme described in Sec. 6.2. . . . 126
248 Distribution of χ^2_{gof} from 1k toy MC experiments generated at the dataset #13 stand-alone 3-flavour ν_e appearance analysis best-fit oscillation point. The χ^2_{gof} value for the dataset #13 (χ^2_{data}) is highlighted. All χ^2_{gof} values were computed using the 3 (single e-like ring) reconstructed energy binning scheme as described in Sec. 6.2. . . . 126
249 $\Delta\chi^2$ as function of $|\Delta m^2|$ for fake dataset #13. At each point, χ^2 was minimized with respect to $\sin^2\theta_{23}$, $\sin^2\theta_{13}$, δ_{CP} and all relevant nuisance parameters for the joint analysis (black) and with respect to $\sin^2\theta_{23}$ and all relevant nuisance parameters for the disappearance analysis (blue). . . . 127
250 $\Delta\chi^2$ as function of $sin^2\theta_{23}$ for fake dataset #13. At each point, χ^2 was minimized with respect to $|\Delta m^2|$, $\sin^2\theta_{13}$, δ_{CP} and all relevant nuisance parameters for the joint analysis (black) and with respect to $\sin^2\theta_{23}$ and all relevant nuisance parameters for the disappearance analysis (blue). . . . 127
251 $\Delta\chi^2$ as function of $sin^2\theta_{13}$ for fake dataset #13. At each point, χ^2 was minimized with respect to $\sin^2\theta_{23}$, $\sin^2\theta_{13}$, δ_{CP} and all relevant nuisance parameters for the joint analysis (black) and with respect to all relevant nuisance parameters (δ_{CP} is fixed to 0) for the appearance analysis (red). . . . 127
252 $\Delta\chi^2$ as function of δ_{CP} for fake dataset #13. At each point, χ^2 was minimized with respect to all oscillation parameters not shown (and not considered to be fixed) and all relevant nuisance parameters. . . . 127
253 68% and 90% CL regions in ($sin^2\theta_{23}$, $|\Delta m^2|$) space for fake dataset #13. At each point, χ^2 was minimized with respect to $\sin^2\theta_{13}$, δ_{CP} and all relevant nuisance parameters for the joint analysis (black) and with respect to all relevant nuisance parameters for the disappearance analysis (blue). . . . 127
254 68% and 90% CL regions in ($sin^2\theta_{13}$, $|\Delta m^2|$) space for fake dataset #13. At each point, χ^2 was minimized with respect to all oscillation parameters not shown (and not considered to be fixed) and all relevant nuisance parameters. . . . 127
255 68% and 90% CL regions in ($sin^2\theta_{13}$, δ_{CP}) space for fake dataset #13. At each point, χ^2 was minimized with respect to $|\Delta m^2|$, $\sin^2\theta_{23}$ and all relevant nuisance parameters for the joint analysis (black) and with respect to all relevant nuisance parameters for the appearance analysis (red). Notice that different methods are used to construct confidence regions for the joint analysis (global minimum) and for the stand-alone appearance analysis (raster scan). . . . 127
256 68% and 90% CL regions in ($sin^2\theta_{23}$, $sin^2\theta_{13}$) space for fake dataset #13. At each point, χ^2 was minimized with respect to all oscillation parameters not shown (and not considered to be fixed) and all relevant nuisance parameters. . . . 127

257 $\Delta\chi^2$ as a function of $|\Delta m^2|$ for true oscillation parameter point #0. χ^2 was averaged over hundreds of toy-MC experiments and, for each experiment, it was minimized with respect to $\sin^2\theta_{23}$, $\sin^2\theta_{13}$, δ_{CP} and all relevant nuisance parameters for the joint analysis (black) and with respect to $\sin^2\theta_{23}$ and all relevant nuisance parameters for the disappearance analysis (blue). . . . 129
258 $\Delta\chi^2$ as function of $\sin^2\theta_{23}$ for true oscillation parameter point #0. χ^2 was averaged over hundreds of toy-MC experiments and, for each experiment, it was minimized with respect to $\sin^2\theta_{23}$, $\sin^2\theta_{13}$, δ_{CP} and all relevant nuisance parameters for the joint analysis (black) and with respect to $\sin^2\theta_{23}$ and all relevant nuisance parameters for the disappearance analysis (blue). . . . 129
259 $\Delta\chi^2$ as function of $\sin^2\theta_{13}$ for true oscillation parameter point #0. χ^2 was averaged over hundreds of toy-MC experiments and, for each experiment, it was minimized with respect to $\sin^2\theta_{23}$, $\sin^2\theta_{13}$, δ_{CP} and all relevant nuisance parameters for the joint analysis (black) and with respect to all relevant nuisance parameters (δ_{CP} is fixed to 0) for the appearance analysis (red). . . . 129
260 $\Delta\chi^2$ as function of δ_{CP} for true oscillation parameter point #0. χ^2 was averaged over hundreds of toy-MC experiments and, for each experiment, it was minimized with respect to $|\Delta m^2|$, $\sin^2\theta_{23}$, $\sin^2\theta_{13}$ and all relevant nuisance parameters. . . . 129
261 $\Delta\chi^2$ as function of $|\Delta m^2|$ for true oscillation parameter point #1. χ^2 was averaged over hundreds of toy-MC experiments and, for each experiment, it was minimized with respect to $\sin^2\theta_{23}$, $\sin^2\theta_{13}$, δ_{CP} and all relevant nuisance parameters for the joint analysis (black) and with respect to $\sin^2\theta_{23}$ and all relevant nuisance parameters for the disappearance analysis (blue). . . . 129
262 $\Delta\chi^2$ as function of $\sin^2\theta_{23}$ for true oscillation parameter point #1. χ^2 was averaged over hundreds of toy-MC experiments and, for each experiment, it was minimized with respect to $|\Delta m^2|$, $\sin^2\theta_{13}$, δ_{CP} and all relevant nuisance parameters for the joint analysis (black) and with respect to $\sin^2\theta_{23}$ and all relevant nuisance parameters for the disappearance analysis (blue). . . . 129
263 $\Delta\chi^2$ as function of $\sin^2\theta_{13}$ for true oscillation parameter point #1. χ^2 was averaged over hundreds of toy-MC experiments and, for each experiment, it was minimized with respect to $\sin^2\theta_{23}$, $\sin^2\theta_{13}$, δ_{CP} and all relevant nuisance parameters for the joint analysis (black) and with respect to all relevant nuisance parameters (δ_{CP} is fixed to 0) for the appearance analysis (red). . . . 129
264 $\Delta\chi^2$ as function of δ_{CP} for true oscillation parameter point #1. χ^2 was averaged over hundreds of toy-MC experiments and, for each experiment, it was minimized with respect to $|\Delta m^2|$, $\sin^2\theta_{23}$, $\sin^2\theta_{13}$ and all relevant nuisance parameters. . . . 129
265 $\Delta\chi^2$ as function of $|\Delta m^2|$ for true oscillation parameter point #2. χ^2 was averaged over hundreds of toy-MC experiments and, for each experiment, it was minimized with respect to $\sin^2\theta_{23}$, $\sin^2\theta_{13}$, δ_{CP} and all relevant nuisance parameters for the joint analysis (black) and with respect to $\sin^2\theta_{23}$ and all relevant nuisance parameters for the disappearance analysis (blue). . . . 130
266 $\Delta\chi^2$ as function of $\sin^2\theta_{23}$ for true oscillation parameter point #2. χ^2 was averaged over hundreds of toy-MC experiments and, for each experiment, it was minimized with respect to $|\Delta m^2|$, $\sin^2\theta_{13}$, δ_{CP} and all relevant nuisance parameters for the joint analysis (black) and with respect to $\sin^2\theta_{23}$ and all relevant nuisance parameters for the disappearance analysis (blue). . . . 130
267 $\Delta\chi^2$ as function of $\sin^2\theta_{13}$ for true oscillation parameter point #2. χ^2 was averaged over hundreds of toy-MC experiments and, for each experiment, it was minimized with respect to $\sin^2\theta_{23}$, $\sin^2\theta_{13}$, δ_{CP} and all relevant nuisance parameters for the joint analysis (black) and with respect to all relevant nuisance parameters (δ_{CP} is fixed to 0) for the appearance analysis (red). . . . 130
268 $\Delta\chi^2$ as function of δ_{CP} for true oscillation parameter point #2. χ^2 was averaged over hundreds of toy-MC experiments and, for each experiment, it was minimized with respect to $|\Delta m^2|$, $\sin^2\theta_{23}$, $\sin^2\theta_{13}$ and all relevant nuisance parameters. . . . 130
269 $\Delta\chi^2$ as function of $|\Delta m^2|$ for true oscillation parameter point #3. χ^2 was averaged over hundreds of toy-MC experiments and, for each experiment, it was minimized with respect to $\sin^2\theta_{23}$, $\sin^2\theta_{13}$, δ_{CP} and all relevant nuisance parameters for the joint analysis (black) and with respect to $\sin^2\theta_{23}$ and all relevant nuisance parameters for the disappearance analysis (blue). . . . 130
270 $\Delta\chi^2$ as function of $\sin^2\theta_{23}$ for true oscillation parameter point #3. χ^2 was averaged over hundreds of toy-MC experiments and, for each experiment, it was minimized with respect to $|\Delta m^2|$, $\sin^2\theta_{13}$, δ_{CP} and all relevant nuisance parameters for the joint analysis (black) and with respect to $\sin^2\theta_{23}$ and all relevant nuisance parameters for the disappearance analysis (blue). . . . 130

271 $\Delta\chi^2$ as function of $\sin^2\theta_{13}$ for true oscillation parameter point #3. χ^2 was averaged over hundreds of toy-MC experiments and, for each experiment, it was minimized with respect to $\sin^2\theta_{23}$, $\sin^2\theta_{13}$, δ_{CP} and all relevant nuisance parameters for the joint analysis (black) and with respect to all relevant nuisance parameters (δ_{CP} is fixed to 0) for the appearance analysis (red). 130
272 $\Delta\chi^2$ as function of δ_{CP} for true oscillation parameter point #3. χ^2 was averaged over hundreds of toy-MC experiments and, for each experiment, it was minimized with respect to $|\Delta m^2|$, $\sin^2\theta_{23}$, $\sin^2\theta_{13}$ and all relevant nuisance parameters. 130
273 $\Delta\chi^2$ as function of $|\Delta m^2|$ for true oscillation parameter point #4. χ^2 was averaged over hundreds of toy-MC experiments and, for each experiment, it was minimized with respect to $\sin^2\theta_{23}$, $\sin^2\theta_{13}$, δ_{CP} and all relevant nuisance parameters for the joint analysis (black) and with respect to $\sin^2\theta_{23}$ and all relevant nuisance parameters for the disappearance analysis (blue). 131
274 $\Delta\chi^2$ as function of $\sin^2\theta_{23}$ for true oscillation parameter point #4. χ^2 was averaged over hundreds of toy-MC experiments and, for each experiment, it was minimized with respect to $|\Delta m^2|$, $\sin^2\theta_{13}$, δ_{CP} and all relevant nuisance parameters for the joint analysis (black) and with respect to $\sin^2\theta_{23}$ and all relevant nuisance parameters for the disappearance analysis (blue). 131
275 $\Delta\chi^2$ as function of $\sin^2\theta_{13}$ for true oscillation parameter point #4. χ^2 was averaged over hundreds of toy-MC experiments and, for each experiment, it was minimized with respect to $\sin^2\theta_{23}$, $\sin^2\theta_{13}$, δ_{CP} and all relevant nuisance parameters for the joint analysis (black) and with respect to all relevant nuisance parameters (δ_{CP} is fixed to 0) for the appearance analysis (red). 131
276 $\Delta\chi^2$ as function of δ_{CP} for true oscillation parameter point #4. χ^2 was averaged over hundreds of toy-MC experiments and, for each experiment, it was minimized with respect to $|\Delta m^2|$, $\sin^2\theta_{23}$, $\sin^2\theta_{13}$ and all relevant nuisance parameters. 131
277 $\Delta\chi^2$ as function of $|\Delta m^2|$ for true oscillation parameter point #5. χ^2 was averaged over hundreds of toy-MC experiments and, for each experiment, it was minimized with respect to $\sin^2\theta_{23}$, $\sin^2\theta_{13}$, δ_{CP} and all relevant nuisance parameters for the joint analysis (black) and with respect to $\sin^2\theta_{23}$ and all relevant nuisance parameters for the disappearance analysis (blue). 131
278 $\Delta\chi^2$ as function of $\sin^2\theta_{23}$ for true oscillation parameter point #5. χ^2 was averaged over hundreds of toy-MC experiments and, for each experiment, it was minimized with respect to $|\Delta m^2|$, $\sin^2\theta_{13}$, δ_{CP} and all relevant nuisance parameters for the joint analysis (black) and with respect to $\sin^2\theta_{23}$ and all relevant nuisance parameters for the disappearance analysis (blue). 131
279 $\Delta\chi^2$ as function of $\sin^2\theta_{13}$ for true oscillation parameter point #5. χ^2 was averaged over hundreds of toy-MC experiments and, for each experiment, it was minimized with respect to $\sin^2\theta_{23}$, $\sin^2\theta_{13}$, δ_{CP} and all relevant nuisance parameters for the joint analysis (black) and with respect to all relevant nuisance parameters (δ_{CP} is fixed to 0) for the appearance analysis (red). 131
280 $\Delta\chi^2$ as function of δ_{CP} for true oscillation parameter point #5. χ^2 was averaged over hundreds of toy-MC experiments and, for each experiment, it was minimized with respect to $|\Delta m^2|$, $\sin^2\theta_{23}$, $\sin^2\theta_{13}$ and all relevant nuisance parameters. 131
281 $\Delta\chi^2$ as function of $|\Delta m^2|$ for the best fit point found for Run1+2+3 with Normal Hierarchy. χ^2 was averaged over hundreds of toy-MC experiments and, for each experiment, it was minimized with respect to $\sin^2\theta_{23}$, $\sin^2\theta_{13}$, δ_{CP} and all relevant nuisance parameters for the joint analysis (black) and with respect to $\sin^2\theta_{23}$ and all relevant nuisance parameters for the disappearance analysis (blue). 132
282 $\Delta\chi^2$ as function of $\sin^2\theta_{23}$ for the best fit point found for Run1+2+3 with Normal Hierarchy. χ^2 was averaged over hundreds of toy-MC experiments and, for each experiment, it was minimized with respect to $\sin^2\theta_{23}$, $\sin^2\theta_{13}$, δ_{CP} and all relevant nuisance parameters for the joint analysis (black) and with respect to $\sin^2\theta_{23}$ and all relevant nuisance parameters for the disappearance analysis (blue). 132
283 $\Delta\chi^2$ as function of $\sin^2\theta_{13}$ for the best fit point found for Run1+2+3 with Normal Hierarchy. χ^2 was averaged over hundreds of toy-MC experiments and, for each experiment, it was minimized with respect to $\sin^2\theta_{23}$, $\sin^2\theta_{13}$, δ_{CP} and all relevant nuisance parameters for the joint analysis (black) and with respect to all relevant nuisance parameters (δ_{CP} is fixed to 0) for the appearance analysis (red). 132
284 $\Delta\chi^2$ as function of δ_{CP} for the best fit point found for Run1+2+3 with Normal Hierarchy. χ^2 was averaged over hundreds of toy-MC experiments and, for each experiment, it was minimized with respect to $|\Delta m^2|$, $\sin^2\theta_{23}$, $\sin^2\theta_{13}$ and all relevant nuisance parameters. 132
285 $\Delta\chi^2$ as function of $|\Delta m^2|$ for the best fit point found for Run1+2+3 with Inverted Hierarchy. χ^2 was averaged over hundreds of toy-MC experiments and, for each experiment, it was minimized with respect to $\sin^2\theta_{23}$, $\sin^2\theta_{13}$, δ_{CP} and all relevant nuisance parameters for the joint analysis (black) and with respect to $\sin^2\theta_{23}$ and all relevant nuisance parameters for the disappearance analysis (blue). 132

286 $\Delta\chi^2$ as function of $\sin^2\theta_{23}$ ffor the best fit point found for Run1+2+3 with Inverted Hierarchy. χ^2 was averaged over hundreds of toy-MC experiments and, for each experiment, it was minimized with respect to $\sin^2\theta_{23}$, $\sin^2\theta_{13}$, δ_{CP} and all relevant nuisance parameters for the joint analysis (black) and with respect to $\sin^2\theta_{23}$ and all relevant nuisance parameters for the disappearance analysis (blue). 132
287 $\Delta\chi^2$ as function of $\sin^2\theta_{13}$ for the best fit point found for Run1+2+3 with Inverted Hierarchy. χ^2 was averaged over hundreds of toy-MC experiments and, for each experiment, it was minimized with respect to $\sin^2\theta_{23}$, $\sin^2\theta_{13}$, δ_{CP} and all relevant nuisance parameters for the joint analysis (black) and with respect to all relevant nuisance parameters (δ_{CP} is fixed to 0) for the appearance analysis (red). 132
288 $\Delta\chi^2$ as function of δ_{CP} for the best fit point found for Run1+2+3 with Inverted Hierarchy. χ^2 was averaged over hundreds of toy-MC experiments and, for each experiment, it was minimized with respect to $|\Delta m^2|$, $\sin^2\theta_{23}$, $\sin^2\theta_{13}$ and all relevant nuisance parameters. 132
289 $\Delta\chi^2$ as function of $|\Delta m^2|$ for the best fit point found for Run1+2+3 with Normal Hierarchy. Oranged line is the result of the sensitivity study, where χ^2 was averaged over hundreds of toy-MC experiments and black line is the result of the Run1+2+3 dataset fit. 133
290 $\Delta\chi^2$ as function of $\sin^2\theta_{23}$ for the best fit point found for Run1+2+3 with Normal Hierarchy. Orange line is the result of the sensitivity study, where χ^2 was averaged over hundreds of toy-MC experiments and black line is the result of the Run1+2+3 dataset fit. 133
291 $\Delta\chi^2$ as function of $\sin^2\theta_{13}$ for the best fit point found for Run1+2+3 with Normal Hierarchy. Orange line is the result of the sensitivity study, where χ^2 was averaged over hundreds of toy-MC experiments and black line is the result of the Run1+2+3 dataset fit. 133
292 $\Delta\chi^2$ as function of δ_{CP} for the best fit point found for Run1+2+3 with Normal Hierarchy. Orange line is the result of the sensitivity study, where χ^2 was averaged over hundreds of toy-MC experiments and black line is the result of the Run1+2+3 dataset fit. 133
293 $\Delta\chi^2$ as function of $|\Delta m^2|$ for the best fit point found for Run1+2+3 with Inverted Hierarchy. Orange line is the result of the sensitivity study, where χ^2 was averaged over hundreds of toy-MC experiments and black line is the result of the Run1+2+3 dataset fit. 133
294 $\Delta\chi^2$ as function of $\sin^2\theta_{23}$ for the best fit point found for Run1+2+3 with Inverted Hierarchy. Orange line is the result of the sensitivity study, where χ^2 was averaged over hundreds of toy-MC experiments and black line is the result of the Run1+2+3 dataset fit. 133
295 $\Delta\chi^2$ as function of $\sin^2\theta_{13}$ for the best fit point found for Run1+2+3 with Inverted Hierarchy. Orange line is the result of the sensitivity study, where χ^2 was averaged over hundreds of toy-MC experiments and black line is the result of the Run1+2+3 dataset fit. 133
296 $\Delta\chi^2$ as function of δ_{CP} for the best fit point found for Run1+2+3 with Inverted Hierarchy. Orange line is the result of the sensitivity study, where χ^2 was averaged over hundreds of toy-MC experiments and black line is the result of the Run1+2+3 dataset fit. 133
297 90% CL region in ($\sin^2\theta_{23}$, $|\Delta m^2|$) space for the best fit point found for Run1+2+3 with Normal Hierarchy. Orange line is the sensitivity contour that was computed by averaging the contours of the ensemble of hundreds of toy MC experiments and, for each experiment, it was minimized with respect to $\sin^2\theta_{13}$, δ_{CP} and all relevant nuisance parameters for the joint analysis. Black line is the result of the Run1+2+3 dataset fit. 134
298 90% CL region in ($\sin^2\theta_{13}$, $|\Delta m^2|$) space for the best fit point found for Run1+2+3 with Normal Hierarchy. Orange line is the sensitivity contour that was computed by averaging the contours of the ensemble of hundreds of toy MC experiments and, for each experiment, it was minimized with respect to $\sin^2\theta_{13}$, δ_{CP} and all relevant nuisance parameters for the joint analysis. Black line is the result of the Run1+2+3 dataset fit. 134
299 90% CL region in ($\sin^2\theta_{23}$, δ_{CP}) space for the best fit point found for Run1+2+3 with Normal Hierarchy. Orange line is the sensitivity contour that was computed by averaging the contours of the ensemble of hundreds of toy MC experiments and, for each experiment, it was minimized with respect to $\sin^2\theta_{13}$, δ_{CP} and all relevant nuisance parameters for the joint analysis. Black line is the result of the Run1+2+3 dataset fit. 134
300 90% CL region in ($\sin^2\theta_{23}$, $\sin^2\theta_{13}$) space for the best fit point found for Run1+2+3 with Normal Hierarchy. Orange line is the sensitivity contour that was computed by averaging the contours of the ensemble of hundreds of toy MC experiments and, for each experiment, it was minimized with respect to $\sin^2\theta_{13}$, δ_{CP} and all relevant nuisance parameters for the joint analysis. Black line is the result of the Run1+2+3 dataset fit. 134
301 90% CL region in ($\sin^2\theta_{23}$, $|\Delta m^2|$) space for the best fit point found for Run1+2+3 with Inverted Hierarchy. Orange line is the sensitivity contour that was computed by averaging the contours of the ensemble of hundreds of toy MC experiments and, for each experiment, it was minimized with respect to $\sin^2\theta_{13}$, δ_{CP} and all relevant nuisance parameters for the joint analysis. Black line is the result of the Run1+2+3 dataset fit. 135

302 90% CL region in ($\sin^2\theta_{13}$, $|\Delta m^2|$) space for the best fit point found for Run1+2+3 with Inverted Hierarchy. Orange line is the sensitivity contour that was computed by averaging the contours of the ensemble of hundreds of toy MC experiments and, for each experiment, it was minimized with respect to $\sin^2\theta_{13}$, δ_{CP} and all relevant nuisance parameters for the joint analysis. Black line is the result of the Run1+2+3 dataset fit. 135
303 90% CL region in ($\sin^2\theta_{13}$, δ_{CP}) space for the best fit point found for Run1+2+3 with Normal Hierarchy. Orange line is the sensitivity contour that was computed by averaging the contours of the ensemble of hundreds of toy MC experiments and, for each experiment, it was minimized with respect to $\sin^2\theta_{13}$, δ_{CP} and all relevant nuisance parameters for the joint analysis. Black line is the result of the Run1+2+3 dataset fit. 135
304 90% CL region in ($\sin^2\theta_{23}$, $\sin^2\theta_{13}$) space for the best fit point found for Run1+2+3 with Normal Hierarchy. Orange line is the sensitivity contour that was computed by averaging the contours of the ensemble of hundreds of toy MC experiments and, for each experiment, it was minimized with respect to $\sin^2\theta_{13}$, δ_{CP} and all relevant nuisance parameters for the joint analysis. Black line is the result of the Run1+2+3 dataset fit. 135
305 The 3-flavour P($\nu_\mu \to \nu_\mu$) with matter effects as a function of $\sin^2\theta_{23}$ for different values of $\sin^2\theta_{13}$ for the normal mass hierarchy (left) and the inverted mass hierarchy (right); $|\Delta m^2_{32}|$ is fixed to 2.4×10^{-3} eV^2/c^4 and δ_{CP} is fixed to 0. 136
306 The 3-flavour P($\nu_\mu \to \nu_\mu$) with matter effects as a function of $\sin^2\theta_{23}$ for the best fit value found for Run1+2+3 dataset fit with Normal Hierarchy (left) and Inverted Hierarchy (right). The values for the left plot are: $\sin^2\theta_{13} = 0.029$, $|\Delta m^2_{32}| = 2.494\times10^{-3}$ eV^2/c^4 and $\delta_{CP} = 2.086$. The values for the right plot are: $\sin^2\theta_{13} = 0.034$, $|\Delta m^2_{32}| = 2.468\times10^{-3}$ eV^2/c^4 and $\delta_{CP} = 0.921$. In both hierarchies the minimum is found at the best-fit value $\sin^2\theta_{23} = 0.516$ (indicated with a green line). 138
307 $\sin^2 2\theta_{23}$ versus Δm^2_{32} confidence regions for the estimated final POT (7×10^{21}). Dark colors for the fit with fixed solar parameters and light colors for the fit with marginalized solar parameters. 139
308 Fitted values of $\sin^2 2\theta_{12}$ (left) and Δm^2_{21} (right) for the joint fit with marginalized solar parameters, for the estimated final POT (7×10^{21}). 139
309 True χ^2 surface in ($\sin^2\theta_{13}$,δ_{CP}) space for a toy experiment with true input values $\sin^2\theta_{23} = 0.5$, $|\Delta m^2| = 2.36\times10^{-3}(eV^2/c^4)$, $\sin^2\theta_{13} = 0.025$ and δ_{CP}=0 and no fluctuations, fixing $\sin^2\theta_{23}$ and $|\Delta m^2|$ to their input values. Right, same true χ^2 surface zoomed around true input value for $\sin^2\theta_{13}$. 140
310 Graphical explanation of the test made to understand the distribution of residuals for δ_{CP}. For the Gaussian distribution of selected values of $\sin^2\theta_{13}$ (left bottom plot) the values of δ_{CP} in the true χ^2 minimal band are found (left top plot) and a histogram is filled with them (right plot). 141
311 Graphical explanation of the test made to understand the distribution of residuals for δ_{CP}. Same as in figure 311 but replacing left top plot with the density of points in the true χ^2 minimal band. 141
312 Result of the test explained in figure 310, i.e. the distribution of selected points vs δ_{CP}. On the left, perfect case. On the right, realistic case including the deviations in $\sin^2\theta_{23}$ and $\sin^2\theta_{13}$ from Fig. 57. 142
313 $P_{\nu_\mu\to\nu_e}$ oscillation probability vs δ_{CP} with values $\sin^2\theta_{23} = 0.5$, $|\Delta m^2| = 2.36\times10^{-3}(eV^2/c^4)$ and $\sin^2\theta_{13} = 0.025$. 142
314 True χ^2 surface in $\sin^2\theta_{13}$,δ_{CP}) space for a toy experiment without fluctuations and with true input values $\sin^2\theta_{23} = 0.5$, $|\Delta m^2| = 2.36\times10^{-3}(eV^2/c^4)$, $\sin^2\theta_{13} = 0.025$ and $\delta_{CP} = \pi/2$, fixing $\sin^2\theta_{23}$ and $|\Delta m^2|$ to their input values. Right, same true χ^2 surface zoomed around true input value for $\sin^2\theta_{13}$. 143
315 True χ^2 surface in $\sin^2\theta_{13}$,δ_{CP}) space for a toy experiment without fluctuations and with true input values $\sin^2\theta_{23} = 0.5$, $|\Delta m^2| = 2.36\times10^{-3}(eV^2/c^4)$, $\sin^2\theta_{13} = 0.025$ and $\delta_{CP} = -\pi/2$, fixing $\sin^2\theta_{23}$ and $|\Delta m^2|$ to their input values. Right, same true χ^2 surface zoomed around true input value for $\sin^2\theta_{13}$. 143
316 Result of the test explained in figure 310, i.e. the distribution of selected points vs δ_{CP}. Left plot is for $\delta_{CP} = \pi/2$ and right plot is for $\delta_{CP} = -\pi/2$. 143
317 Result of the test explained in figure 310, i.e. the distribution of selected points vs δ_{CP} when including the corresponding biases in $\sin^2\theta_{23}$ and $\sin^2\theta_{13}$ from Figs. 63 and 64. Left plot is for $\delta_{CP} = \pi/2$ and right plot is for $\delta_{CP} = -\pi/2$. 144
318 Distribution of residuals of the four oscillation parameters in the '4 + 0' fit for oscillation point with values $\sin^2\theta_{23} = 0.34$, $|\Delta m^2| = 2.4\times10^{-3}(eV^2/c^4)$, $\sin^2\theta_{13} = 0.025$ and $\delta_{CP} = 0$ at the T2K goal POT (7.8×10^{21}) constraining $\sin^2\theta_{13}$ with an error of 10%. 144
319 Distribution of residuals of the four oscillation parameters in the '4 + 0' fit for oscillation point with values $\sin^2\theta_{23} = 0.34$, $|\Delta m^2| = 2.4\times10^{-3}(eV^2/c^4)$, $\sin^2\theta_{13} = 0.025$ and $\delta_{CP} = \pi/2$ at the T2K goal POT (7.8×10^{21}) constraining $\sin^2\theta_{13}$ with an error of 10%. 145
320 Distribution of residuals of the four oscillation parameters in the '4 + 0' fit for oscillation point with values $\sin^2\theta_{23} = 0.34$, $|\Delta m^2| = 2.4\times10^{-3}(eV^2/c^4)$, $\sin^2\theta_{13} = 0.025$ and $\delta_{CP} = -\pi/2$ at the T2K goal POT (7.8×10^{21}). 145

321 P($\nu_\mu \to \nu_\mu$) survival probability in the 2-dimensional oscillation parameter spaces ($\sin^2\theta_{23}$, $|\Delta m^2|$) (left) and ($\sin^2\theta_{23}$, $|\Delta m^2_{32}|$) (right) for a fixed value of P($\nu_\mu \to \nu_\mu$) = 0.05. 146
322 True χ^2 surface for the single ring μ-like sample of the Run1+2+3 dataset in the 2-dimensional oscillation parameter spaces ($\sin^2\theta_{23}$, $|\Delta m^2|$) (left) and ($\sin^2\theta_{23}$, $|\Delta m^2_{32}|$) (right) for a fixed value of true $\chi^2 = 60$. . . . 147
323 90% CL for the Run1+2+3 dataset in the 2-dimensional oscillation parameter spaces ($\sin^2\theta_{23}$, $|\Delta m^2|$) (left) and ($\sin^2\theta_{23}$, $|\Delta m^2_{32}|$) (right) for the stand-alone ν_μ disappearance analysis with Normal Hierarchy (solid line) and Inverted Hierarchy (dashed line) with the constant $\Delta\chi^2$ method. 147
324 Distribution of $\Delta\chi^2$ vs coverage in the $|\Delta m^2|$ parameter space from 1k toy MC experiments generated with the Run 1+2+3 POT with statistical fluctuations at the oscillation point indicated in the legend. 151
325 Distribution of $\Delta\chi^2$ vs coverage in the $|\Delta m^2|$ parameter space from 1k toy MC experiments generated with the Run 1+2+3 POT with statistical fluctuations at the oscillation point indicated in the legend. 151
326 Distribution of $\Delta\chi^2$ vs coverage in the $|\Delta m^2|$ parameter space from 1k toy MC experiments generated with the Run 1+2+3 POT with statistical fluctuations at the oscillation point indicated in the legend. 151
327 Distribution of $\Delta\chi^2$ vs coverage in the $|\Delta m^2|$ parameter space from 1k toy MC experiments generated with the Run 1+2+3 POT with statistical fluctuations at the oscillation point indicated in the legend. 151
328 Summary of figures 324-327 showing the value of $\Delta\chi^2$ at 99%, 90% and 68% confidence intervals vs the value of $|\Delta m^2|$. Horizontal dashed lines show the canonical $\Delta\chi^2$ value for 1 degree of freedom. 151
329 Distribution of $\Delta\chi^2$ vs coverage in the $sin^2\theta_{23}$ parameter space from 1k toy MC experiments generated with the Run 1+2+3 POT with statistical fluctuations at the oscillation point indicated in the legend. 152
330 Distribution of $\Delta\chi^2$ vs coverage in the $sin^2\theta_{23}$ parameter space from 1k toy MC experiments generated with the Run 1+2+3 POT with statistical fluctuations at the oscillation point indicated in the legend. 152
331 Distribution of $\Delta\chi^2$ vs coverage in the $sin^2\theta_{23}$ parameter space from 1k toy MC experiments generated with the Run 1+2+3 POT with statistical fluctuations at the oscillation point indicated in the legend. 152
332 Distribution of $\Delta\chi^2$ vs coverage in the $sin^2\theta_{23}$ parameter space from 1k toy MC experiments generated with the Run 1+2+3 POT with statistical fluctuations at the oscillation point indicated in the legend. 152
333 Summary of figures 329-332 showing the value of $\Delta\chi^2$ at 99%, 90% and 68% confidence intervals vs the value of $sin^2\theta_{23}$. Horizontal dashed lines show the canonical $\Delta\chi^2$ value for 1 degree of freedom. 152
334 Distribution of $\Delta\chi^2$ vs coverage in the $sin^2\theta_{13}$ parameter space from 1k toy MC experiments generated with the Run 1+2+3 POT with statistical fluctuations at the oscillation point indicated in the legend. 153
335 Distribution of $\Delta\chi^2$ vs coverage in the $sin^2\theta_{13}$ parameter space from 1k toy MC experiments generated with the Run 1+2+3 POT with statistical fluctuations at the oscillation point indicated in the legend. 153
336 Distribution of $\Delta\chi^2$ vs coverage in the $sin^2\theta_{13}$ parameter space from 1k toy MC experiments generated with the Run 1+2+3 POT with statistical fluctuations at the oscillation point indicated in the legend. 153
337 Distribution of $\Delta\chi^2$ vs coverage in the $sin^2\theta_{13}$ parameter space from 1k toy MC experiments generated with the Run 1+2+3 POT with statistical fluctuations at the oscillation point indicated in the legend. 153
338 Distribution of $\Delta\chi^2$ vs coverage in the $sin^2\theta_{13}$ parameter space from 1k toy MC experiments generated with the Run 1+2+3 POT with statistical fluctuations at the oscillation point indicated in the legend. 153
339 Summary of figures 334-338 showing the value of $\Delta\chi^2$ at 99%, 90% and 68% confidence intervals vs the value of $sin^2\theta_{13}$. Horizontal dashed lines show the canonical $\Delta\chi^2$ value for 1 degree of freedom. 153
340 Distribution of $\Delta\chi^2$ vs coverage in the δ_{CP} parameter space from 1k toy MC experiments generated with the Run 1+2+3 POT with statistical fluctuations at the oscillation point indicated in the legend. 154
341 Distribution of $\Delta\chi^2$ vs coverage in the δ_{CP} parameter space from 1k toy MC experiments generated with the Run 1+2+3 POT with statistical fluctuations at the oscillation point indicated in the legend. 154
342 Distribution of $\Delta\chi^2$ vs coverage in the δ_{CP} parameter space from 1k toy MC experiments generated with the Run 1+2+3 POT with statistical fluctuations at the oscillation point indicated in the legend. 154
343 Distribution of $\Delta\chi^2$ vs coverage in the δ_{CP} parameter space from 1k toy MC experiments generated with the Run 1+2+3 POT with statistical fluctuations at the oscillation point indicated in the legend. 154
344 Summary of figures 340-343 showing the value of $\Delta\chi^2$ at 99%, 90% and 68% confidence intervals vs the value of δ_{CP}. Horizontal dashed lines show the canonical $\Delta\chi^2$ value for 1 degree of freedom. 154
345 Distribution of $\Delta\chi^2$ vs coverage in the ($sin^2\theta_{23}$,$|\Delta m^2|$) parameter space from 1k toy MC experiments generated with the Run 1+2+3 POT with statistical fluctuations at the oscillation point indicated in the legend. 156
346 Distribution of $\Delta\chi^2$ vs coverage in the ($sin^2\theta_{23}$,$|\Delta m^2|$) parameter space from 1k toy MC experiments generated with the Run 1+2+3 POT with statistical fluctuations at the oscillation point indicated in the legend. 156

347 Distribution of $\Delta\chi^2$ vs coverage in the ($sin^2\theta_{23}$,$|\Delta m^2|$) parameter space from 1k toy MC experiments generated with the Run 1+2+3 POT with statistical fluctuations at the oscillation point indicated in the legend. . . . 156
348 Distribution of $\Delta\chi^2$ vs coverage in the ($sin^2\theta_{23}$,$|\Delta m^2|$) parameter space from 1k toy MC experiments generated with the Run 1+2+3 POT with statistical fluctuations at the oscillation point indicated in the legend. . . . 156
349 Summary of figures 345-348 showing the value of $\Delta\chi^2$ at 99%, 90% and 68% confidence intervals vs the value of $sin^2\theta_{23}$. Horizontal dashed lines show the canonical $\Delta\chi^2$ value for 2 degrees of freedom. . . . 156
350 Distribution of $\Delta\chi^2$ vs coverage in the ($sin^2\theta_{13}$,$|\Delta m^2|$) parameter space from 1k toy MC experiments generated with the Run 1+2+3 POT with statistical fluctuations at the oscillation point indicated in the legend. . . . 157
351 Distribution of $\Delta\chi^2$ vs coverage in the ($sin^2\theta_{13}$,$|\Delta m^2|$) parameter space from 1k toy MC experiments generated with the Run 1+2+3 POT with statistical fluctuations at the oscillation point indicated in the legend. . . . 157
352 Distribution of $\Delta\chi^2$ vs coverage in the ($sin^2\theta_{13}$,$|\Delta m^2|$) parameter space from 1k toy MC experiments generated with the Run 1+2+3 POT with statistical fluctuations at the oscillation point indicated in the legend. . . . 157
353 Distribution of $\Delta\chi^2$ vs coverage in the ($sin^2\theta_{13}$,$|\Delta m^2|$) parameter space from 1k toy MC experiments generated with the Run 1+2+3 POT with statistical fluctuations at the oscillation point indicated in the legend. . . . 157
354 Distribution of $\Delta\chi^2$ vs coverage in the ($sin^2\theta_{13}$,$|\Delta m^2|$) parameter space from 1k toy MC experiments generated with the Run 1+2+3 POT with statistical fluctuations at the oscillation point indicated in the legend. . . . 157
355 Summary of figures 350-354 showing the value of $\Delta\chi^2$ at 99%, 90% and 68% confidence intervals vs the value of $sin^2\theta_{13}$. Horizontal dashed lines show the canonical $\Delta\chi^2$ value for 2 degrees of freedom. . . . 157
356 Distribution of $\Delta\chi^2$ vs coverage in the ($sin^2\theta_{13}$,δ_{CP}) parameter space from 1k toy MC experiments generated with the Run 1+2+3 POT with statistical fluctuations at the oscillation point indicated in the legend. The solid red line shows the canonical $\Delta\chi^2$ pdf for 2 degrees of freedom and the dashed red line shows the canonical $\Delta\chi^2$ pdf for 1 degree of freedom. . . . 158
357 Distribution of $\Delta\chi^2$ vs coverage in the ($sin^2\theta_{13}$,δ_{CP}) parameter space from 1k toy MC experiments generated with the Run 1+2+3 POT with statistical fluctuations at the oscillation point indicated in the legend. The solid red line shows the canonical $\Delta\chi^2$ pdf for 2 degrees of freedom and the dashed red line shows the canonical $\Delta\chi^2$ pdf for 1 degree of freedom. . . . 158
358 Distribution of $\Delta\chi^2$ vs coverage in the ($sin^2\theta_{13}$,δ_{CP}) parameter space from 1k toy MC experiments generated with the Run 1+2+3 POT with statistical fluctuations at the oscillation point indicated in the legend. The solid red line shows the canonical $\Delta\chi^2$ pdf for 2 degrees of freedom and the dashed red line shows the canonical $\Delta\chi^2$ pdf for 1 degree of freedom. . . . 158
359 Distribution of $\Delta\chi^2$ vs coverage in the ($sin^2\theta_{13}$,δ_{CP}) parameter space from 1k toy MC experiments generated with the Run 1+2+3 POT with statistical fluctuations at the oscillation point indicated in the legend. The solid red line shows the canonical $\Delta\chi^2$ pdf for 2 degrees of freedom and the dashed red line shows the canonical $\Delta\chi^2$ pdf for 1 degree of freedom. . . . 158
360 Distribution of $\Delta\chi^2$ vs coverage in the ($sin^2\theta_{13}$,δ_{CP}) parameter space from 1k toy MC experiments generated with the Run 1+2+3 POT with statistical fluctuations at the oscillation point indicated in the legend. The solid red line shows the canonical $\Delta\chi^2$ pdf for 2 degrees of freedom and the dashed red line shows the canonical $\Delta\chi^2$ pdf for 1 degree of freedom. . . . 158
361 Summary of figures 356-360 showing the value of $\Delta\chi^2$ at 99%, 90% and 68% confidence intervals vs the value of $sin^2\theta_{13}$. Horizontal dashed lines show the canonical $\Delta\chi^2$ value for 2 degrees of freedom and 1 degree of freedom (see legend). . . . 158
362 Distribution of $\Delta\chi^2$ vs coverage in the ($sin^2\theta_{13}$,$sin^2\theta_{23}$) parameter space from 1k toy MC experiments generated with the Run 1+2+3 POT with statistical fluctuations at the oscillation point indicated in the legend. . . . 159
363 Distribution of $\Delta\chi^2$ vs coverage in the ($sin^2\theta_{13}$,$sin^2\theta_{23}$) parameter space from 1k toy MC experiments generated with the Run 1+2+3 POT with statistical fluctuations at the oscillation point indicated in the legend. . . . 159

364 Distribution of $\Delta\chi^2$ vs coverage in the ($sin^2\theta_{13}$,$sin^2\theta_{23}$) parameter space from 1k toy MC experiments generated with the Run 1+2+3 POT with statistical fluctuations at the oscillation point indicated in the legend. 159
365 Distribution of $\Delta\chi^2$ vs coverage in the ($sin^2\theta_{13}$,$sin^2\theta_{23}$) parameter space from 1k toy MC experiments generated with the Run 1+2+3 POT with statistical fluctuations at the oscillation point indicated in the legend. 159
366 Distribution of $\Delta\chi^2$ vs coverage in the ($sin^2\theta_{13}$,$sin^2\theta_{23}$) parameter space from 1k toy MC experiments generated with the Run 1+2+3 POT with statistical fluctuations at the oscillation point indicated in the legend. 159
367 Distribution of $\Delta\chi^2$ vs coverage in the ($sin^2\theta_{13}$,$sin^2\theta_{23}$) parameter space from 1k toy MC experiments generated with the Run 1+2+3 POT with statistical fluctuations at the oscillation point indicated in the legend. 160
368 Distribution of $\Delta\chi^2$ vs coverage in the ($sin^2\theta_{13}$,$sin^2\theta_{23}$) parameter space from 1k toy MC experiments generated with the Run 1+2+3 POT with statistical fluctuations at the oscillation point indicated in the legend. 160
369 Distribution of $\Delta\chi^2$ vs coverage in the ($sin^2\theta_{13}$,$sin^2\theta_{23}$) parameter space from 1k toy MC experiments generated with the Run 1+2+3 POT with statistical fluctuations at the oscillation point indicated in the legend. 160
370 Distribution of $\Delta\chi^2$ vs coverage in the ($sin^2\theta_{13}$,$sin^2\theta_{23}$) parameter space from 1k toy MC experiments generated with the Run 1+2+3 POT with statistical fluctuations at the oscillation point indicated in the legend. 160
371 Distribution of $\Delta\chi^2$ vs coverage in the ($sin^2\theta_{13}$,$sin^2\theta_{23}$) parameter space from 1k toy MC experiments generated with the Run 1+2+3 POT with statistical fluctuations at the oscillation point indicated in the legend. 160
372 Distribution of $\Delta\chi^2$ vs coverage in the ($sin^2\theta_{13}$,$sin^2\theta_{23}$) parameter space from 1k toy MC experiments generated with the Run 1+2+3 POT with statistical fluctuations at the oscillation point indicated in the legend. 161
373 Distribution of $\Delta\chi^2$ vs coverage in the ($sin^2\theta_{13}$,$sin^2\theta_{23}$) parameter space from 1k toy MC experiments generated with the Run 1+2+3 POT with statistical fluctuations at the oscillation point indicated in the legend. 161
374 Distribution of $\Delta\chi^2$ vs coverage in the ($sin^2\theta_{13}$,$sin^2\theta_{23}$) parameter space from 1k toy MC experiments generated with the Run 1+2+3 POT with statistical fluctuations at the oscillation point indicated in the legend. 161
375 Distribution of $\Delta\chi^2$ vs coverage in the ($sin^2\theta_{13}$,$sin^2\theta_{23}$) parameter space from 1k toy MC experiments generated with the Run 1+2+3 POT with statistical fluctuations at the oscillation point indicated in the legend. 161
376 Distribution of $\Delta\chi^2$ vs coverage in the ($sin^2\theta_{13}$,$sin^2\theta_{23}$) parameter space from 1k toy MC experiments generated with the Run 1+2+3 POT with statistical fluctuations at the oscillation point indicated in the legend. 161
377 Distribution of $\Delta\chi^2$ vs coverage in the ($sin^2\theta_{13}$,$sin^2\theta_{23}$) parameter space from 1k toy MC experiments generated with the Run 1+2+3 POT with statistical fluctuations at the oscillation point indicated in the legend. 162
378 Distribution of $\Delta\chi^2$ vs coverage in the ($sin^2\theta_{13}$,$sin^2\theta_{23}$) parameter space from 1k toy MC experiments generated with the Run 1+2+3 POT with statistical fluctuations at the oscillation point indicated in the legend. 162
379 Distribution of $\Delta\chi^2$ vs coverage in the ($sin^2\theta_{13}$,$sin^2\theta_{23}$) parameter space from 1k toy MC experiments generated with the Run 1+2+3 POT with statistical fluctuations at the oscillation point indicated in the legend. 162
380 Distribution of $\Delta\chi^2$ vs coverage in the ($sin^2\theta_{13}$,$sin^2\theta_{23}$) parameter space from 1k toy MC experiments generated with the Run 1+2+3 POT with statistical fluctuations at the oscillation point indicated in the legend. 162
381 Distribution of $\Delta\chi^2$ vs coverage in the ($sin^2\theta_{13}$,$sin^2\theta_{23}$) parameter space from 1k toy MC experiments generated with the Run 1+2+3 POT with statistical fluctuations at the oscillation point indicated in the legend. 162
382 Summary of figures 362-381 showing the value of $\Delta\chi^2$ at 99%, 90% and 68% confidence intervals vs the value of $sin^2\theta_{23}$. Horizontal dashed lines show the canonical $\Delta\chi^2$ value for 2 degrees of freedom. 163

383 Summary of figures 362-381 showing the value of $\Delta\chi^2$ at 99%, 90% and 68% confidence intervals vs the value of $sin^2\theta_{13}$. Horizontal dashed lines show the canonical $\Delta\chi^2$ value for 2 degrees of freedom. 163
384 Summary of figures 362-381 showing the value of $\Delta\chi^2$ at 68% confidence intervals in Z axis (color) vs the value of $sin^2\theta_{23}$ in X axis and $sin^2\theta_{13}$ in Y axis. 163
385 Summary of figures 362-381 showing the value of $\Delta\chi^2$ at 90% confidence intervals in Z axis (color) vs the value of $sin^2\theta_{23}$ in X axis and $sin^2\theta_{13}$ in Y axis. 163
386 Summary of figures 362-381 showing the value of $\Delta\chi^2$ at 99% confidence intervals in Z axis (color) vs the value of $sin^2\theta_{23}$ in X axis and $sin^2\theta_{13}$ in Y axis. 163
387 Summary of values of $\Delta\chi^2$ at 99%, 90% and 68% confidence intervals in the 2D parameter space ($sin^2\theta_{23}$,$|\Delta m^2|$) vs the value of $sin^2\theta_{23}$. True input values for the other oscillation parameters: $|\Delta m^2| = 2.36 \times 10^{-3}$, $sin^2\theta_{13} = 0.025$ and δ_{CP} = 0. 165
388 Summary of values of $\Delta\chi^2$ at 99%, 90% and 68% confidence intervals in the 2D parameter space ($sin^2\theta_{13}$,$|\Delta m^2|$) vs the value of $sin^2\theta_{13}$. True input values for the other oscillation parameters: $|\Delta m^2| = 2.36 \times 10^{-3}$, $sin^2\theta_{23} = 0.5$ and δ_{CP} = 0. 165
389 Summary of values of $\Delta\chi^2$ at 99%, 90% and 68% confidence intervals in the 2D parameter space ($sin^2\theta_{13}$,$|\delta_{CP}|$) vs the value of $sin^2\theta_{13}$. True input values for the other oscillation parameters: $|\Delta m^2| = 2.36 \times 10^{-3}$, $sin^2\theta_{23} = 0.5$ and δ_{CP} = 0. 165
390 Summary of values of $\Delta\chi^2$ at 99%, 90% and 68% confidence intervals in the 2D parameter space ($sin^2\theta_{13}$,$sin^2\theta_{23}$) vs the value of $sin^2\theta_{23}$. True input values for the other oscillation parameters: $|\Delta m^2| = 2.36 \times 10^{-3}$ and δ_{CP} = 0. 166
391 Summary of values of $\Delta\chi^2$ at 99%, 90% and 68% confidence intervals in the 2D parameter space ($sin^2\theta_{13}$,$sin^2\theta_{23}$) vs the value of $sin^2\theta_{13}$. True input values for the other oscillation parameters: $|\Delta m^2| = 2.36 \times 10^{-3}$ and δ_{CP} = 0. 166
392 Summary of values of $\Delta\chi^2$ at 68% confidence intervals in Z axis (color) in the 2D parameter space ($sin^2\theta_{13}$,$sin^2\theta_{23}$) vs the value of $sin^2\theta_{23}$ in X axis and $sin^2\theta_{13}$ in Y axis. True input values for the other oscillation parameters: $|\Delta m^2| = 2.36 \times 10^{-3}$ and δ_{CP} = 0. 166
393 Summary of values of $\Delta\chi^2$ at 90% confidence intervals in Z axis (color) in the 2D parameter space ($sin^2\theta_{13}$,$sin^2\theta_{23}$) vs the value of $sin^2\theta_{23}$ in X axis and $sin^2\theta_{13}$ in Y axis. True input values for the other oscillation parameters: $|\Delta m^2| = 2.36 \times 10^{-3}$ and δ_{CP} = 0. 166
394 Summary of values of $\Delta\chi^2$ at 99% confidence intervals in Z axis (color) in the 2D parameter space ($sin^2\theta_{13}$,$sin^2\theta_{23}$) vs the value of $sin^2\theta_{23}$ in X axis and $sin^2\theta_{13}$ in Y axis. True input values for the other oscillation parameters: $|\Delta m^2| = 2.36 \times 10^{-3}$ and δ_{CP} = 0. 166
395 Summary of the values of $\Delta\chi^2$ at 99%, 90% and 68% confidence intervals in the 2D parameter space ($sin^2\theta_{23}$,$|\Delta m^2|$) vs the value of $sin^2\theta_{23}$ with statistical fluctuations only and fitting $sin^2\theta_{13}$ and δ_{CP}. True input values for the other oscillation parameters: $|\Delta m^2| = 2.36 \times 10^{-3}$, $sin^2\theta_{13} = 0.025$ and δ_{CP} = 0. 168
396 Summary of the values of $\Delta\chi^2$ at 99%, 90% and 68% confidence intervals in the 2D parameter space ($sin^2\theta_{23}$,$|\Delta m^2|$) vs the value of $sin^2\theta_{23}$ with statistical fluctuations and systematic variations and fitting $sin^2\theta_{13}$ and δ_{CP}. True input values for the other oscillation parameters: $|\Delta m^2| = 2.36 \times 10^{-3}$, $sin^2\theta_{13} = 0.025$ and δ_{CP} = 0. 168
397 Summary of the values of $\Delta\chi^2$ at 99%, 90% and 68% confidence intervals in the 2D parameter space ($sin^2\theta_{13}$,$|\Delta m^2|$) vs the value of $sin^2\theta_{13}$ with statistical fluctuations only and fitting $sin^2\theta_{23}$ and δ_{CP}. True input values for the other oscillation parameters: $|\Delta m^2| = 2.36 \times 10^{-3}$, $sin^2\theta_{23} = 0.5$ and δ_{CP} = 0. 168
398 Summary of the values of $\Delta\chi^2$ at 99%, 90% and 68% confidence intervals in the 2D parameter space ($sin^2\theta_{13}$,$|\Delta m^2|$) vs the value of $sin^2\theta_{13}$ with statistical fluctuations and systematic variations and fitting $sin^2\theta_{23}$ and δ_{CP}. True input values for the other oscillation parameters: $|\Delta m^2| = 2.36 \times 10^{-3}$, $sin^2\theta_{23} = 0.5$ and δ_{CP} = 0. 168
399 Summary of the values of $\Delta\chi^2$ at 99%, 90% and 68% confidence intervals in the 2D parameter space ($sin^2\theta_{13}$,δ_{CP}) vs the value of $sin^2\theta_{13}$ with statistical fluctuations only and fitting $sin^2\theta_{23}$ and $|\Delta m^2|$. True input values for the other oscillation parameters: $|\Delta m^2| = 2.36 \times 10^{-3}$, $sin^2\theta_{23} = 0.5$ and δ_{CP} = 0. 168
400 Summary of the values of $\Delta\chi^2$ at 99%, 90% and 68% confidence intervals in the 2D parameter space ($sin^2\theta_{13}$,δ_{CP}) vs the value of $sin^2\theta_{13}$ with statistical fluctuations and systematic variations and fitting $sin^2\theta_{23}$ and $|\Delta m_2|$. True input values for the other oscillation parameters: $|\Delta m^2| = 2.36 \times 10^{-3}$, $sin^2\theta_{23} = 0.5$ and δ_{CP} = 0. . . 168
401 Summary of the values of $\Delta\chi^2$ at 99%, 90% and 68% confidence intervals in the 2D parameter space ($sin^2\theta_{13}$,$sin^2\theta_{23}$) vs the value of $sin^2\theta_{23}$ with statistical fluctuations only and fitting $|\Delta m^2|$ and δ_{CP}. True input values for the other oscillation parameters: $|\Delta m^2| = 2.36 \times 10^{-3}$ and δ_{CP} = 0. 169
402 Summary of the values of $\Delta\chi^2$ at 99%, 90% and 68% confidence intervals in the 2D parameter space ($sin^2\theta_{13}$,$sin^2\theta_{23}$) vs the value of $sin^2\theta_{23}$ with statistical fluctuations and systematic variations and fitting $|\Delta m^2|$ and δ_{CP}. True input values for the other oscillation parameters: $|\Delta m^2| = 2.36 \times 10^{-3}$ and δ_{CP} = 0. 169

403 Summary of the values of $\Delta\chi^2$ at 99%, 90% and 68% confidence intervals in the 2D parameter space ($sin^2\theta_{13}$,$sin^2\theta_{23}$) vs the value of $sin^2\theta_{13}$ with statistical fluctuations only and fitting $|\Delta m^2|$ and δ_{CP}. True input values for the other oscillation parameters: $|\Delta m^2| = 2.36 \times 10^{-3}$ and δ_{CP} = 0. 169
404 Summary of the values of $\Delta\chi^2$ at 99%, 90% and 68% confidence intervals in the 2D parameter space ($sin^2\theta_{13}$,$sin^2\theta_{23}$) vs the value of $sin^2\theta_{13}$ with statistical fluctuations and systematic variations and fitting $|\Delta m^2|$ and δ_{CP}. True input values for the other oscillation parameters: $|\Delta m^2| = 2.36 \times 10^{-3}$ and δ_{CP} = 0. 169
405 Summary of values of $\Delta\chi^2$ at 68% confidence intervals in Z axis (color) in the 2D parameter space ($sin^2\theta_{13}$,$sin^2\theta_{23}$) vs the value of $sin^2\theta_{23}$ in X axis and $sin^2\theta_{13}$ in Y axis for toy experiments with statistical fluctuations only and fitting $|\Delta m^2|$ and δ_{CP}. True input values for the other oscillation parameters: $|\Delta m^2| = 2.36 \times 10^{-3}$ and δ_{CP} = 0. 170
406 Summary of values of $\Delta\chi^2$ at 68% confidence intervals in Z axis (color) in the 2D parameter space ($sin^2\theta_{13}$,$sin^2\theta_{23}$) vs the value of $sin^2\theta_{23}$ in X axis and $sin^2\theta_{13}$ in Y axis for toy experiments with statistical fluctuations and systematic fluctuations and fitting $|\Delta m^2|$ and δ_{CP}. True input values for the other oscillation parameters: $|\Delta m^2| = 2.36 \times 10^{-3}$ and δ_{CP} = 0. 170
407 Summary of values of $\Delta\chi^2$ at 90% confidence intervals in Z axis (color) in the 2D parameter space ($sin^2\theta_{13}$,$sin^2\theta_{23}$) vs the value of $sin^2\theta_{23}$ in X axis and $sin^2\theta_{13}$ in Y axis for toy experiments with statistical fluctuations only and fitting $|\Delta m^2|$ and δ_{CP}. True input values for the other oscillation parameters: $|\Delta m^2| = 2.36 \times 10^{-3}$ and δ_{CP} = 0. 170
408 Summary of values of $\Delta\chi^2$ at 90% confidence intervals in Z axis (color) in the 2D parameter space ($sin^2\theta_{13}$,$sin^2\theta_{23}$) vs the value of $sin^2\theta_{23}$ in X axis and $sin^2\theta_{13}$ in Y axis for toy experiments with statistical fluctuations and systematic fluctuations and fitting $|\Delta m^2|$ and δ_{CP}. True input values for the other oscillation parameters: $|\Delta m^2| = 2.36 \times 10^{-3}$ and δ_{CP} = 0. 170
409 Summary of values of $\Delta\chi^2$ at 99% confidence intervals in Z axis (color) in the 2D parameter space ($sin^2\theta_{13}$,$sin^2\theta_{23}$) vs the value of $sin^2\theta_{23}$ in X axis and $sin^2\theta_{13}$ in Y axis for toy experiments with statistical fluctuations only and fitting $|\Delta m^2|$ and δ_{CP}. True input values for the other oscillation parameters: $|\Delta m^2| = 2.36 \times 10^{-3}$ and δ_{CP} = 0. 170
410 Summary of values of $\Delta\chi^2$ at 99% confidence intervals in Z axis (color) in the 2D parameter space ($sin^2\theta_{13}$,$sin^2\theta_{23}$) vs the value of $sin^2\theta_{23}$ in X axis and $sin^2\theta_{13}$ in Y axis for toy experiments with statistical fluctuations and systematic fluctuations and fitting $|\Delta m^2|$ and δ_{CP}. True input values for the other oscillation parameters: $|\Delta m^2| = 2.36 \times 10^{-3}$ and δ_{CP} = 0. 170
411 Summary of the values of $\Delta\chi^2$ at 99%, 90% and 68% confidence intervals in the 2D parameter space ($sin^2\theta_{13}$,$|\Delta m^2|$) vs the value of $sin^2\theta_{13}$ with statistical fluctuations only and **fixing** $sin^2\theta_{23}$ **and** δ_{CP}. True input values for the other oscillation parameters: $|\Delta m^2| = 2.36 \times 10^{-3}$, $sin^2\theta_{23} = 0.35$ and δ_{CP} = 0. 171
412 Summary of the values of $\Delta\chi^2$ at 99%, 90% and 68% confidence intervals in the 2D parameter space ($sin^2\theta_{13}$,$|\Delta m^2|$) vs the value of $sin^2\theta_{13}$ with statistical fluctuations only and **fitting** $sin^2\theta_{23}$ **and fixing** δ_{CP}. True input values for the other oscillation parameters: $|\Delta m^2| = 2.36 \times 10^{-3}$, $sin^2\theta_{23} = 0.35$ and δ_{CP} = 0. 171
413 Summary of the values of $\Delta\chi^2$ at 99%, 90% and 68% confidence intervals in the 2D parameter space ($sin^2\theta_{13}$,$|\Delta m^2|$) vs the value of $sin^2\theta_{13}$ with statistical fluctuations only and **fitting** δ_{CP} **and fixing** $sin^2\theta_{23}$. True input values for the other oscillation parameters: $|\Delta m^2| = 2.36 \times 10^{-3}$, $sin^2\theta_{23} = 0.35$ and δ_{CP} = 0. 171
414 Summary of the values of $\Delta\chi^2$ at 99%, 90% and 68% confidence intervals in the 2D parameter space ($sin^2\theta_{13}$,$|\Delta m^2|$) vs the value of $sin^2\theta_{13}$ with statistical fluctuations only and **fitting** $sin^2\theta_{23}$ **and** δ_{CP}. True input values for the other oscillation parameters: $|\Delta m^2| = 2.36 \times 10^{-3}$, $sin^2\theta_{23} = 0.35$ and δ_{CP} = 0. 171
415 Summary of the values of $\Delta\chi^2$ at 99%, 90% and 68% confidence intervals in the 2D parameter space ($sin^2\theta_{13}$,$|\Delta m^2|$) vs the value of $sin^2\theta_{13}$ with statistical fluctuations and systematic variations and **fitting** $sin^2\theta_{23}$ **and** δ_{CP}. True input values for the other oscillation parameters: $|\Delta m^2| = 2.36 \times 10^{-3}$, $sin^2\theta_{23} = 0.35$ and δ_{CP} = 0. . . . 171
416 Summary of the values of $\Delta\chi^2$ at 99%, 90% and 68% confidence intervals in the 1D parameter space $sin^2\theta_{23}$ vs the value of $sin^2\theta_{23}$ with statistical fluctuations only where $\Delta\chi^2$ was calculated as folllows: a first fit was done fitting only δ_{CP}, fixing the other three oscillation parameters to their true input value, and χ^2_{init} was obtained; then a second fit was done fitting δ_{CP} and $sin^2\theta_{23}$, keeping $sin^2\theta_{13}$ and $|\Delta m^2|$ fixed to their true input values and χ^2_{bf} was obtained, computing finally $\Delta\chi^2 = \chi^2_{init} - \chi^2_{bf}$. True input values for the other oscillation parameters: $|\Delta m^2| = 2.36 \times 10^{-3}$, $sin^2\theta_{13} = 0.025$ and δ_{CP} = 0. 172

417 Summary of the values of $\Delta\chi^2$ at 99%, 90% and 68% confidence intervals in the 1D parameter space $|\Delta m^2|$ vs the value of $|\Delta m^2|$ with statistical fluctuations only where $\Delta\chi^2$ was calculated as folllows: a first fit was done fitting only δ_{CP}, fixing the other three oscillation parameters to their true input value, and χ^2_{init} was obtained; then a second fit was done fitting δ_{CP} and $|\Delta m^2|$, keeping $sin^2\theta_{13}$ and $sin^2\theta_{23}$ fixed to their true input values and χ^2_{bf} was obtained, computing finally $\Delta\chi^2 = \chi^2_{init} - \chi^2_{bf}$. True input values for the other oscillation parameters: $sin^2\theta_{23} = 0.5$, $sin^2\theta_{13} = 0.025$ and δ_{CP} = 0. 172

418 Summary of the values of $\Delta\chi^2$ at 99%, 90% and 68% confidence intervals in the 1D parameter space $sin^2\theta_{13}$ vs the value of $sin^2\theta_{13}$ with statistical fluctuations only where $\Delta\chi^2$ was calculated as folllows: a first fit was done fitting only δ_{CP}, fixing the other three oscillation parameters to their true input value, and χ^2_{init} was obtained; then a second fit was done fitting δ_{CP} and $sin^2\theta_{13}$, keeping $sin^2\theta_{23}$ and $|\Delta m^2|$ fixed to their true input values and χ^2_{bf} was obtained, computing finally $\Delta\chi^2 = \chi^2_{init} - \chi^2_{bf}$. True input values for the other oscillation parameters: $|\Delta m^2| = 2.36 \times 10^{-3}$, $sin^2\theta_{23} = 0.5$ and δ_{CP} = 0. 172

419 Comparison between the value of $sin^2\theta_{13}$ giving the true minimum χ^2 found scanning the ($sin^2\theta_{13}$, δ_{CP}) parameter space with the best-fit value result from the fit over 100 toy experiments created at true input values: $|\Delta m^2| = 2.36\times10^{-3}$, $sin^2\theta_{23} = 0.5$, $sin^2\theta_{13} = 0.025$ and δ_{CP} = 0. Results present a good agreement within the step sizes used ($\delta sin^2\theta_{13}$ = 0.001 and δ_{CP} = 0.02). 173

420 Comparison between the value of δ_{CP} giving the true minimum χ^2 found scanning the ($sin^2\theta_{13}$, δ_{CP}) parameter space with the best-fit value result from the fit over 100 toy experiments created at true input values: $|\Delta m^2| = 2.36\times10^{-3}$, $sin^2\theta_{23} = 0.5$, $sin^2\theta_{13} = 0.025$ and δ_{CP} = 0. Results present a good agreement within the step sizes used ($\delta sin^2\theta_{13}$ = 0.001 and δ_{CP} = 0.02). 173

List of Tables

1 Values used for $\sin^2 2\theta_{12}$ and Δm^2_{21} in the joint oscillation analysis 32

2 List of the MC templates used for the calculation of the *VaLOR* single μ-like ring and single e-like ring event reconstructed energy spectrun p.d.f.s. The symbol ✓indicates, in any row, for which of the samples defined in the last two columns the MC template defined in the first column is used. Notice that the MC templates used for NC modes are different for single μ-like ring and single e-like ring. 34

3 Calculated numbers of single μ-like ring and single e-like ring events without oscillations using the nominal MC templates, the NA61-tuned MC templates and the BANFF-tuned MC templates. The total numbers of events and the numbers of events from each mode considered in this analysis are shown. These numbers were calculated for an exposure of 3.010×10^{20} POT. Note that different NC MC templates are used for predicting the number of single μ-like ring and single e-like ring events. 36

4 Calculated numbers of single μ-like ring and single e-like ring events with oscillations using the nominal MC templates, the NA61-tuned MC templates and the BANFF-tuned MC templates. The total numbers of events and the numbers of events from each mode considered in this analysis are shown. These numbers were calculated for an exposure of 3.010×10^{20} POT and oscillations with δ_{CP}=0, $\sin^2\theta_{13}$=0.025, $\sin^2\theta_{23}$=0.5 and $|\Delta m^2|$=2.4×10^{-3} eV^2/c^4. The 2012 PDG parameters are used for $\sin^2\theta_{12}$ and δm^2. The normal hierarchy is assumed. Note that different NC MC templates are used for predicting the number of single μ-like ring and single e-like ring events. 37

5 Summary table of SuperK detector systematics. The nuisance parameter symbols used in this paper are shown in the first column. An index r in the nuisance parameter symbol denotes dependence on reconstructed energy while an index t denotes dependence on true energy. An index i is used where multiple systematic parameters, typically correlated between themselves, are grouped together. 39

6 Summary table of BANFF systematics. The nuisance parameter symbols used in this paper are shown in the first column. An index r in the nuisance parameter symbol denotes dependence on reconstructed energy while an index t denotes dependence on true energy. An index i is used where multiple systematic parameters, typically correlated between themselves, are grouped together. 40

7 Summary table of Uncorrelated cross-section systematics. The nuisance parameter symbols used in this paper are shown in the first column. An index r in the nuisance parameter symbol denotes dependence on reconstructed energy while an index t denotes dependence on true energy. An index i is used where multiple systematic parameters, typically correlated between themselves, are grouped together. 41

8 Summary table of FSI+SI systematics. The nuisance parameter symbols used in this paper are shown in the first column. An index r in the nuisance parameter symbol denotes dependence on reconstructed energy while an index t denotes dependence on true energy. An index i is used where multiple systematic parameters, typically correlated between themselves, are grouped together. 42

9 List of all systematic parameters included in the joint oscillation analysis. A ✓symbol indicates whether the systematic parameter is applied on the single μ-like ring and single e-like ring MC templates. 43
10 A ✓symbol denotes that the given single μ-like ring MC template is modified when the given systematic parameter is tweaked. The table lists all systematic parameters, relevant to single μ-like ring events, considered in this analysis (first column) and all 28 MC templates used for constructing the single μ-like ring event reconstructed energy spectrum p.d.f (first row). 44
11 A ✓symbol denotes that the given single e-like ring MC template is modified when the given systematic parameter is tweaked. The table lists all systematic parameters, relevant to single e-like ring events, considered in this analysis (first column) and all 32 MC templates used for constructing the single e-like ring event reconstructed energy spectrum p.d.f (first row). 45
12 Effect of 1σ systematic parameter variation on the number of single μ-like ring and single e-like ring events, computed for oscillations with $|\Delta m^2|$=2.36$\times 10^{-3}$ eV^2/c^4. $\sin^2\theta_{23}$=0.5, $\sin^2\theta_{13}$=0.025, δ_{CP}=0. 2012 PDG values are used for the solar parameters and the normal mass hierarchy is assumed. The numbers shown were calculated for an exposure of 3.010$\times 10^{20}$ POT and BANFF-tuned MC templates were used. 46
13 Summary of best-fit parameters for the joint 3-flavour oscillation fit, and the stand-alone 3-flavour ν_μ disappearance and ν_e appearance fits to the Run 1+2+3 dataset. The quoted best-fit χ^2 values were computed from the test-statistic minimized in the fit (likelihood ratio) with the reconstructed energy binning used in each fit. The table also shows the p-values obtained from the goodness-of-fit test of Sec. 6.2. 49
14 Predicted number of ν_e candidate events for the Run1+2+3 POT before BANFF tuning (that is, after external flux reweighting using default 11c SK MC with the 11b tuned version 3.2), for *VaLOR* appearance analysis (black) compared to official appearance analysis (blue) as in Table 1 of [15], using $sin^2(2\theta_{12}) = 0.8704$, $\Delta m^2_{21} = 7.6 \times 10^{-5}$, $sin^2(2\theta_{23}) = 1.0$, $|\Delta m^2_{32}| = 2.4 \times 10^{-3}$, $\delta_{CP} = 0$ and normal hierarchy. 72
15 Predicted number of ν_e candidate events for the Run1+2+3 POT after applying BANFF tuning (post ND280 fitted values) for *VaLOR* appearance analysis (black) compared to official appearance analysis (blue) as in Table 9 of [15],using $sin^2(2\theta_{12}) = 0.8704$, $\Delta m^2_{21} = 7.6 \times 10^{-5}$, $sin^2(2\theta_{23}) = 1.0$, $|\Delta m^2_{32}| = 2.4 \times 10^{-3}$, $\delta_{CP} = 0$ and normal hierarchy. 72
16 Best-fit points and confidence intervals for $sin^2(2\theta_{13})$ obtained from Fig. 55, with $\delta_{CP} = 0$, $sin^2(2\theta_{12}) = 0.8704$, $\Delta m^2_{21} = 7.6 \times 10^{-5}$, $sin^2(2\theta_{23}) = 1.0$ and $|\Delta m^2_{32}| = 2.4 \times 10^{-3}$, for normal (NH) and inverted (IH) hierarchy. 74
17 True input values for the different oscillation points used in the study of fitter performance. 75
18 The numbering of systematic parameters for figures 87 - B.2 80
19 True input values (shown in bold) and VALOR best-fit values for a test ensemble of 6 fake datasets with no statistical fluctuations. 96
20 True input values (shown in bold) and VALOR best-fit values for a test ensemble of 7 fake datasets with statistical fluctuations 103
21 True oscillation parameter points used in the sensitivity study. $\sin^2\theta_{12}$ and δm^2 were fixed to 0.857 and 7.5$\times 10^{-5}$ eV^2/c^4 respectively (2012 PDG values). 128
22 True input values of the oscillation parameters when not varied used for the coverage checks. 149

1. Introduction

In this technical note, we report the results of a joint 3-flavour oscillation analysis, performed by the Valencia-Lancaster-Oxford-Rutherford (*VaLOR*) group, on the combined Run 1+2+3 (3.010×10^{20} POT) dataset. This dataset was collected in three run periods: in January - June 2010 (Run1, 0.323×10^{20} POT), in November 2010 - March 2011 (Run2, 1.108×10^{20} POT) and, following the recovery work from the damage of the 2011 Tohoku earthquake, in March - June 2012 (Run3, 1.579×10^{20} POT). The motivation for our joint 3-flavour oscillation analysis is presented in Sec. 2.

In this analysis, the atmospheric squared-mass splitting $|\Delta m^2|$, the mixing angles $\sin^2\theta_{23}$, $\sin^2\theta_{13}$ and the CP-violating phase δ_{CP}, are determined together through a simultaneous fit of the reconstructed energy spectra of both the SuperK single μ-like ring and single e-like ring event samples. In contrast to the stand-alone ν_e-appearance and ν_μ-disappearance fits, our the joint 3-flavour oscillation fit does not have to assume prior values for any of these four oscillation parameters and all correlations between them are taken into account.

This analysis is a continuation of the work presented in Refs. [1], [2], [3] and [4]. This work brings together the standard *VaLOR* 3-flavour ν_μ-disappearance analysis and a new 3-flavour ν_e-appearance analysis developed within the *VaLOR* analysis framework. A validation of the new 3-flavour ν_e-appearance analysis is presented in Appendix A.

This analysis is performed using neutrino oscillation probabilities computed in a 3-flavour framework including constant-density matter effects. Details of our oscillation probability calculations, estimates of the numerical accuracy of our calculations and comparisons with other oscillation probability codes, are given in Appendices A and B of Ref. [4]. The Fogli-Lisi convention is used for the atmospheric mass-squared splitting, and this is explained in Sec. 3.

We consider a total of 83 efficiency, energy scale, neutrino flux, neutrino cross-section, initial-state nuclear environment and final-state rescattering systematics. These systematic parameters and their effects on the extrapolated single μ-like ring event and single e-like ring event reconstructed energy spectrum are described in Sec. 5.

As in our previous analyses, the oscillation fit was made using the likelihood-ratio method [29]. All 83 systematics considered in this analysis were allowed to float in the fit. The oscillation fitting method is presented in detail in Sec. 6, and the chosen goodness-of-fit test, suitable for the Run 1+2+3 statistics, is described in Sec. 6.2. The fitter performance has been tested in detail using toy MC experiments and the results of these tests are presented in Appendix B.

Joint 3-flavour oscillation fits of fake datasets have been studied in detail and the results are presented in Appendix C. These fits were performed using the complete *VaLOR* analysis with an integrated exposure of 3.010×10^{20} POT. Fit results from the joint 3-flavour oscillation analysis are contrasted with those from the stand-alone ν_e-appearance and ν_μ-disappearance fits. Sensitivity studies have also been performed for an integrated exposure of 3.010×10^{20} POT, and the results are shown in Appendix D.

A sutdy on the coverage of the different confidence intervals using the constant $\Delta\chi^2$ method is presented in Appendix I.

The results of the joint measurement of $|\Delta m^2|$, $\sin^2\theta_{23}$, $\sin^2\theta_{13}$ and δ_{CP}, and the systematic parameter pulls, using the Run 1+2+3 dataset are given in Sec. 7.1, and the goodness-of-fit tests are presented in Sec. 7.2. The best-fit single μ-like ring and single e-like ring event reconstructed energy spectra are shown in Sec. 7.3. In Sec. 7.4, profile $\Delta\chi^2$ distributions are presented for each of $|\Delta m^2|$, $\sin^2\theta_{23}$, $\sin^2\theta_{13}$, δ_{CP} and 68% and 90% confidence regions are presented in following four 2-dimensional oscillation parameter spaces: ($\sin^2\theta_{23}$, $|\Delta m^2|$), ($\sin^2\theta_{13}$, $|\Delta m^2|$), ($\sin^2\theta_{13}$, δ_{CP}) and ($\sin^2\theta_{23}$, $\sin^2\theta_{13}$). Wherever possible, the Run 1+2+3 joint 3-flavour oscillation fit results are compared with the Run 1+2+3 results obtained by the stand-alone ν_e-appearance and ν_μ-disappearance fits.

Finally, a summary is given in Sec. 8.

2. Motivation

To date, two types of T2K oscillation analyses exist [4, 16]:

- ν_e-appearance analyses, in which $\sin^2 2\theta_{13}$ and δ_{CP} are determined simultaneously using the SuperK single e-like ring event sample. In these analyses, the values of $|\Delta m^2_{32}|$ and $\sin^2 2\theta_{23}$ are fixed and a neutrino mass hierarchy is assumed. To find the best-fit point and confidence interval for $\sin^2 2\theta_{13}$, this type of analysis typically fixes δ_{CP} to 0.0. The confidence region in the ($\sin^2 2\theta_{13}$, δ_{CP}) space is usually calculated using a raster scan.

- ν_μ-disappearance analyses, in which $|\Delta m^2_{32}|$ and $\sin^2 2\theta_{23}$ are determined simultaneously using the SuperK single μ-like ring event sample. In these analyses, the values of $\sin^2 2\theta_{13}$ and δ_{CP} are fixed and a neutrino mass hierarchy is assumed.

However the oscillation parameters that are fixed have a non-negligible effect on P($\nu_\mu\to\nu_\mu$) and P($\nu_\mu\to\nu_e$), and this is shown in Fig. 1. The fixed oscillation parameters can also have a significant impact on the confidence regions, as demonstrated in Fig. 2 for the stand-alone ν_e-appearance analysis, which typically uses fixed values of $|\Delta m^2_{32}|$ and $\sin^2 2\theta_{23}$.

The motivation for the joint oscillation analysis is to avoid fixing any of $|\Delta m^2_{32}|$, $\sin^2\theta_{23}$, $\sin^2\theta_{13}$ or δ_{CP} [1] and to perform a joint determination of all four oscillation parameters with a simultaneous 3-flavour fit of the single μ-like ring and single e-like ring event samples.

On the basis that the $\nu_\mu \to \nu_e$ oscillation probability is given, to first order, by

$$P(\nu_\mu \to \nu_e) \approx \sin^2 2\theta_{13} \sin^2\theta_{23} sin^2\left(1.27\Delta m^2_{13}\frac{L}{E}\right) \quad (1)$$

it is claimed in our papers [17] that *"For non-maximal $sin^2 2\theta_{23}$, the confidence intervals remain unchanged to first order by replacing $sin^2 2\theta_{13}$ by $2sin^2\theta_{23}sin^2 2\theta_{13}$."*. But there is a problem with this rescaling of $P(\nu_\mu \to \nu_e)$ by $2\sin^2\theta_{23}$ as the octant of θ_{23} is unknown (if it is non-maximal). Since this mixing angle appears in Eq. 1 as $\sin^2\theta_{23}$, a solution in the second octant ($\sin^2\theta_{23} > 0.5$) would move the contours to the right, while a solution in the first octant ($\sin^2\theta_{23} < 0.5$) would move the contours to the left. As the stand-alone analyses are using $\sin^2 2\theta$ variables, there is no information to decide which of the two rescalings is correct.

The general validity of the cited assumption can be explored by performing a toy demonstration: In Fig. 2, best-fit values and contours are shown for a toy experiment with true $\sin^2 2\theta_{23} = 0.96$, using the true (solid lines) or maximal mixing (dashed lines) priors for $\sin^2 2\theta_{23}$ (and keeping it constant throughout the fitting). Then, in Fig.3, the contours obtained with maximal prior after rescaling them (dashed lines) are shown, and again the contours obtained with the actual true value as prior (solid lines, same as in Fig. 2). It is obvious that a difference remains between the contours obtained with the two methods. This arises from the fact that Eq. 1 is only a first-order approximation and the effect of the subdominant terms can be important, especially for larger values of δ_{CP}.

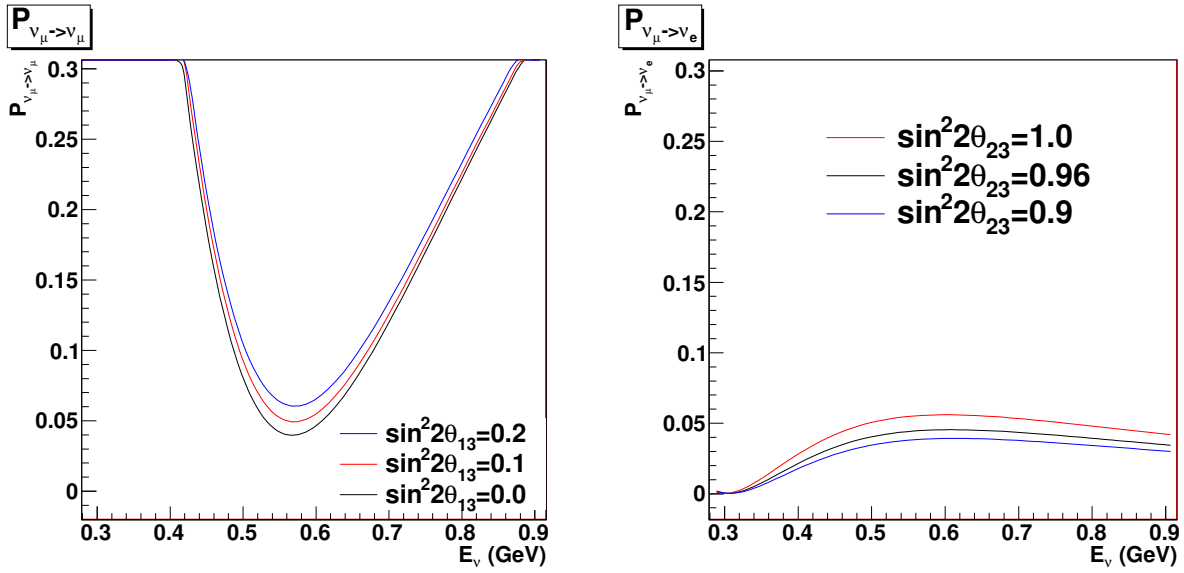

Figure 1: Examples of the effect of the interdependence between the oscillation parameters in the oscillation probabilities $P(\nu_\mu \to \nu_\mu)$(left) and $P(\nu_\mu \to \nu_e)$ (right). These probabilities are computed for different values of $\sin^2 2\theta_{13}$ (left) or $\sin^2 2\theta_{23}$ (right) with the other 3 parameters being fixed at $\sin^2 2\theta_{23}$ = 0.96, $|\Delta m^2_{32}| = 2.4\times10^{-3}$ eV^2/c^4, $\delta_{CP} = 0$ (left) or $\sin^2 2\theta_{13} = 0.1$, $|\Delta m^2_{32}| = 2.4\times10^{-3}$ eV^2/c^4, $\delta_{CP} = 0$ (right).

[1] The effect of including the remaining 12-sector parameters, Δm^2_{21} and $\sin^2\theta_{12}$, in the T2K fit has been studied and it is negligible (see Sec. F).

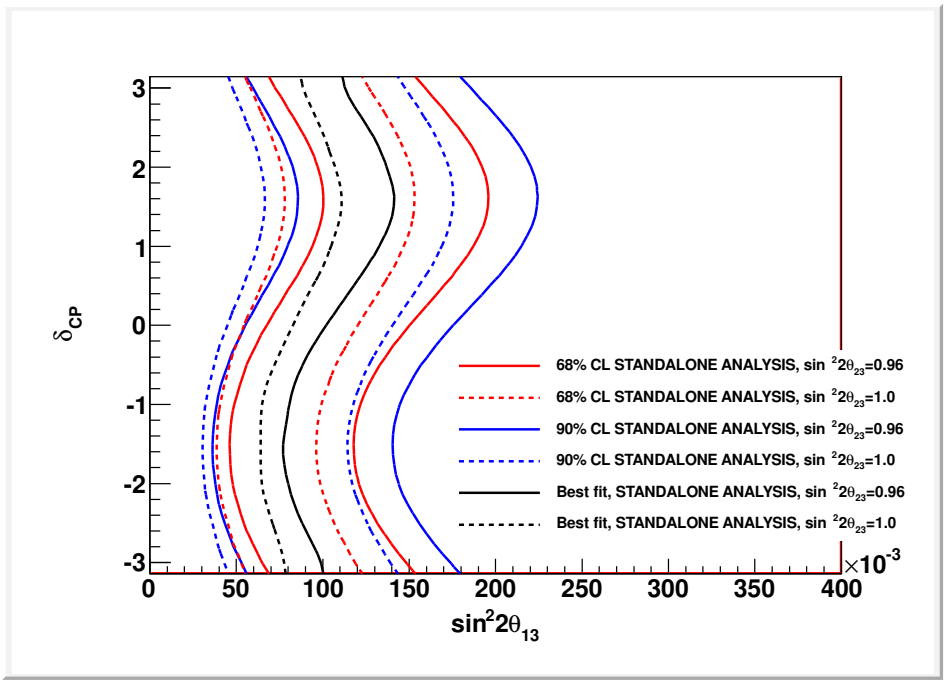

Figure 2: Illustration of the effect of changing the assumed value of $\sin^2 2\theta_{23}$ in the ν_e-appearance contours for 7×10^{21} POT. Dashed lines are contours of the stand-alone ν_e-appearance analysis assuming maximal mixing ($\sin^2 2\theta_{23}$ = 1.0), and solid lines are contours of the stand-alone ν_e-appearance analysis assuming $\sin^2 2\theta_{23}$ = 0.96, the true value with which the toy experiment was created. The other parameters have the following values: $\sin^2 2\theta_{13}$ = 0.12, $|\Delta m^2_{32}|$ = 2.5×10^{-3} eV^2/c^4, and δ_{CP} = 0.5. The confidence regions were constructed using the constant-$\Delta\chi^2$ method, which is described in Sec. 6.

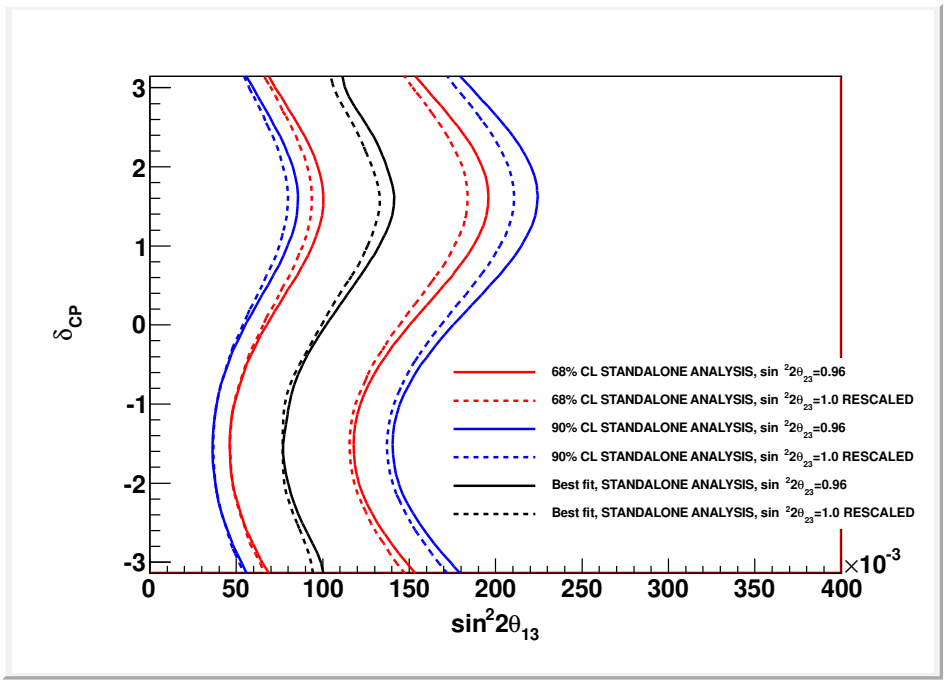

Figure 3: Plot of the same contours as in Fig. 2 rescaling the contours for maximal prior $\sin^2 2\theta_{23}$ = 1.0 with the cited replacement of $\sin^2 2\theta_{13}$ by $2\sin^2\theta_{23}\sin^2 2\theta_{13}$, using for θ_{23} the true value for the toy experiment.

3. Choice of oscillation parameters

This analysis departs from choices which have been followed historically in the T2K stand-alone ν_e-appearance and ν_μ-disappearance analyses by changing the oscillation mixing parameters and the mass-squared splitting parameters. There is a strong motivation for this change in the context of a joint 3-flavour analysis, and it is outlined below.

Neutrino mixing parameters

In the stand-alone ν_μ-disappearance analysis, $\sin^2 2\theta_{23}$ is typically measured since it appears in the first-order approximate formula for the ν_μ survival probability:

$$P(\nu_\mu \to \nu_\mu) \approx 1 - sin^2 2\theta_{23} sin^2 \left(\frac{\Delta m^2_{32} L}{4E_\nu} \right) \tag{2}$$

In the stand-alone analysis, it is nearly impossible to distinguish θ_{23} from $\pi/2 - \theta_{23}$, as both inputs give the same value for $\sin^2 2\theta_{23}$ and, therefore, the same ν_μ-survival probability This is the so-called octant ambiguity.

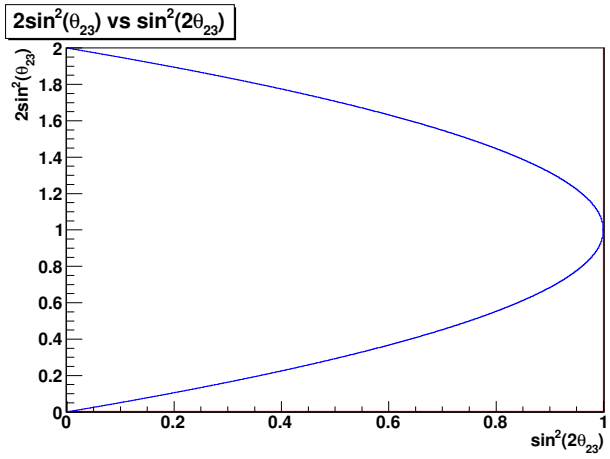

Figure 4: $\sin^2 \theta_{23}$ (appears in leading-order term of P($\nu_\mu \to \nu_e$) vs $\sin^2 2\theta_{23}$(appears in leading-order term of P($\nu_\mu \to \nu_\mu$).

Looking at the leading-order approximation of $P(\nu_\mu \to \nu_e)$, the 23-sector mixing parameter appears as $\sin^2 \theta_{23}$:

$$P(\nu_\mu \to \nu_e) \approx sin^2 2\theta_{13} sin^2 \theta_{23} sin^2 \left(\frac{\Delta m^2_{31} L}{4E_\nu} \right) \tag{3}$$

it is possible to lift the octant degeneracy by combining the ν_μ-disappearance and ν_e-appearance analyses, as shown graphically in Fig. 4. It is therefore a more natural choice for the joint 3-flavour oscillation analysis to fit for $\sin^2 \theta_{ij}$ rather than $\sin^2 2\theta_{ij}$, and this is the choice that has been implemented in the VALOR analysis framework. The option to fit for $\sin^2 2\theta_{ij}$ has also been retained for backward compatibility and to allow validation checks.

Mass-squared splitting parameters

Previous T2K analyses have used the following mass-squared splitting parameters:

$$\left(|\Delta m^2_{32}|, \Delta m^2_{21}\right)$$

which are defined as $\Delta m^2_{ij} = m^2_i - m^2_j$ according to the PDG notation [24]. The mass hierarchy is set through the sign of Δm^2_{32} i.e. $\Delta m^2_{32} = |\Delta m^2_{32}|$ in the normal hierarchy and $\Delta m^2_{32} = -|\Delta m^2_{32}|$ in the inverted hierarchy. The remaining mass-squared splitting is defined as $\Delta m^2_{31} = \Delta m^2_{32} + \Delta m^2_{21}$ for both hierarchies.

In the normal hierarchy (NH) $m^2_1 < m^2_2 << m^2_3$, while in the inverted hierarchy (IH) $m^2_3 << m^2_1 < m^2_2$, i.e. $|\Delta m^2_{31}|$ is the largest mass-squared splitting in the NH, whereas $|\Delta m^2_{32}|$ is the largest in the IH. This means that it is not possible to compare the two hierarchies if the atmospheric mass-squared difference is input as $|\Delta m^2_{32}|$. This has been pointed out by several authors and different schemes are typically employed in global oscillation fits to circumvent this issue. The VaLOR joint oscillation analysis uses the scheme defined by Fogli and Lisi in [21] [25] in which $\left(|\Delta m^2_{32}|, \Delta m^2_{21}\right)$ are replaced by:

$$\left(|\Delta m^2|, \delta m^2\right)$$

where $\Delta m^2 = \left(m_3^2 - \frac{m_1^2+m_2^2}{2}\right) = \left(\frac{\Delta m_{31}^2+\Delta m_{32}^2}{2}\right)$ and $\delta m^2 = \Delta m_{21}^2$. $|\Delta m^2|$ is the "atmospheric" squared-mass splitting, which has the same absolute value for both mass hierarchies. δm^2 is the "solar" squared-mass splitting which is known to be positive. When the mass-squared splittings are input as $\left(\Delta m^2, \delta m^2\right)$, the mass hierarchy is set through the sign of $|\Delta m^2|$, and Δm_{32}^2 and Δm_{31}^2 are calculated as

$$\Delta m_{32}^2 = \Delta m^2 - \frac{\delta m^2}{2}$$
$$\Delta m_{31}^2 = \Delta m^2 + \frac{\delta m^2}{2}$$

for both mass hierarchies. The ability to input the mass-squared differences as $\left(|\Delta m_{32}^2|, \Delta m_{21}^2\right)$ has also been retained for backward compatibility and to allow various validation checks.

The effects of changing the convention for the inputs of the mass-squared splitting parameters on P($\nu_\mu \to \nu_\mu$) and P($\nu_\mu \to \nu_e$) are shown in Fig. 5.

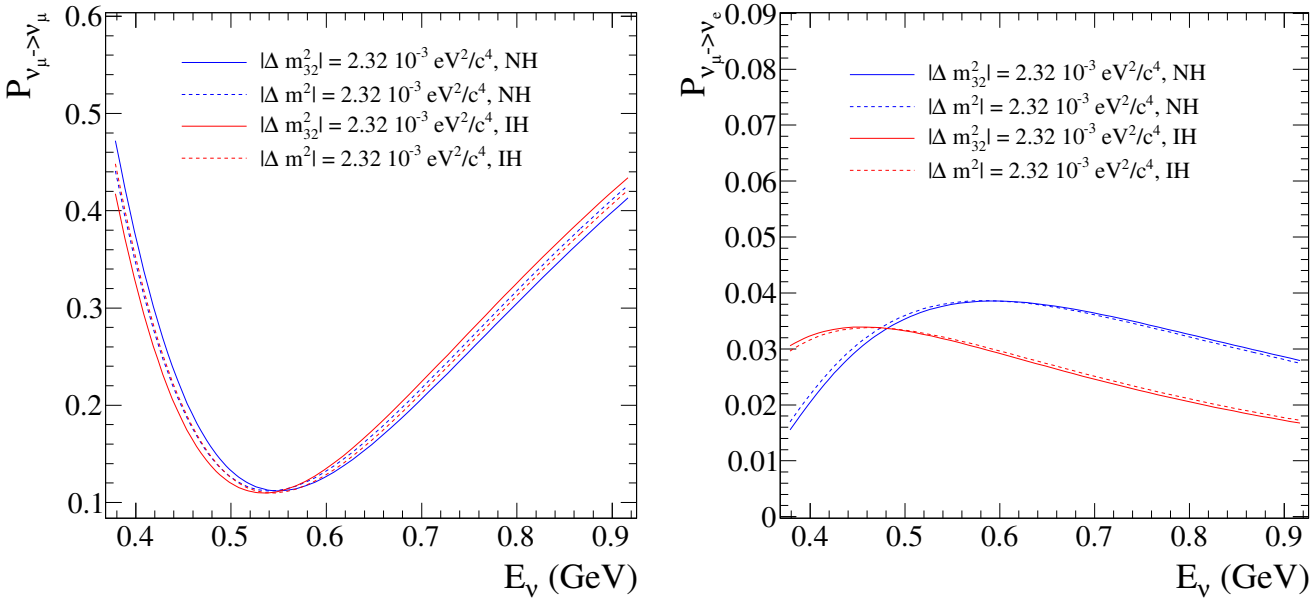

Figure 5: Effects of changing the convention for the inputs of the mass-squared splitting parameters on P($\nu_\mu \to \nu_\mu$) (left) and P($\nu_\mu \to \nu_e$) (right): $|\Delta m_{32}^2|$ = 2.32×10^{-3} eV^2/c^4 (solid lines) and $|\Delta m^2|$ = 2.32×10^{-3} eV^2/c^4 (dashed lines) for the normal hierarchy (blue) and inverted hierarchy (red). The other oscillation parameters are $\sin^2 2\theta_{12}$ = 0.857, δm^2 = 7.5×10^{-5} eV^2/c^4, $\sin^2 2\theta_{13}$ = 0.098 (2012 PDG values), δ_{CP} = 0 and $\sin^2 2\theta_{23}$ = 0.9.

Section H illustrates the difference in the comparison between results in the two mass hierarchies when using the Fogli and Lisi convention $\left(|\Delta m^2|, \delta m^2\right)$ and the previous convention $\left(|\Delta m_{32}^2|, \Delta m_{21}^2\right)$.

Treatment of solar (12-sector) oscillation parameters

A study has been made in which $\sin^2 2\theta_{12}$ and Δm_{21}^2 were allowed to float in the fit of the single μ-like ring Super K sample, and the results are shown in Appendix F. It was found that the fitter returned extreme values of these parameters (see Fig. 308), and this is because they have no effect on the single μ-like ring sample. For this reason, these parameters were fixed throughout this analysis to the values in table 1.

4. Predictions of single μ-like ring and single e-like ring event reconstructed energy spectrum in SuperK

The predicted number $N_{SK;s,r}$ of events in the r^{th} reconstructed energy bin in the SuperK sample s (single μ-like ring or single e-like ring) is computed as follows:

Parameter	Value
$\sin^2 2\theta_{12}$	0.857
$\sin^2 \theta_{12}$	0.311
Δm^2_{21}	7.5×10^{-5} eV^2/c^4

Table 1: Values used for $\sin^2 2\theta_{12}$ and Δm^2_{21} in the joint oscillation analysis

$$N^{exp}_{SK;s,r} = \sum_m \sum_t \sum_{r\prime} P_{m,t} \cdot T_{r,r\prime,f_{\Delta E},s} \cdot S_{s,m,t,r\prime,\mathbf{f}} \cdot N^{MC}_{SK;s,m,r\prime,t} \quad (4)$$

In Eq. 4, $N^{MC}_{SK;s,m,r\prime,t}$ is the input SuperK Monte Carlo (MC) template describing the number of events in the sample s, with true reaction mode m, that can be found in the true energy bin t and in the reconstructed energy bin $r\prime$. Notice that $r\prime$ index indicates a SuperK reconstructed energy bin in absence of a shift in reconstructed energy scale and the index r indicates a SuperK reconstructed energy bin after a shift in the reconstructed energy scale is applied. The construction of the nominal MC templates was presented in detail in Sec. 2.2 of Ref. [4] describing the *VaLOR* 2012 Run 1+2+3 ν_μ-disappearance analysis. The method described there was extended to construct the MC templates relevant for the calculation of the predicted single e-like ring event reconstructed energy p.d.f. The nominal MC templates are reweighted using both flux-tuning weights based on NA61 hadro-production data (see Sec. 2.3 of Ref. [4]) and flux and cross-section tuning weights based on ND280 data (see Sec. 2.4 of Ref. [4]). For the calculation of the single μ-like ring event reconstructed energy p.d.f., the same 28 MC templates are used as in the *VaLOR* 2012 Run 1+2+3 ν_μ-disappearance analysis (see Sec. 2.2.4 in [4]). However 32 MC templates are used for the calculation of the single e-like ring event reconstructed energy p.d.f. as a different choice was made for the NC MC templates. For the single μ-like ring p.d.f. the 'NC1$\pi^\pm$' and 'NC other' MC templates are used, whereas for the single e-like ring p.d.f. the 'NC1π^0', 'NC coherent' and 'NC other' templates are used. Consequently, the definition of 'NC other' is different for the two samples. In total, 60 MC templates are used for the calculation of the combined single μ-like ring and single e-like ring event reconstructed energy p.d.fs. These templates are listed in Tab. 2. The MC template binning for the single μ-like ring sample is unchanged from the *VaLOR* 2012 Run 1+2+3 ν_μ-disappearance analysis[2]. For the single e-like ring sample the MC templates have the same 84 true energy bins used for the single μ-like ring sample and 25 reconstructed energy bins from 0 to 1.25 GeV (50 MeV/bin).

The term $S_{s,m,t,r\prime,\vec{f}}$ in Eq. 4 is an overall, multiplicative, systematic error factor depending on the sample s, the reaction mode m, the true energy bin t, the reconstructed energy bin $r\prime$ and a vector of nuisance (systematic) parameters $\vec{f}$. A summary of the nuisance parameters considered in this analysis is given in Sec. 5 of this note. $T_{r;r\prime;f_{\Delta E}}$ is a transfer function describing the migration of events between the reconstructed energy bins r and $r\prime$ due to a potential shift in the SuperK reconstructed energy scale, expressed here in terms of the nuisance parameter $f_{\Delta E}$. Finally, $P_{m;t}$ is the 3-flavour oscillation probability applied in the true energy bin t of the SuperK MC template which corresponds to mode m. The CC MC templates constructed from the unoscillated MC samples are weighted with the corresponding survival probability: The ν_μ CC templates are weighted with P($\nu_\mu \to \nu_\mu$), the $\bar{\nu}_\mu$ CC templates with P($\bar{\nu}_\mu \to \bar{\nu}_\mu$), the ν_e CC templates with P($\nu_e \to \nu_e$) and the $\bar{\nu}_e$ CC templates with P($\bar{\nu}_e \to \bar{\nu}_e$). The CC MC templates made from the oscillated ν_e MC sample are weighted with P($\nu_\mu \to \nu_e$) (the sample was generated assuming 100% of ν_μ oscillate to ν_e). Contributions from ν_τ-CC and $\bar{\nu}_\tau$-CC are neglected, as their energy threshold is around 3.5 GeV and their effect is negligible. The same oscillation parameters are used for both ν_μ and $\bar{\nu}_\mu$ oscillations. Oscillations are not applied to the NC MC templates since they serve as proxies for the mixtures of $\nu_e + \nu_\mu + \nu_\tau$ NC and $\bar{\nu}_e + \bar{\nu}_\mu + \bar{\nu}_\tau$ NC MC templates which are unchanged under 3-flavour oscillations. All oscillation probabilities are computed in a 3-flavour framework including matter effects in constant-density matter (assuming an Earth crust density of 2.6 g/cm^3). Custom oscillation probability calculation code was developed within the *VaLOR* analysis framework. Details and estimates of the numerical accuracy of this code can be found in Appendices A and B of Ref. [4].

Fig. 6 (Fig. 7) shows the predicted number of single μ-like ring (single e-like ring) events as a function of $\sin^2\theta_{23}$ and $|\Delta m^2|$ ($\sin^2\theta_{13}$ and δ_{CP}), that is, the only two oscillations parameters allowed to float by the stand-alone ν_μ-disappearance (ν_e-appearance) analysis. In Fig. 8 (Fig. 9), the predicted number of single μ-like ring (single e-like ring) events is shown as function of $\sin^2\theta_{13}$ and δ_{CP} ($\sin^2\theta_{23}$ and $|\Delta m^2|$). This dependency has been ignored by the stand-alone ν_μ-disappearance (ν_e-appearance) analysis to date, but it is taken into account in the joint 3-flavour oscillation analysis.

[2] Each MC templates has 6132 2-dimensional bins (= 84 true energy bins × 73 reconstructed energy bins). The 84 true energy bins are arranged as follows: 6 50-MeV bins from 0-0.3 GeV, 28 25-MeV bins from 0.3-1 GeV, 40 50-MeV bins from 1-3 GeV, 5 100-MeV bin from 3-3.5 GeV, 1 bin from 3.5-4 GeV, 1 bin from 4-5 GeV, 1 bin from 5-7 GeV, 1 bin from 7-10 GeV and 1 bin from 10-30 GeV. The 73 reconstructed energy bins are as follows: 60 50-MeV bins from 0-3 GeV, 4 250-MeV bins from 3-4 GeV, 4 500-MeV bins from 4-6 GeV, 4 1000-MeV bins from 6-10 GeV and 1 bin from 10-30 GeV.

Typical single μ-like ring (single e-like ring) event reconstructed energy spectra, and spectral components, are shown in Fig. 10 (Fig. 11) for no oscillations and in Fig. 12 (Fig. 13) for oscillations with typical parameters (see caption). All these plots are generated for an exposure of 3.010×10^{20} POT and using the BANFF-tuned MC templates.

Finally, the calculated numbers of single μ-like ring and single e-like ring events using the nominal MC templates, the NA61-tuned MC templates and the BANFF-tuned MC templates are shown in Tab. 3 for no oscillations and in Tab. 4 for oscillations with typical parameters (see caption). The total numbers of events and the numbers of events from each mode considered in this analysis are shown. These numbers were calculated for an exposure of 3.010×10^{20} POT.

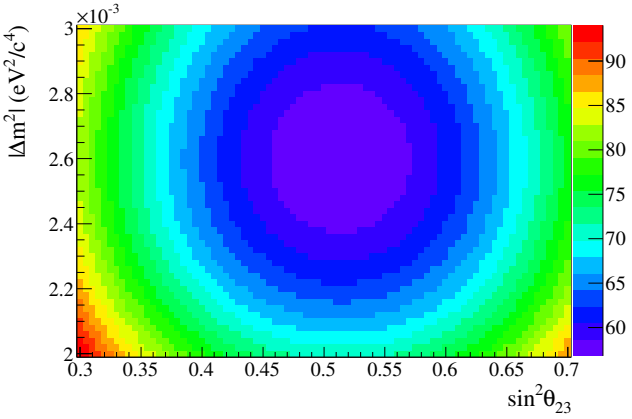

Figure 6: Predicted number of single μ-like ring events, as a function of $\sin^2\theta_{23}$ and $|\Delta m^2|$, for an exposure of 3.010×10^{20} POT. The number of events was calculated using the BANFF-tuned MC templates. 2012 PDG values are used for $\sin^2\theta_{13}$, $\sin^2\theta_{12}$ and δm^2 and δ_{CP}=0. The numbers shown were generated assuming the normal hierarchy.

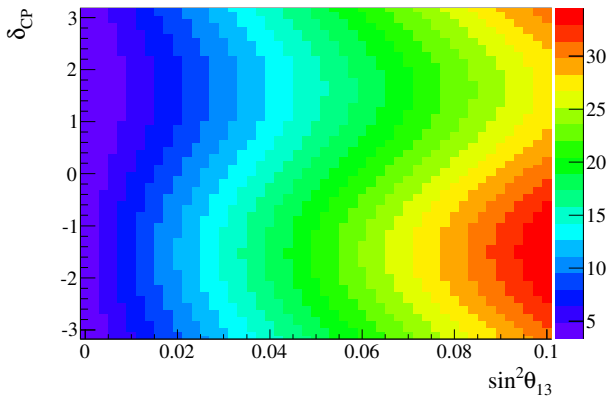

Figure 7: Predicted number of single e-like ring events, as a function of $\sin^2\theta_{13}$ and δ_{CP}, for an exposure of 3.010×10^{20} POT. The number of events was calculated using the BANFF-tuned MC templates. 2012 PDG values are used for $\sin^2\theta_{12}$, $|\Delta m^2|$ and δm^2, while $\sin^2\theta_{23}$ was set to 0.5. The numbers shown were generated assuming the normal hierarchy.

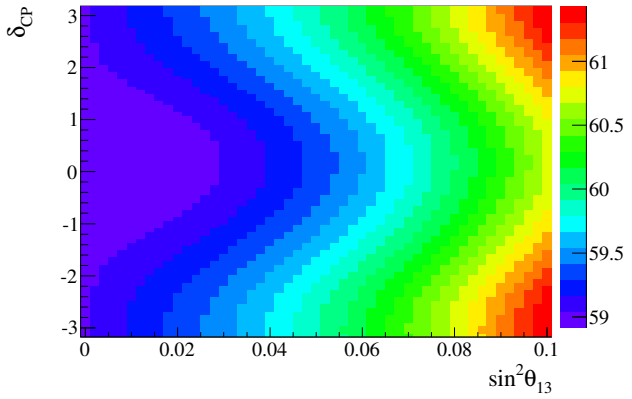

Figure 8: Predicted number of single μ-like ring events, as a function of $\sin^2\theta_{13}$ and δ_{CP}, which are typically fixed to constant values by the stand-alone ν_μ-disappearance analysis, for an exposure of 3.010×10^{20} POT. The number of events was calculated using the BANFF-tuned MC templates. 2012 PDG values are used for $\sin^2\theta_{12}$, $|\Delta m^2|$ and δm^2, while $\sin^2\theta_{23}$ was set to 0.5. The numbers shown were generated assuming the normal hierarchy.

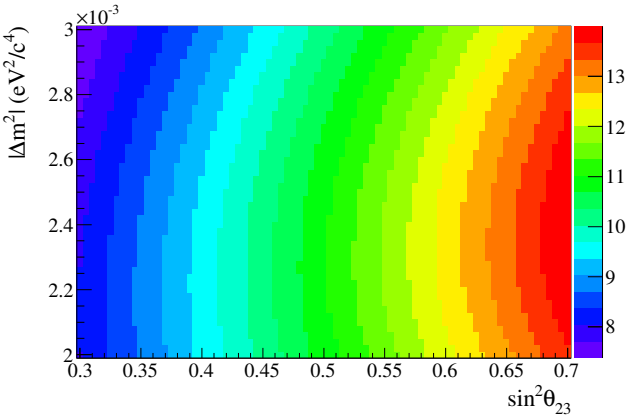

Figure 9: Predicted number of single e-like ring events, as a function of $\sin^2\theta_{23}$ and $|\Delta m^2|$, which are typically fixed to constant values by the stand-alone ν_e-appearance analysis, for an exposure of 3.010×10^{20} POT. The number of events was calculated using the BANFF-tuned MC templates. 2012 PDG values are used for $\sin^2\theta_{13}$, $\sin^2\theta_{12}$ and δm^2 and δ_{CP}=0. The numbers shown were generated assuming the normal hierarchy.

	single μ-like ring sample	single e-like ring sample
ν_μ CCQE	✓	✓
ν_μ CC 1π	✓	✓
ν_μ CC coherent	✓	✓
ν_μ CC other	✓	✓
ν_μ/ν_τ NC $1\pi^{+/-}$	✓	
ν_μ/ν_τ NC $1\pi^0$		✓
ν_μ/ν_τ NC coherent		✓
ν_μ/ν_τ NC other	✓	✓
$\bar{\nu}_\mu$ CCQE	✓	✓
$\bar{\nu}_\mu$ CC 1π	✓	✓
$\bar{\nu}_\mu$ CC coherent	✓	✓
$\bar{\nu}_\mu$ CC other	✓	✓
$\bar{\nu}_\mu/\bar{\nu}_\tau$ NC $1\pi^{+/-}$	✓	
ν_μ/ν_τ NC $1\pi^0$		✓
ν_μ/ν_τ NC coherent		✓
$\bar{\nu}_\mu/\bar{\nu}_\tau$ NC other	✓	✓
ν_e CCQE	✓	✓
ν_e CC 1π	✓	✓
ν_e CC coherent	✓	✓
ν_e CC other	✓	✓
ν_e NC $1\pi^{+/-}$	✓	
ν_μ/ν_τ NC $1\pi^0$		✓
ν_μ/ν_τ NC coherent		✓
$\bar{\nu}_\mu/\bar{\nu}_\tau$ NC other	✓	✓
ν_e CCQE	✓	✓
ν_e CC 1π	✓	✓
ν_e CC coherent	✓	✓
ν_e CC other	✓	✓
ν_e NC $1\pi^{+/-}$	✓	
ν_μ/ν_τ NC $1\pi^0$		✓
ν_μ/ν_τ NC coherent		✓
ν_e NC other	✓	✓
$\bar{\nu}_e$ CCQE	✓	✓
$\bar{\nu}_e$ CC 1π	✓	✓
$\bar{\nu}_e$ CC coherent	✓	✓
$\bar{\nu}_e$ CC other	✓	✓
$\bar{\nu}_e$ NC $1\pi^{+/-}$	✓	
ν_μ/ν_τ NC $1\pi^0$		✓
ν_μ/ν_τ NC coherent		✓
$\bar{\nu}_e$ NC other	✓	✓
Osc. ν_e CCQE	✓	✓
Osc. ν_e CC 1π	✓	✓
Osc. ν_e CC coherent	✓	✓
Osc. ν_e CC other	✓	✓

Table 2: List of the MC templates used for the calculation of the *VaLOR* single μ-like ring and single e-like ring event reconstructed energy spectrun p.d.f.s. The symbol ✓indicates, in any row, for which of the samples defined in the last two columns the MC template defined in the first column is used. Notice that the MC templates used for NC modes are different for single μ-like ring and single e-like ring.

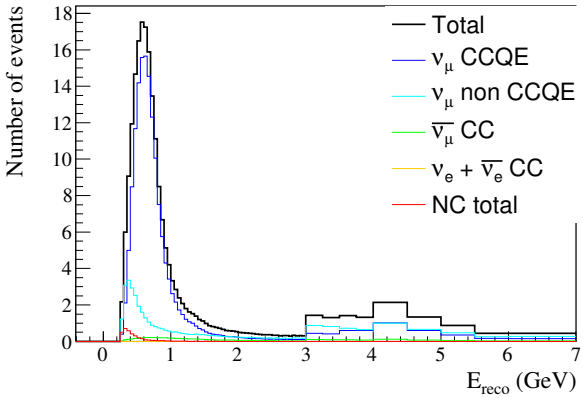

Figure 10: Predicted reconstructed-energy spectrum of single μ-like ring events, and contributions from various true neutrino reaction modes, for no oscillations and for an exposure of 3.010×10^{20} POT. The 28 components of the spectrum are calculated separately in the actual analysis, but, for this plot, are grouped into just 5 categories: ν_μ CCQE, ν_μ CCnonQE, $\bar{\nu}_\mu$ CC, $\nu_e/\bar{\nu}_e$ CC and NC. The spectrum was generated using the BANFF-tuned MC templates.

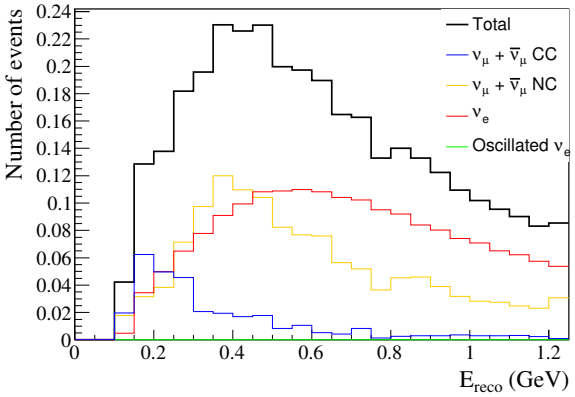

Figure 11: Predicted reconstructed-energy spectrum of single e-like ring events, and contributions from various true neutrino reaction modes, for no oscillations and for an exposure of 3.010×10^{20} POT. The 32 components of the spectrum are calculated separately in the actual analysis, but, for this plot, are grouped into just four categories: ν_μ+$\bar{\nu}_\mu$ CC, ν_μ+$\bar{\nu}_\mu$ NC, ν_e+$\bar{\nu}_e$ (intrinsic beam component) and oscillated ν_e. The spectrum was generated using the BANFF-tuned MC templates.

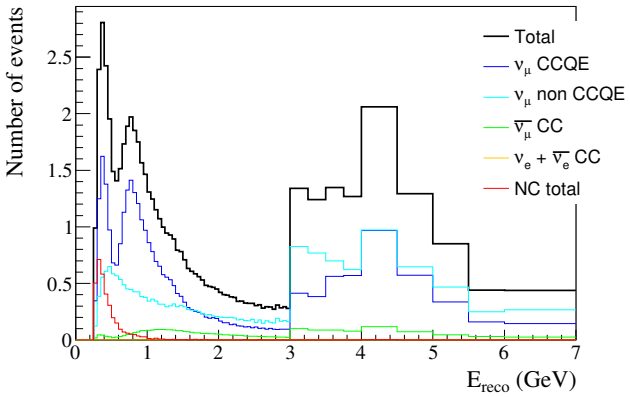

Figure 12: Predicted reconstructed-energy spectrum of single μ-like ring events, and contributions from various true neutrino reaction modes, for oscillations with $\sin^2\theta_{23}$=0.5 and $|\Delta m^2|$=2.4×10^{-3} eV^2/c^4 The spectrum was generated using the BANFF-tuned MC templates. 2012 PDG values are used for $\sin^2\theta_{13}$, $\sin^2\theta_{12}$ and δm^2, while δ_{CP}=0. The spectrum shown was generated assuming the normal hierarchy. Note that the vertical axis is zoomed in by a factor of 4 compared with Fig. 10.

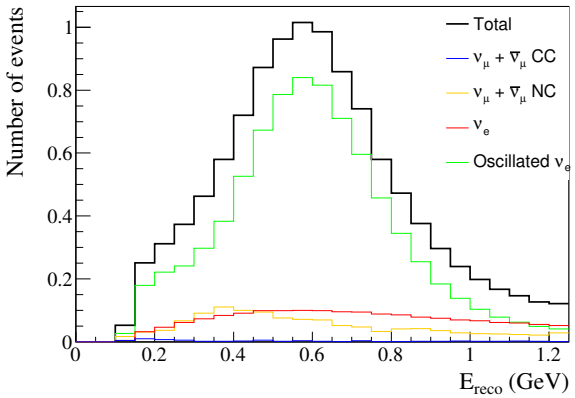

Figure 13: Predicted reconstructed-energy spectrum of single e-like ring events, and contributions from various true neutrino reaction modes, for oscillations with $\sin^2\theta_{23}$=0.5, $|\Delta m^2|$=2.4×10^{-3} eV^2/c^4, $\sin^2\theta_{13}$=0.098 and for an exposure of 3.010×10^{20} POT. The spectrum was generated using the BANFF-tuned MC templates. 2012 PDG values are used for $\sin^2\theta_{12}$ and δm^2, while δ_{CP}=0. The spectrum shown was generated assuming the normal hierarchy.

	N_{SK}					
	single μ-like ring			single e-like ring		
	Nominal	NA61-tuned	BANFF-tuned	Nominal	NA61-tuned	BANFF-tuned
Total	190.986	210.465	204.624	2.971	3.239	3.380
ν_μ CCQE	151.820	166.354	154.915	0.217	0.237	0.223
ν_μ CC 1π	25.718	28.880	34.955	0.060	0.066	0.083
ν_μ CC coherent	0.898	1.005	0.950	0.0	0.0	0.0
ν_μ CC other	3.585	4.315	4.199	0.006	0.007	0.006
ν_μ/ν_τ NC $1\pi^{+/-}$ ($1R\mu$ only)	1.493	1.697	1.626	-	-	-
ν_μ/ν_τ NC $1\pi^0$ ($1R_e$ only)	-	-	-	0.574	0.649	0.715
ν_μ/ν_τ NC coherent ($1R_e$ only)	-	-	-	0.193	0.218	0.208
ν_μ/ν_τ NC other	1.295	1.522	1.467	0.245	0.286	0.275
$\bar{\nu}_\mu$ CCQE	4.119	4.460	3.978	0.002	0.002	0.002
$\bar{\nu}_\mu$ CC 1π	1.337	1.445	1.763	0.0004	0.0004	0.0005
$\bar{\nu}_\mu$ CC coherent	0.195	0.211	0.203	0.0001	0.0001	0.0001
$\bar{\nu}_\mu$ CC other	0.237	0.254	0.248	0.0	0.0	0.0
$\bar{\nu}_\mu/\bar{\nu}_\tau$ NC $1\pi^{+/-}$ ($1R\mu$ only)	0.080	0.092	0.090	-	-	-
ν_μ/ν_τ NC $1\pi^0$ ($1R_e$ only)	-	-	-	0.028	0.031	0.035
ν_μ/ν_τ NC coherent ($1R_e$ only)	-	-	-	0.018	0.020	0.019
$\bar{\nu}_\mu/\bar{\nu}_\tau$ NC other	0.073	0.079	0.078	0.014	0.015	0.015
ν_e CCQE	0.016	0.017	0.016	1.114	1.180	1.134
ν_e CC 1π	0.009	0.010	0.013	0.352	0.377	0.505
ν_e CC coherent	0.0004	0.0004	0.0004	0.005	0.005	0.005
ν_e CC other	0.003	0.003	0.003	0.028	0.030	0.029
ν_e NC $1\pi^{+/-}$ ($1R\mu$ only)	0.042	0.050	0.049	-	-	-
ν_μ/ν_τ NC $1\pi^0$ ($1R_e$ only)	-	-	-	0.015	0.018	0.020
ν_μ/ν_τ NC coherent ($1R_e$ only)	-	-	-	0.004	0.005	0.005
ν_e NC other	0.005	0.057	0.057	0.009	0.010	0.010
$\bar{\nu}_e$ CCQE	0.0008	0.0008	0.0008	0.052	0.052	0.051
$\bar{\nu}_e$ CC 1π	0.0006	0.0006	0.0007	0.021	0.021	0.029
$\bar{\nu}_e$ CC coherent	0.00007	0.00007	0.00007	0.004	0.004	0.004
$\bar{\nu}_e$ CC other	0.0002	0.0002	0.0002	0.002	0.002	0.002
$\bar{\nu}_e$ NC $1\pi^{+/-}$ ($1R\mu$ only)	0.006	0.006	0.006	-	-	-
ν_μ/ν_τ NC $1\pi^0$ ($1R_e$ only)	-	-	-	0.002	0.002	0.002
ν_μ/ν_τ NC coherent ($1R_e$ only)	-	-	-	0.0009	0.0009	0.0009
$\bar{\nu}_e$ NC other		0.006	0.006	0.001	0.001	0.001
Oscillated ν_e CCQE	0	0	0	0	0	0
Oscillated ν_e CC 1π	0	0	0	0	0	0
Oscillated ν_e CC coherent	0	0	0	0	0	0
Oscillated ν_e CC other	0	0	0	0	0	0

Table 3: Calculated numbers of single μ-like ring and single e-like ring events without oscillations using the nominal MC templates, the NA61-tuned MC templates and the BANFF-tuned MC templates. The total numbers of events and the numbers of events from each mode considered in this analysis are shown. These numbers were calculated for an exposure of 3.010×10^{20} POT. Note that different NC MC templates are used for predicting the number of single μ-like ring and single e-like ring events.

	N_{SK}					
	single μ-like ring			single e-like ring		
	Nominal	NA61-tuned	BANFF-tuned	Nominal	NA61-tuned	BANFF-tuned
Total	54.264	60.939	59.799	10.036	10.961	11.012
ν_μ CCQE	30.926	34.183	30.962	0.028	0.031	0.028
ν_μ CC 1π	13.198	15.137	17.572	0.021	0.023	0.029
ν_μ CC coherent	0.377	0.434	0.412	0.000	0.000	0.000
ν_μ CC other	3.210	3.888	3.796	0.003	0.003	0.003
ν_μ/ν_τ NC $1\pi^{+/-}$ (1Rμ-like only)	1.492	1.697	1.626	-	-	-
ν_μ/ν_τ NC $1\pi^0$ (1R$_e$ only)	-	-	-	0.574	0.649	0.715
ν_μ/ν_τ NC coherent (1R$_e$ only)	-	-	-	0.193	0.218	0.208
ν_μ/ν_τ NC other	1.294	1.522	1.466	0.248	0.286	0.274
$\bar{\nu}_\mu$ CCQE	2.071	2.244	1.936	0.0006	0.0007	0.0006
$\bar{\nu}_\mu$ CC 1π	0.976	1.053	1.254	0.0002	0.0002	0.0002
$\bar{\nu}_\mu$ CC coherent	0.107	0.116	0.111	0.00007	0.00007	0.00007
$\bar{\nu}_\mu$ CC other	0.211	0.226	0.221	0.000	0.000	0.000
$\bar{\nu}_\mu/\bar{\nu}_\tau$ NC $1\pi^{+/-}$ (1Rμ only)	0.084	0.092	0.090	-	-	-
ν_μ/ν_τ NC $1\pi^0$ (1R$_e$ only)	-	-	-	0.028	0.030	0.034
ν_μ/ν_τ NC coherent (1R$_e$ only)	-	-	-	0.018	0.019	0.018
$\bar{\nu}_\mu/\bar{\nu}_\tau$ NC other	0.073	0.079	0.077	0.013	0.015	0.014
ν_e CCQE	0.014	0.015	0.014	1.025	1.085	1.042
ν_e CC 1π	0.008	0.009	0.012	0.331	0.355	0.476
ν_e CC coherent	0.0004	0.0004	0.0003	0.004	0.004	0.004
ν_e CC other	0.002	0.003	0.002	0.026	0.029	0.028
ν_e NC $1\pi^{+/-}$ (1Rμ only)	0.042	0.048	0.048	-	-	-
ν_μ/ν_τ NC $1\pi^0$ (1R$_e$ only)	-	-	-	0.015	0.017	0.020
ν_μ/ν_τ NC coherent (1R$_e$ only)	-	-	-	0.004	0.005	0.004
ν_e NC other	0.049	0.057	0.057	0.009	0.010	0.010
$\bar{\nu}_e$ CCQE	0.0008	0.0007	0.0007	0.048	0.048	0.047
$\bar{\nu}_e$ CC 1π	0.0006	0.0005	0.0007	0.020	0.020	0.027
$\bar{\nu}_e$ CC coherent	0.00007	0.00007	0.00007	0.003	0.003	0.003
$\bar{\nu}_e$ CC other	0.0002	0.0002	0.0002	0.002	0.001	0.001
$\bar{\nu}_e$ NC $1\pi^{+/-}$ (1Rμ only)	0.006	0.005	0.005	-	-	-
ν_μ/ν_τ NC $1\pi^0$ (1R$_e$ only)	-	-	-	0.001	0.001	0.002
ν_μ/ν_τ NC coherent (1R$_e$ only)	-	-	-	0.0009	0.0009	0.0009
$\bar{\nu}_e$ NC other	0.006	0.005	0.006	0.001	0.001	0.001
Oscillated ν_e CCQE	0.080	0.088	0.083	6.378	6.965	6.567
Oscillated ν_e CC 1π	0.025	0.026	0.034	0.996	1.090	1.406
Oscillated ν_e CC coherent	0.002	0.002	0.001	0.020	0.022	0.021
Oscillated ν_e CC other	0.0006	0.0006	0.0006	0.014	0.015	0.014

Table 4: Calculated numbers of single μ-like ring and single e-like ring events with oscillations using the nominal MC templates, the NA61-tuned MC templates and the BANFF-tuned MC templates. The total numbers of events and the numbers of events from each mode considered in this analysis are shown. These numbers were calculated for an exposure of 3.010×10^{20} POT and oscillations with δ_{CP}=0, $\sin^2\theta_{13}$=0.025, $\sin^2\theta_{23}$=0.5 and $|\Delta m^2|$=2.4×10^{-3} eV^2/c^4. The 2012 PDG parameters are used for $\sin^2\theta_{12}$ and δm^2. The normal hierarchy is assumed. Note that different NC MC templates are used for predicting the number of single μ-like ring and single e-like ring events.

5. Systematic effects in the prediction of the single μ-like ring and single e-like ring event reconstructed energy spectrum

This analysis considers 83 systematic parameters which can be grouped into 4 categories:

- 20 SuperK detector parameters (see Tab. 5).
- 33 correlated flux and cross-section parameters tuned by the BANFF group to ND280 data (see Tab. 6).
- 12 uncorrelated cross-section parameters (see Tab. 7).
- 18 intranuclear and secondary interaction parameters (see Tab. 8).

A detailed description of the systematics considered in this analysis and their implementation may be found in Sec. 3 of Ref. [4] and in [15, 16].

These systematic parameters are applied to single μ-like ring and single e-like ring MC as shown in Tab. 9. In particular, systematics are applies to single μ-like ring (single e-like ring) MC templates as shown in Tab. 10 (Tab. 11). Tab. 12 shows the effect of 1σ systematic parameter variation on the number of single μ-like ring and single e-like ring events with typical oscillation parameters. In Fig. 14 the total error envelope of the single μ-like ring and the single e-like ring event reconstructed energy spectrum are presented with typical oscillation parameters. In the baseline *VaLOR* joint 3-flavour oscillation analysis reported here, all possible, but currently unknown, correlations between the single μ-like ring and single e-like ring SuperK efficiency systematics are neglected. The effect of these correlations will be reported in a separate technical note.

SuperK detector systematics relevant both to single μ-like ring and single e-like ring events

$f^{SK}_{E;r}$	Reconstructed energy scale systematic. The energy scale uncertainty is estimated to be 2.3% [5]. The effect of the uncertainty is calculated by scaling the bin edges of the MC templates and, assuming uniform distribution of events within the bins, calculating the number of events gained from / lost to neighboring bins.

SuperK detector systematics relevant only to single μ-like ring events

$f^{SK}_{CCQERCi;r}$	ν_μ, $\bar{\nu}_\mu$ CCQE ring-counting efficiency systematic. Three correlated systematic parameters are included (i=0,1,2) corresponding to different reconstructed energy ranges [5].

Parameter	Description	1σ fractional error
0	$E_{reco} <$ 0.4 GeV	1.7%
1	0.4 GeV $\leq E_{reco} \leq$ 1.1 GeV	3.5%
2	$E_{reco} >$ 1.1 GeV	9.3%

$f^{SK}_{CCQEoth;r}$	ν_μ, $\bar{\nu}_\mu$ CCQE other (all but ring-counting) efficiency systematic. Combined systematic due to fiducial volume, reduction chain, OD cut, PID cut, momentum cut and decay electron cut efficiency uncertainties. The estimated uncertainty is 1.8% [5],[6].
$f^{SK}_{CCnonQE;r}$	ν_μ, $\bar{\nu}_\mu$ CCnQE efficiency systematic. The estimated uncertainty is 20% [5],[6].
$f^{SK}_{NC;r}$	NC efficiency systematic. The estimated uncertainty is 111% [5],[6].
$f^{SK}_{\nu_e;r}$	ν_e, $\bar{\nu}_e$ efficiency systematic. The estimated uncertainty is 100% [5],[6].

SuperK detector systematics relevant only to single e-like ring events

$f^{SK}_{1Rei;r}$	Single e-like ring event efficiency systematics. Twelve correlated parameters are included (i=0,...,11) corresponding to different modes and reconstructed energy bins.

Parameter	Description	1σ fractional error
0	Oscillated ν_e CC efficiency, $E_{reco} <$ 0.35 GeV	0.026
1	Oscillated ν_e CC efficiency, 0.35 GeV $\leq E_{reco} \leq$ 0.8 GeV	0.031
2	Oscillated ν_e CC efficiency, $E_{reco} >$ 0.8 GeV	0.034
3	ν_μ CC efficiency, $E_{reco} <$ 0.35 GeV	1.303
4	ν_μ CC efficiency, 0.35 GeV $\leq E_{reco} \leq$ 0.8 GeV	1.087
5	ν_μ CC efficiency, $E_{reco} >$ 0.8 GeV	1.027
6	ν_e CC efficiency, $E_{reco} <$ 0.35 GeV	0.025
7	ν_e CC efficiency, 0.35 GeV $\leq E_{reco} \leq$ 0.8 GeV	0.028
8	ν_e CC efficiency, $E_{reco} >$ 0.8 GeV	0.054
9	NC efficiency, $E_{reco} <$ 0.35 GeV	0.497
10	NC efficiency, 0.35 GeV $\leq E_{reco} \leq$ 0.8 GeV	0.169
11	NC efficiency, $E_{reco} >$ 0.8 GeV	0.170

Table 5: Summary table of SuperK detector systematics. The nuisance parameter symbols used in this paper are shown in the first column. An index r in the nuisance parameter symbol denotes dependence on reconstructed energy while an index t denotes dependence on true energy. An index i is used where multiple systematic parameters, typically correlated between themselves, are grouped together.

Correlated flux and cross-section (BANFF) systematics

Flux and cross-section parameters tuned by BANFF group on ND280 data. Thirty-three correlated parameters are included (i=0,...,32).

Parameter	Description	Best-fit	1σ (pre/post)-fit fractional error
0	ν_μ flux normalisation, E = 0.0 - 0.4 GeV	0.995	0.119/0.092
1	ν_μ flux normalisation, E = 0.4 - 0.5 GeV	1.007	0.129/0.098
2	ν_μ flux normalisation, E = 0.5 - 0.6 GeV	1.002	0.203/0.090
3	ν_μ flux normalisation, E = 0.6 - 0.7 GeV	0.963	0.126/0.081
4	ν_μ flux normalisation, E = 0.7 - 1.0 GeV	0.901	0.140/0.095
5	ν_μ flux normalisation, E = 1.0 - 1.5 GeV	0.910	0.120/0.084
6	ν_μ flux normalisation, E = 1.5 - 2.5 GeV	0.936	0.102/0.076
7	ν_μ flux normalisation, E = 2.5 - 3.5 GeV	0.967	0.093/0.070
8	ν_μ flux normalisation, E = 3.5 - 5.0 GeV	0.988	0.110/0.083
9	ν_μ flux normalisation, E = 5.0 - 7.0 GeV	0.997	0.152/0.107
10	ν_μ flux normalisation, E = 7.0 - 30.0 GeV	1.004	0.189/0.142
11	$\bar{\nu}_\mu$ flux normalisation, E = 0.0 - 0.7 GeV	0.980	0.131/0.108
12	$\bar{\nu}_\mu$ flux normalisation, E = 0.7 - 1.0 GeV	0.958	0.116/0.094
13	$\bar{\nu}_\mu$ flux normalisation, E = 1.0 - 1.5 GeV	0.947	0.119/0.098
14	$\bar{\nu}_\mu$ flux normalisation, E = 1.5 - 2.5 GeV	0.953	0.120/0.106
15	$\bar{\nu}_\mu$ flux normalisation, E = 2.5 -30.0 GeV	0.985	0.120/0.107
16	ν_e flux normalisation, E = 0.0 - 0.5 GeV	0.982	0.126/0.102
17	ν_e flux normalisation, E = 0.5 - 0.7 GeV	0.985	0.122/0.098
18	ν_e flux normalisation, E = 0.7 - 0.8 GeV	0.984	0.137/0.113
19	ν_e flux normalisation, E = 0.8 - 1.5 GeV	0.968	0.104/0.078
20	ν_e flux normalisation, E = 1.5 - 2.5 GeV	0.986	0.102/0.077
21	ν_e flux normalisation, E = 2.5 - 4.0 GeV	0.997	0.122/0.085
22	ν_e flux normalisation, E = 4.0 - 30.0 GeV	1.008	0.168/0.124
23	$\bar{\nu}_e$ flux normalisation, E = 0.0 - 2.5 GeV	0.987	0.191/0.182
24	$\bar{\nu}_e$ flux normalisation, E = 0.0 - 2.5 GeV	1.017	0.139/0.107
25	CCQE axial-mass scaling factor	1.049	0.372/0.160
26	Resonance-production axial-mass scaling factor	1.011	0.183/0.105
27	CCQE normalisation, E = 0.0 - 1.5 GeV	0.951	0.110/0.086
28	CCQE normalisation, E = 1.5 - 3.5 GeV	0.708	0.300/0.209
29	CCQE normalisation, E = 3.5 - 30.0 GeV	1.347	0.300/0.225
30	$CC1\pi$ normalisation, E = 0.0 - 2.5 GeV	1.370	0.317/0.204
31	$CC1\pi$ normalisation, E = 2.5 - 30.0 GeV	1.016	0.400/0.282
32	$NC1\pi^0$ normalisation	1.153	0.328/0.267

$f^{banff}_{i;t,r}$

Table 6: Summary table of BANFF systematics. The nuisance parameter symbols used in this paper are shown in the first column. An index r in the nuisance parameter symbol denotes dependence on reconstructed energy while an index t denotes dependence on true energy. An index i is used where multiple systematic parameters, typically correlated between themselves, are grouped together.

Uncorrelated cross-section systematics	
$f_{pF;t,r}$	Uncertainty in Fermi momentum for ^{16}O was taken to be 225$\pm$30 MeV [12].
$f_{bindE;t,r}$	Uncertainty in binding energy for ^{16}O ws taken to be 27$\pm$9 MeV [12].
$f_{SF;t,r}$	Nuclear environment modeling systematic; switch from Fermi Gas (RFG) to Spectral Function (SF) model (CCQE only). 0 (RFG) - 1 (SF)
$f_{\pi-less\Delta;t,r}$	Systematic due to uncertainty on the fraction of π-less Δ decays in resonance neutrino-production events. A 20% uncertainty was assumed [12].
$f_{CCothShape;t,r}$	Systematic due to the uncertainty in CC multipion, CC DIS and CC resonant η, K and photon production cross-section. A 40% uncertainty was assumed [12].
$f_{Wshape;t,r}$	Systematic due to the uncertainty in the shape of the initial pion momentum distribution (before final-state interactions) in resonance interactions. A 52% uncertainty was assumed [12].
$f_{CCcoh;t}$	Systematic due to the uncertainty on the CC coherent cross-section. A 100% uncertainty was assumed [12].
$f_{NCcoh;t}$	Systematic due to the uncertainty on the NC coherent cross-section. A 30%uncertainty was assumed [12].
$f_{NC1\pi^{\pm};t}$	Systematic due to the uncertainty on the NC1$\pi^{\pm}$ cross-section. A 30% uncertainty was assumed [12].
$f_{NCoth;t}$	Systematic die to the uncertainty on the NC other (all but single $\pi^{\pm}$) cross-section. A 30% uncertainty was assumed [12].
$f_{CC\nu_e;t}$	Systematic due to the uncertainty on the ν_e / ν_μ CC cross-section ratio [11]. A 3% uncertainty was assumed.
$f_{CC\bar{\nu};t}$	Systematic due to the uncertainty on the $\bar{\nu}$ / ν CC cross-section ratio. A 40% uncertainty was assumed.

Table 7: Summary table of Uncorrelated cross-section systematics. The nuisance parameter symbols used in this paper are shown in the first column. An index r in the nuisance parameter symbol denotes dependence on reconstructed energy while an index t denotes dependence on true energy. An index i is used where multiple systematic parameters, typically correlated between themselves, are grouped together.

FSI+SI systematics relevant only to single μ-like ring events

FSI (final state interaction / intranuclear hadron transport) and SI (secondary interaction / detector hadron transport) systematic parameters. Six correlated parameters are included (i=0,...,5) corresponding to different modes and reconstructed energy bins.

$f^{FSI}_{1R\mu i;r}$

Parameter	Description	1σ fractional error
0	ν_μ & $\bar{\nu}_\mu$ CCQE,$E_{reco} <$ 0.4 GeV	3.6×10^{-5}
1	ν_μ & $\bar{\nu}_\mu$ CCQE, 0.4 GeV $\leq E_{reco} \leq$ 1.1 GeV	7.1×10^{-4}
2	ν_μ & $\bar{\nu}_\mu$ CCQE,$E_{reco} >$ 1.1 GeV	2.8×10^{-3}
3	ν_μ & $\bar{\nu}_\mu$ CCnonQE	8.7×10^{-2}
4	ν_e & $\bar{\nu}_e$ CC	1.13×10^{-2}
5	All NC	7.7×10^{-2}

FSI+SI systematics relevant only to single e-like ring events

FSI (final state interaction / intranuclear hadron transport) and SI (secondary interaction / detector hadron transport) systematic parameters. Twelve correlated parameters are included (i=0,...,11) corresponding to different modes and reconstructed energy bins.

$f^{FSI}_{1Rei;r}$

Parameter	Description	1σ fractional error
6	Oscillated ν_e CC, $E_{reco} <$ 0.35 GeV	0.11
7	Oscillated ν_e CC, 0.035 GeV $\leq E_{reco} \leq$ 0.8 GeV	1.2×10^{-2}
8	Oscillated ν_e CC, $E_{reco} >$ 0.8 GeV	7.3×10^{-3}
9	ν_μ CC, $E_{reco} <$ 0.35 GeV	3.7×10^{-2}
10	ν_μ CC, 0.35 GeV $\leq E_{reco} \leq$ 0.8 GeV	6.2×10^{-2}
11	ν_μ CC, $E_{reco} >$ 0.8 GeV	7.7×10^{-2}
12	ν_e CC, $E_{reco} <$ 0.35 GeV	6.0×10^{-2}
13	ν_e CC, 0.35 GeV $\leq E_{reco} \leq$ 0.8 GeV	3.1×10^{-2}
14	ν_e CC, $E_{reco} >$ 0.8 GeV	3.2×10^{-2}
15	NC, $E_{reco} <$ 0.35 GeV	8.5×10^{-2}
16	NC, 0.35 GeV $\leq E_{reco} \leq$ 0.8 GeV	7.6×10^{-2}
17	NC, $E_{reco} >$ 0.8 GeV	4.3×10^{-2}

Table 8: Summary table of FSI+SI systematics. The nuisance parameter symbols used in this paper are shown in the first column. An index r in the nuisance parameter symbol denotes dependence on reconstructed energy while an index t denotes dependence on true energy. An index i is used where multiple systematic parameters, typically correlated between themselves, are grouped together.

Type	Systematics	Comment	$1R_\mu$	$1R_e$	N_{syst}
BANFF	$f^{banff}_{0;t,r}$ - $f^{banff}_{24;t,r}$	ν_μ, $\bar{\nu_\mu}$, ν_e and $\bar{\nu_e}$ flux	✓	✓	25
	$f^{banff}_{25;t,r}$	CCQE axial mass	✓	✓	1
	$f^{banff}_{26;t,r}$	resonance-production axial mass	✓	✓	1
	$f^{banff}_{27;t,r}$ - $f^{banff}_{29;t,r}$	CCQE normalization	✓	✓	3
	$f^{banff}_{30;t,r}$ - $f^{banff}_{31;t,r}$	CC1π normalization	✓	✓	2
	$f^{banff}_{32;t,r}$	NC1π^0	–	✓	1
Uncorrelated cross-section	$f_{pF;t,r}$	Fermi momentum	✓	✓	1
	$f_{bindE;t,r}$	Binding energy	✓	✓	1
	$f_{SF;t,r}$	Nuclear modeling	✓	✓	1
	$f_{Wshape;t,r}$	Shape of the π momentum distribution	✓	✓	1
	$f_{\pi-less\Delta;t,r}$	π-less Δ decay	✓	✓	1
	$f_{CCothShape;t,r}$	CC other shape	✓	✓	1
	$f_{CCcoh;t}$	CC coherent cross-section	✓	✓	1
	$f_{NC1\pi^\pm;t}$	NC1$\pi^\pm$ cross-section	✓	–	1
	$f_{NCcoh;t}$	NC coherent cross-section	–	✓	1
	$f_{NCoth;t}$	NC other cross-section	✓	✓	1
	$f_{CC\nu_e;t}$	σ_{ν_e}/ σ_{ν_μ} ratio	✓	✓	1
	$f_{CC\bar{\nu};t}$	$\sigma_{\bar{\nu}}$/ σ_{ν} ratio	✓	✓	1
SuperK detector	$f^{SK}_{E;r}$	Reconstructed energy scale	✓	✓	1
	$f^{SK}_{CCQERC0;r}$ - $f^{SK}_{CCQERC2;r}$	ν_μ,$\bar{\nu}_\mu$ CCQE ring-counting efficiency	✓	–	3
	$f^{SK}_{CCQEoth;r}$	ν_μ,$\bar{\nu}_\mu$ CCQE other efficiency	✓	–	1
	$f^{SK}_{CCnonQE;r}$	ν_μ,$\bar{\nu}_\mu$ CCnonQE efficiency	✓	–	1
	$f^{SK}_{\nu_e;r}$	ν_e, $\bar{\nu}_e$ CC efficiency	✓	–	1
	$f^{SK}_{NC;r}$	NC efficiency	✓	–	1
	$f^{SK}_{1Re0;r}$ - $f^{SK}_{1Re2;r}$	Osc. ν_e CC efficiency	–	✓	3
	$f^{SK}_{1Re3;r}$ - $f^{SK}_{1Re5;r}$	ν_μ,$\bar{\nu}_\mu$ CC efficiency	–	✓	3
	$f^{SK}_{1Re6;r}$ - $f^{SK}_{1Re8;r}$	ν_e,$\bar{\nu}_e$ CC efficiency	–	✓	3
	$f^{SK}_{1Re9;r}$ - $f^{SK}_{1Re11;r}$	NC efficiency	–	✓	3
FSI+SI	$f^{FSI}_{1R\mu0;r}$ - $f^{FSI}_{1R\mu2;r}$	ν_μ, $\bar{\nu}_\mu$ CCQE	✓	–	3
	$f^{FSI}_{1R\mu3;r}$	ν_μ, $\bar{\nu}_\mu$ CCnonQE	✓	–	1
	$f^{FSI}_{1R\mu4;r}$	ν_e, $\bar{\nu}_e$ CC	✓	–	1
	$f^{FSI}_{1R\mu5;r}$	NC	✓	–	1
	$f^{FSI}_{1Re0;r}$ - $f^{FSI}_{1Re2;r}$	Osc. ν_e	–	✓	3
	$f^{FSI}_{1Re3;r}$ - $f^{FSI}_{1Re5;r}$	ν_μ,$\bar{\nu}_\mu$ CC	–	✓	3
	$f^{FSI}_{1Re6;r}$ - $f^{FSI}_{1Re8;r}$	ν_e,$\bar{\nu}_e$ CC	–	✓	3
	$f^{FSI}_{1Re9;r}$ - $f^{FSI}_{1Re11;r}$	NC	–	✓	3
Total					**83**

Table 9: List of all systematic parameters included in the joint oscillation analysis. A ✓symbol indicates whether the systematic parameter is applied on the single μ-like ring and single e-like ring MC templates.

	ν_μ CCQE	ν_μ CC1π	ν_μ CC coherent	ν_μ CC other	ν_μ NC1$\pi^\pm$	ν_μ NC other	$\bar{\nu_\mu}$ CCQE	$\bar{\nu_\mu}$ CC1π	$\bar{\nu_\mu}$ CC coherent	$\bar{\nu_\mu}$ CC other	$\bar{\nu_\mu}$ NC1$\pi^\pm$	$\bar{\nu_\mu}$ NC other	ν_e CCQE	ν_e CC1π	ν_e CC coherent	ν_e CC other	ν_e NC1$\pi^\pm$	ν_e NC other	$\bar{\nu_e}$ CCQE	$\bar{\nu_e}$ CC1π	$\bar{\nu_e}$ CC coherent	$\bar{\nu_e}$ CC other	$\bar{\nu_e}$ NC1$\pi^\pm$	$\bar{\nu_e}$ NC other	Osc-ν_e CCQE	Osc-ν_e CC1π	Osc-ν_e CC coherent	Osc-ν_e CC other
$f^{SK}_{E;r}$	✓	✓	✓	✓	✓	✓	✓	✓	✓	✓	✓	✓	✓	✓	✓	✓	✓	✓	✓	✓	✓	✓	✓	✓	✓	✓	✓	✓
$f^{SK}_{CCQERC0;r}$	✓						✓																					
$f^{SK}_{CCQERC1;r}$	✓						✓																					
$f^{SK}_{CCQERC2;r}$	✓						✓																					
$f^{SK}_{CCQEoth;r}$	✓						✓																					
$f^{SK}_{CCnQE;r}$		✓	✓	✓				✓	✓	✓																		
$f^{SK}_{NC;r}$					✓	✓					✓	✓					✓	✓					✓	✓				
$f^{SK}_{\nu_e;r}$													✓	✓	✓	✓			✓	✓	✓	✓			✓	✓	✓	✓
$f^{banff}_{0;t,r}$ - $f^{banff}_{10;t,r}$	✓	✓	✓	✓	✓	✓																						
$f^{banff}_{11;t,r}$ - $f^{banff}_{15;t,r}$							✓	✓	✓	✓	✓	✓																
$f^{banff}_{16;t,r}$ - $f^{banff}_{22;t,r}$													✓	✓	✓	✓	✓	✓										
$f^{banff}_{23;t,r}$ - $f^{banff}_{24;t,r}$																			✓	✓	✓	✓	✓	✓				
$f^{banff}_{25;t,r}$	✓						✓						✓						✓						✓			
$f^{banff}_{26;t,r}$		✓		✓	✓	✓		✓		✓	✓	✓		✓		✓	✓	✓		✓		✓	✓	✓		✓		✓
$f^{banff}_{27;t,r}$	✓						✓						✓						✓						✓			
$f^{banff}_{28;t,r}$	✓						✓						✓						✓						✓			
$f^{banff}_{29;t,r}$	✓						✓						✓						✓						✓			
$f^{banff}_{30;t,r}$		✓						✓						✓						✓						✓		
$f^{banff}_{31;t,r}$		✓						✓						✓						✓						✓		
$f_{pF;t,r}$	✓						✓						✓						✓						✓			
$f_{SF;t,r}$	✓						✓						✓						✓						✓			
$f_{\pi-less\Delta;t,r}$		✓			✓	✓		✓			✓	✓		✓			✓	✓		✓			✓	✓		✓		
$f_{bindE;t,r}$	✓						✓						✓						✓						✓			
$f_{CCothShape;t,r}$				✓						✓						✓						✓						✓
$f_{Wshape;t,r}$					✓	✓					✓	✓					✓	✓					✓	✓				
$f_{CCcoh;t}$			✓						✓						✓						✓						✓	
$f_{NC1\pi^\pm;t}$					✓						✓						✓						✓					
$f_{NCoth;t}$						✓						✓						✓						✓				
$f_{CC\nu_e;t}$													✓	✓	✓	✓			✓	✓	✓	✓			✓	✓	✓	✓
$f_{CC\bar{\nu};t}$							✓	✓	✓	✓									✓	✓	✓	✓						
$f^{FSI}_{1R\mu0;r}$	✓						✓																					
$f^{FSI}_{1R\mu1;r}$	✓						✓																					
$f^{FSI}_{1R\mu2;r}$	✓						✓																					
$f^{FSI}_{1R\mu3;r}$		✓	✓	✓				✓	✓	✓																		
$f^{FSI}_{1R\mu4;r}$													✓	✓	✓	✓			✓	✓	✓	✓			✓	✓	✓	✓
$f^{FSI}_{1R\mu5;r}$					✓	✓					✓	✓					✓	✓					✓	✓				

Table 10: A ✓symbol denotes that the given single μ-like ring MC template is modified when the given systematic parameter is tweaked. The table lists all systematic parameters, relevant to single μ-like ring events, considered in this analysis (first column) and all 28 MC templates used for constructing the single μ-like ring event reconstructed energy spectrum p.d.f (first row).

	ν_μ CCQE	ν_μ CC1π	ν_μ CC coherent	ν_μ CC other	ν_μ NC1π^0	ν_μ NC coherent	ν_μ NC other	$\bar{\nu_\mu}$ CCQE	$\bar{\nu_\mu}$ CC1π	$\bar{\nu_\mu}$ CC coherent	$\bar{\nu_\mu}$ CC other	$\bar{\nu_\mu}$ NC1π^0	$\bar{\nu_\mu}$ NC coherent	$\bar{\nu_\mu}$ NC other	ν_e CCQE	ν_e CC1π	ν_e CC coherent	ν_e CC other	ν_e NC1π^0	ν_e NC coherent	ν_e NC other	$\bar{\nu_e}$ CCQE	$\bar{\nu_e}$ CC1π	$\bar{\nu_e}$ CC coherent	$\bar{\nu_e}$ CC other	$\bar{\nu_e}$ NC1π^0	$\bar{\nu_e}$ NC coherent	$\bar{\nu_e}$ NC other	Osc-ν_e CCQE	Osc-ν_e CC1π	Osc-ν_e CC coherent	Osc-ν_e CC other
$f^{SK}_{E;r}$	✓	✓	✓	✓	✓	✓	✓	✓	✓	✓	✓	✓	✓	✓	✓	✓	✓	✓	✓	✓	✓	✓	✓	✓	✓	✓	✓	✓	✓	✓	✓	✓
$f^{SK}_{1Re0;r}$ - $f^{SK}_{1Re2;r}$																														✓	✓	✓	✓
$f^{SK}_{1Re3;r}$ - $f^{SK}_{1Re5;r}$	✓	✓	✓	✓				✓	✓	✓	✓																						
$f^{SK}_{1Re6;r}$ - $f^{SK}_{1Re8;r}$															✓	✓	✓	✓				✓	✓	✓	✓								
$f^{SK}_{1Re9;r}$ - $f^{SK}_{1Re11;r}$					✓	✓	✓					✓	✓	✓					✓	✓	✓					✓	✓	✓					
$f^{banff}_{0;t,r}$ - $f^{banff}_{10;t,r}$	✓	✓	✓	✓	✓	✓	✓																										
$f^{banff}_{11;t,r}$ - $f^{banff}_{15;t,r}$								✓	✓	✓	✓	✓	✓	✓																			
$f^{banff}_{16;t,r}$ - $f^{banff}_{22;t,r}$															✓	✓	✓	✓	✓	✓	✓												
$f^{banff}_{23;t,r}$ - $f^{banff}_{24;t,r}$																						✓	✓	✓	✓	✓	✓	✓	✓				
$f^{banff}_{25;t,r}$	✓							✓							✓							✓							✓				
$f^{banff}_{26;t,r}$		✓		✓	✓	✓	✓		✓		✓	✓	✓	✓		✓		✓	✓	✓	✓		✓		✓		✓	✓		✓			✓
$f^{banff}_{27;t,r}$	✓							✓							✓							✓							✓				
$f^{banff}_{28;t,r}$	✓							✓							✓							✓							✓				
$f^{banff}_{29;t,r}$	✓							✓							✓							✓							✓				
$f^{banff}_{30;t,r}$		✓							✓							✓							✓							✓		
$f^{banff}_{31;t,r}$							✓							✓							✓							✓				
$f^{banff}_{32;t,r}$									✓							✓							✓							✓		
$f_{pF;t,r}$	✓							✓							✓							✓							✓				
$f_{SF;t,r}$	✓							✓							✓							✓							✓				
$f_{\pi-less\Delta;t,r}$		✓			✓		✓		✓			✓		✓		✓			✓		✓		✓			✓		✓		✓			
$f_{bindE;t,r}$	✓							✓							✓							✓							✓				
$f_{CCothShape;t,r}$				✓							✓							✓							✓							✓
$f_{Wshape;t,r}$					✓		✓					✓		✓					✓		✓					✓		✓					
$f_{CCcoh;t}$			✓							✓							✓							✓							✓		
$f_{NC1\pi^0;t}$					✓							✓								✓								✓					
$f_{NCoth;t}$							✓							✓							✓							✓					
$f_{CC\nu_e;t}$															✓	✓	✓	✓				✓	✓	✓	✓				✓	✓	✓	✓
$f_{CC\bar{\nu};t}$								✓	✓	✓	✓											✓	✓	✓	✓							
$f^{FSI}_{1Re0;r}$ - $f^{FSI}_{1Re2;r}$																													✓	✓	✓	✓
$f^{FSI}_{1Re3;r}$ - $f^{FSI}_{1Re5;r}$	✓	✓	✓	✓				✓	✓	✓	✓																						
$f^{FSI}_{1Re6;r}$ - $f^{FSI}_{1Re8;r}$															✓	✓	✓	✓				✓	✓	✓	✓								
$f^{FSI}_{1Re9;r}$ - $f^{FSI}_{1Re11;r}$					✓	✓	✓					✓	✓	✓					✓	✓	✓					✓	✓	✓					

Table 11: A ✓symbol denotes that the given single e-like ring MC template is modified when the given systematic parameter is tweaked. The table lists all systematic parameters, relevant to single e-like ring events, considered in this analysis (first column) and all 32 MC templates used for constructing the single e-like ring event reconstructed energy spectrum p.d.f (first row).

Source of uncertainty	1Rμ $\delta N_{SK}/N_{SK}$	1Re $\delta N_{SK}/N_{SK}$
SuperK detector	10.05%	3.20%
BANFF (prefit)	21.66%	24.57%
BANFF (postfit)	4.13%	4.71%
Uncorrelated XSec	6.34%	4.18%
FSI+SI	3.49%	2.30%
Total (BANFF prefit)	25.33%	25.14%
Total (BANFF postfit)	13.32%	7.52%

Table 12: Effect of 1σ systematic parameter variation on the number of single μ-like ring and single e-like ring events, computed for oscillations with $|\Delta m^2|$=2.36$\times 10^{-3}$ eV^2/c^4. $\sin^2\theta_{23}$=0.5, $\sin^2\theta_{13}$=0.025, δ_{CP}=0. 2012 PDG values are used for the solar parameters and the normal mass hierarchy is assumed. The numbers shown were calculated for an exposure of 3.010$\times 10^{20}$ POT and BANFF-tuned MC templates were used.

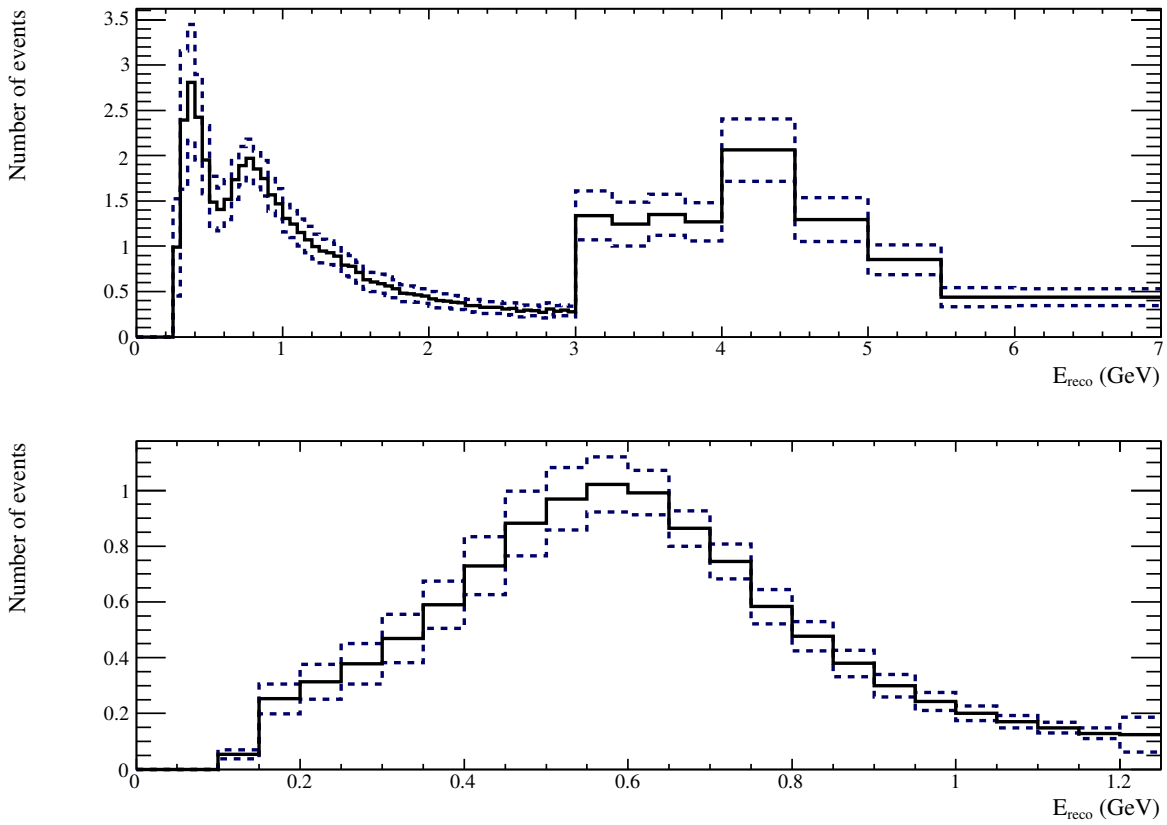

Figure 14: Total error envelope of the single μ-like ring event reconstructed energy spectrum (top) and total error envelope of the single e-like ring event reconstructed energy spectrum (bottom), for oscillations with $|\Delta m^2|$=2.36$\times 10^{-3}$ eV^2/c^4. $\sin^2\theta_{23}$=0.5, $\sin^2\theta_{13}$=0.025, δ_{CP}=0. 2012 PDG values are used for the solar parameters and the normal mass hierarchy is assumed. The plot shown was calculated for an exposure of 3.010$\times 10^{20}$ POT and BANFF-tuned MC templates were used.

6. Neutrino oscillation fitting

6.1. Minimization method

The *VaLOR* joint 3-flavour analysis uses a binned likelihood-ratio method. Measurements of the oscillation parameters $|\Delta m^2|$, $\sin^2\theta_{23}$, $\sin^2\theta_{13}$ and δ_{CP}[3] are obtained by comparing the observed and predicted reconstructed single μ-like ring and single e-like ring energy spectra in SuperK. Let N_μ and N_e be the numbers of reconstructed energy bins considered for the single μ-like ring and single e-like ring samples respectively, and $\mathbf{a}$ be a $1 \times N_s$ - dimensional array of systematic (nuisance) parameters that affect the SuperK reconstructed energy spectrum prediction of either sample e.g. parameters that control the beam, neutrino interaction simulations and the detector response. Best-fit values are obtained by minimizing:

$$\begin{aligned} -2\ln\lambda(|\Delta m^2|, sin^2\theta_{23}, \sin^2\theta_{13}, \delta_{CP}; \mathbf{a}) = & 2 \cdot \sum_{r=0}^{N_\mu - 1} \left[(N^{exp}_{SK;\mu,r} - N^{obs}_{SK;\mu,r}) + N^{obs}_{SK;\mu,r} \cdot ln \left(\frac{N^{obs}_{SK;\mu,r}}{N^{exp}_{SK;\mu,r}} \right) \right] \\ & + 2 \cdot \sum_{r=0}^{N_e - 1} \left[(N^{exp}_{SK;e,r} - N^{obs}_{SK;e,r}) + N^{obs}_{SK;e,r} \cdot ln \left(\frac{N^{obs}_{SK;e,r}}{N^{exp}_{SK;e,r}} \right) \right] \\ & + (\mathbf{a} - \mathbf{a_0})^T \cdot \mathbf{C}^{-1} \cdot (\mathbf{a} - \mathbf{a_0}) \end{aligned} \quad (5)$$

where $N^{obs}_{SK;\mu,r}$ ($N^{obs}_{SK;e,r}$) is the observed number of single μ-like ring (single e-like ring) events in the r^{th} bin, and $N^{exp}_{SK;\mu,r}$ ($N^{exp}_{SK;e,r}$) is the corresponding expected number of events; this expected number is a function of $|\Delta m^2|$, $\sin^2\theta_{23}$, $\sin^2\theta_{13}$ and δ_{CP} and the nuisance parameter vector $\mathbf{a}$. Also $\mathbf{a_0}$ is a $1 \times N_s$ - dimensional array containing the nominal values of the systematic parameters, $\mathbf{a}^T$ is the transpose of $\mathbf{a}$, and $\mathbf{C}$ is the systematic parameter covariance matrix of dimension $N_s \times N_s$. For the stand-alone ν_μ-disappearance (ν_e-appearance) fit, only the single μ-like ring (single e-like ring) sample is used and the corresponding term in Eq. 5 is dropped.

The likelihood-ratio method used in this analysis is equivalent to the extended maximum likelihood method used in the alternative T2K oscillation analysis (see [1, 29] for more details). The advantage of the likelihood-ratio method, compared with the extended maximum-likelihood method, is that in the large-sample limit, the quantity $-2\ln\lambda(|\Delta m^2|, \sin^2\theta_{23}, \sin^2\theta_{13}, \delta_{CP}; \mathbf{a})$ in Eq.5 has a χ^2 distribution and it can therefore be used as a goodness-of-fit test. In this note $-2\ln\lambda(|\Delta m^2|, \sin^2\theta_{23}, \sin^2\theta_{13}, \delta_{CP}; \mathbf{a})$ and $\chi^2(|\Delta m^2|, \sin^2\theta_{23}, \sin^2\theta_{13}, \delta_{CP}; \mathbf{a})$ are used interchangeably.

In the joint 3-flavour oscillation analysis fits, all 83 systematic parameters are allowed to float, whereas in the stand-alone analyses (which use a single SuperK sample) only the relevant systematics are used (see Tab. 9).

The search for the minimum value of $-2\ln\lambda(|\Delta m^2|, \sin^2\theta_{23}, \sin^2\theta_{13}, \delta_{CP}; \mathbf{a})$ is performed in the range 1.0×10^{-3} eV^2/c^4 $\leq |\Delta m^2| \leq 6.0 \times 10^{-3}$ eV^2/c^4, $0.0 \leq \sin^2\theta_{23} \leq 1.0$, $0.0 \leq \sin^2\theta_{13} \leq 1.0$ and $-\pi \leq \delta_{CP} \leq \pi$. Systematic parameters included in the oscillation fit are constrained in the range [-2σ_s, +2σ_s] where σ_s is the one standard deviation error assigned to each systematic parameter[4]. Validations studies were done with systematic parameters fitted in a wider range [-5σ_s, +5σ_s] with no difference in the results. However, the Run1+2+3 data fit will be updated with a wider range such as [-5σ_s, +5σ_s] . Values of systematic parameters that give a negative predicted number of events in any reconstructed energy bin are not allowed. If this scenario arises, the number of events is changed to +1E-8 in that bin. This is done for the sum of all the interaction modes rather than for each mode separately.

The minimization is performed with Minuit [30], using the Migrad method. If Migrad does not converge, the starting values of the oscillation parameters are re-initialised: the new initial values are randomly drawn from uniform distributions in the ranges $2.0 \cdot 10^{-3} \leq |\Delta m^2| \leq 3.0 \cdot 10^{-3}$, $0.35 \leq \sin^2\theta_{23} \leq 0.65$, $0.015 \leq \sin^2\theta_{13} \leq 0.035$ and the fit is retried. This is repeated 25 times. If the fits still fail to converge, the Simplex algorithm is used.

6.2. Goodness-of-fit tests

The problem of defining a general goodness-of-fit for sparsely populated distributions was discussed in detail during the development of the Run 1+2+3 stand-alone ν_μ-disappearance and ν_e-appearance analyses. See for example [31]. It was pointed out that, for the Run 1+2+3 statistics, the shape information is not as helpful in forming p-values as the rate information. It was decided that p-values will be calculated using the rate and the reconstructed energy distribution, and that the distribution will use a very coarse binning scheme to ensure that there are sufficient numbers of events in each bin.

[3] A study has been made in which $\sin^2\theta_{12}$ and δm^2 were allowed to float in the fit and the results are shown in Appendix F. The effect was negligible and, in the analysis reported here, they were simply fixed to $\sin^2\theta_{12} = 0.311$ and $\delta m^2 = 7.5 \times 10^{-5}$ eV^2/c^4.

[4] Such an error is defined for all but one of the systematic parameters considered in this analysis. The exception is the systematic parameter f_{SF} which parametrises the uncertainty on nuclear modelling, switching between the Relativistic Fermi Gas (RFG) and Spectral Function (SF) models. The allowed range of the parameter f_{SF} in the oscillation fit is [0,1].

A similar approach is used for the joint 3-flavour analysis presented here. For the single μ-like ring sample, 5 reconstructed energy bins are used: 0-0.4, 0.4-0.7, 0.7-1.0, 1.0-2.0 and 2.0-30.0 GeV. For the single e-like ring sample, 3 reconstructed energy bins are used: 0-0.35, 0.35-0.80, 0.80-1.25 GeV. In this note, p-values for the joint 3-flavour fit are computed following the 5+3 binning scheme described above. When p-values are quoted for the stand-alone ν_μ-disappearance (ν_e-appearance) analysis, the corresponding 5 (3) bin scheme of the single μ-like ring (single e-like ring) event sample is used.

The goodness-of-fit tests that will be shown are built using 1000 toy MC experiments created at the best-fit point to be tested, with statistical and systematic fluctuations. Then, each toy MC experiment is fitted in the coarse binning described above, including the four oscillation parameters and all systematics in the joint 3-flavour fit. For the stand-alone disappearance the fit is performed for $sin^2\theta_{23}, \Delta m^2$ and the relevant systematics, being the other two oscillation parameters $sin^2\theta_{13}, \delta_{CP}$ fixed to the usual values. For the stand-alone appearance the fit is performed for $sin^2\theta_{13}$ and the relevant systematics, being the other oscillation parameters fixed to the usual values (with maximal mixing $sin^2\theta_{23} = 0.5$ and $\delta_{CP} = 0$).

6.3. Toy-MC study of fitter performance

The performance of the fitter has been evaluated using ensembles of 1k toy MC experiments generated at different oscillation points with an exposure of 3.010×10^{20} POT. Two kinds of studies were performed with toy MC experiments. First, the simulated experiments included only statistical fluctuations and were fitted with the '4 + 0' fit, i.e. fitting only for oscillation parameters. A second ensemble of toy MC experiments including not only statistical fluctuations but also fluctuations of all systematic parameters was created. Those toy MC experiments were fitted with the '4 + 83' fit, i.e. fitting for oscillation parameters and for all systematic parameters. No issue was identified regarding the fitter performance, the results from these studies were as expected. In addition, the distributions of residuals for the oscillation parameters from both studies, doing '4 + 0' or '4 + 83' fits are consistent, indicating that no unexpected features appear when including fluctuations of the systematic parameters and when fitting for them.

6.4. Construction of confidence regions

In the analysis reported here, confidence regions are constructed using the constant $\Delta\chi^2$ method. 68% and 90% CL limits will be reported for each of $|\Delta m^2|$, $sin^2\theta_{23}$, $sin^2\theta_{13}$ and δ_{CP} oscillation parameters. In addition, 2-dimensional confidence regions for 68% and 90% CL will be shown for the following combinations of parameters: ($sin^2\theta_{23}$, $|\Delta m^2|$), ($sin^2\theta_{13}$, $|\Delta m^2|$), ($sin^2\theta_{13}$, δ_{CP}) and ($sin^2\theta_{23}$, $sin^2\theta_{13}$).

The first step to construct confidence contours in an oscillation parameter space is to build the $\Delta\chi^2$ surface in that space. The oscillation parameter space is divided into a regular grid. The following grid spacing is used in all confidence region construction methods: $\delta|\Delta m^2| = 0.05 \times 10^{-3} eV^2/c^4$, $\delta \sin^2\theta_{23} = 0.01$, $\delta \sin^2\theta_{13} = 0.005$ and $\delta(\delta_{CP}) = 2\pi/50$. For the joint 3-flavour analysis confidence regions, the χ^2 is minimized at each grid point with respect to all 83 nuisance parameters considered in this analysis and all oscillation parameters not shown on the plot (and not considered to be fixed). For the stand-alone analyses, only the relevant systematics were used.

The confidence regions for the joint analysis are constructed by finding the global best-fit point (fitting all oscillation parameters and all systematic parameters at the same time) and calculating the lines of *constant* $\Delta\chi^2$ from this point[5]. In the case of the stand-alone appearance analysis, a special procedure is followed to construct the confidence regions in ($sin^2\theta_{13}$, δ_{CP}) space imitating the actual stand-alone analyses in T2K. In this method, called *raster scan*, a best-fit value of $sin^2\theta_{13}$ is found for each fixed value of δ_{CP}, resulting in a line of best-fit points instead of a single best-fit point. Then, confidence intervals in $sin^2\theta_{13}$ at a fixed δ_{CP} are found with respect to each best-fit $sin^2\theta_{13}$ using the 1D $\Delta\chi^2$ critical values [27].

A full Feldman-Cousins construction in the 4-dimensional ($|\Delta m^2|$, $sin^2\theta_{23}$, $sin^2\theta_{13}$ and δ_{CP}) space, including all 83 systematics, is computationally prohibitive. This analysis produces limits on each of the 4 oscillation parameters and, also, confidence regions in 4 2-dimensional surfaces within the 4-dimensional oscillational parameter space. There is no established procedure on how to sample the 4-dimensional oscillation space and generate a toy-MC ensemble for the calculation of the critical $\Delta\chi^2$ values needed for producing the limits or the 2-dimensional contours. We were confronted with this issue both for the Run 1+2 disappearance analysis PRD paper and the Run 1+2+3 disappearance analysis PRL paper, but no satisfactory solution was found. We are aware that the same issue has baffled other collaborations too. In the presence of this ambiguity over how to produce profile Feldman-Cousins contours, we propose that this analysis produces contours only using the constant $\Delta\chi^2$ method. Coverage studies are presented in Sec. I. If a non-ambiguous procedure is found, based on our experience running the Feldman-Cousins confidence region construction for the ν_μ-disappearance analysis, we estimate that about ~50,000 CPU·days would be needed for the joint analysis. The VaLOR group could prepare these contours in the time-scale of two months.

[5] For 1 fit parameter, the critical values of $\Delta\chi^2$ used are 1.00 (68% CL), 2.71 (90% CL), 3.84 (95% CL), 6.63 (99% CL). For 2 parameters fitted simultaneously, the critical values of $\Delta\chi^2$ used are 2.30 (68% CL), 4.61 (90% CL), 5.99 (95% CL), 9.21 (99% CL).

7. Results of the joint oscillation analysis with the Run 1+2+3 (3.010×10^{20} POT) dataset

7.1. Best-fit oscillation parameters and systematic parameter pulls

A joint 3-flavour oscillation fit, using the method described in Sec. 6 was performed simultaneously on the single e-like ring and single μ-like ring event reconstructed energy spectra of the 3.010×10^{20} POT Run 1+2+3 dataset. This fit allowed all 83 nuisance parameters considered in this work to float. This analysis found $|\Delta m^2|$ = 2.494 $\times10^{-3}$ eV^2/c^4, $\sin^2\theta_{23}$ = 0.516, $\sin^2\theta_{13}$ = 0.029 and δ_{CP} = 2.086 to be the joint 3-flavour oscillation best-fit values for the Run 1+2+3 dataset for Normal Hierarchy and $|\Delta m^2|$ = 2.468 $\times10^{-3}$ eV^2/c^4, $\sin^2\theta_{23}$ = 0.516, $\sin^2\theta_{13}$ = 0.034 and δ_{CP} = 0.921 for Inverted Hierarchy.

Stand-alone 3-flavour ν_μ disappearance and ν_e appearance analyses were also performed on the Run 1+2+3 dataset. In the stand-alone ν_μ disappearance analysis, $|\Delta m^2|$ and $\sin^2\theta_{23}$ were determined by fitting the single μ-like ring event reconstructed energy spectrum keeping $\sin^2\theta_{13}$ and δ_{CP} fixed, as was done in our published result, and allowing all 57 nuisance parameters relevant to this analysis to float. Similarly, in the stand-alone ν_e appearance analysis, $\sin^2\theta_{13}$ and δ_{CP} were determined by fitting the single e-like ring event reconstructed energy spectrum, keeping $|\Delta m^2|$ and $\sin^2\theta_{23}$ fixed, as was done in our published result, and allowing all 69 nuisance parameters relevant to this analysis to float. The results of these fits are summarized in Tab. 13. In this table are the relevant best-fit oscillation parameters, the observed and expected number of single e-like ring and single μ-like ring events, and goodness-of-fit figures. Notice that the best-fit value for $\sin^2\theta_{23}$ is the same in both hierarchies although the best-fit value for the other parameters is different. The reason for this result will be investigated in Sec. E.

The pull for each systematic parameter f included in the fit, is calculated as

$$\frac{f_{bf} - f_{nom}}{\sigma_{bf}}, \tag{6}$$

where f_{bf} is the best-fit value of the systematic parameter, f_{nom} is the nominal value of the parameter (corresponding to no systematic variation), and σ_{bf} is the Migrad error output from Minuit. The pulls of all systematic parameters allowed to float in the joint 3-flavour oscillation fit to the Run 1+2+3 dataset are shown in Figs. 15 for the fit assuming Normal Hierarchy, and in Fig. 16 for the fit assuming Inverted Hierarchy. From these figures, it is apparent that most systematic parameters barely move from their nominal values. We note that, although all relevant systematic parameters are allowed to float in these fits, few of them move by more than $\pm0.1\sigma$. When a systematic parameter that is free to move stays close to its nominal value, this means that the reduction in χ^2 from moving that parameter is less than the corresponding increase in the penalty term in equation 5. Only certain systematics are able to change the predicted reconstructed energy spectrum to a sufficient extent to offset the penalty term.

7.2. Goodness-of-fit tests

Goodness-of-fit tests were performed as described in Sec. 6.2, and the p-values for the joint 3-flavour oscillation fit and the stand-alone ν_μ disappearance and ν_e appearance fits to the Run 1+2+3 dataset are shown in Tab. 13. The χ^2 distributions from which the p-values were calculated are shown for the Run 1+2+3 joint 3-flavour oscillation fit in Fig. 17 (20), while for the stand-alone ν_μ disappearance fit it is shown in Fig. 18 (21) and for the stand-alone ν_e appearance it is shown in Fig. 19 (22) for Normal (Inverted) Hierarchy. All fits have a high degree of plausibility.

Analysis	Run	Hierarchy/ Octant	$\lvert\Delta m^2\rvert$ $10^{-3}eV^2/c^4$	$\sin^2\theta_{23}$	$\sin^2\theta_{13}$	δ_{CP}	$N_{obs}^{1R\mu}$	$N_{exp}^{1R\mu}$	N_{obs}^{1Re}	N_{exp}^{1Re}	χ^2/ndf	p-value
2012 joint	1+2+3	NH/1st	2.494	0.516	0.029	2.086	58	57.697	11	10.452	72.26/94	0.86
2012 ν_μ disap.	1+2+3	NH/1st	2.479	0.514	–	–	58	57.901	11	–	56.05/71	0.90
2012 ν_e app.	1+2+3	NH/1st	–	–	0.023	0(fixed)	58	–	11	10.477	16.47/24	0.67
2012 joint	1+2+3	NH/2nd	2.493	0.516	0.029	2.074	58	57.712	11	10.452	72.26/94	
2012 ν_μ disap.	1+2+3	NH/2nd	2.479	0.514	–	–	58	57.903	11	–	56.05/71	
2012 ν_e app.	1+2+3	NH/2nd	–	–	0.023	0(fixed)	58	–	11	10.477	16.47/24	
2012 joint	1+2+3	IH/1st	2.468	0.516	0.034	0.921	58	57.715	11	10.454	72.26/94	0.85
2012 ν_μ disap.	1+2+3	IH/1st	2.474	0.512	–	–	58	57.891	11	–	56.05/71	0.90
2012 ν_e app.	1+2+3	IH/1st	–	–	0.029	0(fixed)	58	–	11	10.435	16.42/24	0.58
2012 joint	1+2+3	IH/2nd	2.468	0.516	0.034	0.922	58	57.723	11	10.454	72.26/94	
2012 ν_μ disap.	1+2+3	IH/2nd	2.474	0.512	–	–	58	57.891	11	–	56.05/71	
2012 ν_e app.	1+2+3	IH/2nd	–	–	0.029	0(fixed)	58	–	11	10.435	16.42/24	

Table 13: Summary of best-fit parameters for the joint 3-flavour oscillation fit, and the stand-alone 3-flavour ν_μ disappearance and ν_e appearance fits to the Run 1+2+3 dataset. The quoted best-fit χ^2 values were computed from the test-statistic minimized in the fit (likelihood ratio) with the reconstructed energy binning used in each fit. The table also shows the p-values obtained from the goodness-of-fit test of Sec. 6.2.

7.3. Best-fit single e-like ring and single μ-like ring event reconstructed energy spectra

The reconstructed neutrino energy distribution of single μ-like ring (single e-like ring) events in the Run 1+2+3 dataset is shown in Fig. 23 (Fig. 24) along with best-fit prediction of the joint 3-flavour oscillation analysis, assuming Normal Hierarchy.

In Fig. 23 we superimpose the best-fit prediction from the stand-alone 3-flavour ν_μ disappearance analysis, while in In Fig. 24 we superimpose the best-fit prediction from the stand-alone 3-flavour ν_e appearance analysis. The distributions are shown with the reconstructed neutrino energy binning that was used in the fitting procedure (see footnote 2 in Sec. 4). The single μ-like ring (single e-like ring) best-fit prediction of the joint 3-flavour oscillation analysis, assuming Inverted Hierarchy, are shown in Fig. 25 (Fig. 26).

Since the reconstructed energy binning used in the fit is relatively fine, it can be beneficial to see the above distributions using a coarser binning scheme[6]. The re-binned reconstructed neutrino energy distribution of single μ-like ring and single e-like ring events for both mass hierarchies are shown in Figs. 27 - 30.

Finally, the ratio of the best-fit reconstructed neutrino energy distribution of single μ-like ring (single e-like ring) events obtained from the joint 3-flavour oscillation analysis and the stand-alone ν_μ disappearance (ν_e appearance) analysis is shown in Fig. 31 (Fig. 32) for Normal Hierarchy and in Fig. 33 (Fig. 34) for Inverted Hierarchy.

The best-fit single μ-like ring reconstructed energy spectrum from the joint analysis is almost identical to that from the stand-alone ν_μ-disappearance analysis from 0.6 - 1.2 GeV, but is slightly lower from 0.3 - 0.6 GeV and $>$1.2 GeV, and this is true for both mass hierarchies. Meanwhile the ratio of the best-fit single e-like ring reconstructed energy spectrum from the joint analysis to that from the stand-alone ν_e-appearance analysis shows different behaviour for the two hierarchies. For the normal hierarchy (NH), this ratio is $<$1 from 0.1 - 0.3 GeV, $>$1 from 0.3 - 0.55 GeV, and $<$1 above 0.55 GeV. However, for the inverted hierarchy (IH) the ratio is $<$1 from 0.1 - 0.6 GeV and $>$1 above 0.6 GeV.

7.4. Confidence regions

The marginalized $\Delta\chi^2$ distribution as function of each of $|\Delta m^2|$, $sin^2\theta_{23}$, $sin^2\theta_{13}$ and δ_{CP} oscillation parameters for the joint 3-flavour oscillation fit to the Run 1+2+3 dataset is shown in Figs. 35 - 38. From these plots, the 90% (68%) CL allowed region for the four oscillation parameters can be summarized as 2.227$\times10^{-3}$ (2.332$\times10^{-3}$) $eV^2/c^4 < |\Delta m^2| <$ 2.773$\times10^{-3}$ (2.659$\times10^{-3}$) eV^2/c^4, 0.401 (0.433) $< sin^2\theta_{23} <$ 0.628 (0.596), 0.006 (0.012) $< sin^2\theta_{13} <$ 0.058 (0.048) and -π (-π) $< \delta_{CP} < \pi$ (π) for Normal Hierarchy and 2.218 $\times10^{-3}$ (2.311$\times10^{-3}$) $eV^2/c^4 < |\Delta m^2| <$ 2.729 $\times10^{-3}$ (2.627$\times10^{-3}$) eV^2/c^4, 0.397 (0.433) $< sin^2\theta_{23} <$ 0.627 (0.596), 0.006 (0.013) $< sin^2\theta_{13} <$ 0.069 (0.054) and -π (-π) $< \delta_{CP} < \pi$ (π) for Inverted Hierarchy.

The correlations between the oscillation parameters were also studied. In Figs. 39 - 42, we present, respectively, the the 68% and 90% CL regions in the following four 2-dimensional oscillation parameter spaces: ($sin^2\theta_{23}$, $|\Delta m^2|$), ($sin^2\theta_{13}$, $|\Delta m^2|$), ($sin^2\theta_{13}$, δ_{CP}) and ($sin^2\theta_{23}$, $sin^2\theta_{13}$). Results from the stand-alone Run 1+2+3 ν_μ disappearance and ν_e appearance analyses are superimposed wherever possible.

Comparisons between the confidence regions obtain from the joint 3-flavour oscillation fits under difference mass hierarchy assumptions are shown in Figs. 43 - 50.

To construct the plots shown in this subsection, the same procedure is followed as in Appendix C. In joint 3-flavour analysis plots, the value of χ^2 was minimized with respect to all 83 nuisance parameters and the oscillation parameters not shown on the plot (except from the solar parameters, $sin^2\theta_{12}$ and δm^2 which, as shown in Appendix F, have a negligible effect and they are fixed to constant values for all the joint and stand-alone analyses). In the plots shown for the stand-alone ν_μ disappearance analysis, unless explicitly stated, $sin^2\theta_{13}$ and δ_{CP} are fixed to constant values, as was done for our published results, and χ^2 was minimized with respect to all 48 nuisance parameters relevant to that analysis. Similarly, for the stand-alone ν_e appearance analysis, unless explicitly stated, $sin^2\theta_{23}$ and $|\Delta m^2|$ are also fixed to constant values, as was done for our published results, and χ^2 was minimized with respect to all 64 nuisance parameters relevant to that analysis.

The $\Delta\chi^2$ distributions of $|\Delta m^2|$ and $\sin^2\theta_{23}$ are almost identical for the joint analysis and the stand-alone ν_μ-disappearance analysis. However the $\Delta\chi^2$ distribution of $\sin^2\theta_{13}$ is wider for the joint analysis than for the stand-alone ν_e-appearance analysis. This is due to the partial degeneracy of this parameter with $\sin^2\theta_{23}$ when fitting the single e-like ring sample. Since $\sin^2\theta_{23}$ is fitted in the joint analysis, the $\Delta\chi^2$ distribution of $\sin^2\theta_{13}$ is wider than in the stand-alone analysis in which $\sin^2\theta_{23}$ is fixed. There is very good agreement between the confidence contours in the ($\sin^2\theta_{23}$, $|\Delta m^2|$) space from the joint analysis and those from the stand-alone ν_μ-disappearance analysis. Contours in the ($\sin^2\theta_{13}$, δ_{CP}) space are wider for the joint analysis with respect to the contours obtained for the stand-alone appearance analysis. The main reason is the different method used (global minimum vs raster scan). In Figs. 51 and 52 the same method (raster scan) was used for both the joint and the stand-alone appearance analysis to fit Run1+2+3 dataset in Normal and Inverted Hierarchy respectively. Contours from the joint analysis agree very well with those from the stand-alone ν_e-appearance analysis when using the raster scan method in both analyses.

[6] For the single μ-like ring event sample 16 reconstructed energy bins are used arranged as follows: 1 0.3-GeV bin in 0 - 0.3 GeV, 8 0.1-GeV bins in 0.3 - 1.1 GeV, 1 0.15-GeV bin in 1.1 GeV - 1.25 GeV, 1 0.25-GeV bin in 1.25 - 1.5 GeV GeV, 1 0.5-GeV bin in 1.5 - 2 GeV, 2 1-GeV bin in 2-4 GeV, 1 2-GeV bin in 4-6 GeV and 1 bin above 6 GeV. For the single e-like ring event sample 4 0.3 GeV bins in 0-1.2 GeV are used.

The $\Delta\chi^2$ distributions for $|\Delta m^2|$ and $\sin^2\theta_{23}$ are very similar between the NH and IH. However the distribution for $\sin^2\theta_{13}$ and δ_{CP} is shifted to higher values for the IH compared with the NH, while the distribution for δ_{CP} is shifted to lower values. The confidence contours in the ($\sin^2\theta_{23}$, $|\Delta m^2|$) space agree very well between the NH and IH, but the upper limit in the ($\sin^2\theta_{13}$, δ_{CP}) space is higher for the IH than for the NH.

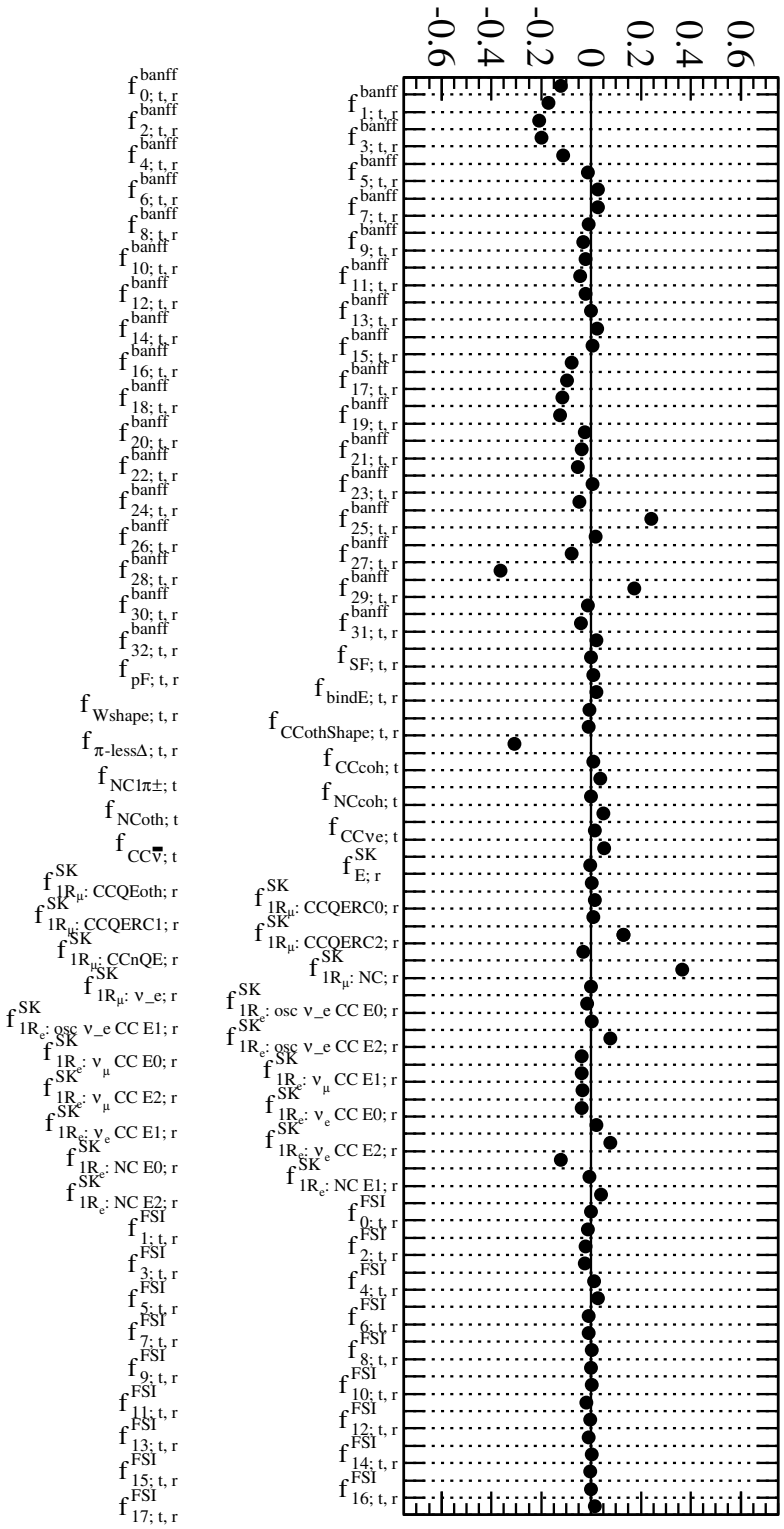

Figure 15: Systematic parameter pulls for the 83 systematics allowed to float in the Run 1+2+3 joint 3-flavour oscillation fit with Normal Hierarchy.

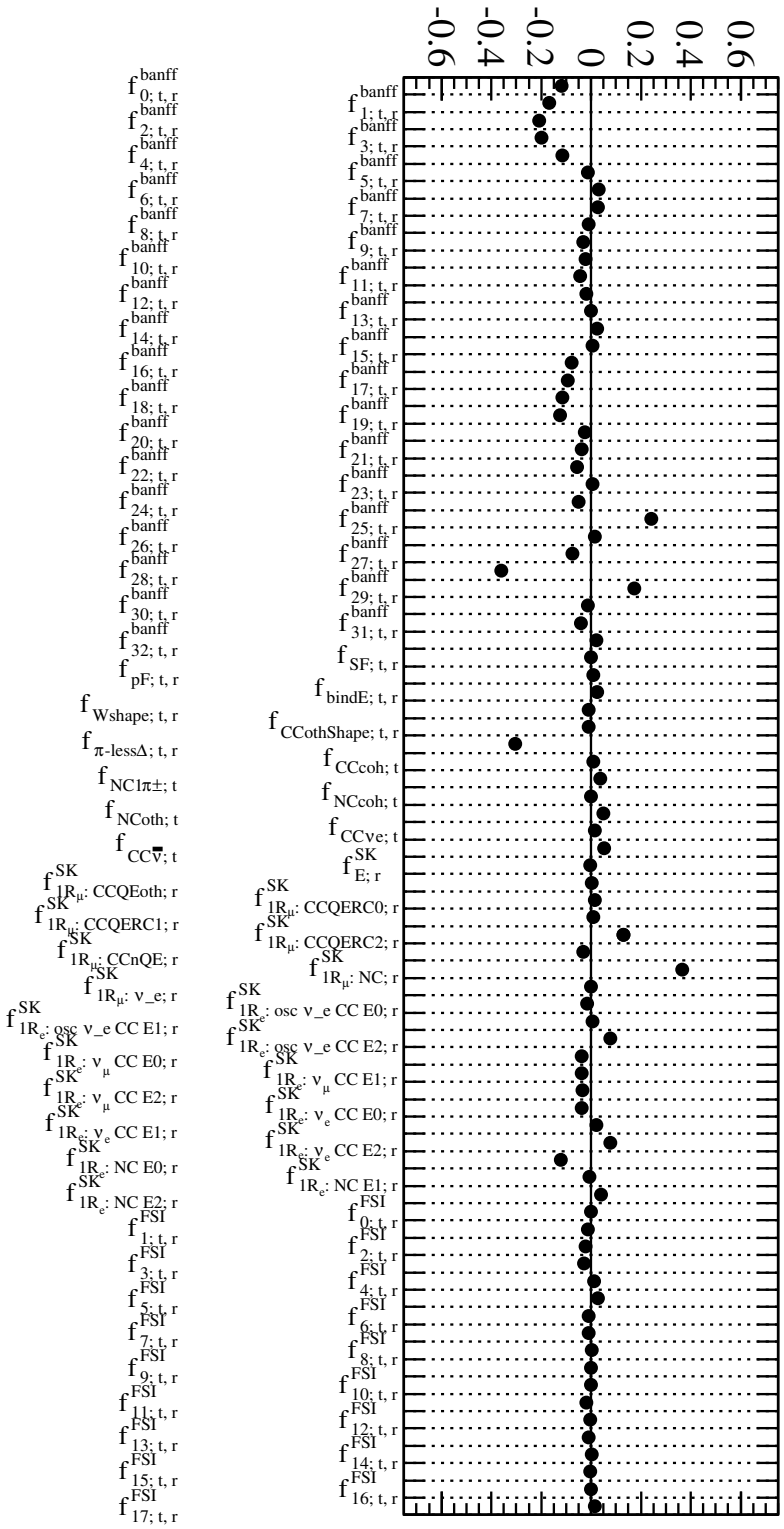

Figure 16: Systematic parameter pulls for the 83 systematics allowed to float in the Run 1+2+3 joint 3-flavour oscillation fit with Inverted Hierarchy.

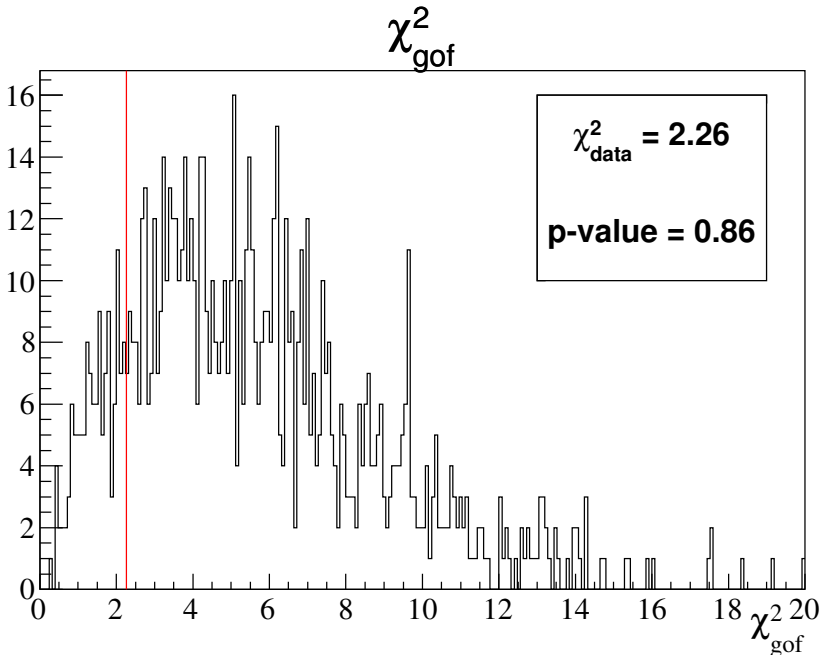

Figure 17: Distribution of χ^2_{gof}, the goodness-of-fit (gof) χ^2, from 1k toy MC experiments generated at the Run 1+2+3 joint 3-flavour analysis best-fit oscillation point with Normal Hierarchy. The χ^2_{gof} value for the Run 1+2+3 data (χ^2_{data}) is highlighted. All χ^2_{gof} values were computed using the 5 (single μ-like ring) + 3 (single e-like ring) reconstructed energy binning scheme described in Sec. 6.2,

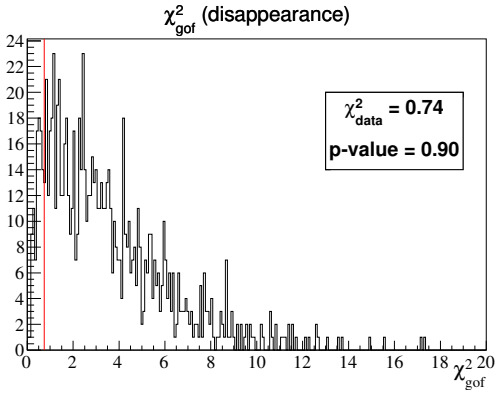

Figure 18: Distribution of χ^2_{gof} from 1k toy MC experiments generated at the Run 1+2+3 stand-alone 3-flavour ν_μ disappearance analysis best-fit oscillation point with Normal Hierarchy. The χ^2_{gof} value for the Run 1+2+3 data (χ^2_{data}) is highlighted. All χ^2_{gof} values were computed using the 5 (single μ-like ring) reconstructed energy binning scheme described in Sec. 6.2,

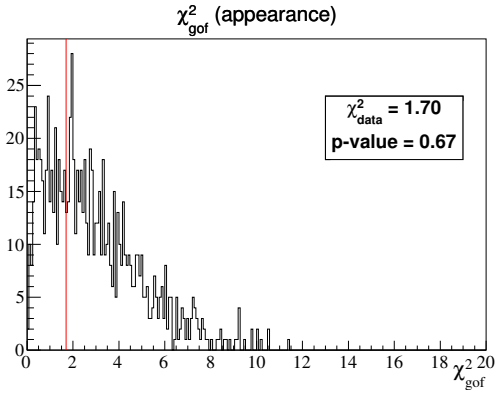

Figure 19: Distribution of χ^2_{gof} from 1k toy MC experiments generated at the Run 1+2+3 stand-alone 3-flavour ν_e appearance analysis best-fit oscillation point with Normal Hierarchy. The χ^2_{gof} value for the Run 1+2+3 data (χ^2_{data}) is highlighted. All χ^2_{gof} values were computed using the 3 (single e-like ring) reconstructed energy binning scheme as described in Sec. 6.2,

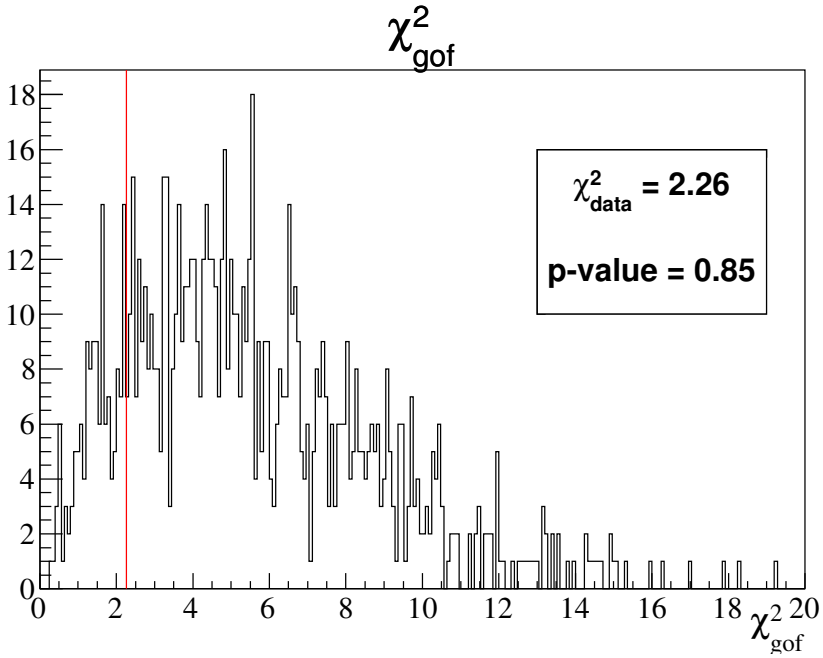

Figure 20: Distribution of χ^2_{gof}, the goodness-of-fit (gof) χ^2, from 1k toy MC experiments generated at the Run 1+2+3 joint 3-flavour analysis best-fit oscillation point with Inverted Hierarchy. The χ^2_{gof} value for the Run 1+2+3 data (χ^2_{data}) is highlighted. All χ^2_{gof} values were computed using the 5 (single μ-like ring) + 3 (single e-like ring) reconstructed energy binning scheme described in Sec. 6.2.

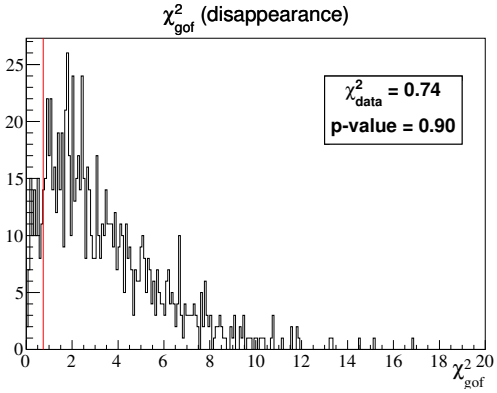

Figure 21: Distribution of χ^2_{gof} from 1k toy MC experiments generated at the Run 1+2+3 stand-alone 3-flavour ν_μ disappearance analysis best-fit oscillation point with Inverted Hierarchy. The χ^2_{gof} value for the Run 1+2+3 data (χ^2_{data}) is highlighted. All χ^2_{gof} values were computed using the 5 (single μ-like ring) reconstructed energy binning scheme described in Sec. 6.2.

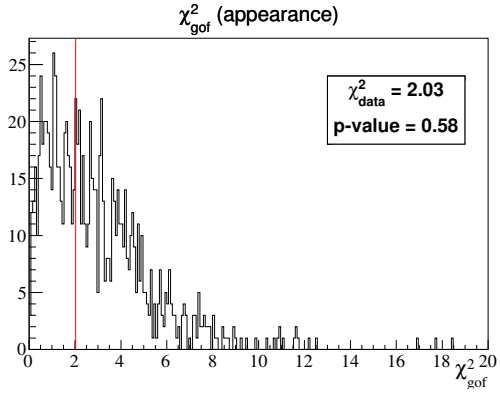

Figure 22: Distribution of χ^2_{gof} from 1k toy MC experiments generated at the Run 1+2+3 stand-alone 3-flavour ν_e appearance analysis best-fit oscillation point with Inverted Hierarchy. The χ^2_{gof} value for the Run 1+2+3 data (χ^2_{data}) is highlighted. All χ^2_{gof} values were computed using the 3 (single e-like ring) reconstructed energy binning scheme as described in Sec. 6.2.

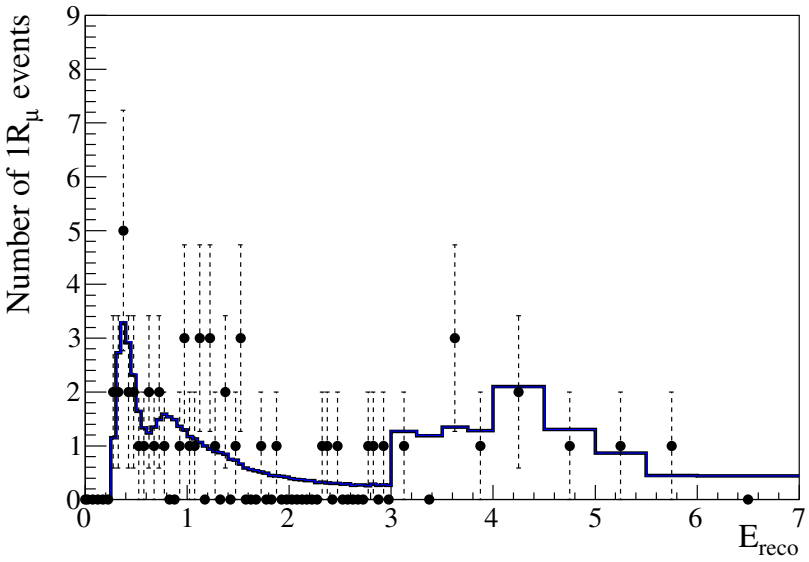

Figure 23: Run 1+2+3 best-fit single μ-like ring event reconstructed energy spectrum for the fit with Normal Hierarchy (black: joint 3-flavour oscillation analysis, blue: stand-alone ν_μ disappearance analysis). The distributions are shown with the binning used in the fit.

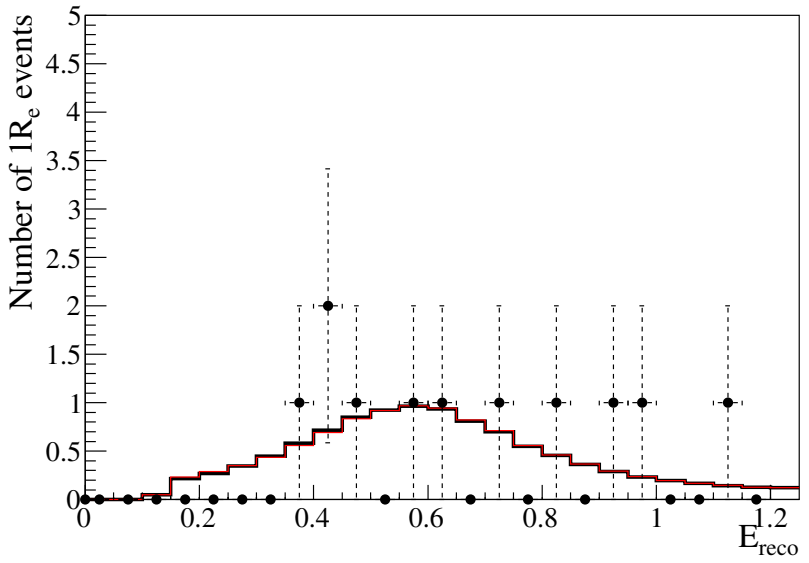

Figure 24: Run 1+2+3 best-fit single e-like ring event reconstructed energy spectrum for the fit with Normal Hierarchy (black: joint 3-flavour oscillation analysis, red: stand-alone ν_e disappearance analysis). The distributions are shown with the binning used in the fit.

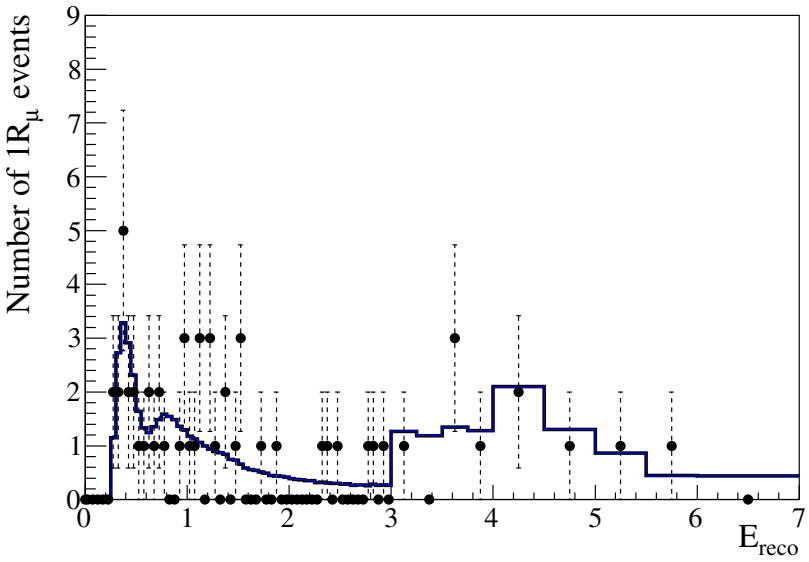

Figure 25: Run 1+2+3 best-fit single μ-like ring event reconstructed energy spectrum for the fit with Inverted Hierarchy (black: joint 3-flavour oscillation analysis, blue: stand-alone ν_μ disappearance analysis). The distributions are shown with the binning used in the fit.

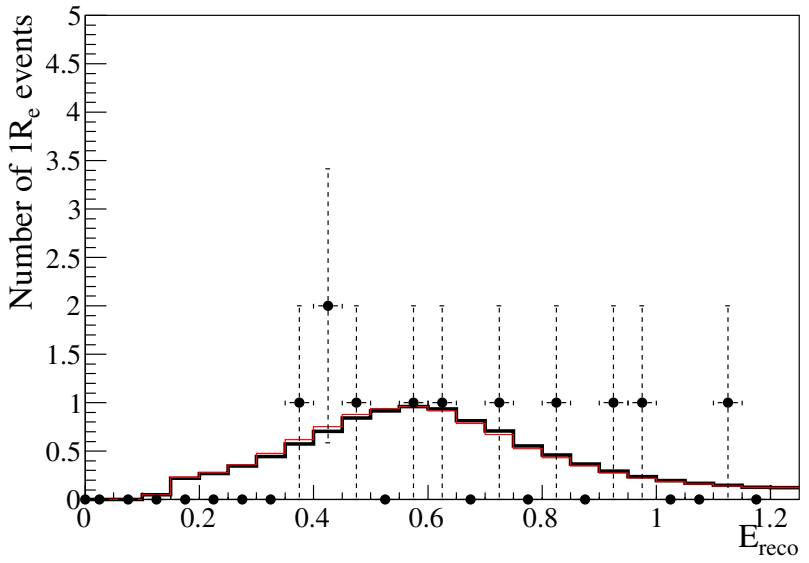

Figure 26: Run 1+2+3 best-fit single e-like ring event reconstructed energy spectrum for the fit with inverted Hierarchy (black: joint 3-flavour oscillation analysis, red: stand-alone ν_e disappearance analysis). The distributions are shown with the binning used in the fit.

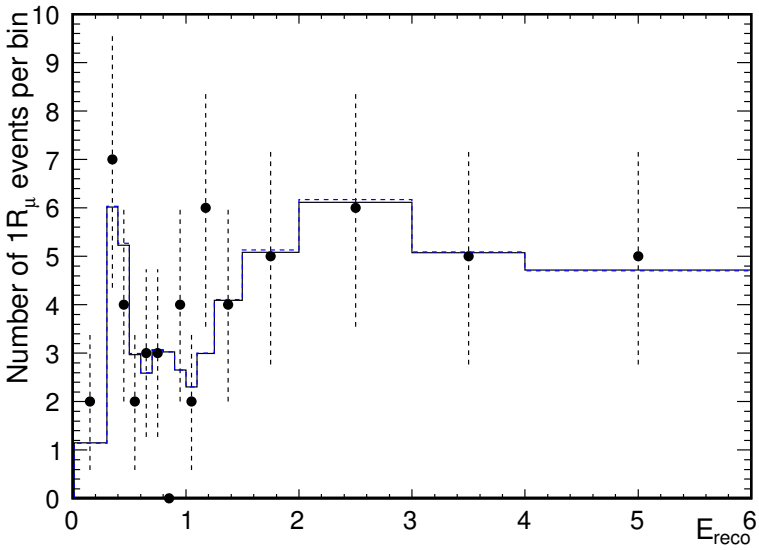

Figure 27: Run 1+2+3 best-fit single μ-like ring event reconstructed energy spectrum for the fit with Normal Hierarchy (black: joint 3-flavour oscillation analysis, blue: stand-alone ν_μ disappearance analysis). The distributions are shown with the coarse binning defined in the main text.

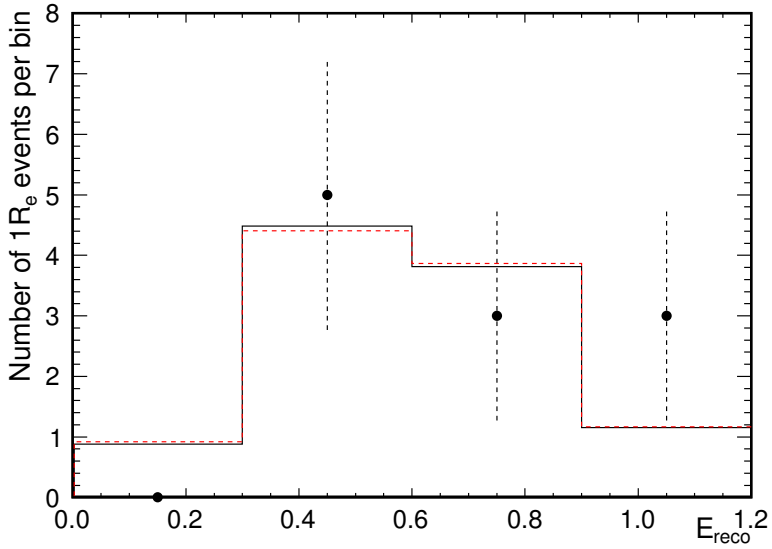

Figure 28: Run 1+2+3 best-fit single e-like ring event reconstructed energy spectrum for the fit with Normal Hierarchy (black: joint 3-flavour oscillation analysis, red: stand-alone ν_e disappearance analysis). The distributions are shown with the coarse binning defined in the main text.

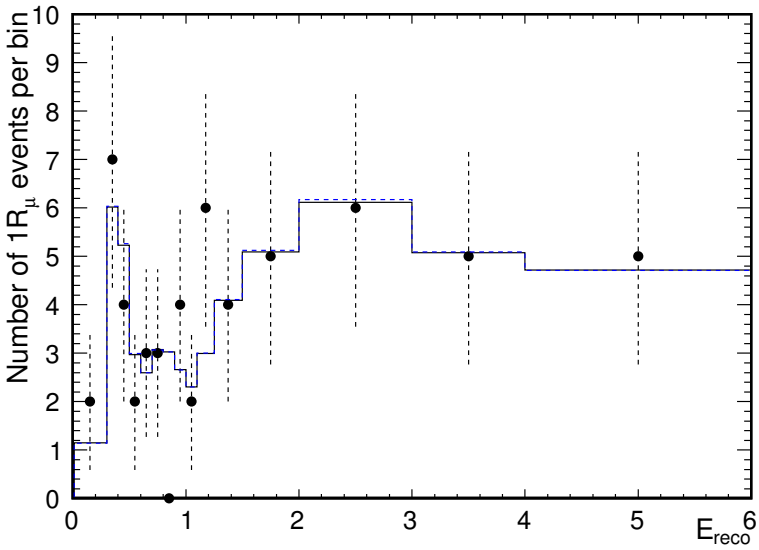

Figure 29: Run 1+2+3 best-fit single μ-like ring event reconstructed energy spectrum for the fit with Inverted Hierarchy (black: joint 3-flavour oscillation analysis, blue: stand-alone ν_μ disappearance analysis). The distributions are shown with the coarse binning defined in the main text.

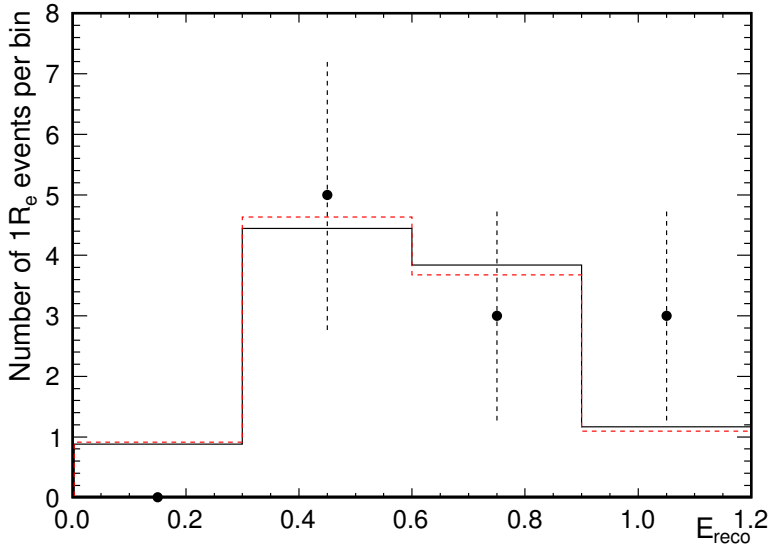

Figure 30: Run 1+2+3 best-fit single e-like ring event reconstructed energy spectrum for the fit with inverted Hierarchy (black: joint 3-flavour oscillation analysis, red: stand-alone ν_e disappearance analysis). The distributions are shown with the coarse binning defined in the main text.

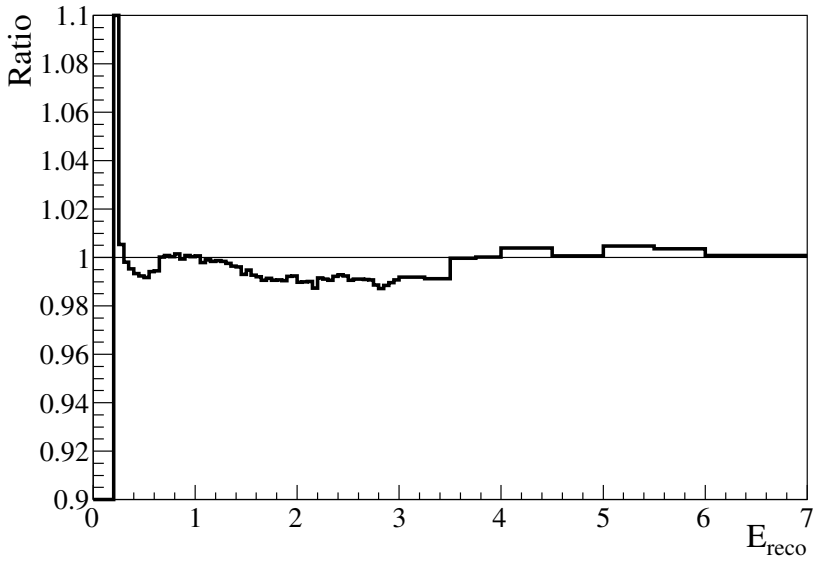

Figure 31: Ratio of the Run 1+2+3 best-fit single μ-like ring event reconstructed energy spectra obtained from the joint 3-flavour oscillation and the stand-alone ν_μ disappearance analyses (joint / stand-alone) with Normal Hierarchy. The distributions are shown with the binning used in the fit.

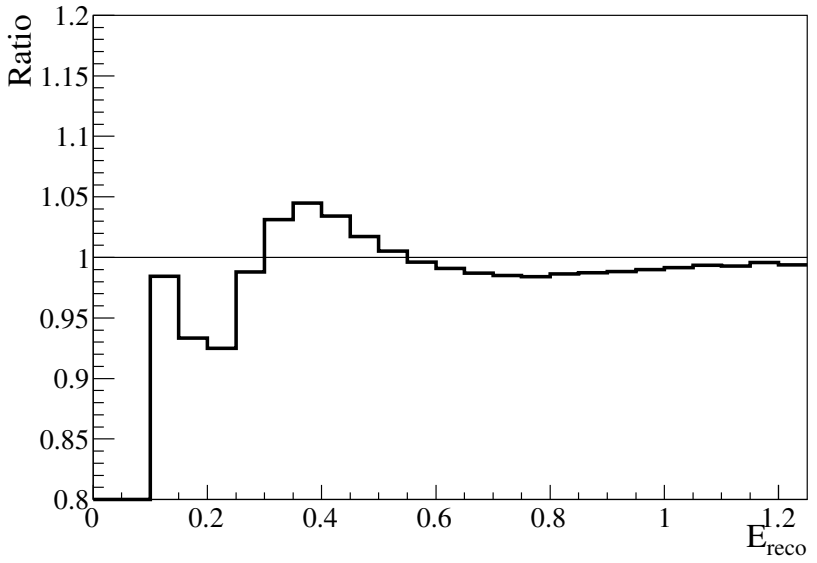

Figure 32: Ratio of the Run 1+2+3 best-fit single e-like ring event reconstructed energy spectra obtained from the joint 3-flavour oscillation and the stand-alone ν_e appearance analyses. (joint / stand-alone) with Normal Hierarchy. The distributions are shown with the binning used in the fit.

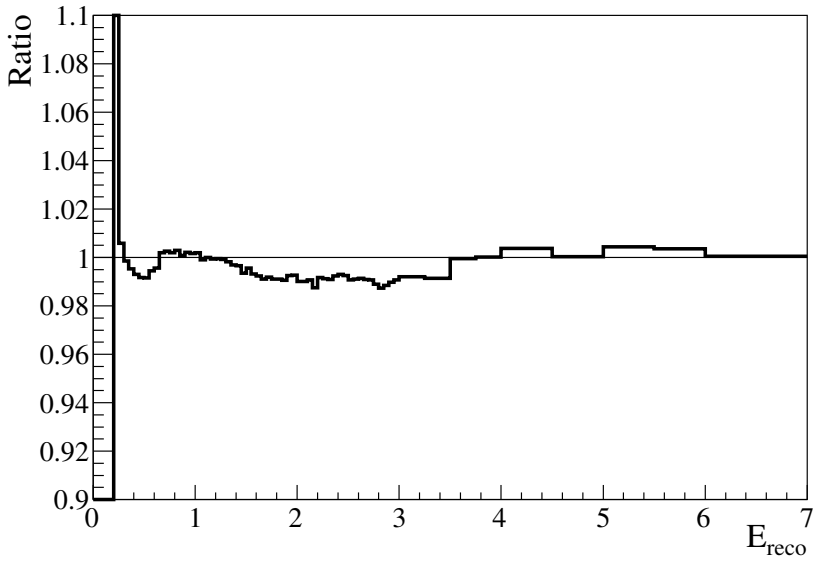

Figure 33: Ratio of the Run 1+2+3 best-fit single μ-like ring event reconstructed energy spectra obtained from the joint 3-flavour oscillation and the stand-alone ν_μ disappearance analyses (joint / stand-alone) with Inverted Hierarchy. The distributions are shown with the binning used in the fit.

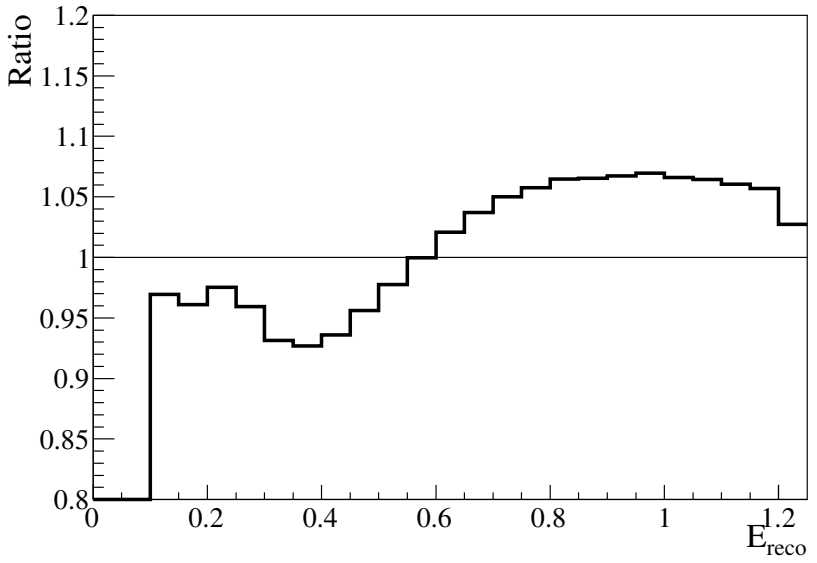

Figure 34: Ratio of the Run 1+2+3 best-fit single e-like ring event reconstructed energy spectra obtained from the joint 3-flavour oscillation and the stand-alone ν_e appearance analyses. (joint / stand-alone) with Inverted Hierarchy. The distributions are shown with the binning used in the fit.

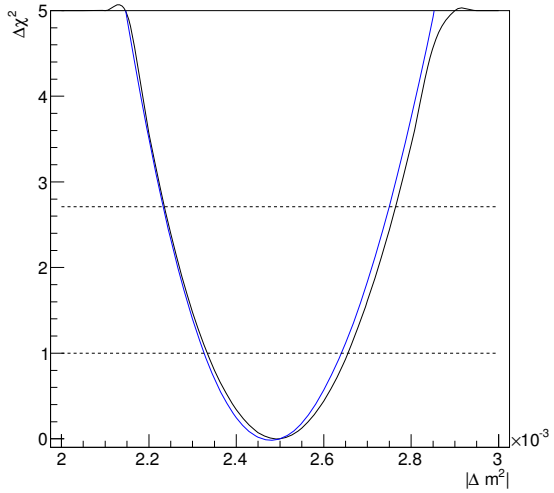

Figure 35: $\Delta\chi^2$ as function of $|\Delta m^2|$ from the analysis of the Run 1+2+3 dataset comparing the joint analysis (black) with the stand-alone ν_μ disappearance (blue) for Normal Hierarchy. At each point, χ^2 was minimized with respect to all oscillation parameters not shown (and not considered to be fixed) and all relevant nuisance parameters.

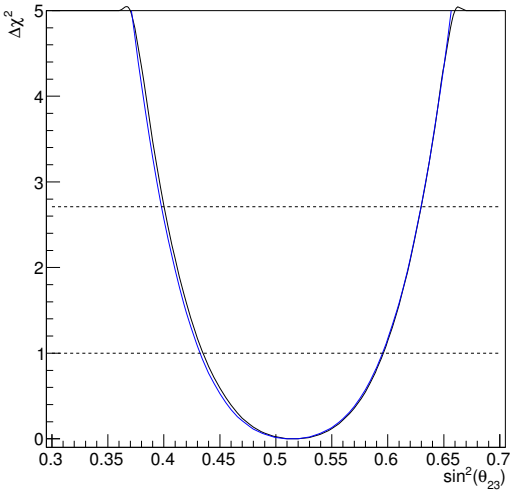

Figure 36: $\Delta\chi^2$ as function of $sin^2\theta_{23}$ from the analysis of the Run 1+2+3 dataset comparing the joint analysis (black) with the stand-alone ν_μ disappearance (blue) for Normal Hierarchy. At each point, χ^2 was minimized with respect to all oscillation parameters not shown (and not considered to be fixed) and all relevant nuisance parameters.

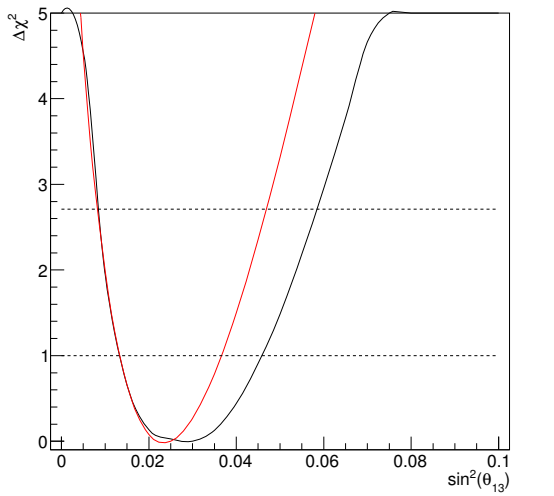

Figure 37: $\Delta\chi^2$ as function of $sin^2\theta_{13}$ from the analysis of the Run 1+2+3 dataset comparing the joint analysis (black) with the stand-alone ν_e appearance (red) for Normal Hierarchy. At each point, χ^2 was minimized with respect to all oscillation parameters not shown (and not considered to be fixed) and all relevant nuisance parameters.

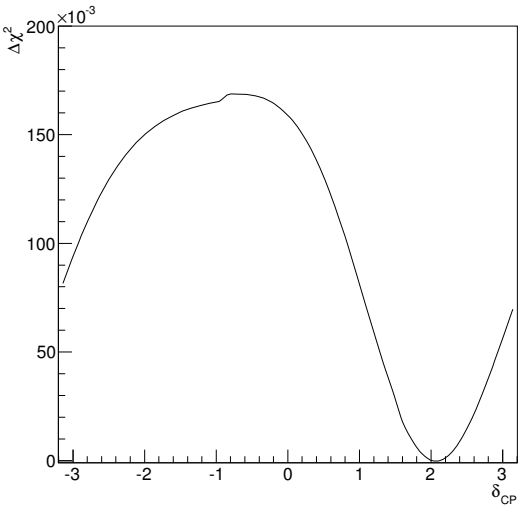

Figure 38: $\Delta\chi^2$ as function of δ_{CP} from the analysis of the Run 1+2+3 dataset for Normal Hierarchy. At each point, χ^2 was minimized with respect to all oscillation parameters not shown (and not considered to be fixed) and all relevant nuisance parameters.

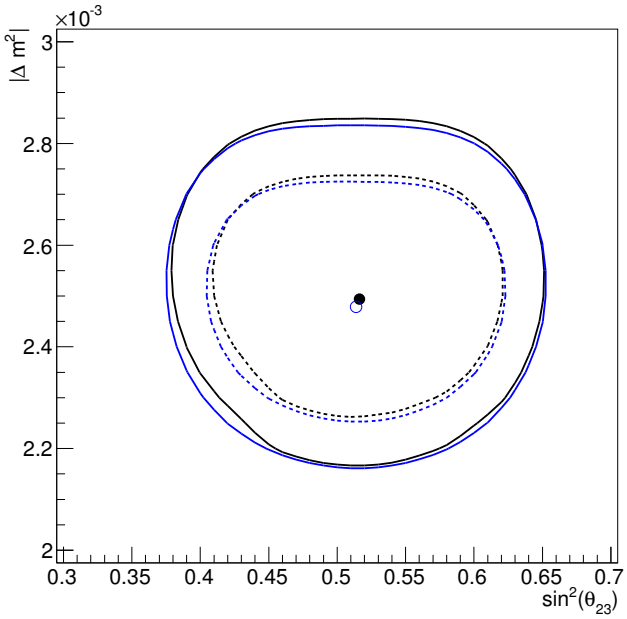

Figure 39: 68% (dashed lines) and 90% (solid lines) CL regions in ($sin^2\theta_{23}$, $|\Delta m^2|$) space from the analysis of the Run 1+2+3 dataset comparing the joint analysis (black) with the stand-alone ν_μ disappearance (blue) for Normal Hierarchy. At each point, χ^2 was minimized with respect to all oscillation parameters not shown (and not considered to be fixed) and all relevant nuisance parameters.

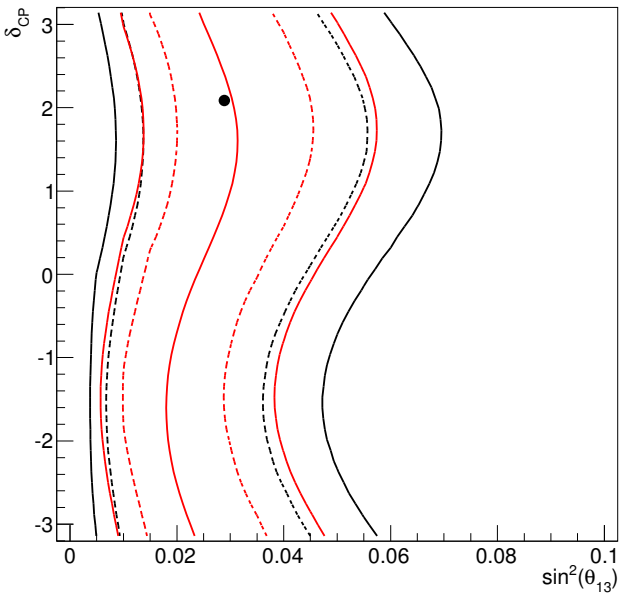

Figure 40: 68% (dashed lines) and 90% (solid lines) CL regions in ($sin^2\theta_{13}$, δ_{CP}) space from the analysis of the Run 1+2+3 dataset comparing the joint analysis (black) with the stand-alone ν_e appearance (red) for Normal Hierarchy. At each point, χ^2 was minimized with respect to all oscillation parameters not shown (and not considered to be fixed) and all relevant nuisance parameters. Notice that different methods are used to construct confidence regions for the joint analysis (global minimum) and for the stand-alone appearance analysis (raster scan). Middle solid red line is the line of best-fit points from the raster scan in the stand-alone appearance analysis.

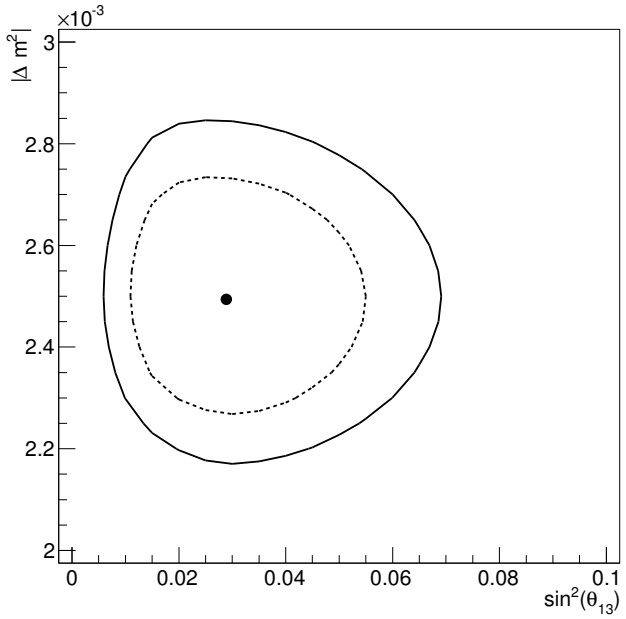

Figure 41: 68% (dashed lines) and 90% (solid lines) CL regions in ($sin^2\theta_{13}$, $|\Delta m^2|$) space from the analysis of the Run 1+2+3 dataset for Normal Hierarchy. At each point, χ^2 was minimized with respect to all oscillation parameters not shown (and not considered to be fixed) and all relevant nuisance parameters.

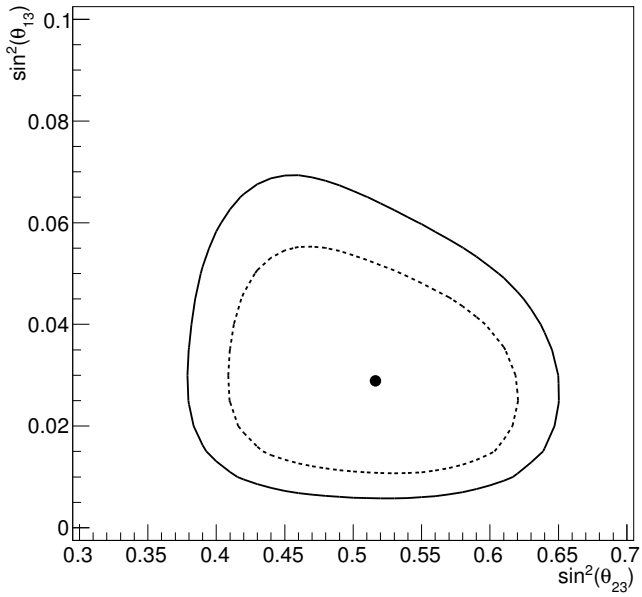

Figure 42: 68% (dashed lines) and 90% (solid lines) CL regions in ($sin^2\theta_{23}$, $sin^2\theta_{13}$) space from the analysis of the Run 1+2+3 dataset for Normal Hierarchy. At each point, χ^2 was minimized with respect to all oscillation parameters not shown (and not considered to be fixed) and all relevant nuisance parameters.

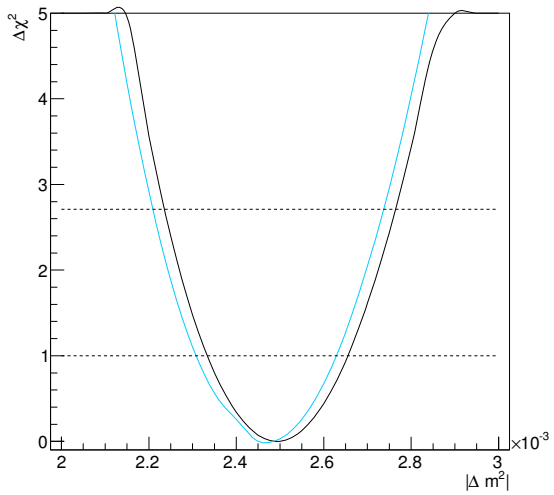

Figure 43: $\Delta\chi^2$ as function of $|\Delta m^2|$ from the joint 3-flavour oscillation analysis of the Run 1+2+3 dataset. Comparing $\Delta\chi^2$ curves for Normal Hierarchy (black) and Inverted Hierarchy (azure). At each point, χ^2 was minimized with respect to all oscillation parameters not shown (and not considered to be fixed) and all relevant nuisance parameters.

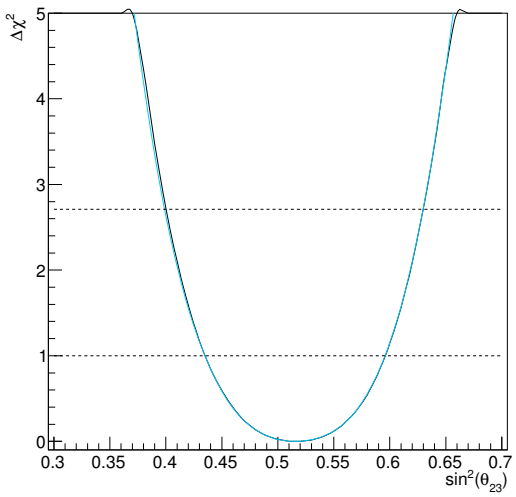

Figure 44: $\Delta\chi^2$ as function of $sin^2\theta_{23}$ from the 3-flavour oscillation analysis of the Run 1+2+3 dataset. Comparing $\Delta\chi^2$ curves for Normal Hierarchy (black) and Inverted Hierarchy (azure). At each point, χ^2 was minimized with respect to all oscillation parameters not shown (and not considered to be fixed) and all relevant nuisance parameters.

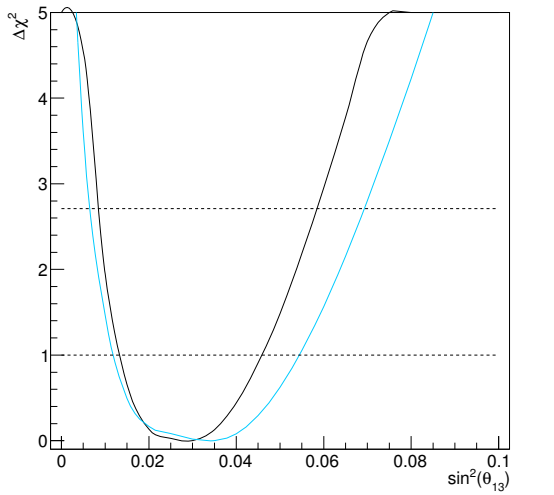

Figure 45: $\Delta\chi^2$ as function of $sin^2\theta_{13}$ from the 3-flavour oscillation analysis of the Run 1+2+3 dataset. Comparing $\Delta\chi^2$ curves for Normal Hierarchy (black) and Inverted Hierarchy (azure). At each point, χ^2 was minimized with respect to all oscillation parameters not shown (and not considered to be fixed) and all relevant nuisance parameters.

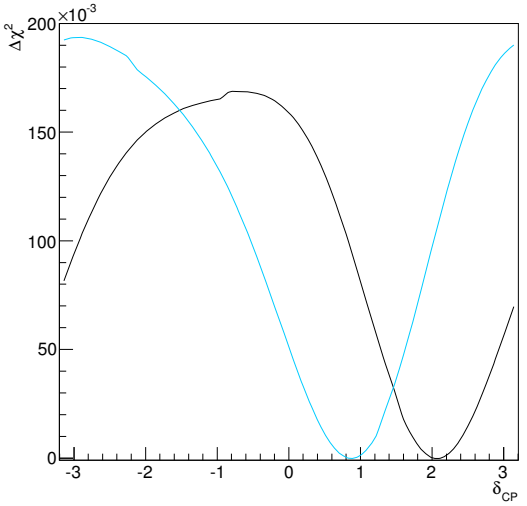

Figure 46: $\Delta\chi^2$ as function of δ_{CP} from the 3-flavour oscillation analysis of the Run 1+2+3 dataset. Comparing $\Delta\chi^2$ curves for Normal Hierarchy (black) with Inverted Hierarchy (azure). At each point, χ^2 was minimized with respect to all oscillation parameters not shown (and not considered to be fixed) and all relevant nuisance parameters.

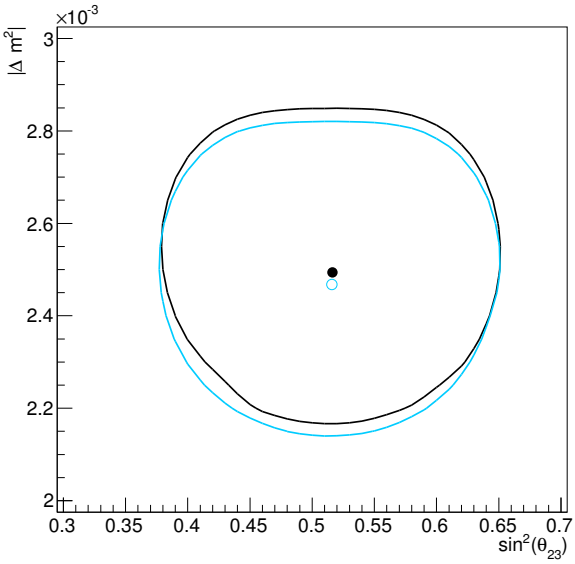

Figure 47: 90% CL regions in ($sin^2\theta_{23}$, $|\Delta m^2|$) space from the joint 3-flavour oscillation analysis of the Run 1+2+3 dataset, comparing contours for the Normal Hierarchy (black) and Inverted Hierarchy (azure). At each point, χ^2 was minimized with respect to all oscillation parameters not shown (and not considered to be fixed) and all relevant nuisance parameters.

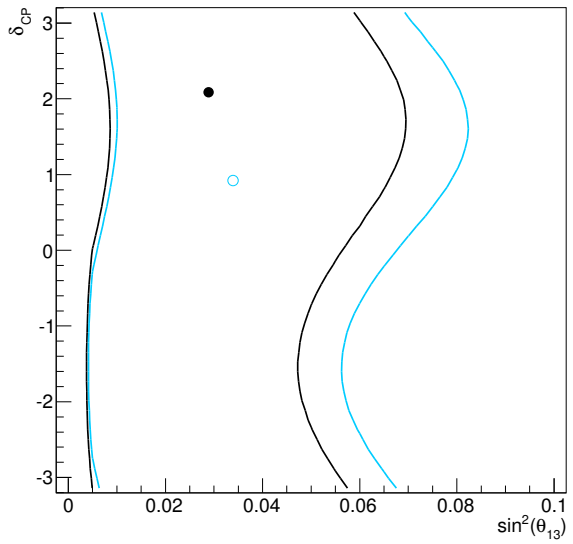

Figure 48: 90% CL regions in ($sin^2\theta_{13}$, δ_{CP}) space from the joint 3-flavour oscillation analysis of the Run 1+2+3 dataset, comparing contours for the Normal Hierarchy (black) and Inverted Hierarchy (azure). At each point, χ^2 was minimized with respect to all oscillation parameters not shown (and not considered to be fixed) and all relevant nuisance parameters.

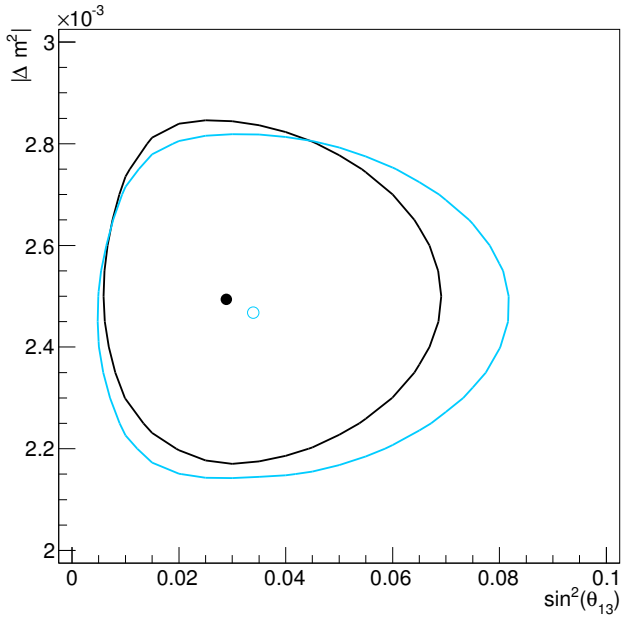

Figure 49: 90% CL regions in ($sin^2\theta_{13}$, $|\Delta m^2|$) space from the joint 3-flavour oscillation analysis of the Run 1+2+3 dataset, comparing contours for the Normal Hierarchy (black) and Inverted Hierarchy (azure). At each point, χ^2 was minimized with respect to all oscillation parameters not shown (and not considered to be fixed) and all relevant nuisance parameters.

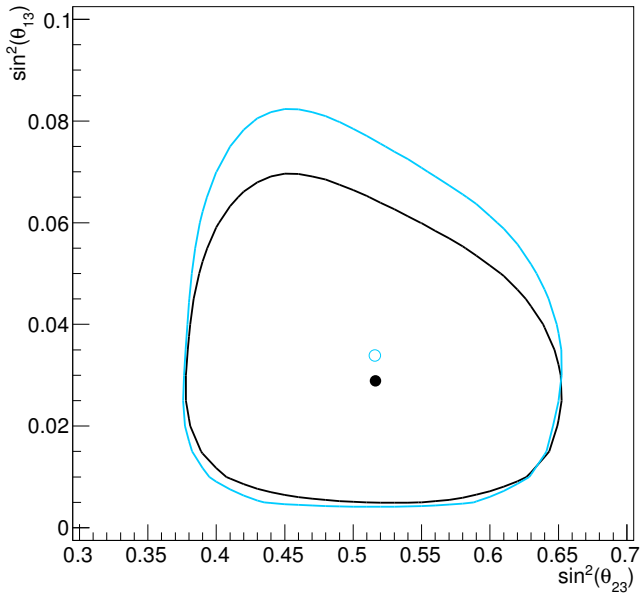

Figure 50: 90% CL regions in ($sin^2\theta_{23}$, $sin^2\theta_{13}$) space from the joint 3-flavour oscillation analysis of the Run 1+2+3 dataset, comparing contours for the Normal Hierarchy (black) and Inverted Hierarchy (azure). At each point, χ^2 was minimized with respect to all oscillation parameters not shown (and not considered to be fixed) and all relevant nuisance parameters.

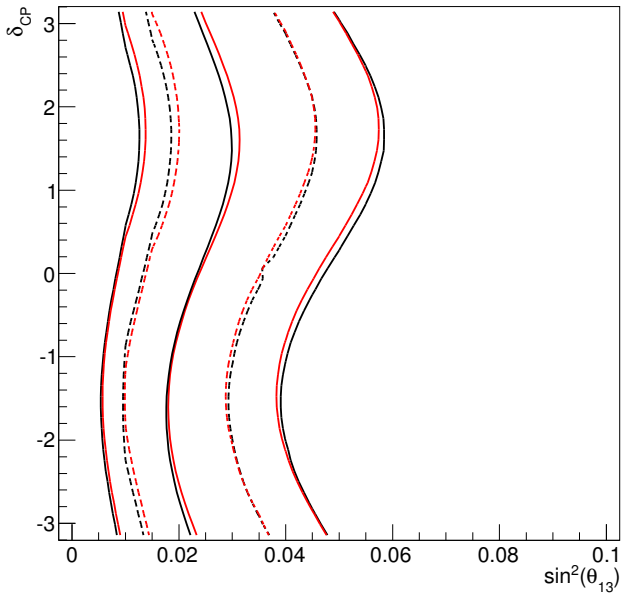

Figure 51: 68% (dashed lines) and 90% (solid lines) CL regions in ($sin^2\theta_{13}$, δ_{CP}) space from the analysis of the Run 1+2+3 dataset comparing the joint analysis (black) with the stand-alone ν_e appearance (red) for Normal Hierarchy, using the raster scan in both analyses. Middle solid black (red) line is the line of best-fit points from the raster scan in the joint (stand-alone appearance) analysis.

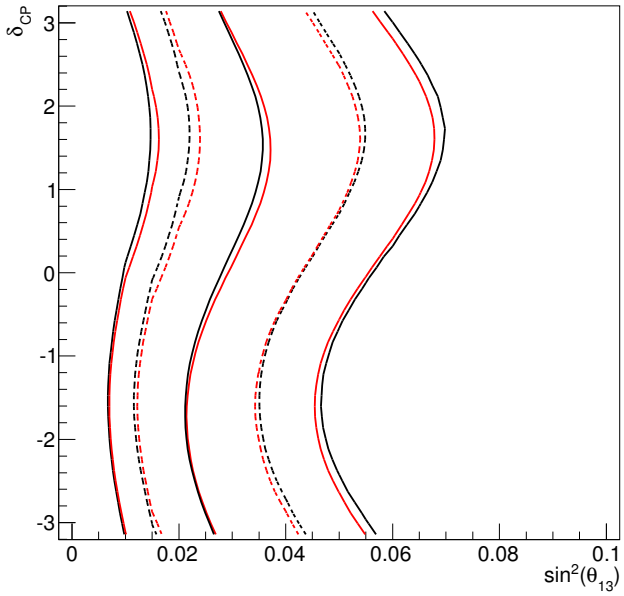

Figure 52: 68% (dashed lines) and 90% (solid lines) CL regions in ($sin^2\theta_{13}$, δ_{CP}) space from the analysis of the Run 1+2+3 dataset comparing the joint analysis (black) with the stand-alone ν_e appearance (red) for Inverted Hierarchy, using the raster scan in both analyses. Middle solid black (red) line is the line of best-fit points from the raster scan in the joint (stand-alone appearance) analysis.

8. Summary

This technical note reports a joint 3-flavour oscillation analysis by the VaLOR group on the combined Run 1+2+3 dataset, which corresponds to an integrated neutrino beam exposure of 3.020×10^{20} POT. The joint analysis determines $|\Delta m^2|$, $\sin^2\theta_{23}$, $\sin^2\theta_{13}$ and δ_{CP} together by making a simultaneous fit of the reconstructed energy spectra of the single μ-like ring and single e-like ring SuperK event samples. This fit is performed in a 3-flavour framework including constant-density matter effects. Official 2012 T2K analysis inputs are used, and all 83 systematic parameters considered in the analysis (see Sec. 5) are allowed to float in the fit. The Fogli-Lisi convention is used for the "atmospheric" mass-squared splitting $|\Delta m^2|$ (see Sec. 3). The "solar" oscillation parameters $\sin^2\theta_{12}$ and Δm^2_{21} have been found to have a negligible effect (see appendix F), and are fixed at 0.311 and 7.5×10^{-5} eV^2/c^4 respectively (the 2012 PDG values).

This analysis has been extensively validated. The ν_μ-disappearance analysis is identical to the 2012 VaLOR analysis reported in Ref. [4], and the ν_e-appearance analysis has been validated against the official 2012 analyses (see appendix A). Studies have been made of fitter residuals (appendix B), fits of 3.020×10^{20} POT fake datasets (appendix C) and the T2K expected sensitivity for 3.020×10^{20} POT (appendix D). These studies have shown that the joint analysis fitter is performing as expected.

In the present version of the analysis, correlations between the single μ-like ring and single e-like ring systematic uncertainties have been neglected, but they will be studied and reported in a future version.

For the normal hierarchy (NH), the joint analysis fit of the reconstructed energy spectra of the single μ-like ring and single e-like ring SuperK event samples gives $|\Delta m^2| = 2.494\times10^{-3}\ eV^2/c^4$, $\sin^2\theta_{23} = 0.516$, $\sin^2\theta_{13} = 0.029$ and $\delta_{CP} = 2.086$. The corresponding best-fit values for the inverted hierarchy (IH) are $|\Delta m^2| = 2.468\times10^{-3}\ eV^2/c^4$, $\sin^2\theta_{23} = 0.516$, $\sin^2\theta_{13} = 0.034$ and $\delta_{CP} = 0.922$.

Confidence regions are constructed using the constant-$\Delta\chi^2$ method. For the NH, the 90% (68%) C.L. allowed region for the four fitted oscillation parameters can be summarized as 2.227×10^{-3} (2.332×10^{-3}) eV^2/c^4 $< |\Delta m^2| <$ 2.773×10^{-3} (2.659×10^{-3}) eV^2/c^4, 0.401 (0.433) $< \sin^2\theta_{23} <$ 0.628 (0.596), 0.006 (0.012) $< \sin^2\theta_{13} <$ 0.058 (0.048) and -π (-π) $< \delta_{CP} < \pi$ (π). For the IH, the corresponding 90% (68%) C.L. allowed regions are 2.218×10^{-3} (2.311×10^{-3}) eV^2/c^4 $< |\Delta m^2| <$ 2.729×10^{-3} (2.627×10^{-3}) eV^2/c^4, 0.397 (0.433) $< \sin^2\theta_{23} <$ 0.627 (0.596), 0.006 (0.013) $< \sin^2\theta_{13} <$ 0.069 (0.054) and -π (-π) $< \delta_{CP} < \pi$ (π).

The joint analysis has the advantage compared with the stand-alone analyses that it does not need to assume the values of any of the oscillation parameters $|\Delta m^2|$, $\sin^2\theta_{23}$, $\sin^2\theta_{13}$ and δ_{CP}. In particular, the value of $\sin^2\theta_{23}$ is not assumed as in the stand-alone ν_e-appearance analysis, but is constrained by the fit of the reconstructed energy spectrum of the single μ-like ring SuperK event sample.

References

[1] C.Andreopoulos, T.Dealtry, J.Dobson, N.Grant, M.Haigh, J.Ilic, G.Pearce and A.Weber, T2K 3.23×10^{19}-POT Muon-Neutrino Disappearance Analysis, T2K-TN-036(v4), http://www.t2k.org/docs/technotes/036

[2] C.Andreopoulos, T.Dealtry, J.Dobson, N.Grant, M.Haigh, J.Ilic, G.Pearce and A.Weber, T2K 1.431×10^{20}-POT Muon-Neutrino Disappearance Analysis, T2K-TN-064(v3), http://www.t2k.org/docs/technotes/064

[3] C.Andreopoulos, T.Dealtry, L.Escudero and N.Grant, T2K 1.431×10^{20}-POT 3-Flavour Muon-Neutrino Disappearance Analysis, T2K-TN-087(v1), http://www.t2k.org/docs/technotes/087

[4] C.Andreopoulos, T.Dealtry, L.Escudero and N.Grant, T2K 3.010×10^{20}-POT 3-Flavour Muon-Neutrino Disappearance Analysis T2K-TN-141(v5), http://www.t2k.org/docs/technotes/141

[5] M. Otani and J. Kameda, Super K events and updated systematic errors with 1.43×10^{20} POT, T2K-TN-065(v8), http://www.t2k.org/docs/technotes/065

[6] J. Kameda and R. Wendell, Study on Super-K events and systematic errors relevant for the ν_μ disappearance analysis with T2K 3.23×10^{19} POT data T2K-TN-034, http://www.t2k.org/docs/technotes/034

[7] ND280 number of selected events and systematics (10dv3 flux), http://www.t2k.org/asg/oagroup/nd280-offaxis See also T2K-TN-015(v5) at http://www.t2k.org/docs/technotes/015

[8] Beam working group, NSK/NND normalisation uncertainty v3.1, http://www.t2k.org/beam/NuFlux/FluxRelease/10d/nsknnderrv3

[9] Beam working group, 10dv3 shape error for SK ν_μ flux, http://www.t2k.org/beam/NuFlux/FluxRelease/10d/shapeerrorv31 See also T2K-TN-066(v3) at http://www.t2k.org/docs/technotes/066

[10] NIWG group, NIWG errors for 10a analysis, http://www.t2k.org/asg/oagroup/oa_niwg

[11] P. de Perio et al., Cross section parameters for the 2012a oscillation analysis, T2K-TN-108(v1.3a)

[12] P. de Perio et al., Implementation of the NIWG cross-section parametrization, T2K-TN-113(v1.2)

[13] J. Albert and K. Okumura, First ν_e oscillation analysis with T2K 2010a beam data, T2K-TN-042(v1.2.1), http://www.t2k.org/docs/technotes/042

[14] J. Albert and K. Okumura, Updated ν_e oscillation analysis with Run 1+2 data, T2K-TN-052(v1.1), http://www.t2k.org/docs/technotes/052

[15] S. Nakayama, ν_e appearance analysis with maximum likelihood fit to neutrino energy spectrum, T2K-TN-109(v7.1), http://www.t2k.org/docs/technotes/109

[16] K. Sakashita et al., Electron neutrino appearance analysis with electron momentum and angle distribution T2K-TN-114(v8), http://www.t2k.org/docs/technotes/114

[17] K.Abe, et al., Indication of Electron Neutrino Appearance from an Accelerator-produced Off-axis Muon Neutrino Beam, Phys. Rev. Lett. 107, 041801 (2011).

[18] Official release of electron neutrino appearance code and results (internal) http://www.t2k.org/asg/oagroup/anacode

[19] Study on SK ν_e candidates and systematic errors with T2K 3.23 $\times10^{19}$ POT data http://www.t2k.org/docs/technotes/028, T2K-TN-028

[20] Y.Hayato, A neutrino interaction simulation program library NEUT, Acta Phys.Polon.B40:2477-2489,2009.

[21] G.L.Fogli, E.Lisi et al., Evidence of theta(13)>0 from global neutrino data analysis, arXiv:1106.6028 [hep-ph]

[22] M. C. Gonzalez-Garcia, Michele Maltoni, Jordi Salvado, Thomas Schwetz, Global fit to three neutrino mixing: critical look at present precision, arXiv:1209.3023 [hep-ph]

[23] The KamLAND collaboration, Precision Measurement of Neutrino Oscillation Parameters with KamLAND, arXiv:0801.4589 [hep-ex]

[24] J. Beringer et al. (Particle Data Group), PR D86, 010001 (2012) (URL: http://pdg.lbl.gov)

[25] G.Fogli's talk (pages 4,5,6) in NNN05 conference, http://nnn05.in2p3.fr/schedule.html

[26] Numerical recipes: the art of scientific computing, Cambridge University Press, 3rd edition, ISBN 978-0-521-88068-0, pp100-102

[27] G.J. Feldman and R.D. Cousins, A Unified approach to the classical statistical analysis of small signals, Phys.Rev.D57:3873-3889,1998; physics/9711021

[28] R.D. Cousins and V.L.Highland, Nucl.Instr. and Meth. A320:331035, 1992.

[29] G. Cowan (1998) Statistical data analysis, Oxford University Press, ISBN 0-19-850155-2.

[30] F.James, M.Roos, Minuit: A System for Function Minimization and Analysis of the Parameter Errors and Correlations, Comput.Phys.Commun. 10:343 (1975)

[31] http://www.t2k.org/asg/oagroup/meeting/20120416/lowstat/view

A. Implementation of ν_e-appearance analysis in the *VaLOR* analysis framework

The analysis presented in this note uses a modified version of the framework used by the 2012 3-flavour ν_μ-disappearance analysis performed by the Rutherford-Oxford-Lancs group and reported in [4]. One of the main extensions of the framework is the ability to analyze single e-like ring events, a mandatory ingredient for the joint fit. This new *VaLOR* ν_e-appearance analysis uses the same inputs as the official 2012 ν_e-appearance analysis [15, 16].

In order to validate the *VaLOR* ν_e-appearance implementation a comparison with the the official 2012 ν_e-appearance analysis in [15] (the one using reconstructed energy spectrum) will be presented now. For this comparison, the same values of oscillation parameters are used: $sin^2(2\theta_{12}) = 0.8704$, $\Delta m^2_{21} = 7.6 \times 10^{-5}$, $sin^2(2\theta_{23}) = 1.0$, $|\Delta m^2_{32}| = 2.4 \times 10^{-3}$, $\delta_{CP} = 0$ and normal hierarchy.

Tables 14 and 15 show the predicted number of ν_e candidate events corresponding to Run1+2+3 POT for both analyses, before (Table 14) and after (Table 15) BANFF tuning. The agreement is excellent before BANFF tuning, while small differences in Table 15 are due to different BANFF versions used (*VaLOR*, as explained in [4], is using a more recent BANFF version than the one used for the 2012 official appearance analyses).

Events	$sin^2(2\theta_{13}) = 0$ (official)	$sin^2(2\theta_{13}) = 0$ (*VaLOR*)	$sin^2(2\theta_{13}) = 0.1$ (official)	$sin^2(2\theta_{13}) = 0.1$ (*VaLOR*)
Total	**3.18**	**3.175**	**11.11**	**11.106**
ν_μ	1.21	1.211	1.21	1.211
$\bar{\nu_\mu}$	0.07	0.067	0.07	0.067
ν_e	1.62	1.622	1.50	1.505
$\bar{\nu_e}$	0.08	0.083	0.08	0.079
osc. ν_e	0.19	0.192	8.24	8.245

Table 14: Predicted number of ν_e candidate events for the Run1+2+3 POT before BANFF tuning (that is, after external flux reweighting using default 11c SK MC with the 11b tuned version 3.2), for *VaLOR* appearance analysis (black) compared to official appearance analysis (blue) as in Table 1 of [15], using $sin^2(2\theta_{12}) = 0.8704$, $\Delta m^2_{21} = 7.6 \times 10^{-5}$, $sin^2(2\theta_{23}) = 1.0$, $|\Delta m^2_{32}| = 2.4 \times 10^{-3}$, $\delta_{CP} = 0$ and normal hierarchy.

Events	$sin^2(2\theta_{13}) = 0$ (official)	$sin^2(2\theta_{13}) = 0$ (*VaLOR*)	$sin^2(2\theta_{13}) = 0.1$ (official)	$sin^2(2\theta_{13}) = 0.1$ (*VaLOR*)
Total	**3.29**	**3.210**	**11.19**	**11.052**
ν_μ	1.18	1.163	1.18	1.163
$\bar{\nu_\mu}$	0.07	0.065	0.07	0.065
ν_e	1.75	1.703	1.63	1.581
$\bar{\nu_e}$	0.09	0.089	0.09	0.084
osc. ν_e	0.19	0.189	8.23	8.158

Table 15: Predicted number of ν_e candidate events for the Run1+2+3 POT after applying BANFF tuning (post ND280 fitted values) for *VaLOR* appearance analysis (black) compared to official appearance analysis (blue) as in Table 9 of [15],using $sin^2(2\theta_{12}) = 0.8704$, $\Delta m^2_{21} = 7.6 \times 10^{-5}$, $sin^2(2\theta_{23}) = 1.0$, $|\Delta m^2_{32}| = 2.4 \times 10^{-3}$, $\delta_{CP} = 0$ and normal hierarchy.

Fig. 53 presents the MC predicted reconstructed neutrino energy distribution (area-normalized) for $\nu_\mu \rightarrow \nu_e$ CC signal, intrinsic ν_e CC background and NC background components obtained with the *VaLOR* framework, in excellent agreement with Fig. 1 in [15] for the official appearance analysis.

A p-value test similar to the one described in [15] has been performed. 11 ν_e candidates has been observed in the Run1+2+3 data-set. The p-value is defined as the probability for observing 11 or more ν_e candidate events in the 3.010×10^{20} POT data with the $sin^2(2\theta_{13}) = 0$ hypothesis. 1×10^6 toy experiments with statistical and systematic variations were created in order to compute that probability. Fig. 54 shows the distribution of the number of ν_e candidate events observed. The p-value, corresponding to the area above 11 (white region), is $\approx 8 \times 10^{-4}$, equivalent to a $\approx 3\sigma$ significance. These values,

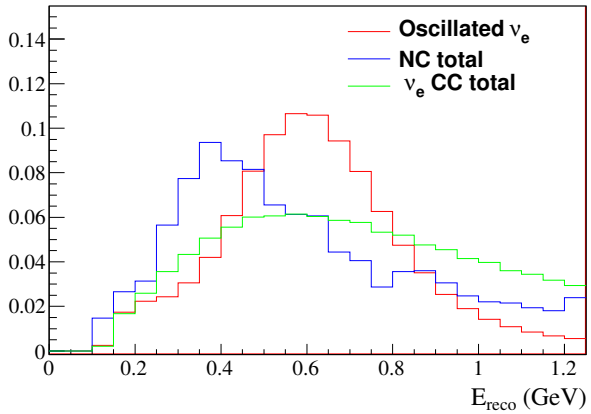

Figure 53: MC predicted reconstructed neutrino energy distribution (area-normalized) for $\nu_\mu \rightarrow \nu_e$ CC signal (red), intrinsic ν_e CC background (green) and NC background (blue) components obtained with *VaLOR* framework, using $sin^2(2\theta_{12}) = 0.8704$, $\Delta m^2_{21} = 7.6 \times 10^{-5}$, $sin^2(2\theta_{23}) = 1.0$, $|\Delta m^2_{32}| = 2.4 \times 10^{-3}$, $\delta_{CP} = 0$ and normal hierarchy.

1827 although computed with 100 times less toy experiments, are very close to the ones obtained in [15] (p-value = 8.6×10^{-4}, 3.1σ
1828 significance).

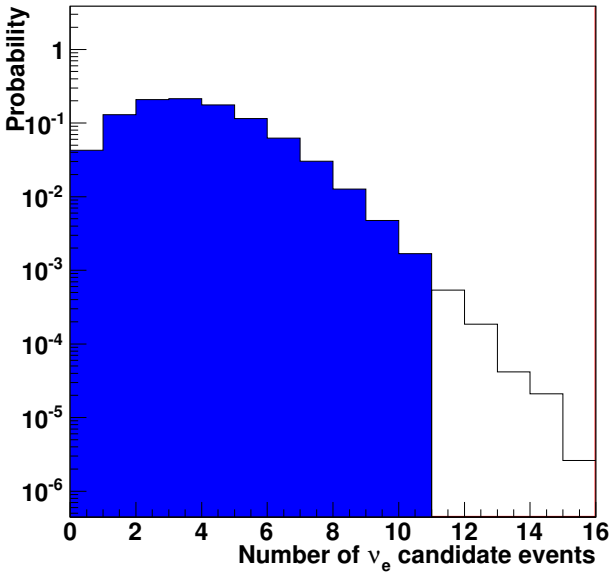

Figure 54: Distribution of predicted number of nu_e candidate events over 1×10^6 toy experiments with $sin^2(2\theta_{13}) = 0$, including statistical and systematic variations, for 3.010×10^{20} POT, $sin^2(2\theta_{12}) = 0.8704$, $\Delta m^2_{21} = 7.6 \times 10^{-5}$, $sin^2(2\theta_{23}) = 1.0$, $|\Delta m^2_{32}| = 2.4 \times 10^{-3}$, $\delta_{CP} = 0$ and normal hierarchy.

1829 The fit to the Run1+2+3 data-set is the next step in the validation. Fig. 55 shows the $\Delta\chi^2$ curve for normal (left) and
1830 inverted (right) hierarchy, in great agreement with Fig. 20 in [15]. The corresponding best-fit point and confidence intervals for
1831 $sin^2(2\theta_{13})$ are summarized in table 16. Finally, the reconstructed energy spectrum at the best-fit point is presented in Fig. 56,
1832 which is again in excellent agreement with Fig. 21 in [15].
1833 From these comparisons and other detailed tests not shown here, it is concluded that the 2012 *VaLOR* stand-alone ν_e-
1834 appearance analysis gives equivalent results to the T2K official appearance analyses.

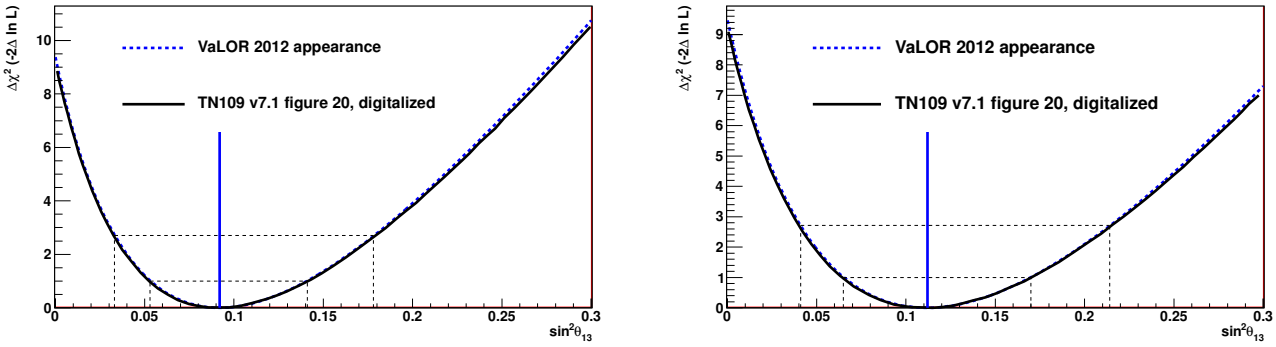

Figure 55: $\Delta\chi^2$ distribution for the Run1+2+3 data fit assuming normal (left) and inverted (right) mass hierarchy, for 2012 *VaLOR* appearance analysis (dashed blue) and 2012 official results from Fig. 21 in [15] (solid black - digitalized). Fixed values used: $sin^2(2\theta_{12}) = 0.8704$, $\Delta m^2_{21} = 7.6 \times 10^{-5}$, $sin^2(2\theta_{23}) = 1.0$, $|\Delta m^2_{32}| = 2.4 \times 10^{-3}$ and $\delta_{CP} = 0$.

	NH (TN109)	NH (*VaLOR*)	IH (TN109)	IH (*VaLOR*)
Best fit	0.092	0.092	0.112	0.112
68 % C.L.	0.053-0.141	0.053-0.141	0.065-0.170	0.065 - 0.170
90 % C.L.	0.033-0.179	0.033-0.178	0.040-0.215	0.041 - 0.214

Table 16: Best-fit points and confidence intervals for $sin^2(2\theta_{13})$ obtained from Fig. 55, with $\delta_{CP} = 0$, $sin^2(2\theta_{12}) = 0.8704$, $\Delta m^2_{21} = 7.6 \times 10^{-5}$, $sin^2(2\theta_{23}) = 1.0$ and $|\Delta m^2_{32}| = 2.4 \times 10^{-3}$, for normal (NH) and inverted (IH) hierarchy.

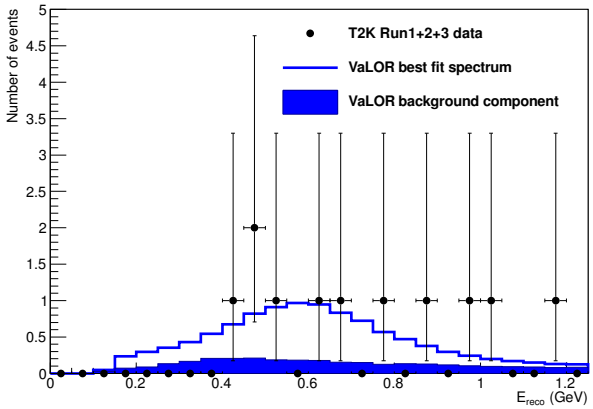

Figure 56: Reconstructed energy spectrum at the best-fit point for Run1+2+3 data fit with the *VaLOR* appearance analysis, assuming $\delta_{CP} = 0$, $sin^2(2\theta_{12}) = 0.8704$, $\Delta m^2_{21} = 7.6 \times 10^{-5}$, $sin^2(2\theta_{23}) = 1.0$, $|\Delta m^2_{32}| = 2.4 \times 10^{-3}$ and normal hierarchy.

B. Fitter performance. Study of residuals.

The fitter performance has been evaluated for different configurations: oscillation points, number of POT, levels of throwing systematics and fitters were varied. Residual distributions (best fit value - input value) are presented in this section. For each study, 1000 toy datasets were created and fitted using MINUIT (MIGRAD), as explained in Sec. 6. Table 17 shows the true input values of the oscillation parameters for the different oscillation points studied.

Oscillation point	$\lvert\Delta m^2\rvert$ (eV^2/c^4)	sin$^2\theta_{23}$	sin$^2\theta_{13}$	δ_{CP}	Mass Hierarchy
0	2.36	0.5	0.025	0	NH
1	2.36	0.38	0.025	0	NH
2	2.36	0.62	0.025	0	NH
3	2.36	0.5	0.015	0	NH
4	2.36	0.5	0.035	0	NH
5	2.36	0.5	0.025	$-\frac{\pi}{2}$	NH
6	2.36	0.5	0.025	$\frac{\pi}{2}$	NH
7	2.2	0.5	0.025	0	NH
8	2.8	0.5	0.025	0	NH
9	2.36	0.5	0.025	0	IH

Table 17: True input values for the different oscillation points used in the study of fitter performance.

B.1. '4 + 0' fit

Figs. 57 - 66 show the distribution of residuals of the four oscillation parameters for each set described in table 17 at 3.010×10^{20} POT. The distribution of residuals for δ_{CP} should not be taken into account due to the insensitivity to this parameter at current POT. A pileup similar to the one observed at maximal mixing $sin^2(2\theta_{23}) = 1.0$ in the stand-alone disappearance analysis is now appearing at the center of symmetry of the P($\nu_\mu \rightarrow \nu_\mu$) curve, which corresponds with the maximal disappearance (the difference between $sin^2(\theta_{23})$ values for maximal disappearance and maximal mixing is explained in Sec. E). This pile-up is reduced when the input value for $sin^2(\theta_{23})$ is far from 0.5 (see figures 59 and 60) and disappears if the POT is increased, as shown in figure 67. In general there are no unexpected features.

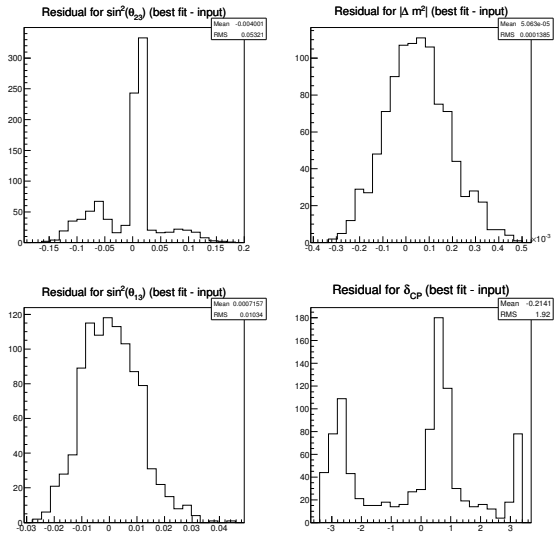

Figure 57: Distribution of residuals of the four oscillation parameters in the '4 + 0' fit for oscillation point # 0.

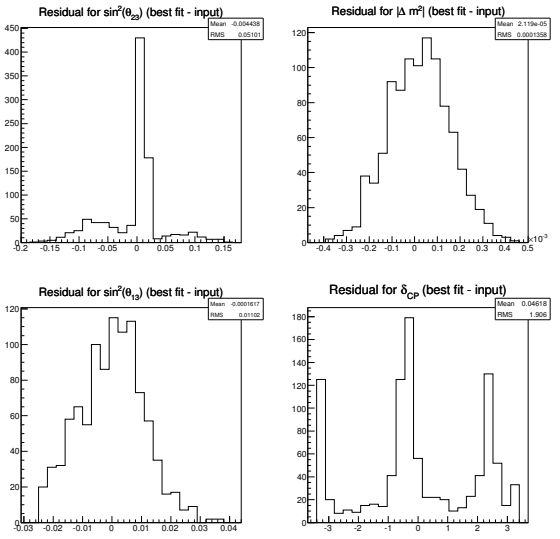

Figure 58: Distribution of residuals of the four oscillation parameters in the '4 + 0' fit for oscillation point # 9.

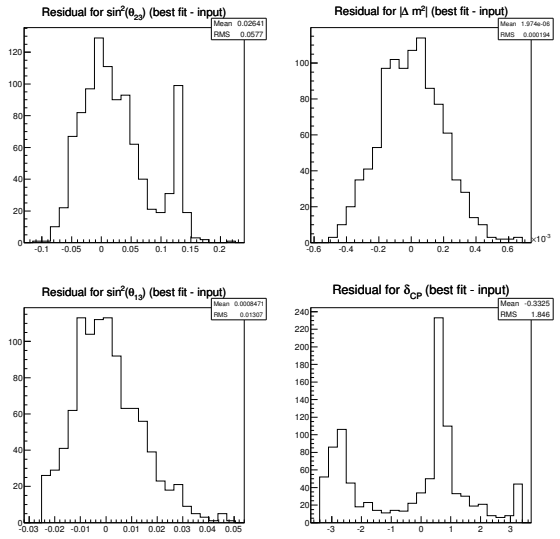

Figure 59: Distribution of residuals of the four oscillation parameters in the '4 + 0' fit for oscillation point # 1.

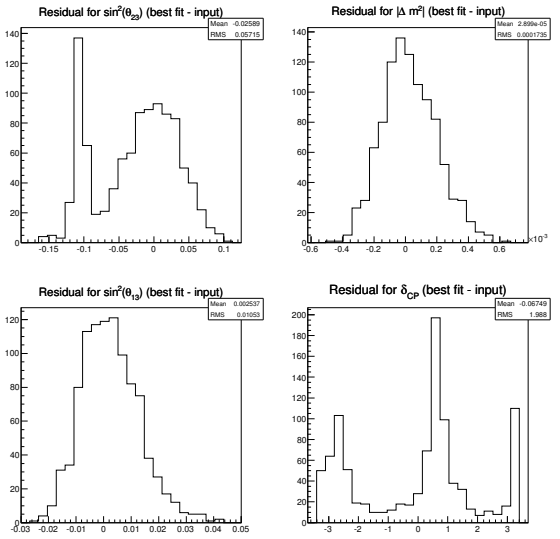

Figure 60: Distribution of residuals of the four oscillation parameters in the '4 + 0' fit for oscillation point # 2.

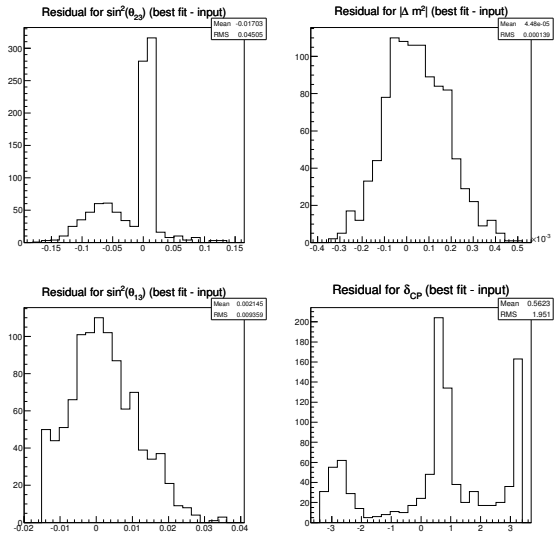

Figure 61: Distribution of residuals of the four oscillation parameters in the '4 + 0' fit for oscillation point # 3.

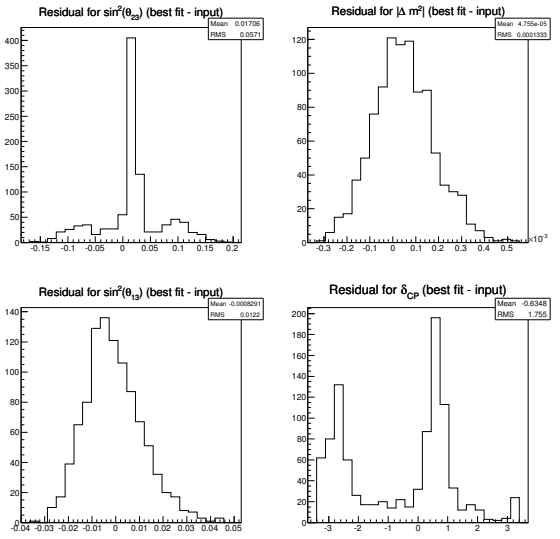

Figure 62: Distribution of residuals of the four oscillation parameters in the '4 + 0' fit for oscillation point # 4.

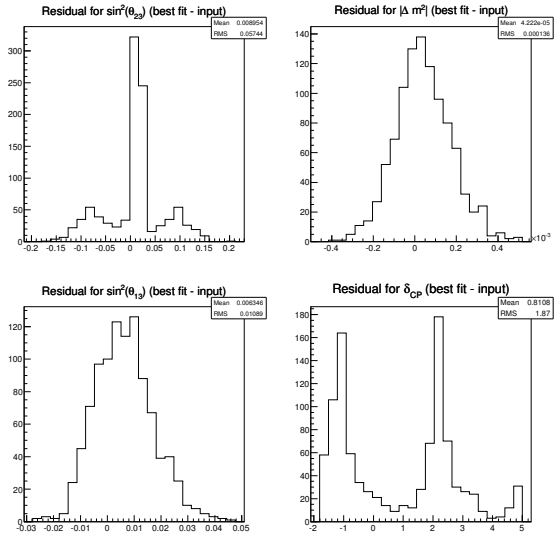

Figure 63: Distribution of residuals of the four oscillation parameters in the '4 + 0' fit for oscillation point # 5.

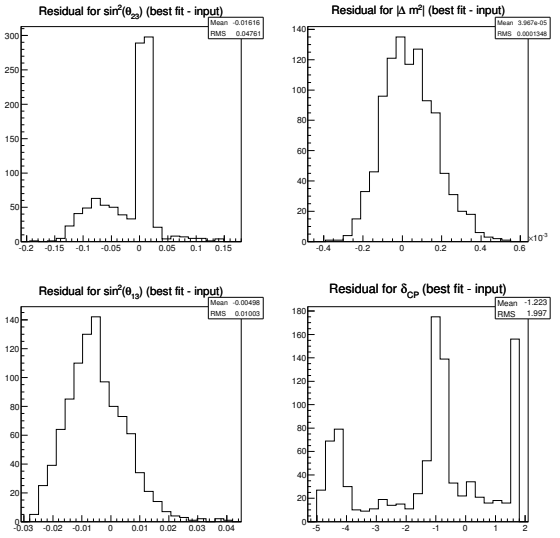

Figure 64: Distribution of residuals of the four oscillation parameters in the '4 + 0' fit for oscillation point # 6.

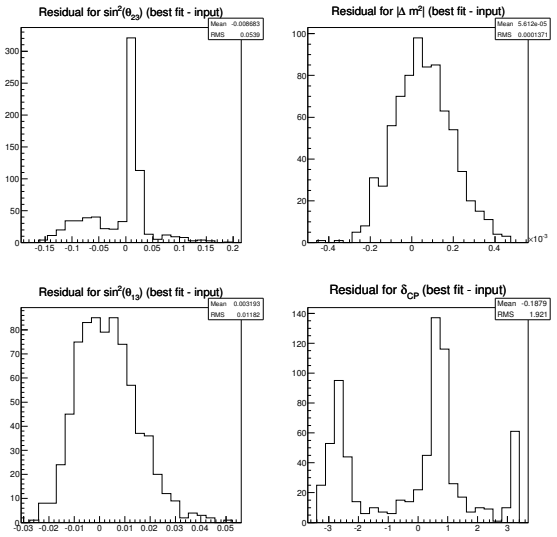

Figure 65: Distribution of residuals of the four oscillation parameters in the '4 + 0' fit for oscillation point # 7.

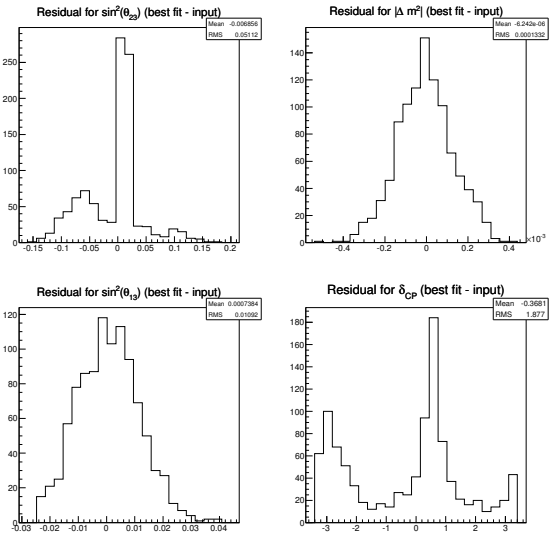

Figure 66: Distribution of residuals of the four oscillation parameters in the '4 + 0' fit for oscillation point # 8.

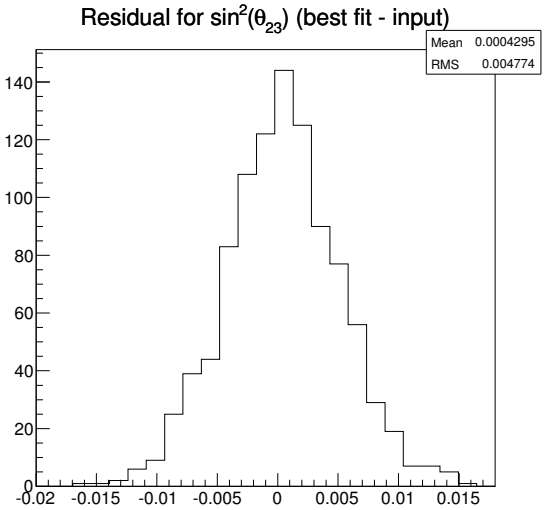

Figure 67: Distribution of residuals for $sin^2(\theta_{23})$ in the '4 + 0' fit for oscillation point # 1 with 3.010×10^{22} POT.

B.2. '4 + 83' fit

Figs. 68 - 77 show the distribution of residuals of the four oscillation parameters for each set described in table 17 at 3.010×10^{20} POT, with all systematic fluctuations. As an example, Figs. 78 - 86 show the distribution of residuals for each systematic parameter for oscillation point # 0. For the rest of oscillation points only summary plots showing the mean and its error ($\frac{RMS}{\sqrt{N}}$) for all systematic parameters will be presented (Figs. 87 - B.2) The numbering convention for the systematic parameters in those figures can be found in table 18. After comparing figures 68 - 77 with 57 - 66 it can be concluded that fitting all systematics does not change the distributions of residuals for the oscillation parameters. From Figs. 87 - B.2 there are three systematics with a "biased" mean of the distribution of residuals. The reason for this was found and will be explained now. Apart from that there are still no unexpected features.

The three systematics with a "biased" mean of the distribution of residuals are:

1. **Spectral function**: The reason for the distribution of residuals for this parameter to be "biased" is the special distribution function used to tweak this systematic parameter, which is uniform from 0 to 1, centered at 0.5, instead of gaussian. It was checked that when using a gaussian distribution as for the rest, this "bias" disappeared. However, the use of a uniform function will be kept for this parameter as it was done for the disappearance analysis.
2. **Pi-less delta decay**:The explanation for the "bias" in its distribution of residuals comes from the special response function used for this for this parameter, which was only calculated up to -1σ and then propagated to -3σ with the same value as for -1σ. This pathology disappears when constraining this parameter with boundaries -1σ to 1σ.
3. $1R_\mu$ **NC efficiency**:The reason for this parameter to have a "biased" distribution of residuals comes from the low statistics at current POT. When Poisson fluctuations are made of the bin contents of the E_{reco} distributions, a downward fluctuation is more likely than an upward fluctuation (see replies to comments and revision history for TN141). Adding the fact that the NC modes are distributed around the oscillation maximum, the (most likely) downwards Poisson fluctuations translate into a (most likely) negative value of the NC efficiency, explaining a "bias" to negative values for this parameter. It was checked that the "bias" in the distribution depends on the true input value of $sin^2\theta_{23}$, disappearing when $sin^2\theta_{23}$ is far away from 0.5; and also that it decreases as well when increasing the POT.

#	Systematic
0 -24	BANFF ν_μ, $\bar{\nu_\mu}$, ν_e and $\bar{\nu_e}$ flux bins
25	BANFF CCQE axial mass
26	BANFF resonance-production axial mass
27-29	CCQE normalization
30-31	CC 1π normalization
32	NC$1\pi0$
33	Fermi momentum
34	Nuclear modeling (Spectral function)
35	Binding energy
36	Shape of π momentum distribution (W shape)
37	CC other shape
38	π-less Δ decay
39	CC coherent normalization
40	NC $1\pi^{\pm}$ normalization
41	NC coherent normalization
42	NC other normalizarion
43	$\sigma_{\nu_e}/\sigma_{\nu_\mu}$ ratio
44	$\sigma_{\bar{\nu}}/\sigma_{\nu}$ ratio
45	Reconstructed energy scale
46-48	ν_μ, $\bar{\nu_\mu}$ CCQE ring counting efficiency
49	ν_μ, $\bar{\nu_\mu}$ CCQE other efficiency
50	ν_μ, $\bar{\nu_\mu}$ CCnonQE efficiency
51	NC efficiency
52	ν_e, $\bar{\nu_e}$ CC efficiency
53-55	$1R_e$ osc. ν_e CC efficiency
56-58	$1R_e$ ν_μ, $\bar{\nu_\mu}$ CC efficiency
59-61	$1R_e$ ν_e, $\bar{\nu_e}$ CC efficiency
62-64	$1R_e$ NC efficiency
65-67	$1R_\mu$ FSI: ν_μ, $\bar{\nu_\mu}$ CCQE
68	R_μ FSI: ν_μ, $\bar{\nu_\mu}$ CCnonQE efficiency
69	R_μ FSI: ν_e, $\bar{\nu_e}$ CC
70	R_μ FSI: NC
71-73	$1R_e$ FS: osc. ν_e CC
74-76	$1R_e$ FSI: ν_μ, $\bar{\nu_\mu}$ CC
77-79	$1R_e$ FSI: ν_e, $\bar{\nu_e}$ CC
80-82	$1R_e$ FSI: NC

Table 18: The numbering of systematic parameters for figures 87 - B.2

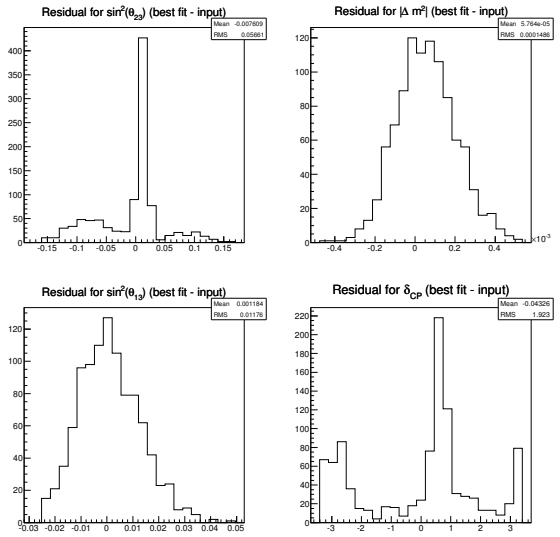

Figure 68: Distribution of residuals of the four oscillation parameters in the '4 + 83' fit for oscillation point # 0.

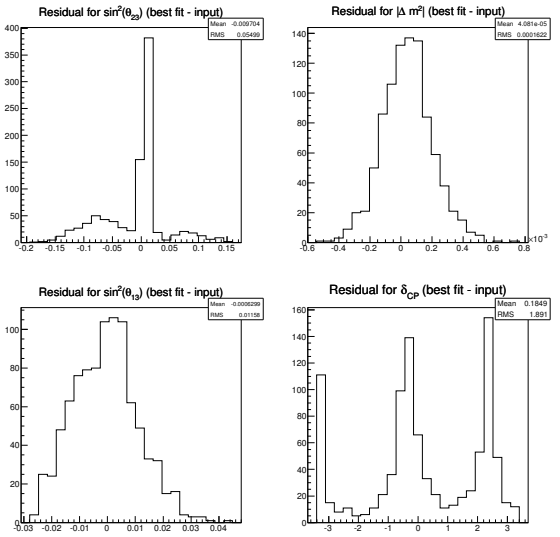

Figure 69: Distribution of residuals of the four oscillation parameters in the '4 + 83' fit for oscillation point # 9.

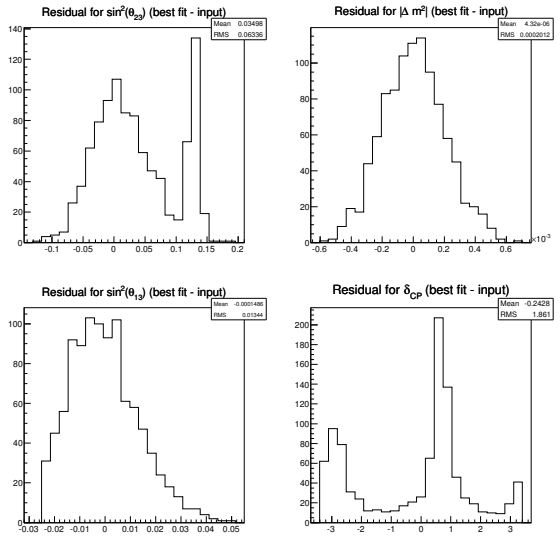

Figure 70: Distribution of residuals of the four oscillation parameters in the '4 + 83' fit for oscillation point # 1.

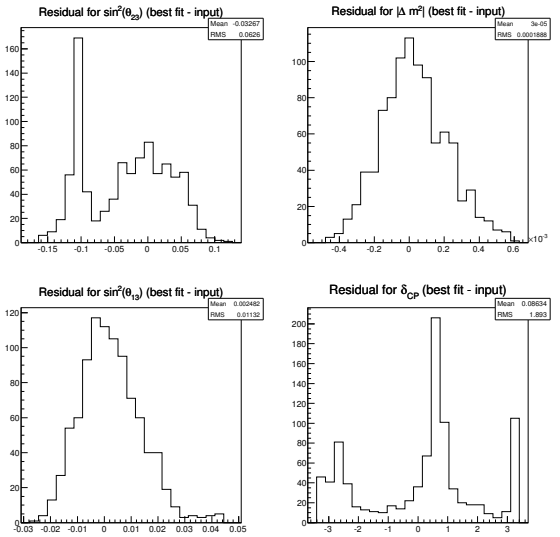

Figure 71: Distribution of residuals of the four oscillation parameters in the '4 + 83' fit for oscillation point # 2.

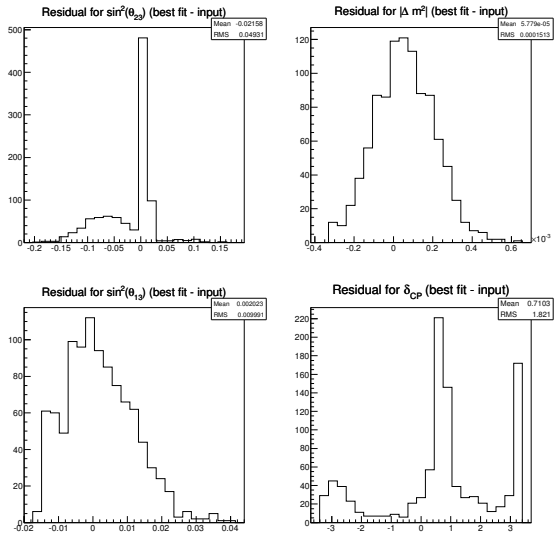

Figure 72: Distribution of residuals of the four oscillation parameters in the '4 + 83' fit for oscillation point # 3.

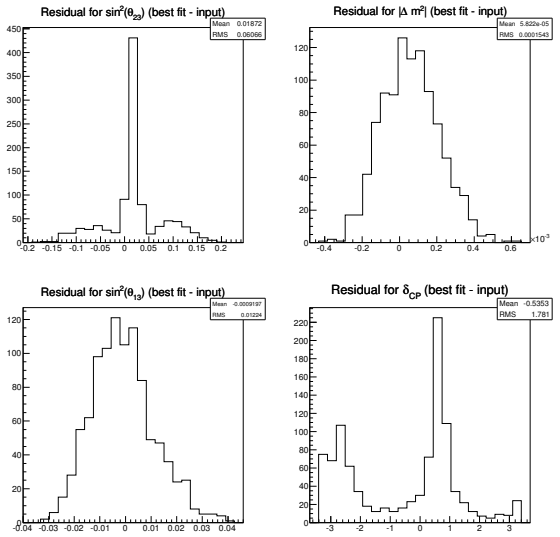

Figure 73: Distribution of residuals of the four oscillation parameters in the '4 + 83' fit for oscillation point # 4.

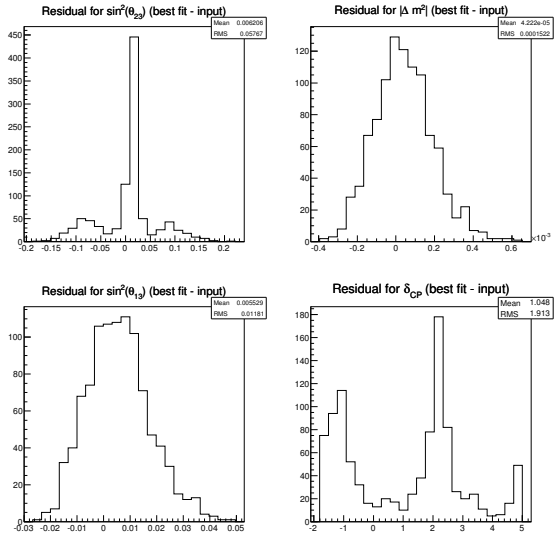

Figure 74: Distribution of residuals of the four oscillation parameters in the '4 + 83' fit for oscillation point # 5.

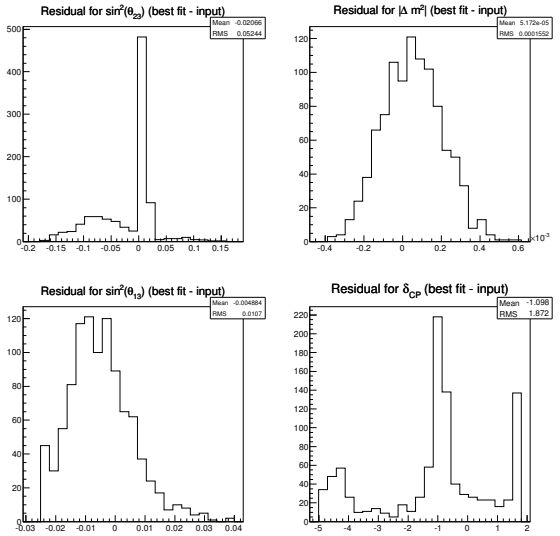

Figure 75: Distribution of residuals of the four oscillation parameters in the '4 + 83' fit for oscillation point # 6.

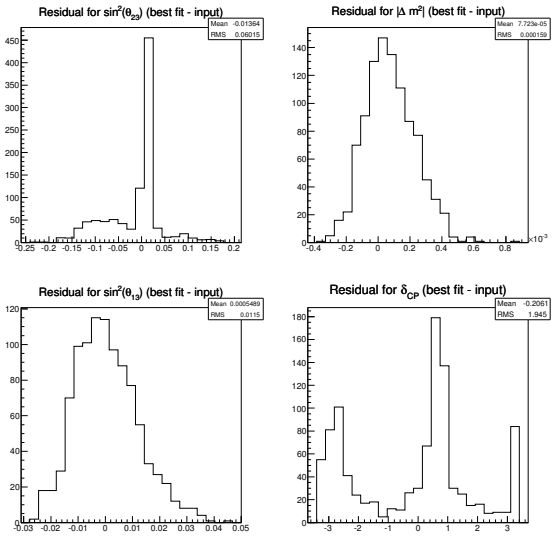

Figure 76: Distribution of residuals of the four oscillation parameters in the '4 + 83' fit for oscillation point # 7.

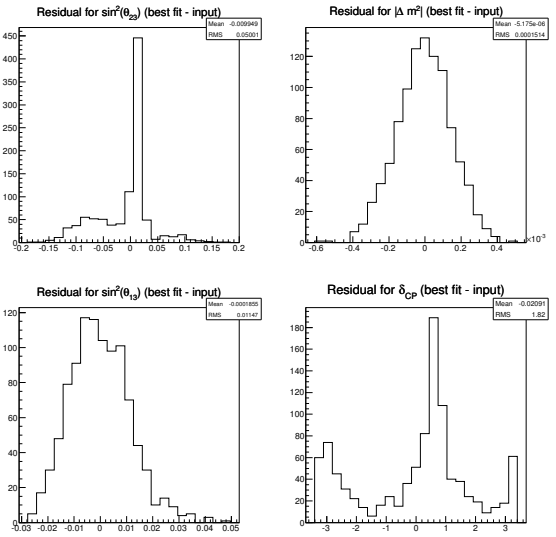

Figure 77: Distribution of residuals of the four oscillation parameters in the '4 + 83' fit for oscillation point # 8.

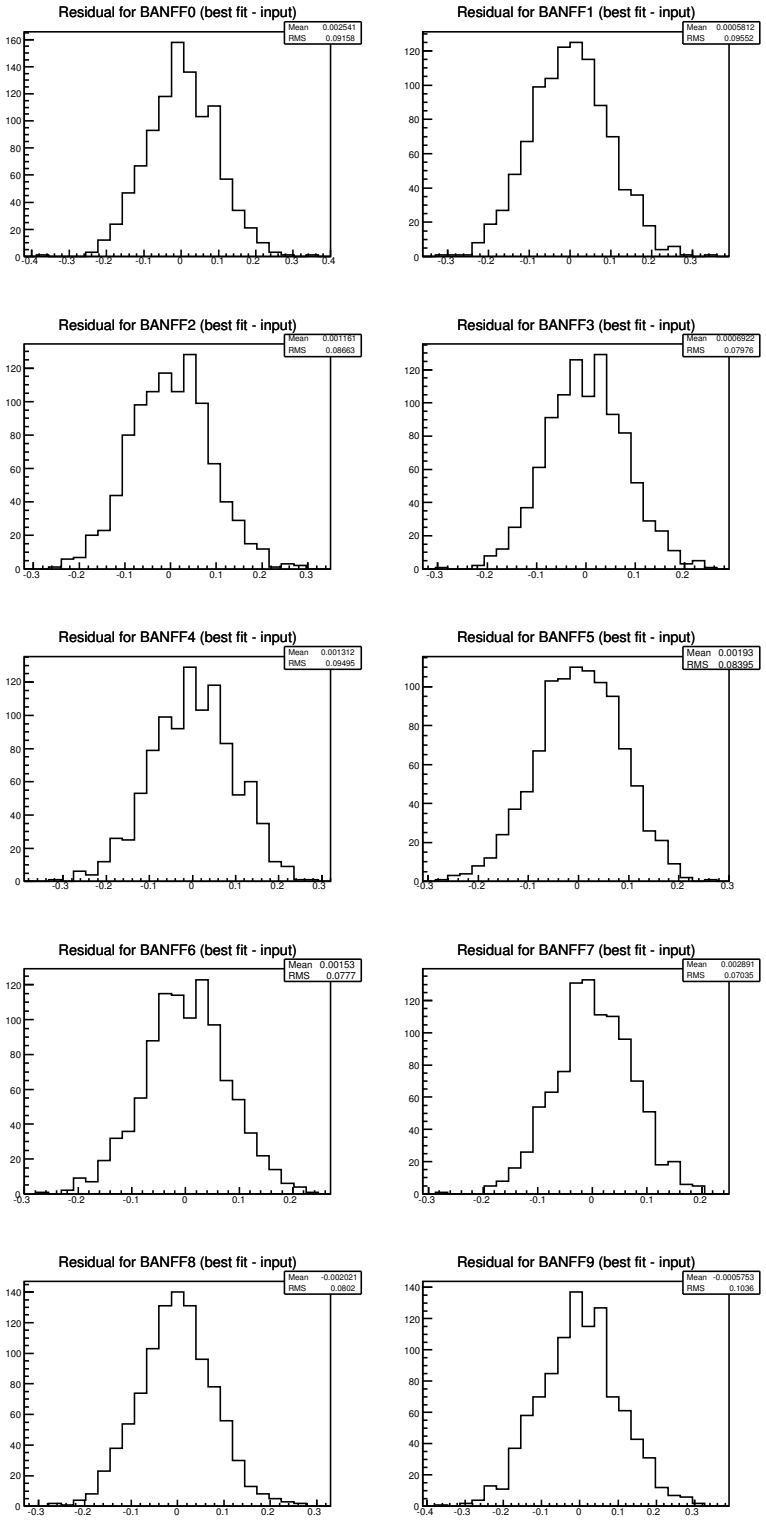

Figure 78: Distribution of residuals of the BANFF (0-9) systematic parameters in the '4 + 83' fit for oscillation point # 0.

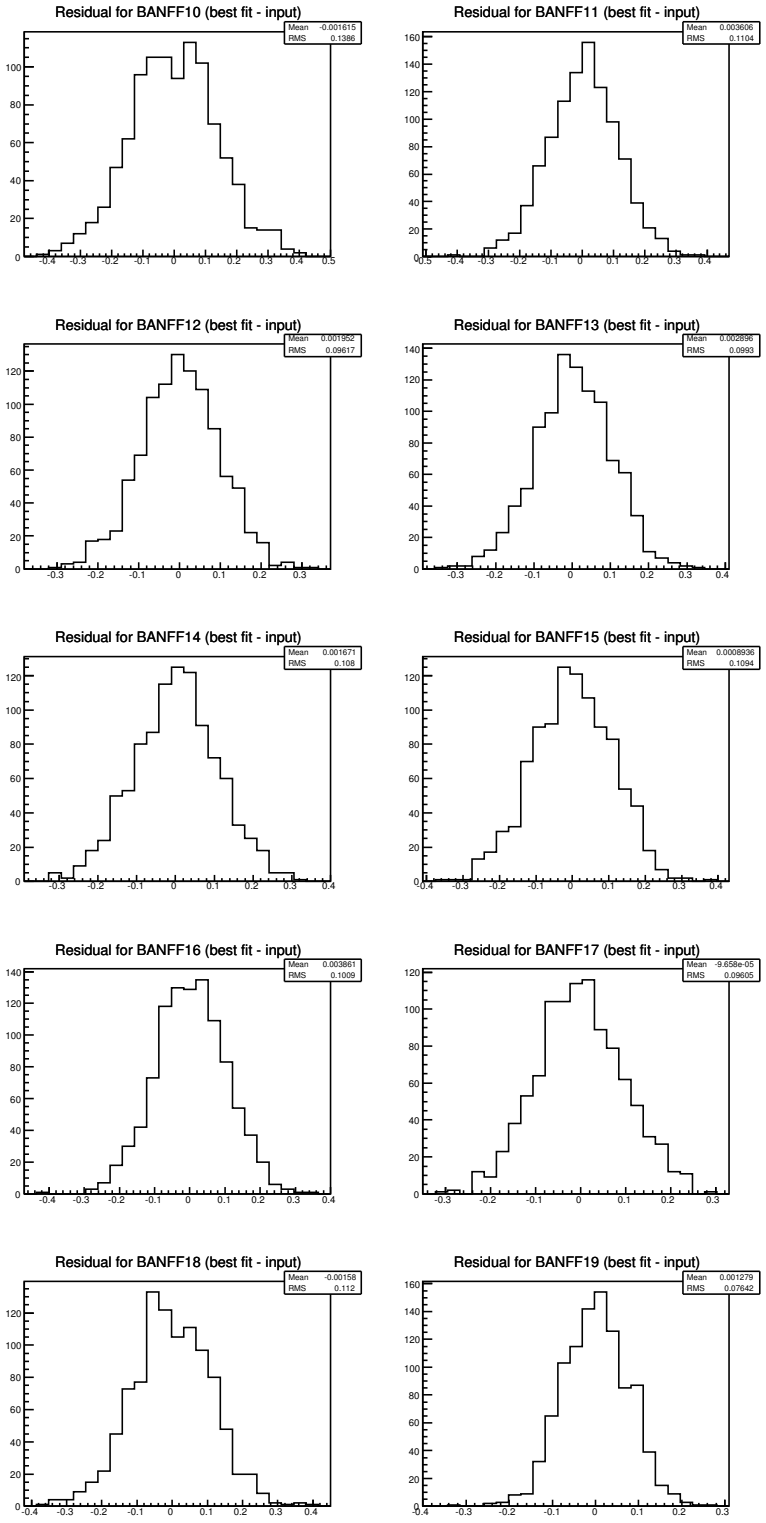

Figure 79: Distribution of residuals of the BANFF (10-19) systematic parameters in the '4 + 83' fit for oscillation point # 0.

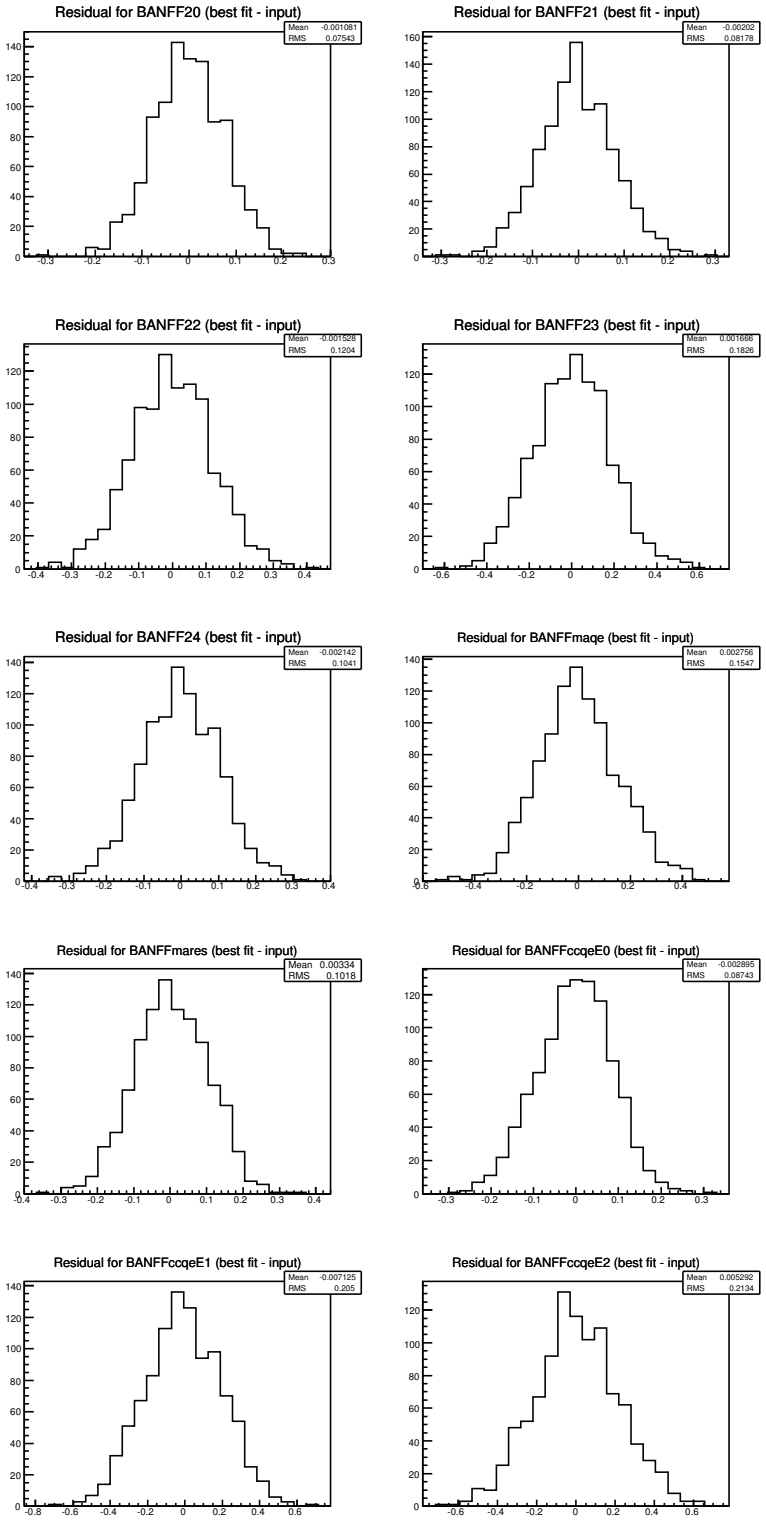

Figure 80: Distribution of residuals of the BANFF (20-29) systematic parameters in the '4 + 83' fit for oscillation point # 0.

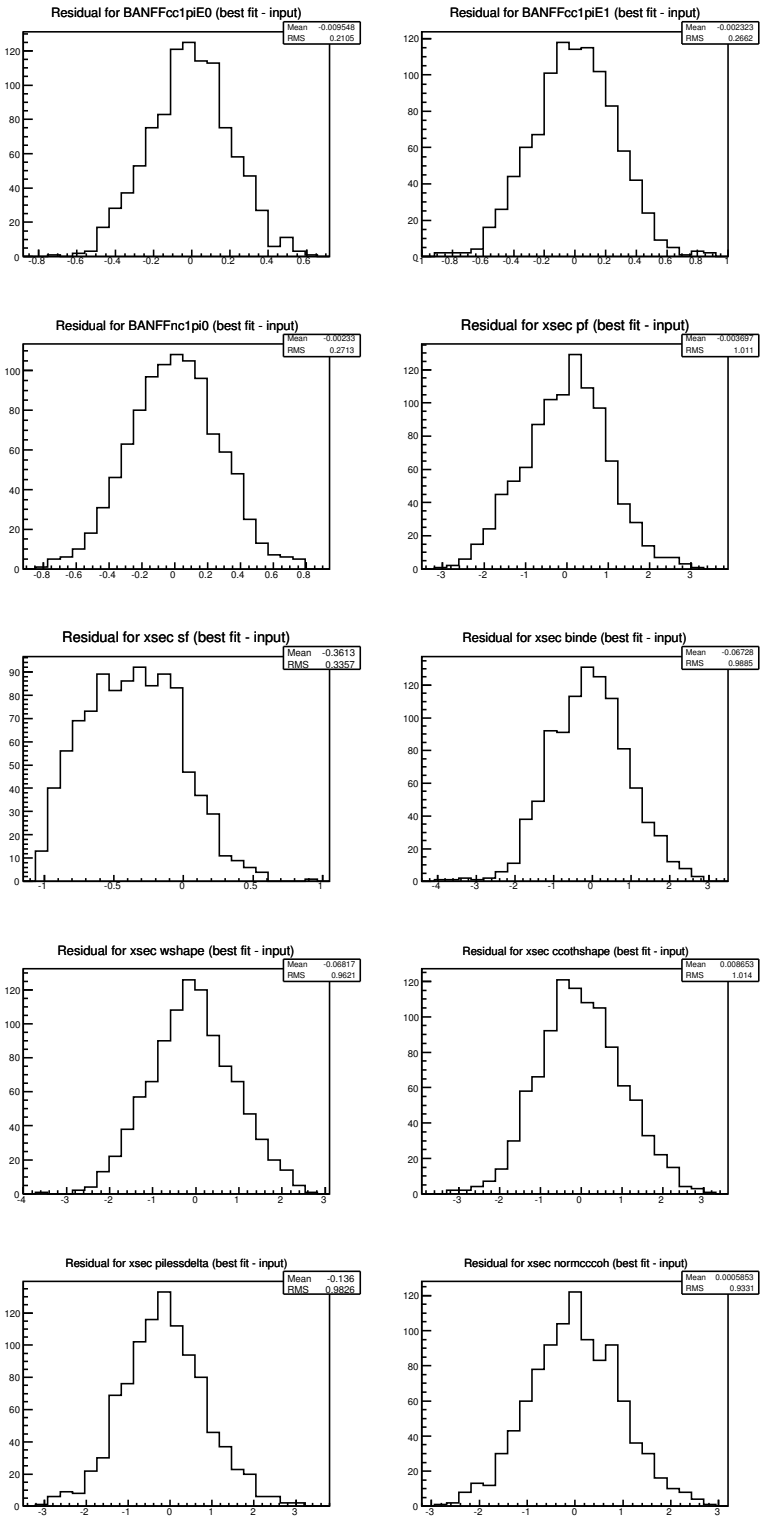

Figure 81: Distribution of residuals of the BANFF (30-32) and uncorrelated cross sections (I) systematic parameters in the '4 + 83' fit for oscillation point # 0.

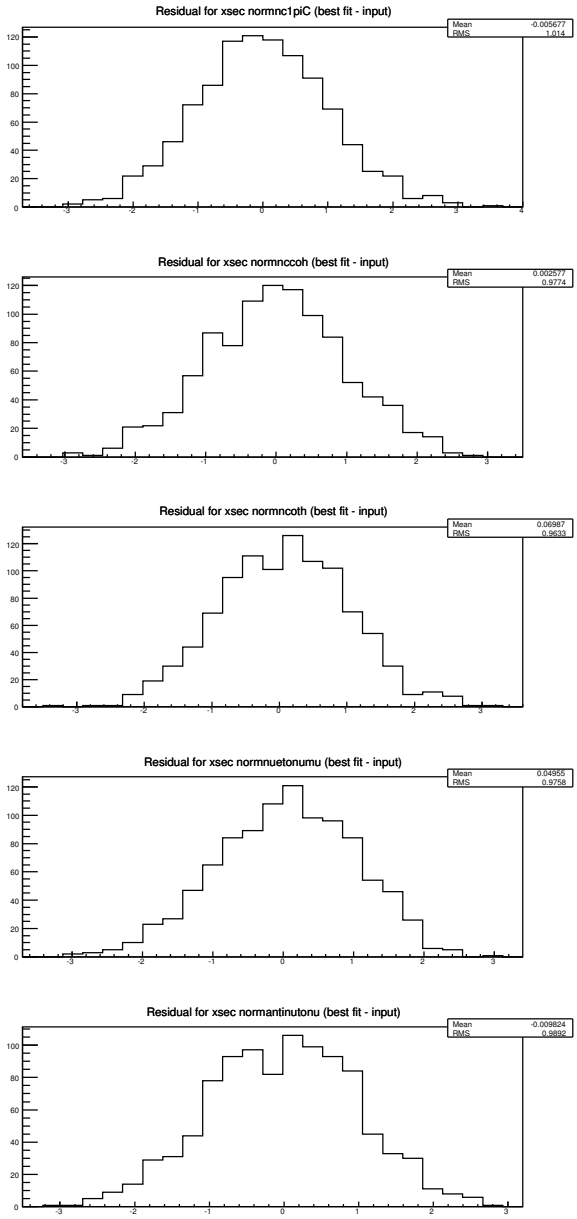

Figure 82: Distribution of residuals of uncorrelated cross sections (II) systematic parameters in the '4 + 83' fit for oscillation point # 0.

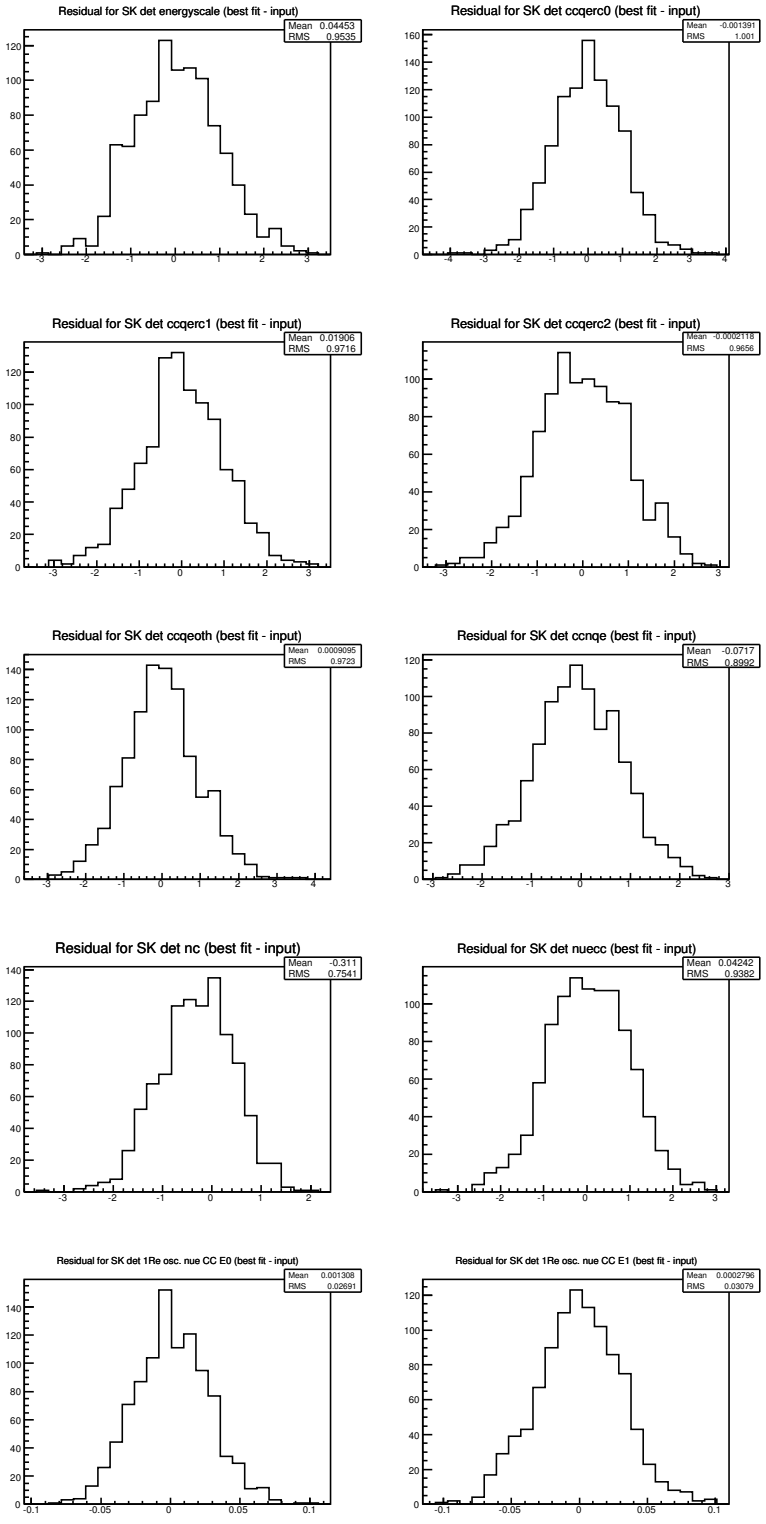

Figure 83: Distribution of residuals of SK detector (I) systematic parameters in the '4 + 83' fit for oscillation point # 0.

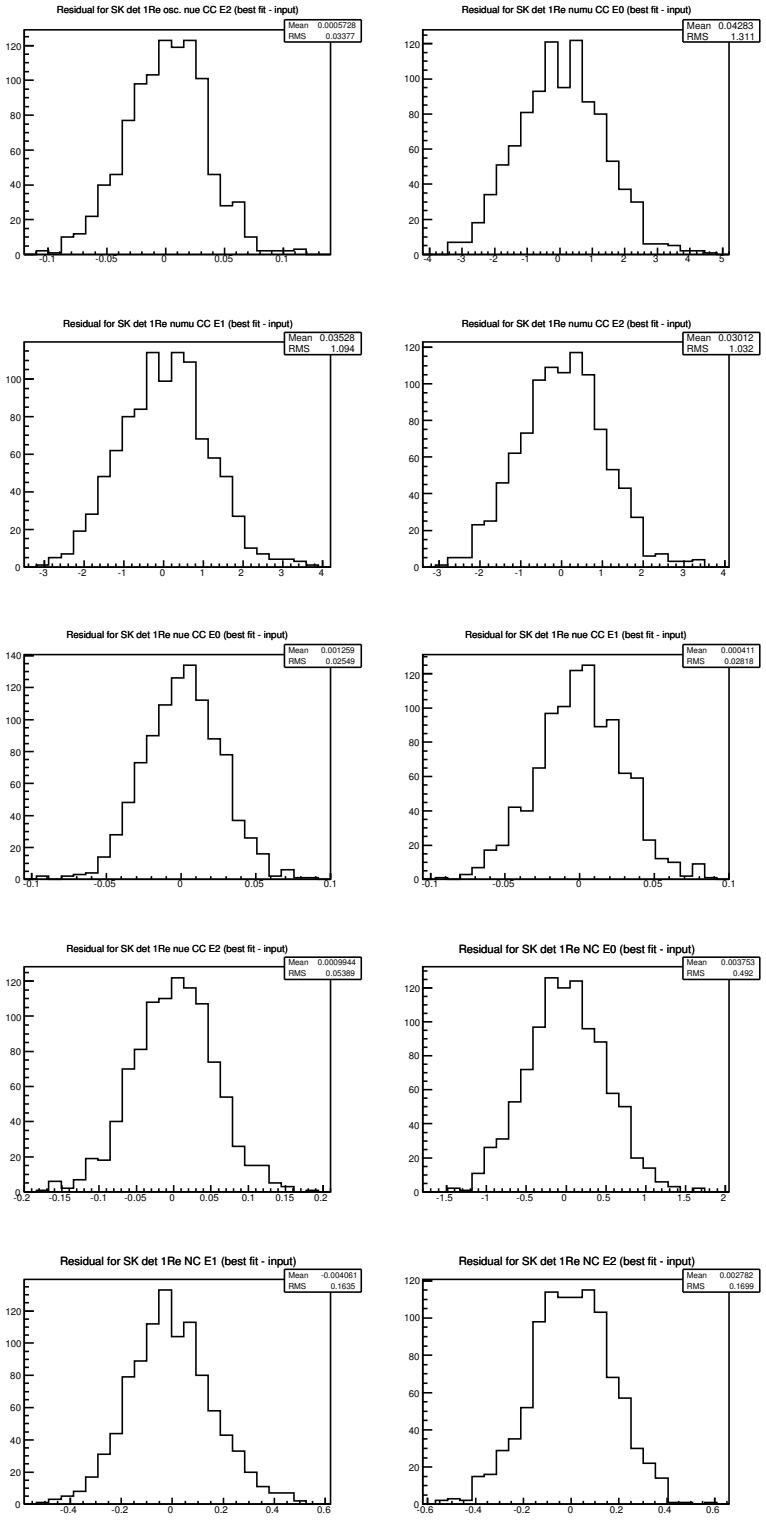

Figure 84: Distribution of residuals of SK detector (II) systematic parameters in the '4 + 83' fit for oscillation point # 0.

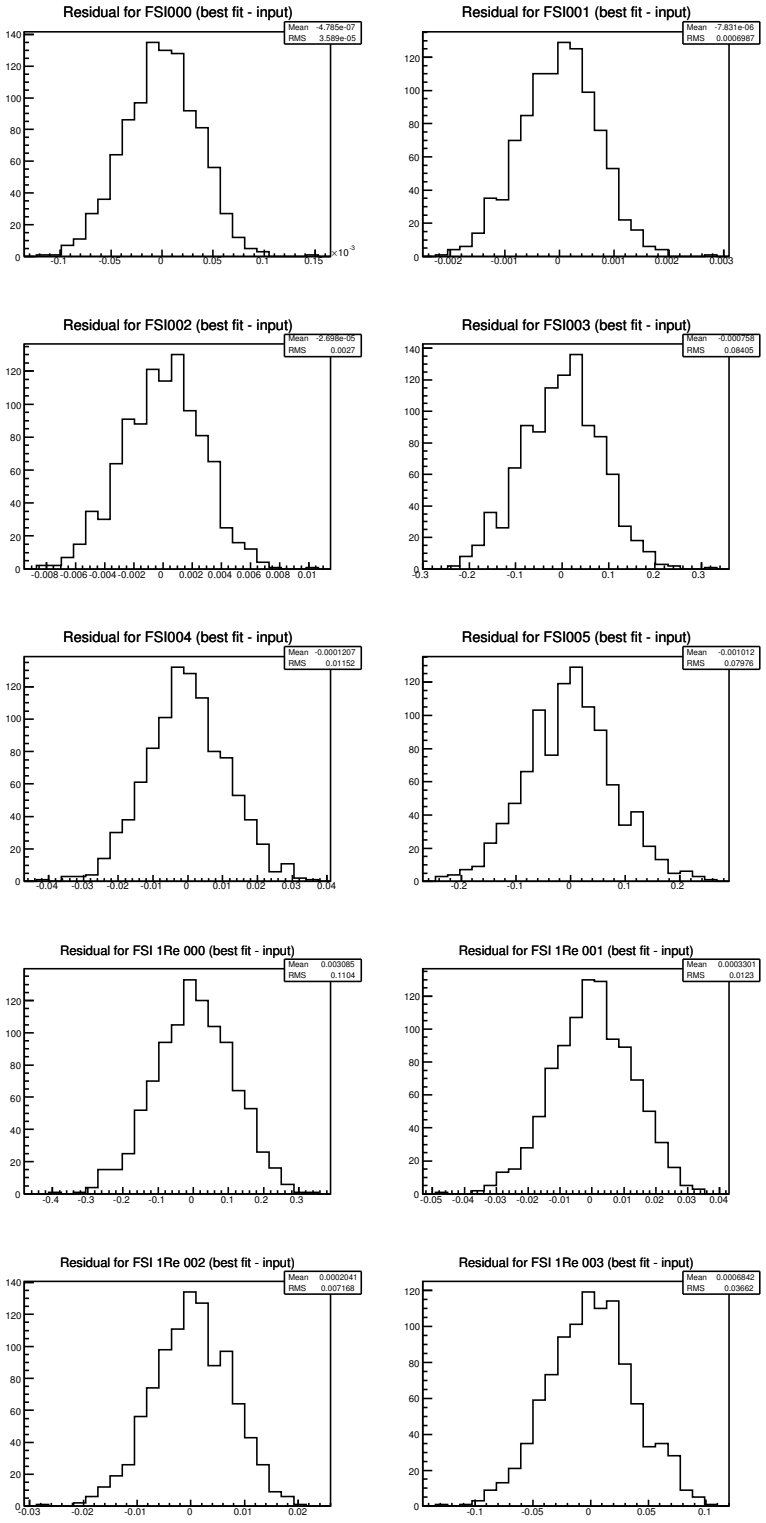

Figure 85: Distribution of residuals of FSI+SI (I) systematic parameters in the '4 + 83' fit for oscillation point # 0.

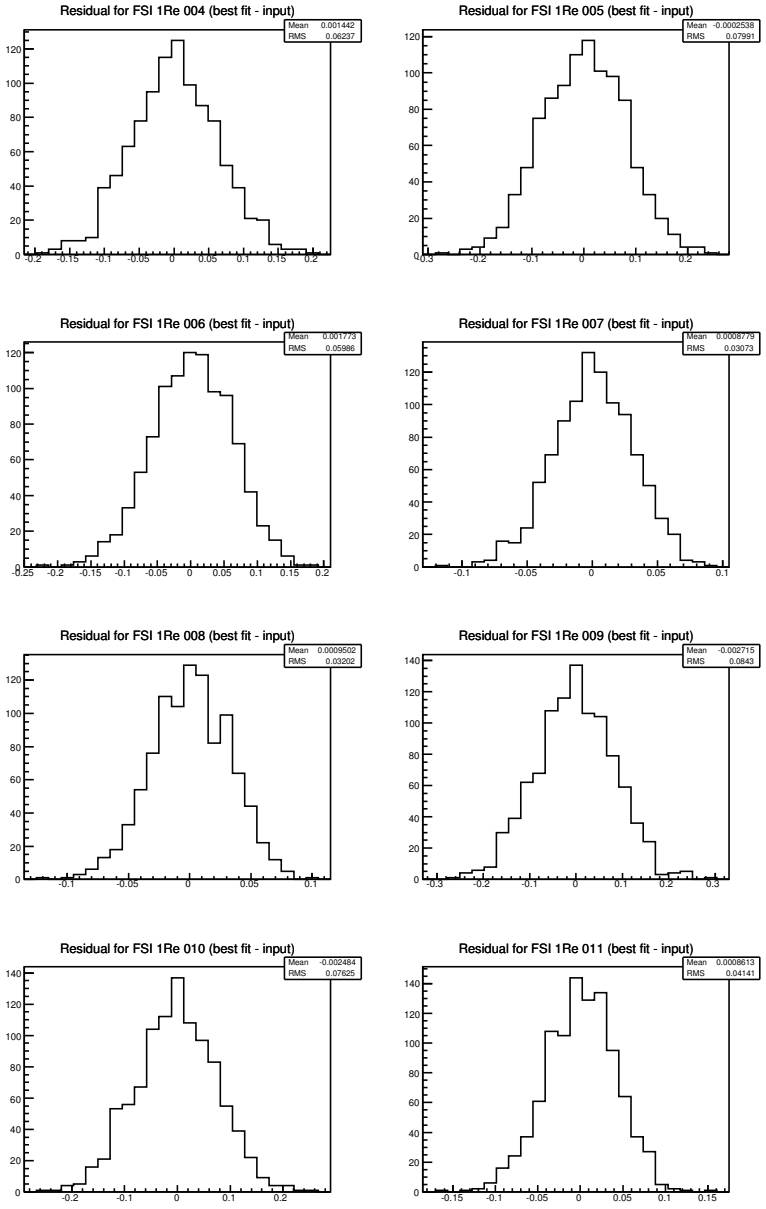

Figure 86: Distribution of residuals of FSI+SI (I) systematic parameters in the '4 + 83' fit for oscillation point # 0.

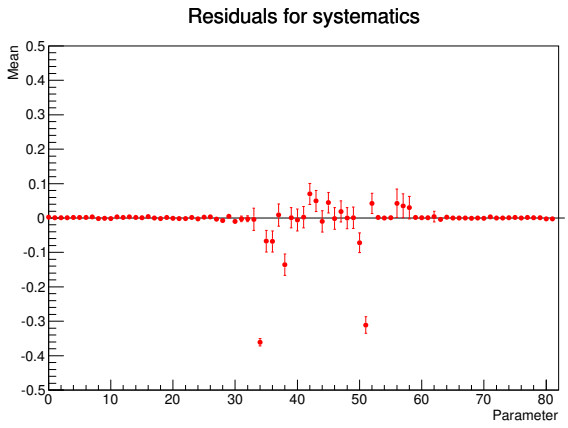

Figure 87: Summary of distribution of residuals of systematic parameters in the '4 + 83' fit for oscillation point # 0.

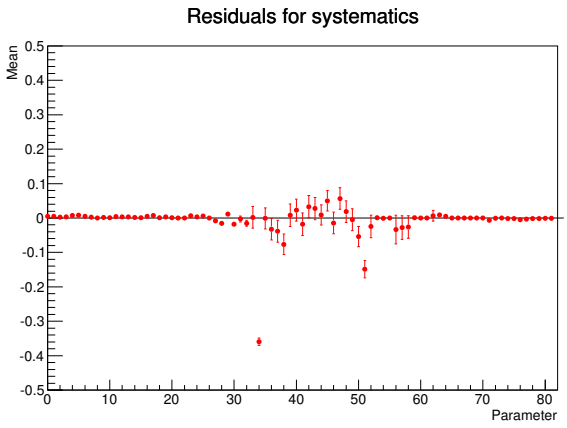

Figure 88: Summary of distribution of residuals of systematic parameters in the '4 + 83' fit for oscillation point # 1.

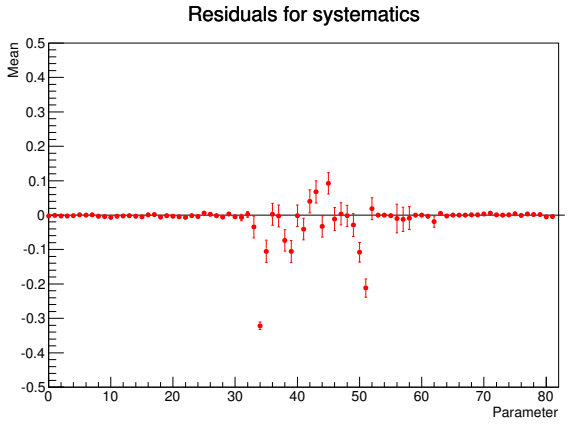

Figure 89: Summary of distribution of residuals of systematic parameters in the '4 + 83' fit for oscillation point # 2.

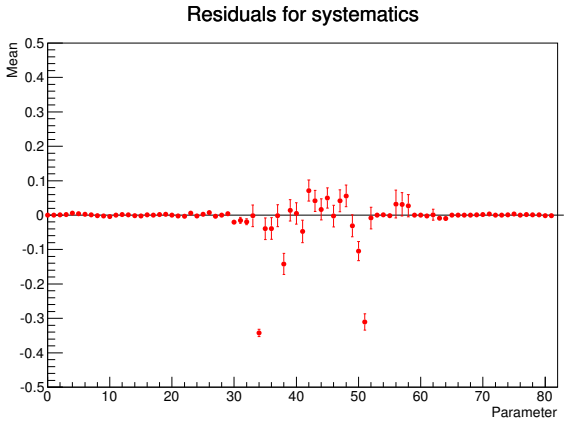

Figure 90: Summary of distribution of residuals of systematic parameters in the '4 + 83' fit for oscillation point # 3.

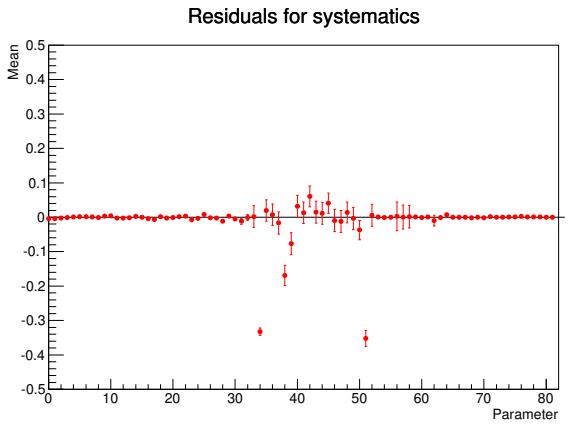

Figure 91: Summary of distribution of residuals of systematic parameters in the '4 + 83' fit for oscillation point # 4.

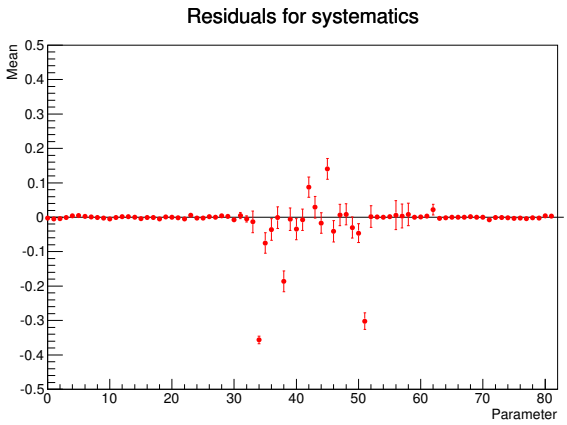

Figure 92: Summary of distribution of residuals of systematic parameters in the '4 + 83' fit for oscillation point # 5.

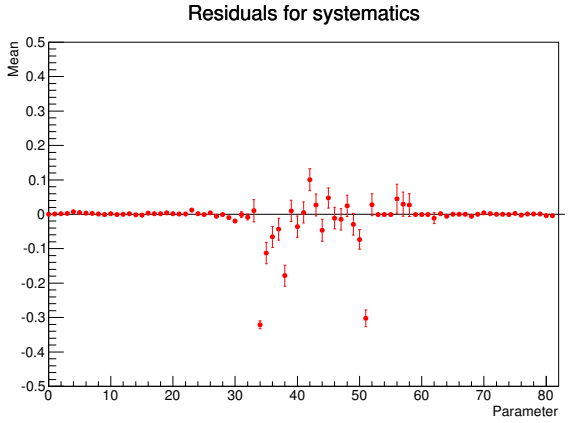

Figure 93: Summary of distribution of residuals of systematic parameters in the '4 + 83' fit for oscillation point # 6.

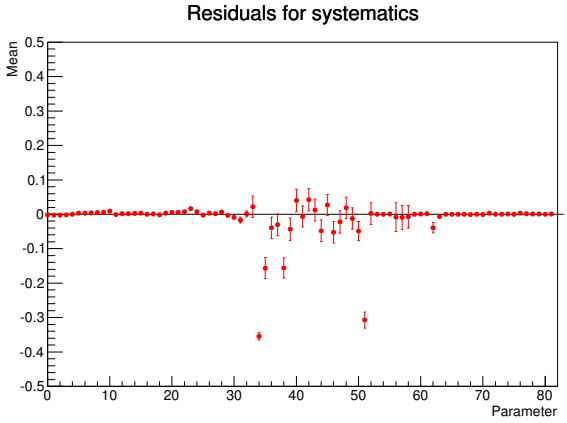

Figure 94: Summary of distribution of residuals of systematic parameters in the '4 + 83' fit for oscillation point # 7.

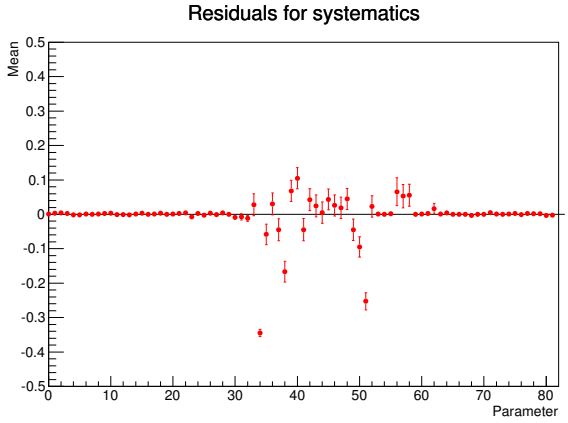

Figure 95: Summary of distribution of residuals of systematic parameters in the '4 + 83' fit for oscillation point # 8.

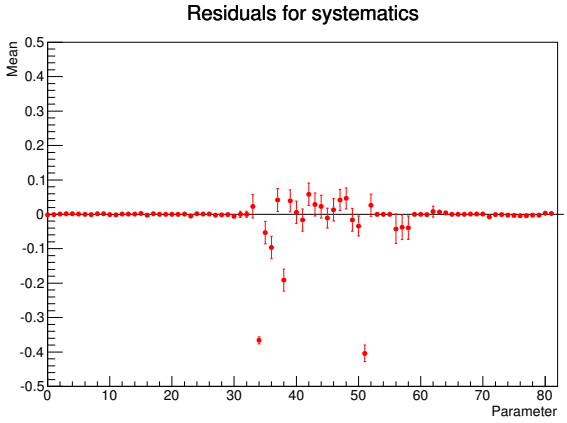

Figure 96: Summary of distribution of residuals of systematic parameters in the '4 + 83' fit for oscillation point # 9.

C. 3.010×10^{20} POT fake dataset fits

In order to validate the joint 3-flavour analysis, fake single μ-like ring and single e-like ring datasets were created for an equivalent exposure of 3.010×10^{20} POT. Two different studies were done: 1) using data sets without statistical fluctuations and 2) using datasets with statistical fluctuations. For each of these datasets, the true oscillation parameters, mass hierarchy, systematic variations and the generated numbers of single μ-like ring and single e-like ring events are shown in Tab. 19 for datasets with no statistical fluctuations and in Tab. 20 for datasets with statistical fluctuations. Each of these datasets was fitted three times: 1) using the *VaLOR* joint 3-flavour oscillation analysis, 2) with the *VaLOR* stand-alone ν_e appearance analysis and 3) with the *VaLOR* stand-alone ν_μ-disappearance analysis. The best-fit values of the oscillation parameters for those fits are also given in Tables 19 and 20, along with the goodness-of-fit and the number of single μ-like ring and single e-like ring events computed from the best-fit spectra. The corresponding figures are 97-144 for fake data sets with no statistical fluctuations and 145-161 for fake data sets with statistical fluctuations.

The profile $\Delta\chi^2$ distribution is also presented for the fit of each fake dataset as a function of each of the oscillation parameters $|\Delta m^2|$, $\sin^2\theta_{23}$, $\sin^2\theta_{13}$ and δ_{CP}. In addition, the 68% and 90% CL regions are given in the following four 2-dimensional oscillation parameter spaces: ($\sin^2\theta_{23}$, $|\Delta m^2|$), ($\sin^2\theta_{13}$, $|\Delta m^2|$), ($\sin^2\theta_{13}$, δ_{CP}) and ($\sin^2\theta_{23}$, $\sin^2\theta_{13}$).

In all profile $\Delta\chi^2$ and confidence region plots shown for the joint 3-flavour analysis, the value of χ^2 was minimized with respect to all 83 nuisance parameters and the oscillation parameters from $|\Delta m^2|$, $\sin^2\theta_{23}$, $\sin^2\theta_{13}$ and δ_{CP} not shown on the plot (as explained in App. F, $\sin^2\theta_{12}$ and δm^2 have a negligible effect and they are fixed to 0.311 and 7.5×10^{-5} eV^2/c^4 respectively for all the joint and stand-alone ν_e-appearance and ν_μ-disappearance analyses). In the profile $\Delta\chi^2$ and confidence region plots shown for the stand-alone ν_e appearance analysis, $\sin^2\theta_{23}$ and $|\Delta m^2|$ are also fixed to 0.5 and 2.4×10^{-3} eV^2/c^4 respectively, and the χ^2 was minimized with respect to $\sin^2\theta_{13}$, δ_{CP} and all 69 nuisance parameters relevant for that analysis. Similarly, for ν_μ disappearance, $\sin^2\theta_{13}$ and δ_{CP} are fixed to 0.025 and 0 respectively, and the χ^2 was minimized with respect to $\sin^2\theta_{23}$, $|\Delta m^2|$ and all 57 nuisance parameters relevant to that analysis. These fixed values of the oscillation parameters are the same as those used in the T2K published results.

Confidence regions are found with respect to a χ^2 global minimum reported in Tab. 19 or in Tab. 20 (except for the stand-alone ν_e appearance result in ($\sin^2\theta_{13}$, δ_{CP}) space where the raster scan was used) using the constant-$\Delta\chi^2$ method (see Section 6).

The following color scheme is used for all plots:

- green $\rightarrow$ true,
- black $\rightarrow$ *VaLOR* joint 3-flavour oscillation analysis,
- red $\rightarrow$ *VaLOR* stand-alone ν_e appearance analysis, and
- blue $\rightarrow$ *VaLOR* stand-alone ν_μ disappearance analysis.

From the results of the joint oscillation analysis in these fake dataset fits the following conclusions can be extracted:

1. The results show in general a good recovery of the true input value of the oscillation parameters at the best fit point.
2. There is no sensitivity to δ_{CP} at current POT as can be observed for instance in Fig. 100.
3. As expected, when a best fit value of δ_{CP} is different to the true one, this can cause, due to their intrinsic degeneracy, a bias in the best fit value of $sin^2\theta_{13}$. This bias in $sin^2\theta_{13}$ translates, in turn, into a bias in $sin^2\theta_{23}$.
4. Other interesting confidence regions in oscillation parameter spaces different to the usual ones, ($\sin^2\theta_{13}$, $|\Delta m^2|$) and ($\sin^2\theta_{23}$, $\sin^2\theta_{13}$), can be studied with satisfactory results when using the joint oscillation analysis.
5. In this work, the difference in the confidence regions for the disappearance oscillation parameters ($\sin^2\theta_{23}$, $|\Delta m^2|$) with different mass hierarchies was studied for the first time (compare Fig. 101 with Fig. 141).
6. Using the joint oscillation analysis it is also possible to investigate the octant degeneracy in $\sin^2\theta_{23}$ as the single e-like ring sample has been added (see for instance Figs. 106, 109 and 112) .

Comparing the results of stand-alone analyses with the ones for the joint analysis:

1. A larger uncertainty is found for $\sin^2\theta_{13}$ with the joint analysis (wider χ^2 profiles in Figs. 99, 107, 115, 123, 131 and 139) because its correlations with $\sin^2\theta_{23}$ and δ_{CP} are taken into account.
2. For the stand-alone appearance analysis, biases appear in the best-fit value of $\sin^2\theta_{13}$ when the value of $\sin^2\theta_{23}$ or δ_{CP} does not correspond to the value assumed as prior (typically $\sin^2\theta_{23}$=0.5 and δ_{CP}=0), as shown in Table 19 for sets #1 and #3. Fitting them in the joint analysis solves this problem.
3. The confidence regions in the 2-dimensional oscillation parameter spaces obtained with the joint analysis are comparable in size with the ones obtained with stand-alone analyses, because despite the fact that more parameters are included in the fit, this is compensated by the extra information added when working simultaneously with the single μ-like ring and single e-like ring samples.

Set	Fit	$\lvert\Delta m^2\rvert$ ($\times 10^{-3}$ eV^2/c^4)	$\sin^2\theta_{23}$	$\sin^2\theta_{13}$	δ_{CP}	MH	$N_{SK}^{1R\mu}$	N_{SK}^{1Re}	Figures
0	true	**2.36**	**0.5**	**0.025**	**0.0**	**Normal**	**59.745**	**10.981**	
	fit (joint)	2.361	0.500	0.023	-0.279	(fixed)	59.742	10.975	97 - 104
	fit (ν_e app.)	–	–	0.025	0(fixed)		–	10.982	
	fit (ν_μ disapp.)	2.361	0.497	–	–		59.759	–	
1	true	**2.36**	**0.38**	**0.025**	**0.0**	**Normal**	**69.475**	**9.199**	
	fit (joint)	2.360	0.380	0.025	0.014	(fixed)	69.474	9.202	105 - 112
	fit (ν_e app.)	–	–	0.019	0(fixed)		–	9.200	
	fit (ν_μ disapp.)	2.360	0.380	–	–		69.471	–	
2	true	**2.36**	**0.5**	**0.015**	**0.0**	**Normal**	**59.688**	**7.993**	
	fit (joint)	2.360	0.506	0.017	0.322	(fixed)	59.676	7.997	113 - 120
	fit (ν_e app.)	–	–	0.015	0(fixed)		–	7.991	
	fit (ν_μ disapp.)	2.360	0.500	–	–		59.726	–	
3	true	**2.36**	**0.5**	**0.025**	$-\pi/2$	**Normal**	**60.006**	**12.838**	
	fit (joint)	2.360	0.529	0.024	-1.522	(fixed)	60.017	12.848	121 - 128
	fit (ν_e app.)	–	–	0.031	0(fixed)		–	12.860	
	fit (ν_μ disapp.)	2.349	0.497	–	–		60.018	–	
4	true	**2.2**	**0.5**	**0.025**	**0.0**	**Normal**	**64.195**	**10.956**	
	fit (joint)	2.200	0.527	0.024	0.076	(fixed)	64.188	10.955	129 - 136
	fit (ν_e app.)	–	–	0.025	0(fixed)		–	10.962	
	fit (ν_μ disapp.)	2.199	0.501	–	–		64.206	–	
5	true	**2.36**	**0.5**	**0.025**	**0.0**	**Inverted**	**59.577**	**9.559**	
	fit (joint)	2.359	0.496	0.022	-0.445	(fixed)	59.583	9.558	137 - 144
	fit (ν_e app.)	–	–	0.025	0(fixed)		–	9.560	
	fit (ν_μ disapp.)	2.361	0.496	–	–		59.593	–	

Table 19: True input values (shown in bold) and VALOR best-fit values for a test ensemble of 6 fake datasets with no statistical fluctuations.

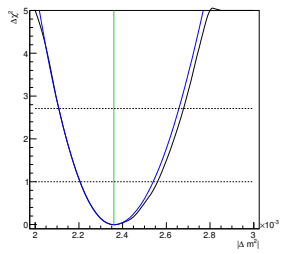

Figure 97: $\Delta\chi^2$ as function of $|\Delta m^2|$ for fake dataset #0. At each point, χ^2 was minimized with respect to $\sin^2\theta_{23}$, $\sin^2\theta_{13}$, δ_{CP} and all relevant nuisance parameters for the joint analysis (black) and with respect to $\sin^2\theta_{23}$ and all relevant nuisance parameters for the disappearance analysis (blue).

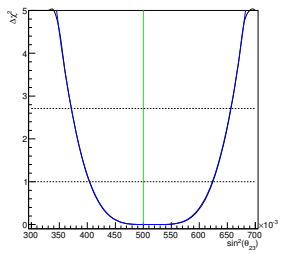

Figure 98: $\Delta\chi^2$ as function of $sin^2\theta_{23}$ for fake dataset #0. At each point, χ^2 was minimized with respect to $|\Delta m^2|$, $\sin^2\theta_{13}$, δ_{CP} and all relevant nuisance parameters for the joint analysis (black) and with respect to $\sin^2\theta_{23}$ and all relevant nuisance parameters for the disappearance analysis (blue).

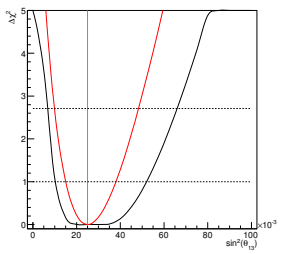

Figure 99: $\Delta\chi^2$ as function of $sin^2\theta_{13}$ for fake dataset #0. At each point, χ^2 was minimized with respect to $\sin^2\theta_{23}$, $\sin^2\theta_{13}$, δ_{CP} and all relevant nuisance parameters for the joint analysis (black) and with respect to all relevant nuisance parameters (δ_{CP} is fixed to 0) for the appearance analysis (red).

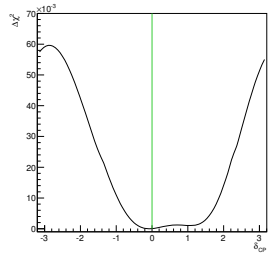

Figure 100: $\Delta\chi^2$ as function of δ_{CP} for fake dataset #0. At each point, χ^2 was minimized with respect to all oscillation parameters not shown (and not considered to be fixed) and all relevant nuisance parameters.

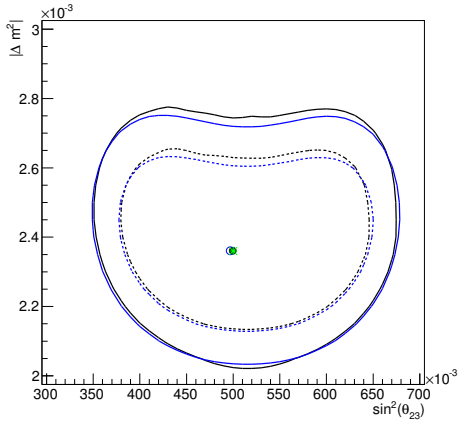

Figure 101: 68% and 90% CL regions in ($sin^2\theta_{23}$, $|\Delta m^2|$) space for fake dataset #0. At each point, χ^2 was minimized with respect to $\sin^2\theta_{13}$, δ_{CP} and all relevant nuisance parameters for the joint analysis (black) and with respect to all relevant nuisance parameters for the disappearance analysis (blue).

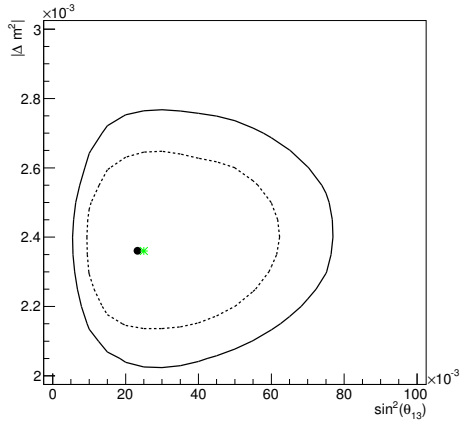

Figure 102: 68% and 90% CL regions in ($sin^2\theta_{13}$, $|\Delta m^2|$) space for fake dataset #0. At each point, χ^2 was minimized with respect to all oscillation parameters not shown (and not considered to be fixed) and all relevant nuisance parameters.

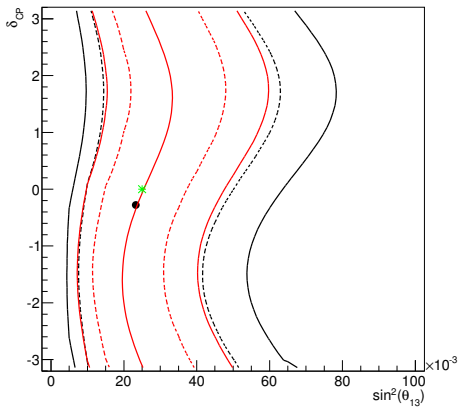

Figure 103: 68% and 90% CL regions in ($sin^2\theta_{13}$, δ_{CP}) space for fake dataset #0. At each point, χ^2 was minimized with respect to $|\Delta m^2|$, $\sin^2\theta_{23}$ and all relevant nuisance parameters for the joint analysis (black) and with respect to all relevant nuisance parameters for the appearance analysis (red). Notice that different methods are used to construct confidence regions for the joint analysis (global minimum) and for the stand-alone appearance analysis (raster scan).

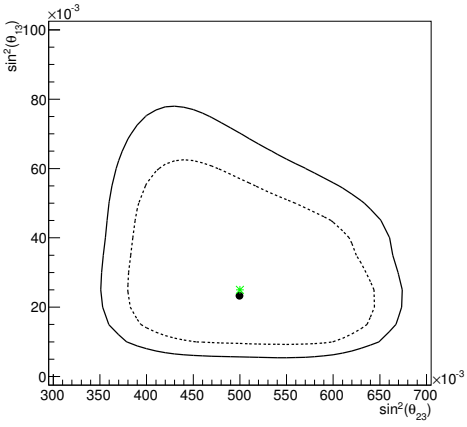

Figure 104: 68% and 90% CL regions in ($sin^2\theta_{23}$, $sin^2\theta_{13}$) space for fake dataset #0. At each point, χ^2 was minimized with respect to all oscillation parameters not shown (and not considered to be fixed) and all relevant nuisance parameters.

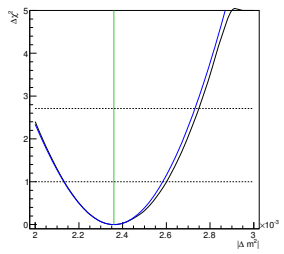

Figure 105: $\Delta\chi^2$ as function of $|\Delta m^2|$ for fake dataset #1. At each point, χ^2 was minimized with respect to $\sin^2\theta_{23}$, $\sin^2\theta_{13}$, δ_{CP} and all relevant nuisance parameters for the joint analysis (black) and with respect to $\sin^2\theta_{23}$ and all relevant nuisance parameters for the disappearance analysis (blue).

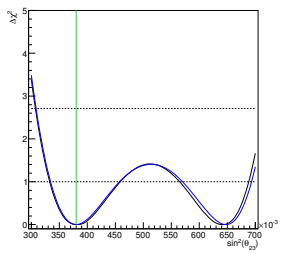

Figure 106: $\Delta\chi^2$ as function of $sin^2\theta_{23}$ for fake dataset #1. At each point, χ^2 was minimized with respect to $|\Delta m^2|$, $\sin^2\theta_{13}$, δ_{CP} and all relevant nuisance parameters for the joint analysis (black) and with respect to $\sin^2\theta_{23}$ and all relevant nuisance parameters for the disappearance analysis (blue).

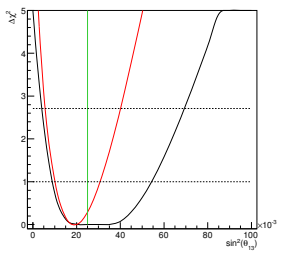

Figure 107: $\Delta\chi^2$ as function of $sin^2\theta_{13}$ for fake dataset #1. At each point, χ^2 was minimized with respect to $\sin^2\theta_{23}$, $\sin^2\theta_{13}$, δ_{CP} and all relevant nuisance parameters for the joint analysis (black) and with respect to all relevant nuisance parameters (δ_{CP} is fixed to 0) for the appearance analysis (red).

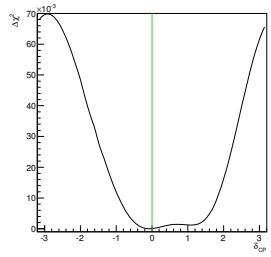

Figure 108: $\Delta\chi^2$ as function of δ_{CP} for fake dataset #1. At each point, χ^2 was minimized with respect to all oscillation parameters not shown (and not considered to be fixed) and all relevant nuisance parameters.

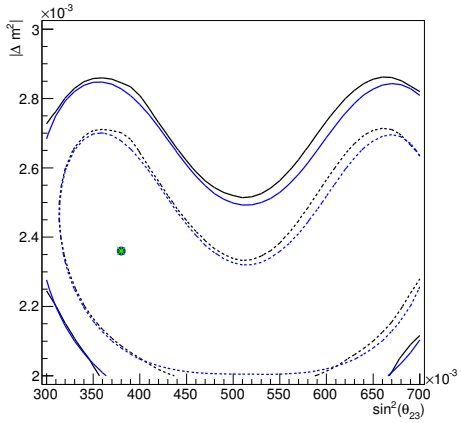

Figure 109: 68% and 90% CL regions in ($sin^2\theta_{23}$, $|\Delta m^2|$) space for fake dataset #1. At each point, χ^2 was minimized with respect to $\sin^2\theta_{13}$, δ_{CP} and all relevant nuisance parameters for the joint analysis (black) and with respect to all relevant nuisance parameters for the disappearance analysis (blue).

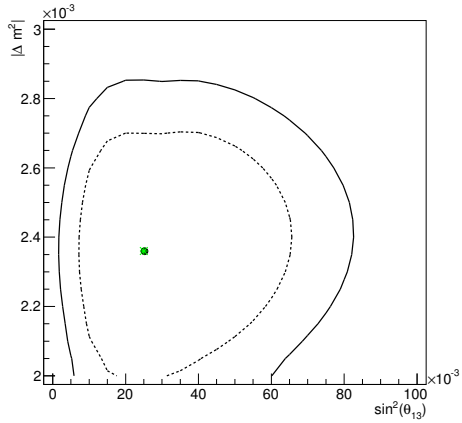

Figure 110: 68% and 90% CL regions in ($sin^2\theta_{13}$, $|\Delta m^2|$) space for fake dataset #1. At each point, χ^2 was minimized with respect to all oscillation parameters not shown (and not considered to be fixed) and all relevant nuisance parameters.

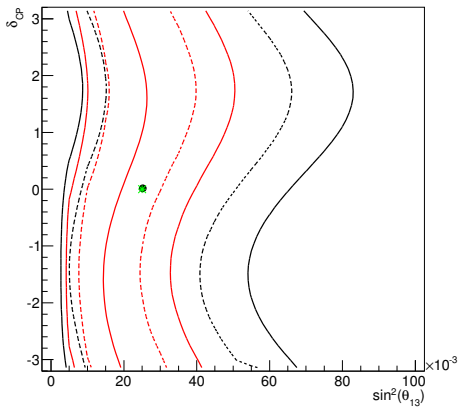

Figure 111: 68% and 90% CL regions in ($sin^2\theta_{13}$, δ_{CP}) space for fake dataset #1. At each point, χ^2 was minimized with respect to $|\Delta m^2|$, $\sin^2\theta_{23}$ and all relevant nuisance parameters for the joint analysis (black) and with respect to all relevant nuisance parameters for the appearance analysis (red). Notice that different methods are used to construct confidence regions for the joint analysis (global minimum) and for the stand-alone appearance analysis (raster scan).

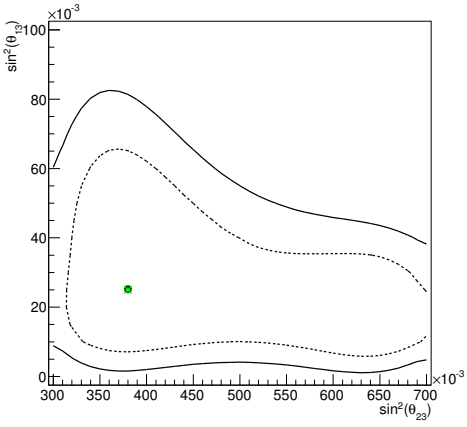

Figure 112: 68% and 90% CL regions in ($sin^2\theta_{23}$, $sin^2\theta_{13}$) space for fake dataset #1. At each point, χ^2 was minimized with respect to all oscillation parameters not shown (and not considered to be fixed) and all relevant nuisance parameters.

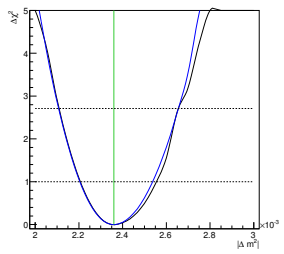

Figure 113: $\Delta\chi^2$ as function of $|\Delta m^2|$ for fake dataset #2. At each point, χ^2 was minimized with respect to $\sin^2\theta_{23}$, $\sin^2\theta_{13}$, δ_{CP} and all relevant nuisance parameters for the joint analysis (black) and with respect to $\sin^2\theta_{23}$ and all relevant nuisance parameters for the disappearance analysis (blue).

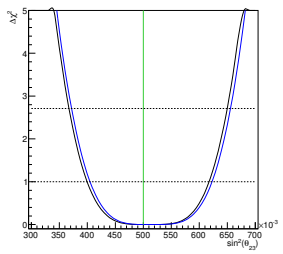

Figure 114: $\Delta\chi^2$ as function of $sin^2\theta_{23}$ for fake dataset #2. At each point, χ^2 was minimized with respect to $|\Delta m^2|$, $\sin^2\theta_{13}$, δ_{CP} and all relevant nuisance parameters for the joint analysis (black) and with respect to $\sin^2\theta_{23}$ and all relevant nuisance parameters for the disappearance analysis (blue).

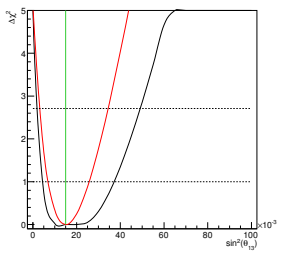

Figure 115: $\Delta\chi^2$ as function of $sin^2\theta_{13}$ for fake dataset #2. At each point, χ^2 was minimized with respect to $\sin^2\theta_{23}$, $\sin^2\theta_{13}$, δ_{CP} and all relevant nuisance parameters for the joint analysis (black) and with respect to all relevant nuisance parameters (δ_{CP} is fixed to 0) for the appearance analysis (red).

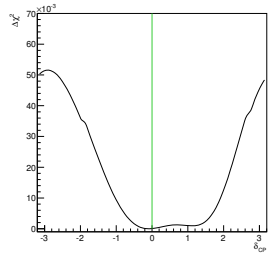

Figure 116: $\Delta\chi^2$ as function of δ_{CP} for fake dataset #2. At each point, χ^2 was minimized with respect to all oscillation parameters not shown (and not considered to be fixed) and all relevant nuisance parameters.

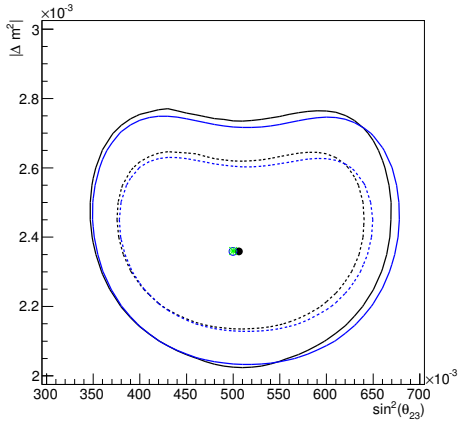

Figure 117: 68% and 90% CL regions in ($sin^2\theta_{23}$, $|\Delta m^2|$) space for fake dataset #2. At each point, χ^2 was minimized with respect to $\sin^2\theta_{13}$, δ_{CP} and all relevant nuisance parameters for the joint analysis (black) and with respect to all relevant nuisance parameters for the disappearance analysis (blue).

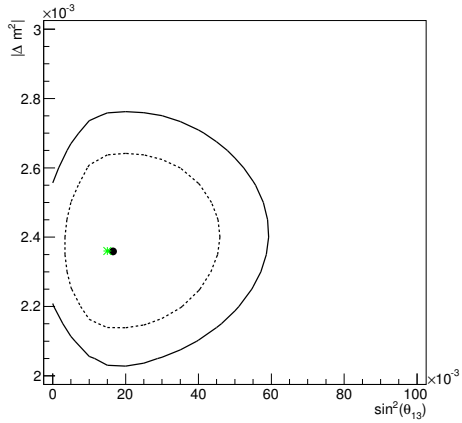

Figure 118: 68% and 90% CL regions in ($sin^2\theta_{13}$, $|\Delta m^2|$) space for fake dataset #2. At each point, χ^2 was minimized with respect to all oscillation parameters not shown (and not considered to be fixed) and all relevant nuisance parameters.

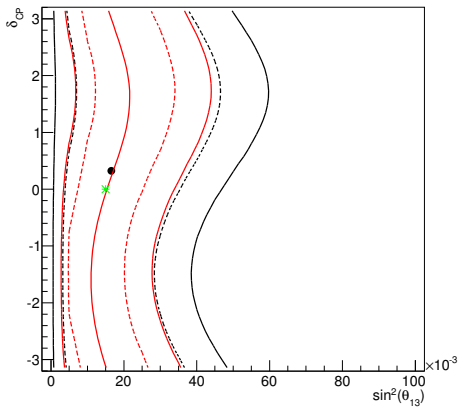

Figure 119: 68% and 90% CL regions in ($sin^2\theta_{13}$, δ_{CP}) space for fake dataset #2. At each point, χ^2 was minimized with respect to $|\Delta m^2|$, $\sin^2\theta_{23}$ and all relevant nuisance parameters for the joint analysis (black) and with respect to all relevant nuisance parameters for the appearance analysis (red). Notice that different methods are used to construct confidence regions for the joint analysis (global minimum) and for the stand-alone appearance analysis (raster scan).

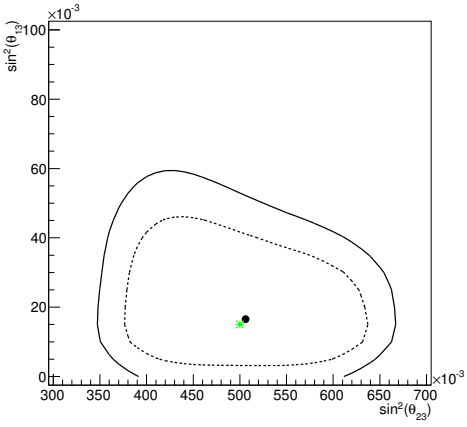

Figure 120: 68% and 90% CL regions in ($sin^2\theta_{23}$, $sin^2\theta_{13}$) space for fake dataset #2. At each point, χ^2 was minimized with respect to all oscillation parameters not shown (and not considered to be fixed) and all relevant nuisance parameters.

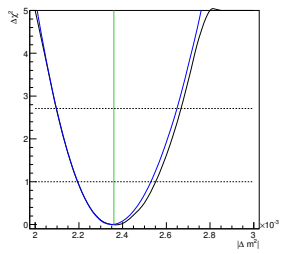

Figure 121: $\Delta\chi^2$ as function of $|\Delta m^2|$ for fake dataset #3. At each point, χ^2 was minimized with respect to $\sin^2\theta_{23}$, $\sin^2\theta_{13}$, δ_{CP} and all relevant nuisance parameters for the joint analysis (black) and with respect to $\sin^2\theta_{23}$ and all relevant nuisance parameters for the disappearance analysis (blue).

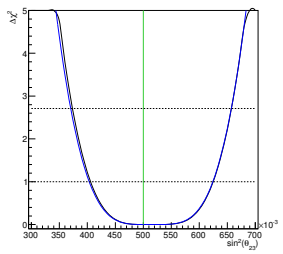

Figure 122: $\Delta\chi^2$ as function of $sin^2\theta_{23}$ for fake dataset #3. At each point, χ^2 was minimized with respect to $|\Delta m^2|$, $\sin^2\theta_{13}$, δ_{CP} and all relevant nuisance parameters for the joint analysis (black) and with respect to $\sin^2\theta_{23}$ and all relevant nuisance parameters for the disappearance analysis (blue).

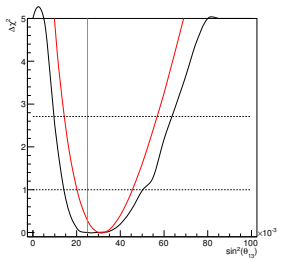

Figure 123: $\Delta\chi^2$ as function of $sin^2\theta_{13}$ for fake dataset #3. At each point, χ^2 was minimized with respect to $\sin^2\theta_{23}$, $\sin^2\theta_{13}$, δ_{CP} and all relevant nuisance parameters for the joint analysis (black) and with respect to all relevant nuisance parameters (δ_{CP} is fixed to 0) for the appearance analysis (red).

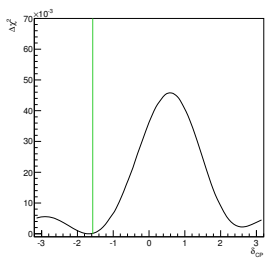

Figure 124: $\Delta\chi^2$ as function of δ_{CP} for fake dataset #3. At each point, χ^2 was minimized with respect to all oscillation parameters not shown (and not considered to be fixed) and all relevant nuisance parameters.

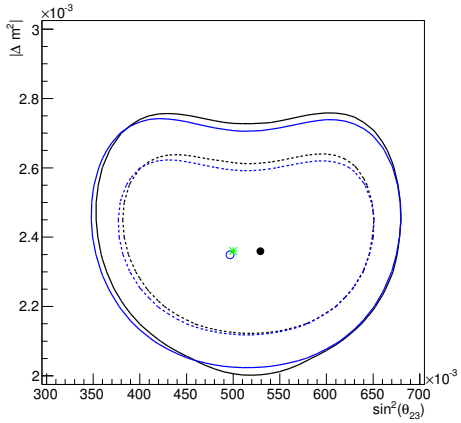

Figure 125: 68% and 90% CL regions in ($sin^2\theta_{23}$, $|\Delta m^2|$) space for fake dataset #3. At each point, χ^2 was minimized with respect to $\sin^2\theta_{13}$, δ_{CP} and all relevant nuisance parameters for the joint analysis (black) and with respect to all relevant nuisance parameters for the disappearance analysis (blue).

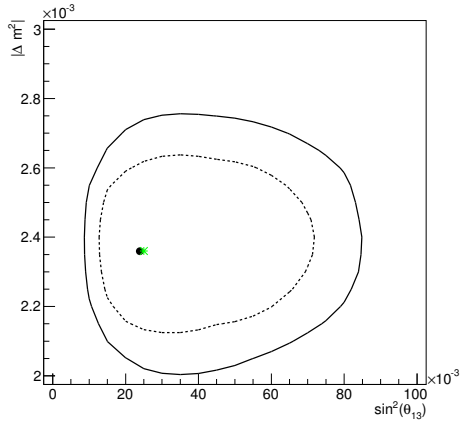

Figure 126: 68% and 90% CL regions in ($sin^2\theta_{13}$, $|\Delta m^2|$) space for fake dataset #3. At each point, χ^2 was minimized with respect to all oscillation parameters not shown (and not considered to be fixed) and all relevant nuisance parameters.

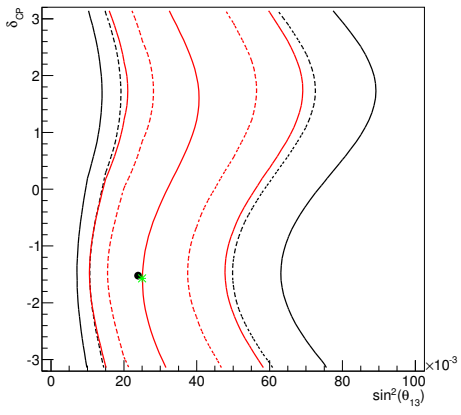

Figure 127: 68% and 90% CL regions in ($sin^2\theta_{13}$, δ_{CP}) space for fake dataset #3. At each point, χ^2 was minimized with respect to $|\Delta m^2|$, $\sin^2\theta_{23}$ and all relevant nuisance parameters for the joint analysis (black) and with respect to all relevant nuisance parameters for the appearance analysis (red). Notice that different methods are used to construct confidence regions for the joint analysis (global minimum) and for the stand-alone appearance analysis (raster scan).

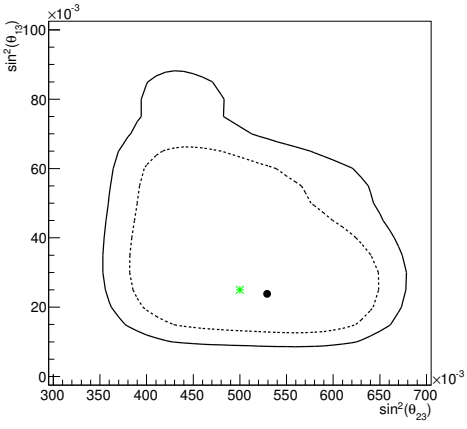

Figure 128: 68% and 90% CL regions in ($sin^2\theta_{23}$, $sin^2\theta_{13}$) space for fake dataset #3. At each point, χ^2 was minimized with respect to all oscillation parameters not shown (and not considered to be fixed) and all relevant nuisance parameters.

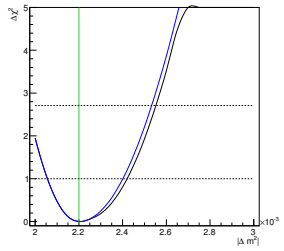

Figure 129: $\Delta\chi^2$ as function of $|\Delta m^2|$ for fake dataset #4. At each point, χ^2 was minimized with respect to $\sin^2\theta_{23}$, $\sin^2\theta_{13}$, δ_{CP} and all relevant nuisance parameters for the joint analysis (black) and with respect to $\sin^2\theta_{23}$ and all relevant nuisance parameters for the disappearance analysis (blue).

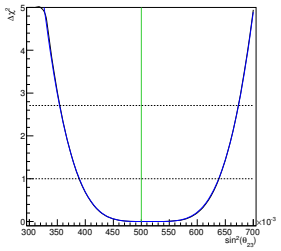

Figure 130: $\Delta\chi^2$ as function of $sin^2\theta_{23}$ for fake dataset #4. At each point, χ^2 was minimized with respect to $|\Delta m^2|$, $\sin^2\theta_{13}$, δ_{CP} and all relevant nuisance parameters for the joint analysis (black) and with respect to $\sin^2\theta_{23}$ and all relevant nuisance parameters for the disappearance analysis (blue).

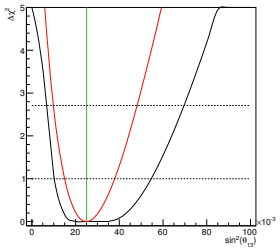

Figure 131: $\Delta\chi^2$ as function of $sin^2\theta_{13}$ for fake dataset #4. At each point, χ^2 was minimized with respect to $\sin^2\theta_{23}$, $\sin^2\theta_{13}$, δ_{CP} and all relevant nuisance parameters for the joint analysis (black) and with respect to all relevant nuisance parameters (δ_{CP} is fixed to 0) for the appearance analysis (red).

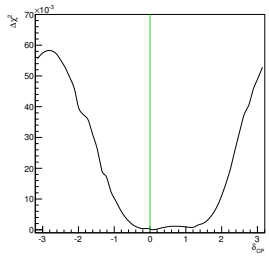

Figure 132: $\Delta\chi^2$ as function of δ_{CP} for fake dataset #4. At each point, χ^2 was minimized with respect to all oscillation parameters not shown (and not considered to be fixed) and all relevant nuisance parameters.

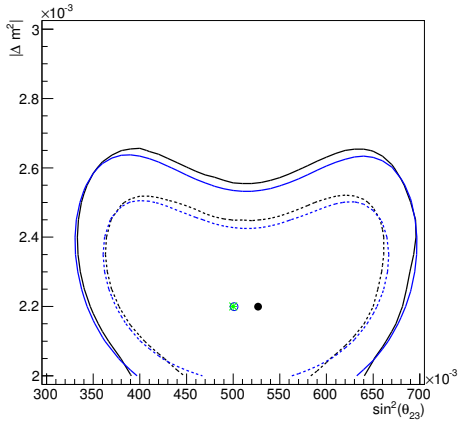

Figure 133: 68% and 90% CL regions in ($sin^2\theta_{23}$, $|\Delta m^2|$) space for fake dataset #4. At each point, χ^2 was minimized with respect to $\sin^2\theta_{13}$, δ_{CP} and all relevant nuisance parameters for the joint analysis (black) and with respect to all relevant nuisance parameters for the disappearance analysis (blue).

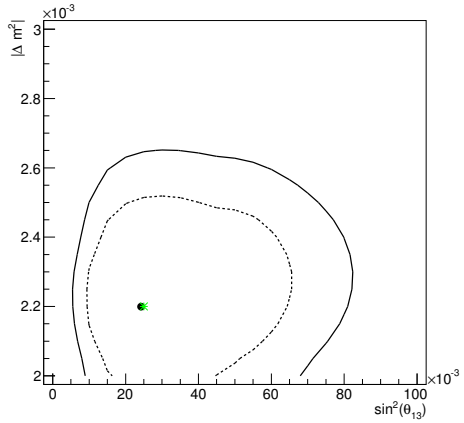

Figure 134: 68% and 90% CL regions in ($sin^2\theta_{13}$, $|\Delta m^2|$) space for fake dataset #4. At each point, χ^2 was minimized with respect to all oscillation parameters not shown (and not considered to be fixed) and all relevant nuisance parameters.

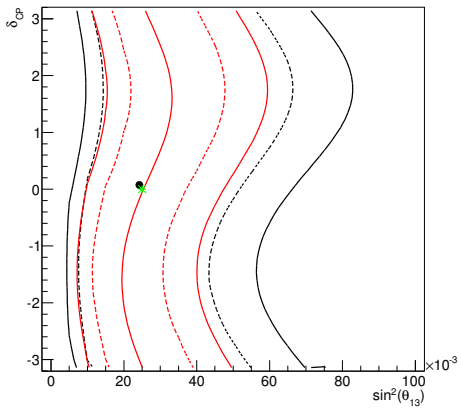

Figure 135: 68% and 90% CL regions in ($sin^2\theta_{13}$, δ_{CP}) space for fake dataset #4. At each point, χ^2 was minimized with respect to $|\Delta m^2|$, $\sin^2\theta_{23}$ and all relevant nuisance parameters for the joint analysis (black) and with respect to all relevant nuisance parameters for the appearance analysis (red). Notice that different methods are used to construct confidence regions for the joint analysis (global minimum) and for the stand-alone appearance analysis (raster scan).

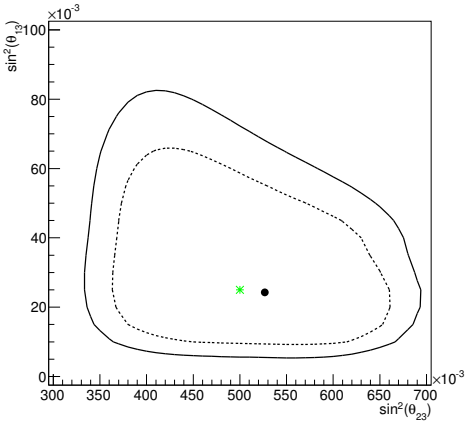

Figure 136: 68% and 90% CL regions in ($sin^2\theta_{23}$, $sin^2\theta_{13}$) space for fake dataset #4. At each point, χ^2 was minimized with respect to all oscillation parameters not shown (and not considered to be fixed) and all relevant nuisance parameters.

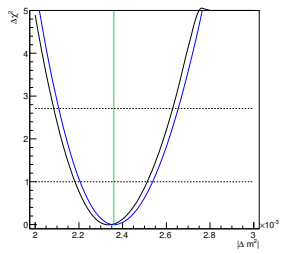

Figure 137: $\Delta\chi^2$ as function of $|\Delta m^2|$ for fake dataset #5. At each point, χ^2 was minimized with respect to $\sin^2\theta_{23}$, $\sin^2\theta_{13}$, δ_{CP} and all relevant nuisance parameters for the joint analysis (black) and with respect to $\sin^2\theta_{23}$ and all relevant nuisance parameters for the disappearance analysis (blue).

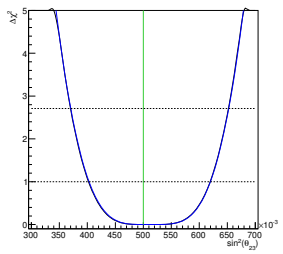

Figure 138: $\Delta\chi^2$ as function of $sin^2\theta_{23}$ for fake dataset #5. At each point, χ^2 was minimized with respect to $|\Delta m^2|$, $\sin^2\theta_{13}$, δ_{CP} and all relevant nuisance parameters for the joint analysis (black) and with respect to $\sin^2\theta_{23}$ and all relevant nuisance parameters for the disappearance analysis (blue).

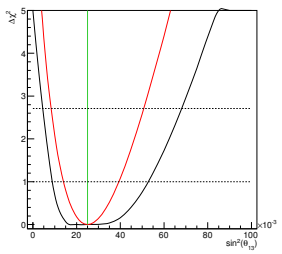

Figure 139: $\Delta\chi^2$ as function of $sin^2\theta_{13}$ for fake dataset #5. At each point, χ^2 was minimized with respect to $\sin^2\theta_{23}$, $\sin^2\theta_{13}$, δ_{CP} and all relevant nuisance parameters for the joint analysis (black) and with respect to all relevant nuisance parameters (δ_{CP} is fixed to 0) for the appearance analysis (red).

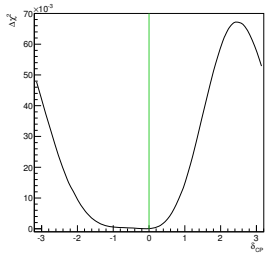

Figure 140: $\Delta\chi^2$ as function of δ_{CP} for fake dataset #5. At each point, χ^2 was minimized with respect to all oscillation parameters not shown (and not considered to be fixed) and all relevant nuisance parameters.

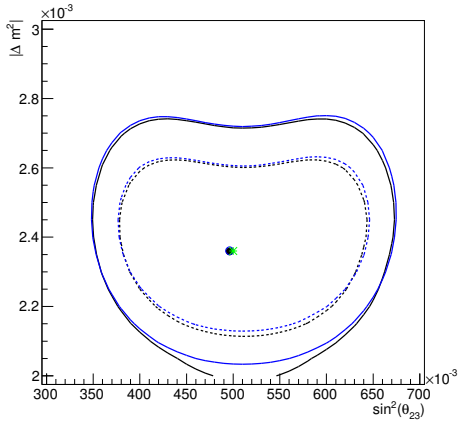

Figure 141: 68% and 90% CL regions in ($sin^2\theta_{23}$, $|\Delta m^2|$) space for fake dataset #5. At each point, χ^2 was minimized with respect to $\sin^2\theta_{13}$, δ_{CP} and all relevant nuisance parameters for the joint analysis (black) and with respect to all relevant nuisance parameters for the disappearance analysis (blue).

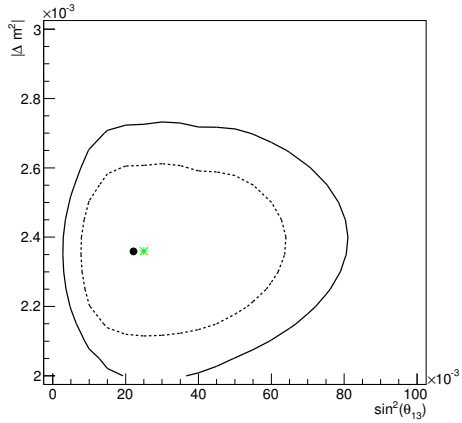

Figure 142: 68% and 90% CL regions in ($sin^2\theta_{13}$, $|\Delta m^2|$) space for fake dataset #5. At each point, χ^2 was minimized with respect to all oscillation parameters not shown (and not considered to be fixed) and all relevant nuisance parameters.

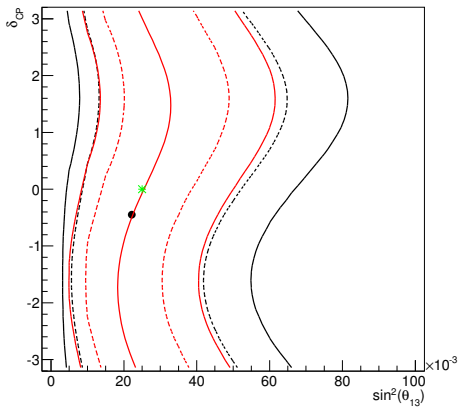

Figure 143: 68% and 90% CL regions in ($sin^2\theta_{13}$, δ_{CP}) space for fake dataset #5. At each point, χ^2 was minimized with respect to $|\Delta m^2|$, $\sin^2\theta_{23}$ and all relevant nuisance parameters for the joint analysis (black) and with respect to all relevant nuisance parameters for the appearance analysis (red). Notice that different methods are used to construct confidence regions for the joint analysis (global minimum) and for the stand-alone appearance analysis (raster scan).

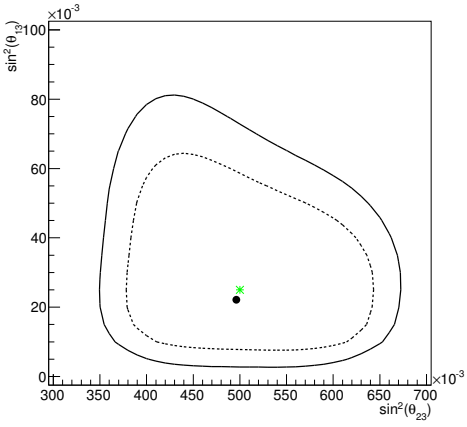

Figure 144: 68% and 90% CL regions in ($sin^2\theta_{23}$, $sin^2\theta_{13}$) space for fake dataset #5. At each point, χ^2 was minimized with respect to all oscillation parameters not shown (and not considered to be fixed) and all relevant nuisance parameters.

Set		$\|\Delta m^2\|$ ($\times 10^{-3}$ eV^2/c^4)	$\sin^2\theta_{23}$	$\sin^2\theta_{13}$	δ_{CP}	MH	$N_{SK}^{1R\mu}$	N_{SK}^{1Re}	χ^2/ndf	p-value	Systematics
6	true	**2.36**	**0.5**	**0.025**	**0.0**	**Normal**	**63**	**7**	–	–	**Nominal**
	fit (joint)	2.369	0.509	0.016	2.110	(fixed)	60.887	6.752	81.85/94	0.95	See Fig. 145 -
	fit (ν_e app.)	–	–	0.011	0(fixed)		–	6.741	16.98/24	0.98	158
	fit (ν_μ disapp.)	2.356	0.514	–	–		61.010	–	65.09/71	0.81	
7	true	**2.36**	**0.5**	**0.025**	**0.0**	**Normal**	**55**	**11**	–	–	**Random**
	fit (joint)	2.511	0.516	0.030	0.722	(fixed)	54.802	10.962	73.86/94	0.35	See Fig. 159 -
	fit (ν_e app.)	–	–	0.026	0(fixed)		–	10.894	22.70/24	0.20	172
	fit (ν_μ disapp.)	2.492	0.514	–	–		55.406	–	52.24/71	0.53	
8	true	**2.36**	**0.5**	**0.025**	**0.0**	**Normal**	**55**	**12**	–	–	E_{reco} **scale: -1**σ
	fit (joint)	2.431	0.520	0.036	0.707	(fixed)	56.166	12.679	74.34/94	0.17	See Fig. 173 -
	fit (ν_e app.)	–	–	0.032	0(fixed)		–	12.695	16.65/24	0.39	186
	fit (ν_μ disapp.)	2.431	0.514	–	–		56.821	–	58.10/71	0.09	
9	true	**2.36**	**0.38**	**0.025**	**0.0**	**Normal**	**53**	**11**	–	–	**Nominal**
	fit (joint)	2.317	0.400	0.030	-0.263	(fixed)	61.157	11.138	101.18/94	0.73	See Fig. 187 -
	fit (ν_e app.)	–	–	0.026	0(fixed)		–	11.272	29.70/24	0.71	200
	fit (ν_μ disapp.)	2.278	0.403	–	–		60.964	–	72.07/71	0.49	
10	true	**2.36**	**0.5**	**0.015**	**0.0**	**Normal**	**57**	**5**	–	–	**Nominal**
	fit (joint)	2.427	0.505	0.009	1.072	(fixed)	56.061	5.087	78.51/94	0.30	See Fig. 201 -
	fit (ν_e app.)	–	–	0.006	0(fixed)		–	5.047	17.13/24	0.43	214
	fit (ν_μ disapp.)	2.420	0.514	–	–		56.235	–	62.16/71	0.27	
11	true	**2.36**	**0.5**	**0.025**	**-**$\pi/2$	**Normal**	**69**	**13**	–	–	**Nominal**
	fit (joint)	2.455	0.389	0.048	0.706	(fixed)	68.012	12.594	75.27/94	0.25	See Fig. 215 -
	fit (ν_e app.)	–	–	0.031	0(fixed)		–	12.541	24.58/24	0.08	228
	fit (ν_μ disapp.)	2.411	0.384	–	–		68.452	–	50.88/71	0.80	
12	true	**2.2**	**0.5**	**0.025**	**0.0**	**Normal**	**53**	**7**	–	–	**Nominal**
	fit (joint)	2.234	0.506	0.013	3.141	(fixed)	57.620	6.972	90.38/94	0.93	See Fig. 229 -
	fit (ν_e app.)	–	–	0.012	0(fixed)		–	6.961	18.67/24	0.85	242
	fit (ν_μ disapp.)	2.220	0.513	–	–		57.665	–	72.36/71	0.76	
13	true	**2.36**	**0.5**	**0.025**	**0.0**	**Inverted**	**52**	**11**	–	–	**Nominal**
	fit (joint)	2.503	0.513	0.029	-0.379	(fixed)	54.485	11.374	73.72/94	0.58	See Fig. 243 -
	fit (ν_e app.)	–	–	0.033	0(fixed)		–	11.450	15.82/24	0.60	256
	fit (ν_μ disapp.)	2.513	0.511	–	–		54.708	–	58.09/71	0.53	

Table 20: True input values (shown in bold) and VALOR best-fit values for a test ensemble of 7 fake datasets with statistical fluctuations

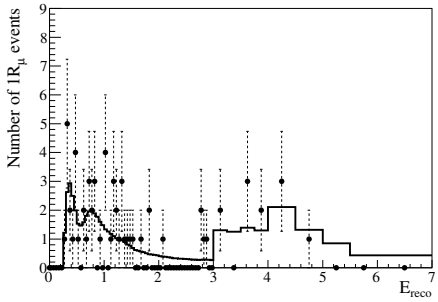

Figure 145: Single μ-like ring event best-fit reconstructed energy spectrum to fake dataset #6.

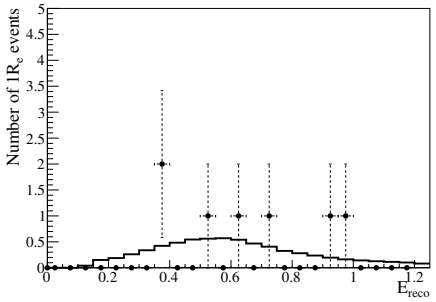

Figure 146: Single e-like ring event best-fit reconstructed energy spectrum to fake dataset #6.

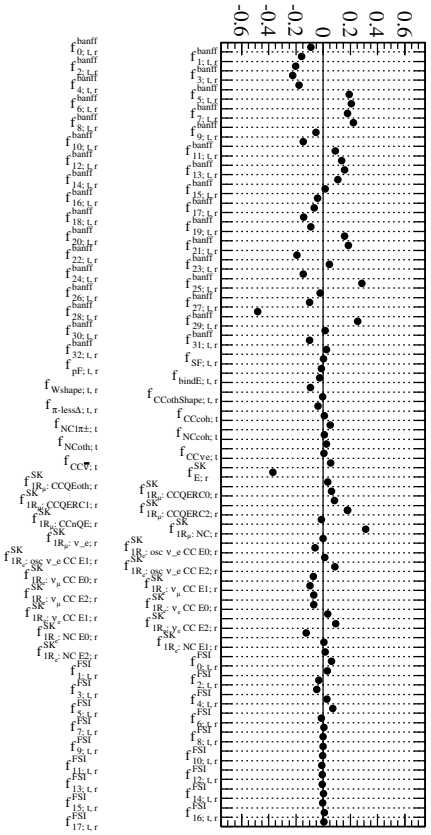

Figure 147: Systematic parameter pulls for the oscillation fit to fake dataset #6.

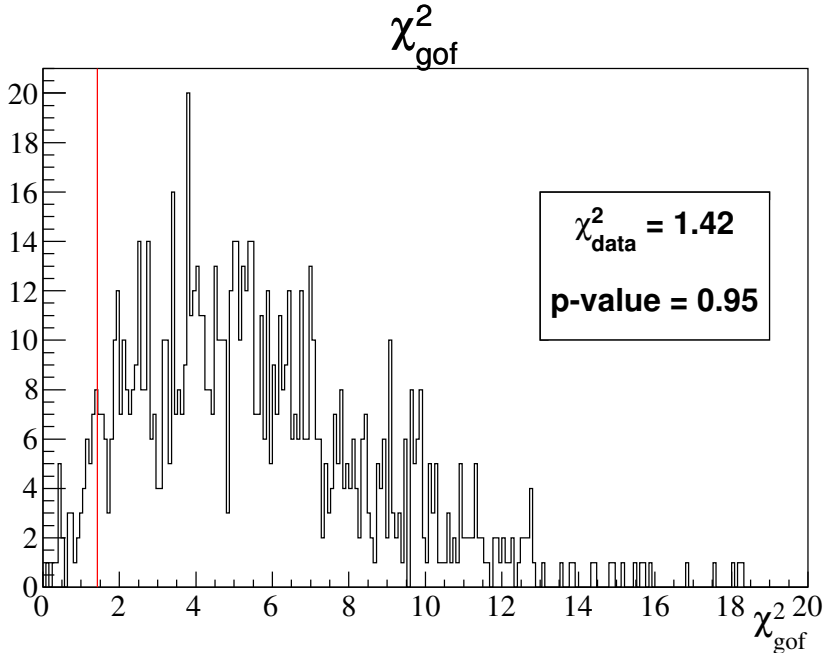

Figure 148: Distribution of χ^2_{gof}, the goodness-of-fit (gof) χ^2, from 1k toy MC experiments generated at dataset #6 joint 3-flavour analysis best-fit oscillation point. The χ^2_{gof} value for the dataset #6 (χ^2_{data}) is highlighted. All χ^2_{gof} values were computed using the 5 (single μ-like ring) + 1 (single e-like ring) reconstructed energy binning scheme described in Sec. 6.2,

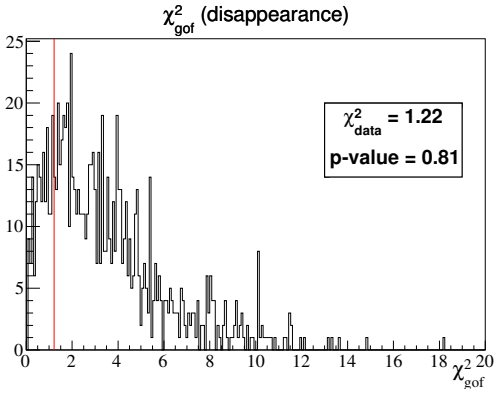

Figure 149: Distribution of χ^2_{gof} from 1k toy MC experiments generated at the dataset #6 stand-alone 3-flavour ν_μ disappearance analysis best-fit oscillation point. The χ^2_{gof} value for the dataset #6 (χ^2_{data}) is highlighted. All χ^2_{gof} values were computed using the 5 (single μ-like ring) reconstructed energy binning scheme described in Sec. 6.2,

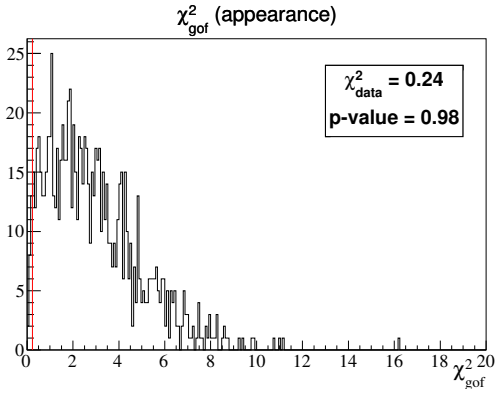

Figure 150: Distribution of χ^2_{gof} from 1k toy MC experiments generated at the dataset #6 stand-alone 3-flavour ν_e appearance analysis best-fit oscillation point. The χ^2_{gof} value for the dataset #6 (χ^2_{data}) is highlighted. All χ^2_{gof} values were computed using a single reconstructed energy bin, as described in Sec. 6.2,

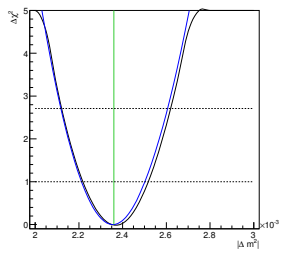

Figure 151: $\Delta\chi^2$ as function of $|\Delta m^2|$ for fake dataset #6. At each point, χ^2 was minimized with respect to $\sin^2\theta_{23}$, $\sin^2\theta_{13}$, δ_{CP} and all relevant nuisance parameters for the joint analysis (black) and with respect to $\sin^2\theta_{23}$ and all relevant nuisance parameters for the disappearance analysis (blue).

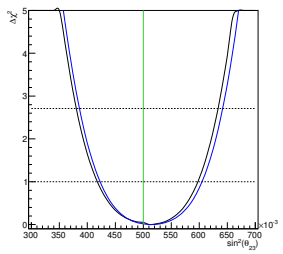

Figure 152: $\Delta\chi^2$ as function of $sin^2\theta_{23}$ for fake dataset #6. At each point, χ^2 was minimized with respect to $|\Delta m^2|$, $\sin^2\theta_{13}$, δ_{CP} and all relevant nuisance parameters for the joint analysis (black) and with respect to $\sin^2\theta_{23}$ and all relevant nuisance parameters for the disappearance analysis (blue).

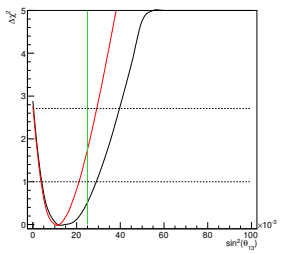

Figure 153: $\Delta\chi^2$ as function of $sin^2\theta_{13}$ for fake dataset #6. At each point, χ^2 was minimized with respect to $\sin^2\theta_{23}$, $\sin^2\theta_{13}$, δ_{CP} and all relevant nuisance parameters for the joint analysis (black) and with respect to all relevant nuisance parameters (δ_{CP} is fixed to 0) for the appearance analysis (red).

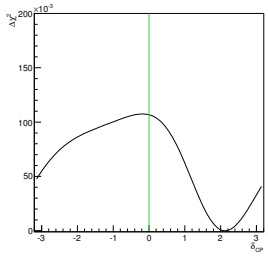

Figure 154: $\Delta\chi^2$ as function of δ_{CP} for fake dataset #6. At each point, χ^2 was minimized with respect to all oscillation parameters not shown (and not considered to be fixed) and all relevant nuisance parameters.

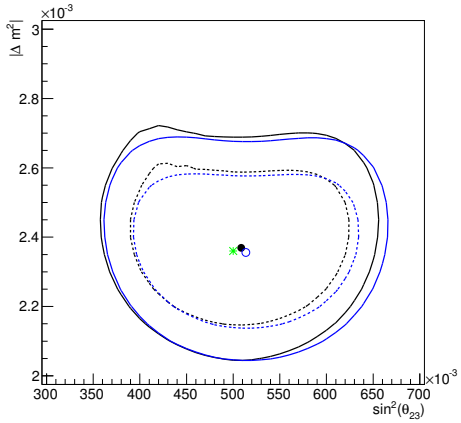

Figure 155: 68% and 90% CL regions in ($sin^2\theta_{23}$, $|\Delta m^2|$) space for fake dataset #6. At each point, χ^2 was minimized with respect to $\sin^2\theta_{13}$, δ_{CP} and all relevant nuisance parameters for the joint analysis (black) and with respect to all relevant nuisance parameters for the disappearance analysis (blue).

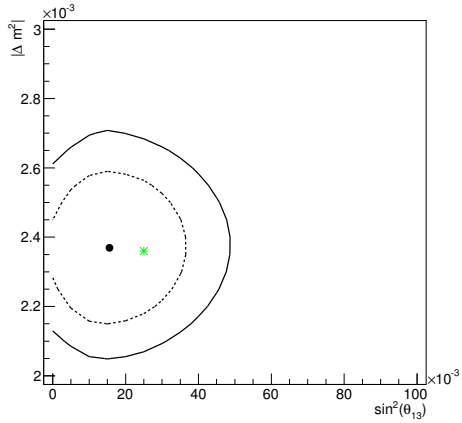

Figure 156: 68% and 90% CL regions in ($sin^2\theta_{13}$, $|\Delta m^2|$) space for fake dataset #6. At each point, χ^2 was minimized with respect to all oscillation parameters not shown (and not considered to be fixed) and all relevant nuisance parameters.

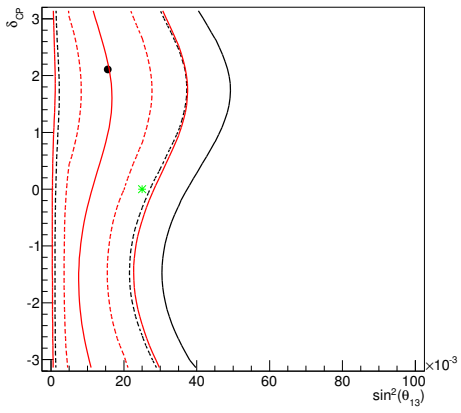

Figure 157: 68% and 90% CL regions in ($sin^2\theta_{13}$, δ_{CP}) space for fake dataset #6. At each point, χ^2 was minimized with respect to $|\Delta m^2|$, $\sin^2\theta_{23}$ and all relevant nuisance parameters for the joint analysis (black) and with respect to all relevant nuisance parameters for the appearance analysis (red). Notice that different methods are used to construct confidence regions for the joint analysis (global minimum) and for the stand-alone appearance analysis (raster scan).

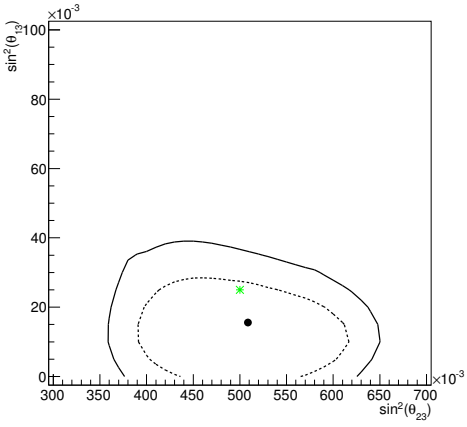

Figure 158: 68% and 90% CL regions in ($sin^2\theta_{23}$, $sin^2\theta_{13}$) space for fake dataset #6. At each point, χ^2 was minimized with respect to all oscillation parameters not shown (and not considered to be fixed) and all relevant nuisance parameters.

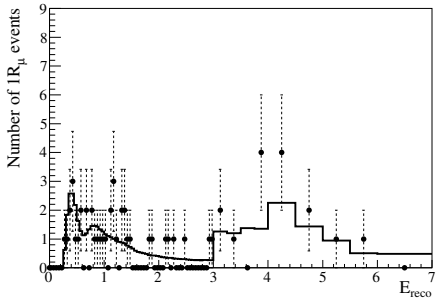

Figure 159: Single μ-like ring event best-fit reconstructed energy spectrum to fake dataset #7.

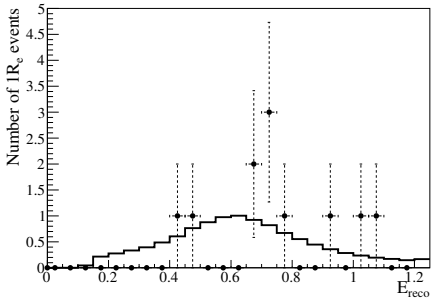

Figure 160: Single e-like ring event best-fit reconstructed energy spectrum to fake dataset #7.

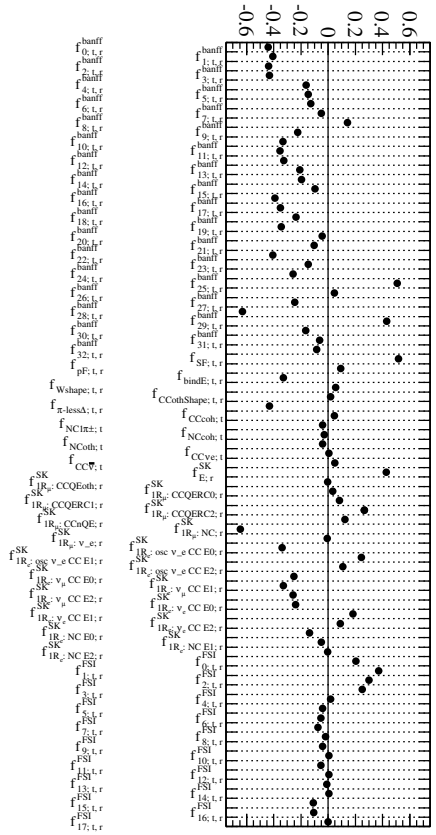

Figure 161: Systematic parameter pulls for the oscillation fit to fake dataset #7.

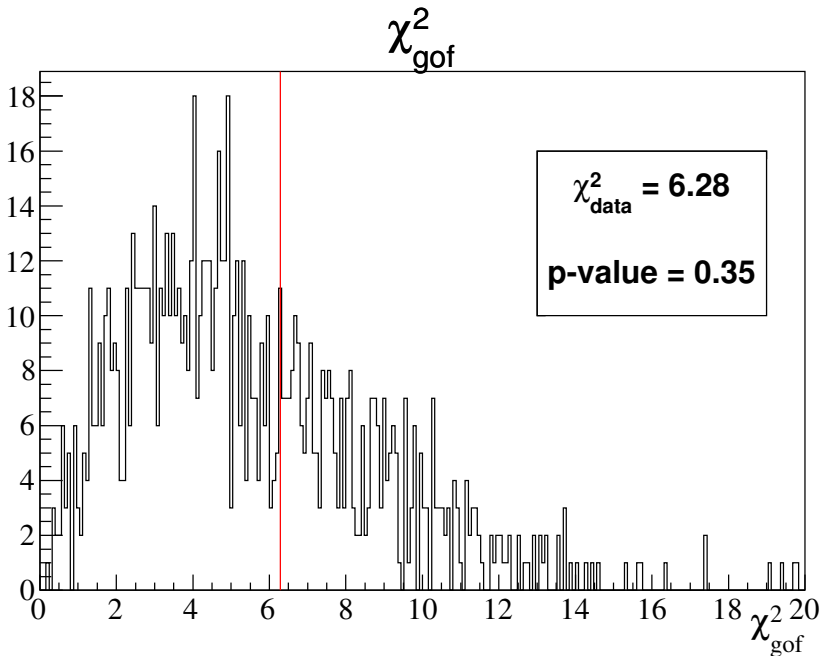

Figure 162: Distribution of χ^2_{gof}, the goodness-of-fit (gof) χ^2, from 1k toy MC experiments generated at dataset #7 joint 3-flavour analysis best-fit oscillation point. The χ^2_{gof} value for the dataset #7 (χ^2_{data}) is highlighted. All χ^2_{gof} values were computed using the 5 (single μ-like ring) + 3 (single e-like ring) reconstructed energy binning scheme described in Sec. 6.2.

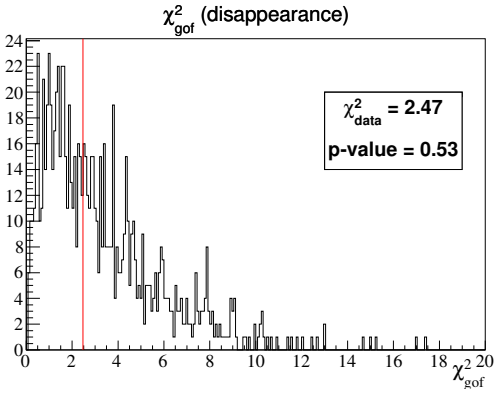

Figure 163: Distribution of χ^2_{gof} from 1k toy MC experiments generated at the dataset #7 stand-alone 3-flavour ν_μ disappearance analysis best-fit oscillation point. The χ^2_{gof} value for the dataset #7 (χ^2_{data}) is highlighted. All χ^2_{gof} values were computed using the 5 (single μ-like ring) reconstructed energy binning scheme described in Sec. 6.2.

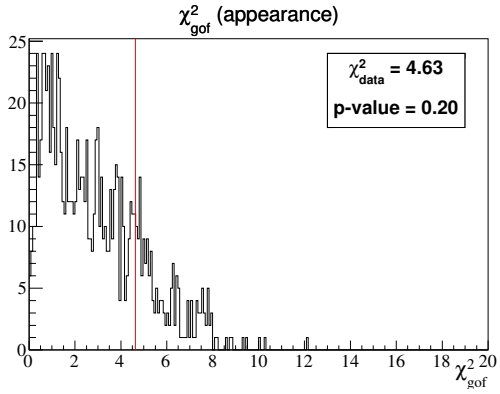

Figure 164: Distribution of χ^2_{gof} from 1k toy MC experiments generated at the dataset #7 stand-alone 3-flavour ν_e appearance analysis best-fit oscillation point. The χ^2_{gof} value for the dataset #7 (χ^2_{data}) is highlighted. All χ^2_{gof} values were computed using the 3 (single e-like ring) reconstructed energy binning scheme as described in Sec. 6.2.

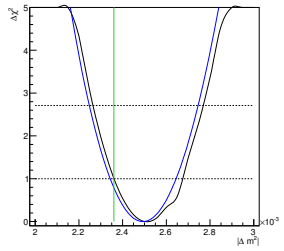

Figure 165: $\Delta\chi^2$ as function of $|\Delta m^2|$ for fake dataset #7. At each point, χ^2 was minimized with respect to $\sin^2\theta_{23}$, $\sin^2\theta_{13}$, δ_{CP} and all relevant nuisance parameters for the joint analysis (black) and with respect to $\sin^2\theta_{23}$ and all relevant nuisance parameters for the disappearance analysis (blue).

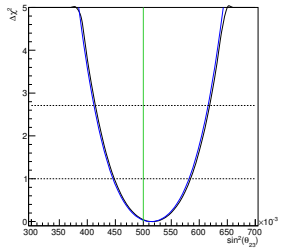

Figure 166: $\Delta\chi^2$ as function of $sin^2\theta_{23}$ for fake dataset #7. At each point, χ^2 was minimized with respect to $|\Delta m^2|$, $\sin^2\theta_{13}$, δ_{CP} and all relevant nuisance parameters for the joint analysis (black) and with respect to $\sin^2\theta_{23}$ and all relevant nuisance parameters for the disappearance analysis (blue).

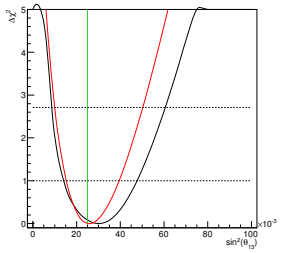

Figure 167: $\Delta\chi^2$ as function of $sin^2\theta_{13}$ for fake dataset #7. At each point, χ^2 was minimized with respect to $\sin^2\theta_{23}$, $\sin^2\theta_{13}$, δ_{CP} and all relevant nuisance parameters for the joint analysis (black) and with respect to all relevant nuisance parameters (δ_{CP} is fixed to 0) for the appearance analysis (red).

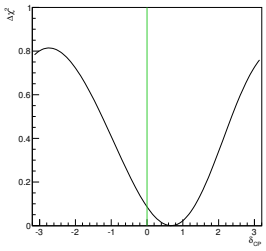

Figure 168: $\Delta\chi^2$ as function of δ_{CP} for fake dataset #7. At each point, χ^2 was minimized with respect to all oscillation parameters not shown (and not considered to be fixed) and all relevant nuisance parameters.

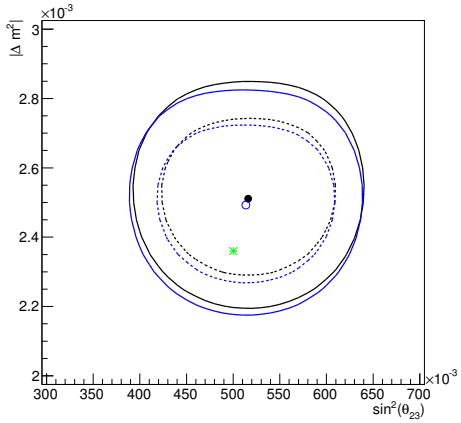

Figure 169: 68% and 90% CL regions in ($sin^2\theta_{23}$, $|\Delta m^2|$) space for fake dataset #7. At each point, χ^2 was minimized with respect to $\sin^2\theta_{13}$, δ_{CP} and all relevant nuisance parameters for the joint analysis (black) and with respect to all relevant nuisance parameters for the disappearance analysis (blue).

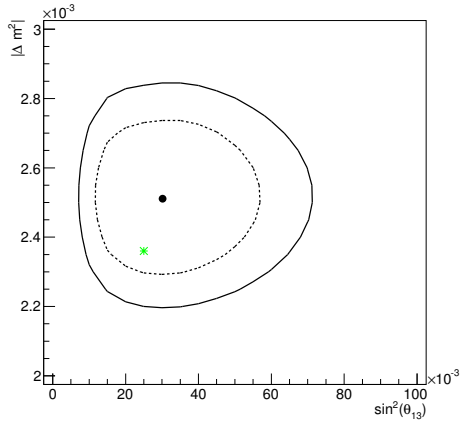

Figure 170: 68% and 90% CL regions in ($sin^2\theta_{13}$, $|\Delta m^2|$) space for fake dataset #7. At each point, χ^2 was minimized with respect to all oscillation parameters not shown (and not considered to be fixed) and all relevant nuisance parameters.

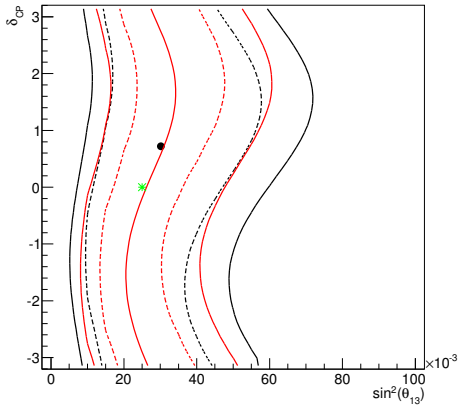

Figure 171: 68% and 90% CL regions in ($sin^2\theta_{13}$, δ_{CP}) space for fake dataset #7. At each point, χ^2 was minimized with respect to $|\Delta m^2|$, $\sin^2\theta_{23}$ and all relevant nuisance parameters for the joint analysis (black) and with respect to all relevant nuisance parameters for the appearance analysis (red). Notice that different methods are used to construct confidence regions for the joint analysis (global minimum) and for the stand-alone appearance analysis (raster scan).

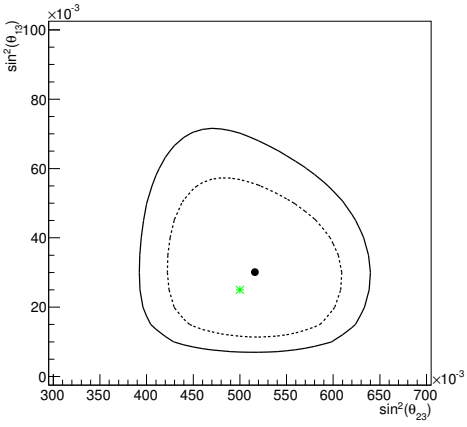

Figure 172: 68% and 90% CL regions in ($sin^2\theta_{23}$, $sin^2\theta_{13}$) space for fake dataset #7. At each point, χ^2 was minimized with respect to all oscillation parameters not shown (and not considered to be fixed) and all relevant nuisance parameters.

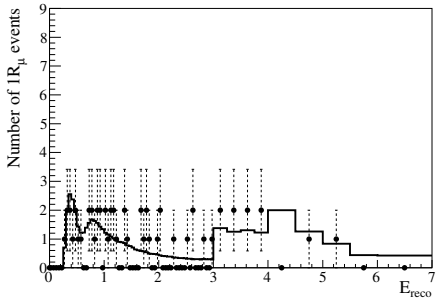

Figure 173: Single μ-like ring event best-fit reconstructed energy spectrum to fake dataset #8.

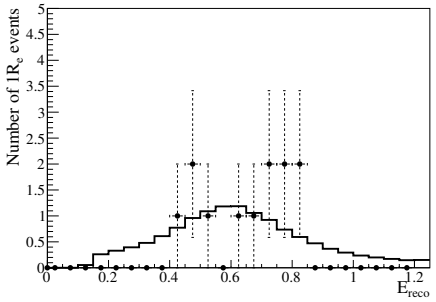

Figure 174: Single e-like ring event best-fit reconstructed energy spectrum to fake dataset #8.

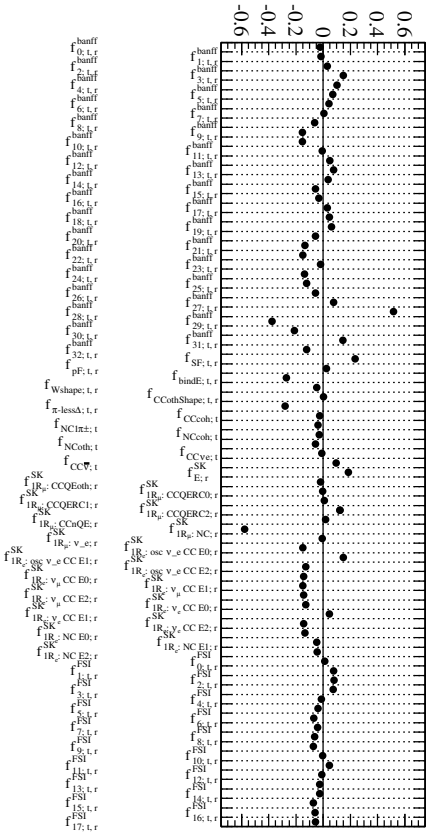

Figure 175: Systematic parameter pulls for the oscillation fit to fake dataset #8.

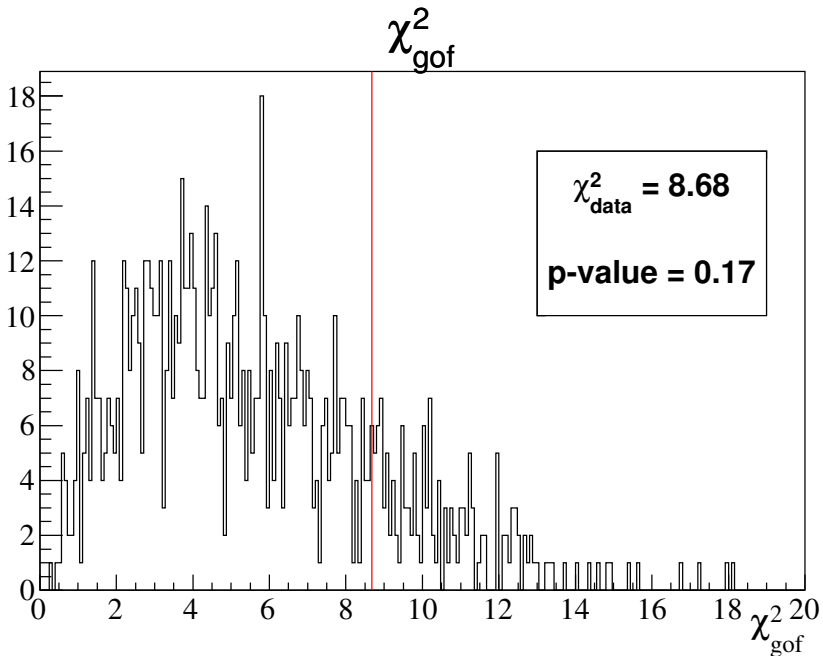

Figure 176: Distribution of χ^2_{gof}, the goodness-of-fit (gof) χ^2, from 1k toy MC experiments generated at dataset #8 joint 3-flavour analysis best-fit oscillation point. The χ^2_{gof} value for the dataset #8 (χ^2_{data}) is highlighted. All χ^2_{gof} values were computed using the 5 (single μ-like ring) + 3 (single e-like ring) reconstructed energy binning scheme described in Sec. 6.2.

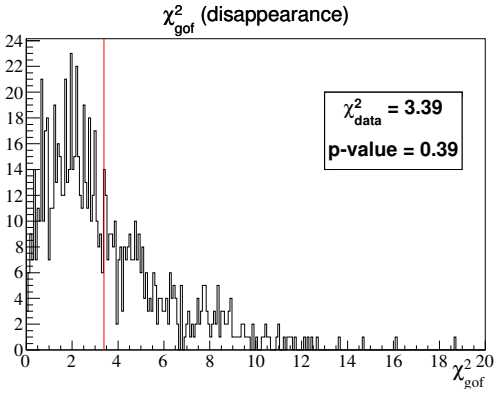

Figure 177: Distribution of χ^2_{gof} from 1k toy MC experiments generated at the dataset #8 stand-alone 3-flavour ν_μ disappearance analysis best-fit oscillation point. The χ^2_{gof} value for the dataset #8 (χ^2_{data}) is highlighted. All χ^2_{gof} values were computed using the 5 (single μ-like ring) reconstructed energy binning scheme described in Sec. 6.2.

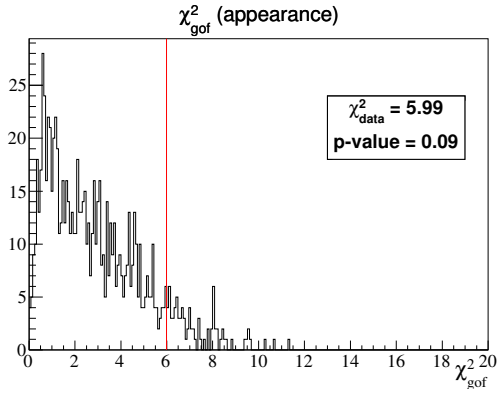

Figure 178: Distribution of χ^2_{gof} from 1k toy MC experiments generated at the dataset #8 stand-alone 3-flavour ν_e appearance analysis best-fit oscillation point. The χ^2_{gof} value for the dataset #8 (χ^2_{data}) is highlighted. All χ^2_{gof} values were computed using the 3 (single e-like ring) reconstructed energy binning scheme as described in Sec. 6.2.

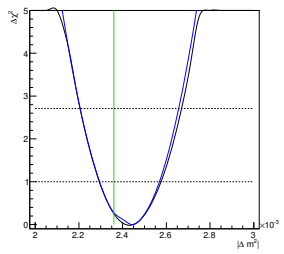

Figure 179: $\Delta\chi^2$ as function of $|\Delta m^2|$ for fake dataset #8. At each point, χ^2 was minimized with respect to $\sin^2\theta_{23}$, $\sin^2\theta_{13}$, δ_{CP} and all relevant nuisance parameters for the joint analysis (black) and with respect to $\sin^2\theta_{23}$ and all relevant nuisance parameters for the disappearance analysis (blue).

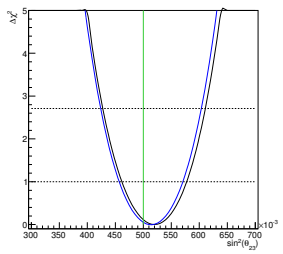

Figure 180: $\Delta\chi^2$ as function of $sin^2\theta_{23}$ for fake dataset #8. At each point, χ^2 was minimized with respect to $|\Delta m^2|$, $\sin^2\theta_{13}$, δ_{CP} and all relevant nuisance parameters for the joint analysis (black) and with respect to $\sin^2\theta_{23}$ and all relevant nuisance parameters for the disappearance analysis (blue).

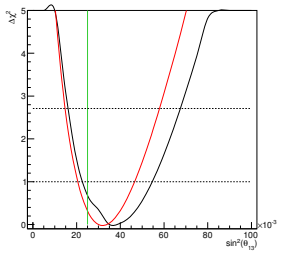

Figure 181: $\Delta\chi^2$ as function of $sin^2\theta_{13}$ for fake dataset #8. At each point, χ^2 was minimized with respect to $\sin^2\theta_{23}$, $\sin^2\theta_{13}$, δ_{CP} and all relevant nuisance parameters for the joint analysis (black) and with respect to all relevant nuisance parameters (δ_{CP} is fixed to 0) for the appearance analysis (red).

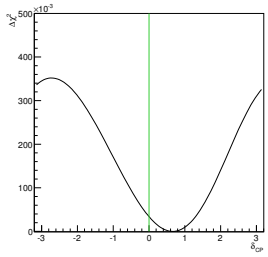

Figure 182: $\Delta\chi^2$ as function of δ_{CP} for fake dataset #8. At each point, χ^2 was minimized with respect to all oscillation parameters not shown (and not considered to be fixed) and all relevant nuisance parameters.

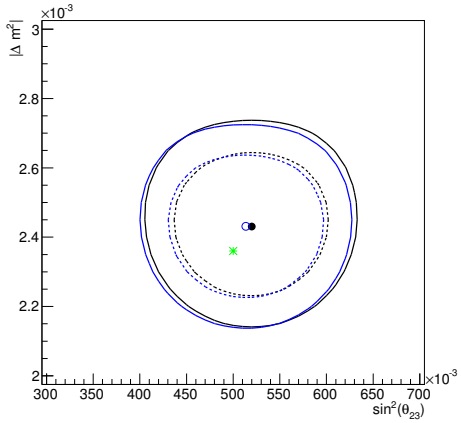

Figure 183: 68% and 90% CL regions in $(sin^2\theta_{23}, |\Delta m^2|)$ space for fake dataset #8. At each point, χ^2 was minimized with respect to $\sin^2\theta_{13}$, δ_{CP} and all relevant nuisance parameters for the joint analysis (black) and with respect to all relevant nuisance parameters for the disappearance analysis (blue).

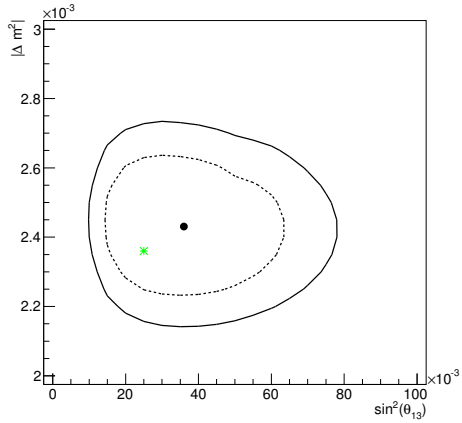

Figure 184: 68% and 90% CL regions in $(sin^2\theta_{13}, |\Delta m^2|)$ space for fake dataset #8. At each point, χ^2 was minimized with respect to all oscillation parameters not shown (and not considered to be fixed) and all relevant nuisance parameters.

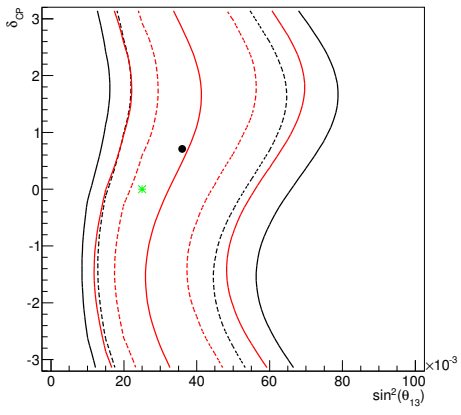

Figure 185: 68% and 90% CL regions in $(sin^2\theta_{13}, \delta_{CP})$ space for fake dataset #8. At each point, χ^2 was minimized with respect to $|\Delta m^2|$, $\sin^2\theta_{23}$ and all relevant nuisance parameters for the joint analysis (black) and with respect to all relevant nuisance parameters for the appearance analysis (red). Notice that different methods are used to construct confidence regions for the joint analysis (global minimum) and for the stand-alone appearance analysis (raster scan).

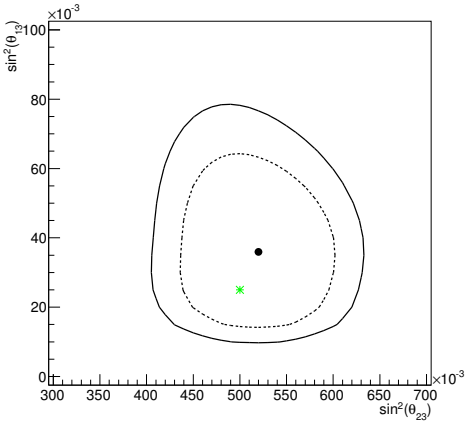

Figure 186: 68% and 90% CL regions in $(sin^2\theta_{23}, sin^2\theta_{13})$ space for fake dataset #8. At each point, χ^2 was minimized with respect to all oscillation parameters not shown (and not considered to be fixed) and all relevant nuisance parameters.

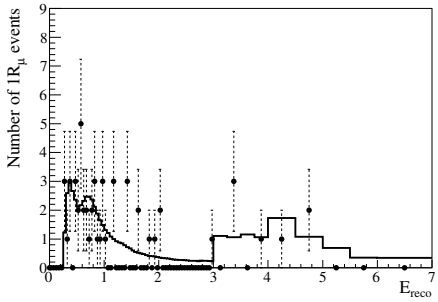

Figure 187: Single μ-like ring event best-fit reconstructed energy spectrum to fake dataset #9.

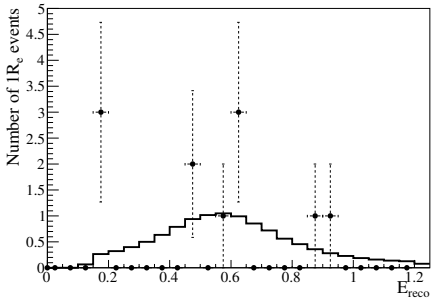

Figure 188: Single e-like ring event best-fit reconstructed energy spectrum to fake dataset #9.

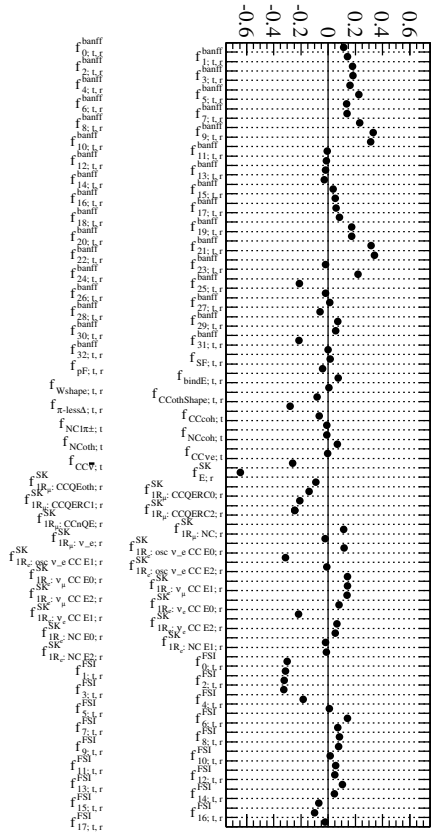

Figure 189: Systematic parameter pulls for the oscillation fit to fake dataset #9.

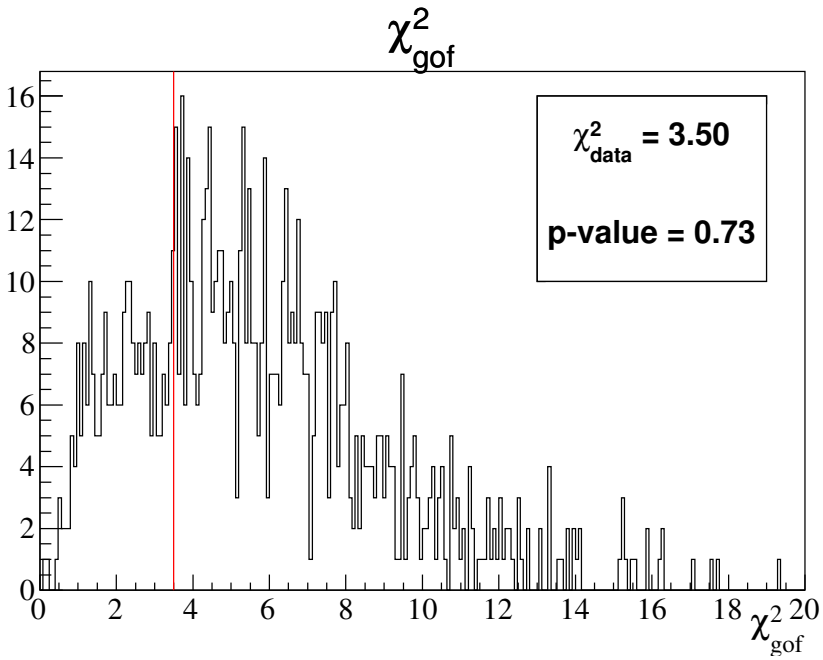

Figure 190: Distribution of χ^2_{gof}, the goodness-of-fit (gof) χ^2, from 1k toy MC experiments generated at dataset #9 joint 3-flavour analysis best-fit oscillation point. The χ^2_{gof} value for the dataset #9 (χ^2_{data}) is highlighted. All χ^2_{gof} values were computed using the 5 (single μ-like ring) + 3 (single e-like ring) reconstructed energy binning scheme described in Sec. 6.2.

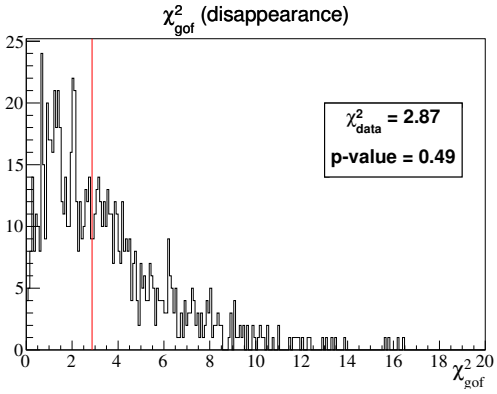

Figure 191: Distribution of χ^2_{gof} from 1k toy MC experiments generated at the dataset #9 stand-alone 3-flavour ν_μ disappearance analysis best-fit oscillation point. The χ^2_{gof} value for the dataset #9 (χ^2_{data}) is highlighted. All χ^2_{gof} values were computed using the 5 (single μ-like ring) reconstructed energy binning scheme described in Sec. 6.2.

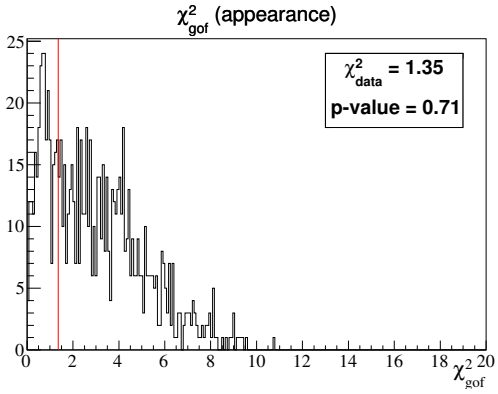

Figure 192: Distribution of χ^2_{gof} from 1k toy MC experiments generated at the dataset #9 stand-alone 3-flavour ν_e appearance analysis best-fit oscillation point. The χ^2_{gof} value for the dataset #9 (χ^2_{data}) is highlighted. All χ^2_{gof} values were computed using the 3 (single e-like ring) reconstructed energy binning scheme as described in Sec. 6.2.

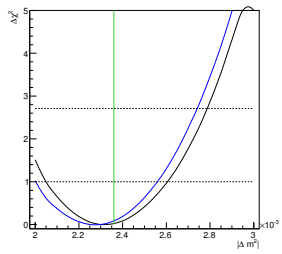

Figure 193: $\Delta\chi^2$ as function of $|\Delta m^2|$ for fake dataset #9. At each point, χ^2 was minimized with respect to $\sin^2\theta_{23}$, $\sin^2\theta_{13}$, δ_{CP} and all relevant nuisance parameters for the joint analysis (black) and with respect to $\sin^2\theta_{23}$ and all relevant nuisance parameters for the disappearance analysis (blue).

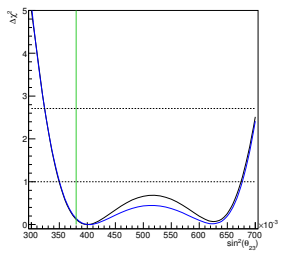

Figure 194: $\Delta\chi^2$ as function of $sin^2\theta_{23}$ for fake dataset #9. At each point, χ^2 was minimized with respect to $|\Delta m^2|$, $\sin^2\theta_{13}$, δ_{CP} and all relevant nuisance parameters for the joint analysis (black) and with respect to $\sin^2\theta_{23}$ and all relevant nuisance parameters for the disappearance analysis (blue).

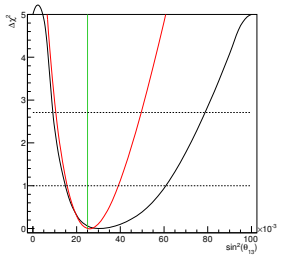

Figure 195: $\Delta\chi^2$ as function of $sin^2\theta_{13}$ for fake dataset #9. At each point, χ^2 was minimized with respect to $\sin^2\theta_{23}$, $\sin^2\theta_{13}$, δ_{CP} and all relevant nuisance parameters for the joint analysis (black) and with respect to all relevant nuisance parameters (δ_{CP} is fixed to 0) for the appearance analysis (red).

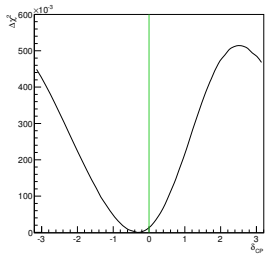

Figure 196: $\Delta\chi^2$ as function of δ_{CP} for fake dataset #9. At each point, χ^2 was minimized with respect to all oscillation parameters not shown (and not considered to be fixed) and all relevant nuisance parameters.

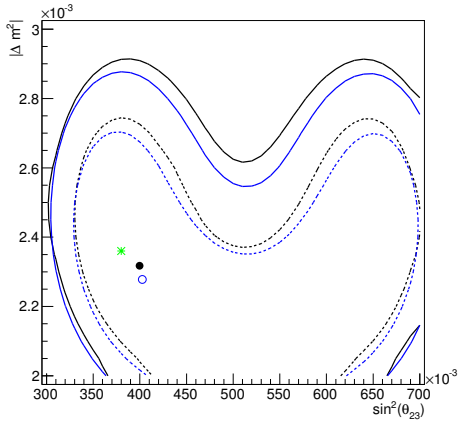

Figure 197: 68% and 90% CL regions in ($sin^2\theta_{23}$, $|\Delta m^2|$) space for fake dataset #9. At each point, χ^2 was minimized with respect to $\sin^2\theta_{13}$, δ_{CP} and all relevant nuisance parameters for the joint analysis (black) and with respect to all relevant nuisance parameters for the disappearance analysis (blue).

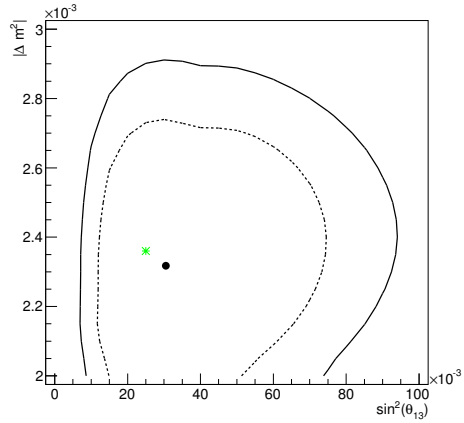

Figure 198: 68% and 90% CL regions in ($sin^2\theta_{13}$, $|\Delta m^2|$) space for fake dataset #9. At each point, χ^2 was minimized with respect to all oscillation parameters not shown (and not considered to be fixed) and all relevant nuisance parameters.

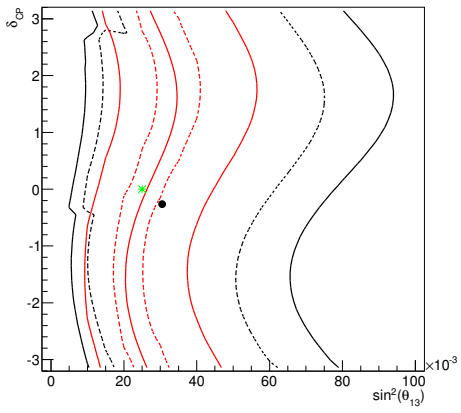

Figure 199: 68% and 90% CL regions in ($sin^2\theta_{13}$, δ_{CP}) space for fake dataset #9. At each point, χ^2 was minimized with respect to $|\Delta m^2|$, $\sin^2\theta_{23}$ and all relevant nuisance parameters for the joint analysis (black) and with respect to all relevant nuisance parameters for the appearance analysis (red). Notice that different methods are used to construct confidence regions for the joint analysis (global minimum) and for the stand-alone appearance analysis (raster scan).

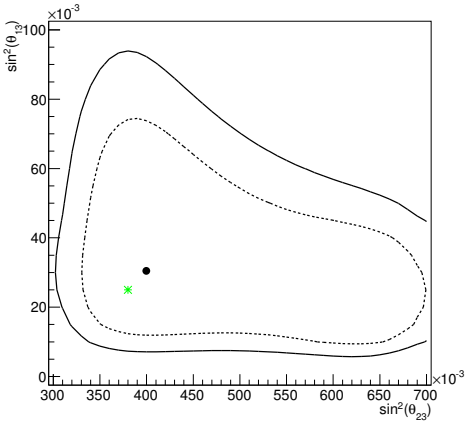

Figure 200: 68% and 90% CL regions in ($sin^2\theta_{23}$, $sin^2\theta_{13}$) space for fake dataset #9. At each point, χ^2 was minimized with respect to all oscillation parameters not shown (and not considered to be fixed) and all relevant nuisance parameters.

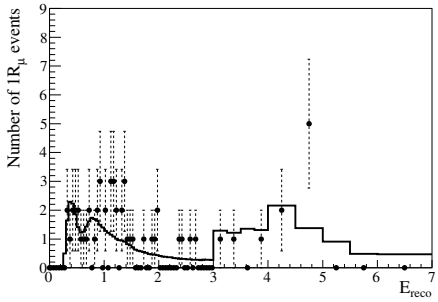

Figure 201: Single μ-like ring event best-fit reconstructed energy spectrum to fake dataset #10.

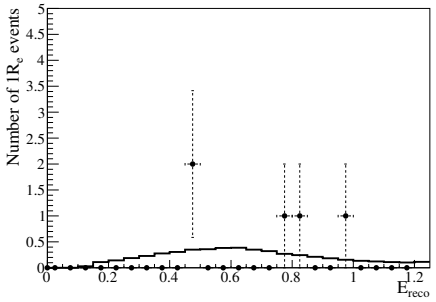

Figure 202: Single e-like ring event best-fit reconstructed energy spectrum to fake dataset #10.

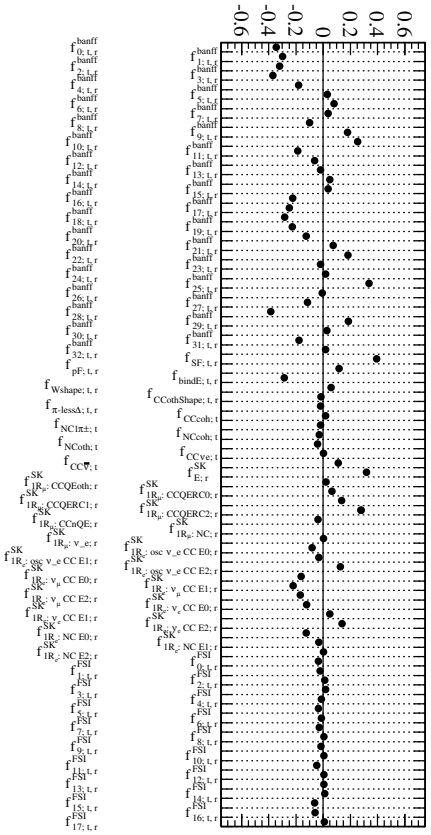

Figure 203: Systematic parameter pulls for the oscillation fit to fake dataset #10.

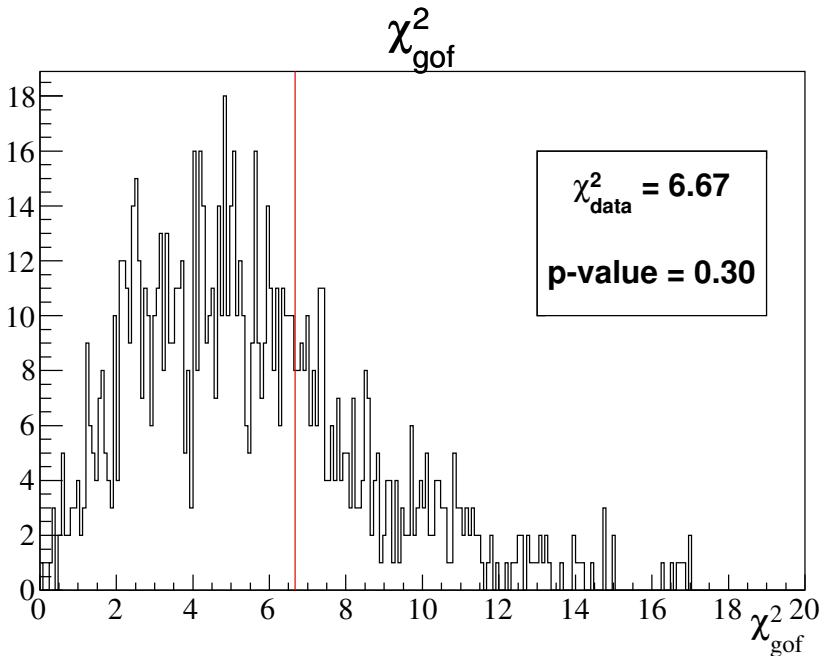

Figure 204: Distribution of χ^2_{gof}, the goodness-of-fit (gof) χ^2, from 1k toy MC experiments generated at dataset #10 joint 3-flavour analysis best-fit oscillation point. The χ^2_{gof} value for the dataset #10 (χ^2_{data}) is highlighted. All χ^2_{gof} values were computed using the 5 (single μ-like ring) + 3 (single e-like ring) reconstructed energy binning scheme described in Sec. 6.2.

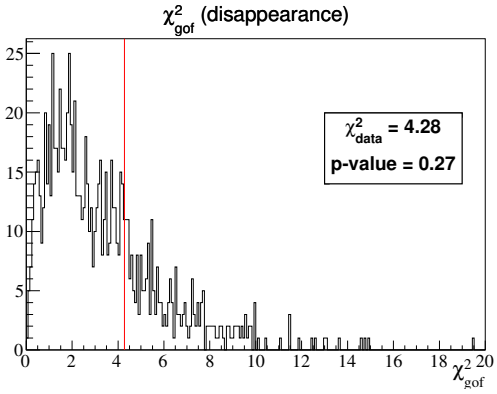

Figure 205: Distribution of χ^2_{gof} from 1k toy MC experiments generated at the dataset #10 stand-alone 3-flavour ν_μ disappearance analysis best-fit oscillation point. The χ^2_{gof} value for the dataset #10 (χ^2_{data}) is highlighted. All χ^2_{gof} values were computed using the 5 (single μ-like ring) reconstructed energy binning scheme described in Sec. 6.2.

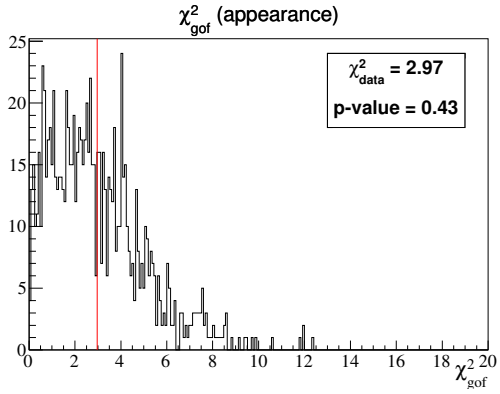

Figure 206: Distribution of χ^2_{gof} from 1k toy MC experiments generated at the dataset #10 stand-alone 3-flavour ν_e appearance analysis best-fit oscillation point. The χ^2_{gof} value for the dataset #10 (χ^2_{data}) is highlighted. All χ^2_{gof} values were computed using the 3 (single e-like ring) reconstructed energy binning scheme as described in Sec. 6.2.

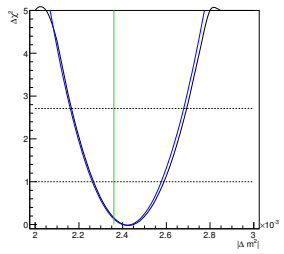

Figure 207: $\Delta\chi^2$ as function of $|\Delta m^2|$ for fake dataset #10. At each point, χ^2 was minimized with respect to $\sin^2\theta_{23}$, $\sin^2\theta_{13}$, δ_{CP} and all relevant nuisance parameters for the joint analysis (black) and with respect to $\sin^2\theta_{23}$ and all relevant nuisance parameters for the disappearance analysis (blue).

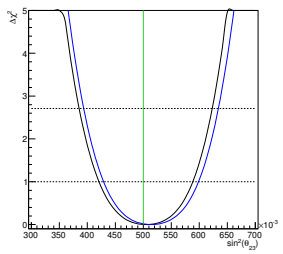

Figure 208: $\Delta\chi^2$ as function of $sin^2\theta_{23}$ for fake dataset #10. At each point, χ^2 was minimized with respect to $|\Delta m^2|$, $\sin^2\theta_{13}$, δ_{CP} and all relevant nuisance parameters for the joint analysis (black) and with respect to $\sin^2\theta_{23}$ and all relevant nuisance parameters for the disappearance analysis (blue).

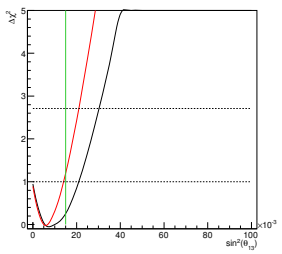

Figure 209: $\Delta\chi^2$ as function of $sin^2\theta_{13}$ for fake dataset #10. At each point, χ^2 was minimized with respect to $\sin^2\theta_{23}$, $\sin^2\theta_{13}$, δ_{CP} and all relevant nuisance parameters for the joint analysis (black) and with respect to all relevant nuisance parameters (δ_{CP} is fixed to 0) for the appearance analysis (red).

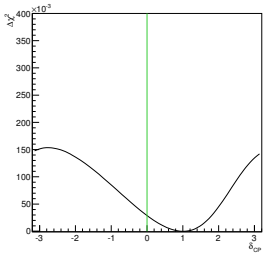

Figure 210: $\Delta\chi^2$ as function of δ_{CP} for fake dataset #10. At each point, χ^2 was minimized with respect to all oscillation parameters not shown (and not considered to be fixed) and all relevant nuisance parameters.

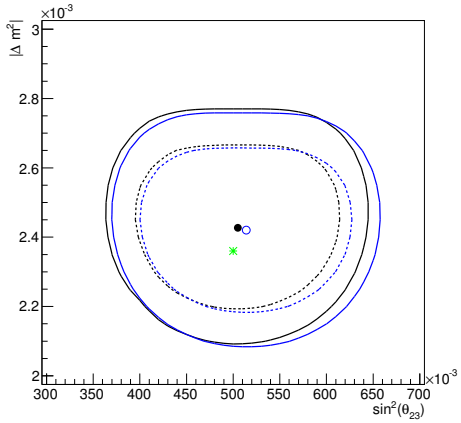

Figure 211: 68% and 90% CL regions in ($sin^2\theta_{23}$, $|\Delta m^2|$) space for fake dataset #10. At each point, χ^2 was minimized with respect to $\sin^2\theta_{13}$, δ_{CP} and all relevant nuisance parameters for the joint analysis (black) and with respect to all relevant nuisance parameters for the disappearance analysis (blue).

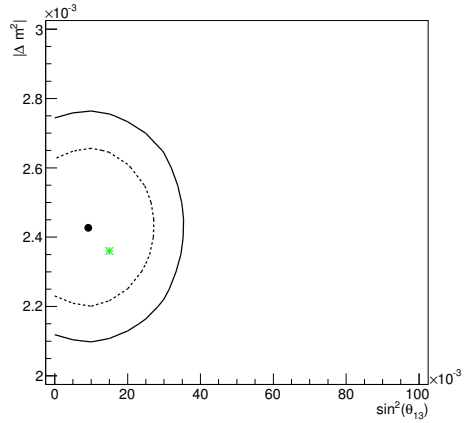

Figure 212: 68% and 90% CL regions in ($sin^2\theta_{13}$, $|\Delta m^2|$) space for fake dataset #10. At each point, χ^2 was minimized with respect to all oscillation parameters not shown (and not considered to be fixed) and all relevant nuisance parameters.

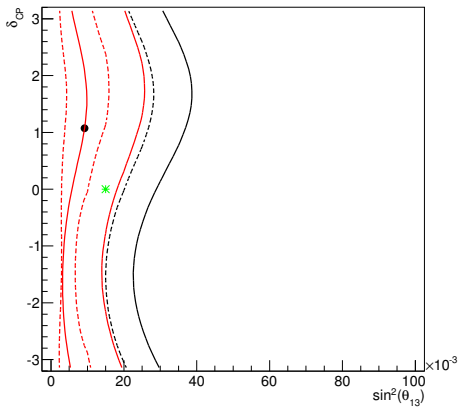

Figure 213: 68% and 90% CL regions in ($sin^2\theta_{13}$, δ_{CP}) space for fake dataset #10. At each point, χ^2 was minimized with respect to $|\Delta m^2|$, $\sin^2\theta_{23}$ and all relevant nuisance parameters for the joint analysis (black) and with respect to all relevant nuisance parameters for the appearance analysis (red). Notice that different methods are used to construct confidence regions for the joint analysis (global minimum) and for the stand-alone appearance analysis (raster scan).

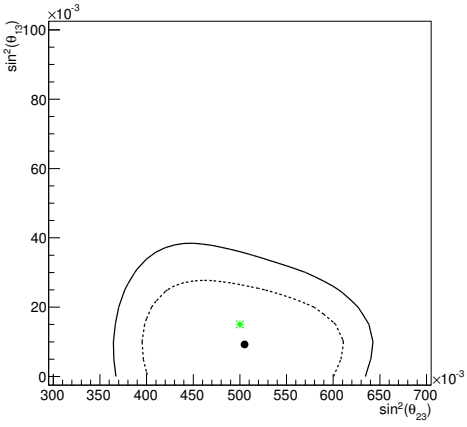

Figure 214: 68% and 90% CL regions in ($sin^2\theta_{23}$, $sin^2\theta_{13}$) space for fake dataset #10. At each point, χ^2 was minimized with respect to all oscillation parameters not shown (and not considered to be fixed) and all relevant nuisance parameters.

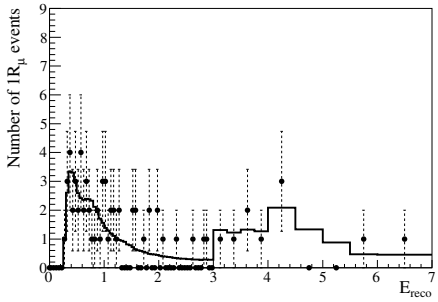

Figure 215: Single μ-like ring event best-fit reconstructed energy spectrum to fake dataset #11.

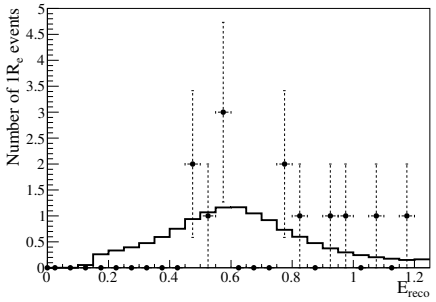

Figure 216: Single e-like ring event best-fit reconstructed energy spectrum to fake dataset #11.

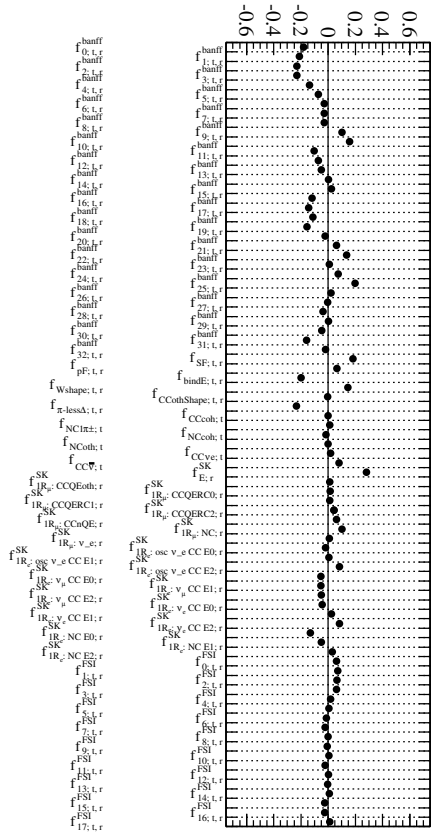

Figure 217: Systematic parameter pulls for the oscillation fit to fake dataset #11.

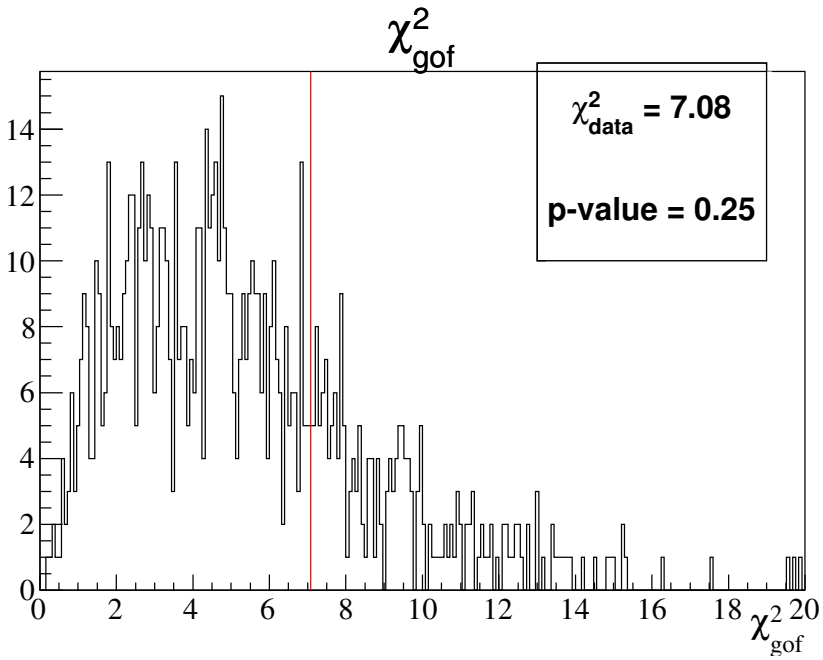

Figure 218: Distribution of χ^2_{gof}, the goodness-of-fit (gof) χ^2, from 1k toy MC experiments generated at dataset #11 joint 3-flavour analysis best-fit oscillation point. The χ^2_{gof} value for the dataset #11 (χ^2_{data}) is highlighted. All χ^2_{gof} values were computed using the 5 (single μ-like ring) + 3 (single e-like ring) reconstructed energy binning scheme described in Sec. 6.2.

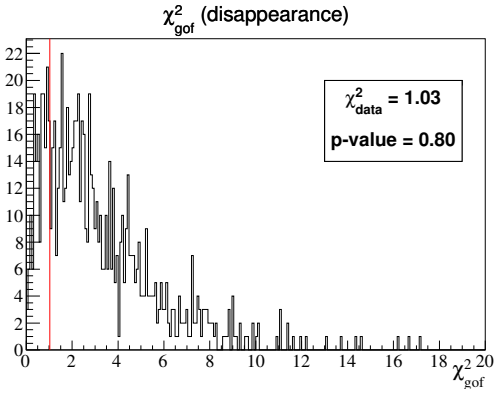

Figure 219: Distribution of χ^2_{gof} from 1k toy MC experiments generated at the dataset #11 stand-alone 3-flavour ν_μ disappearance analysis best-fit oscillation point. The χ^2_{gof} value for the dataset #11 (χ^2_{data}) is highlighted. All χ^2_{gof} values were computed using the 5 (single μ-like ring) reconstructed energy binning scheme described in Sec. 6.2.

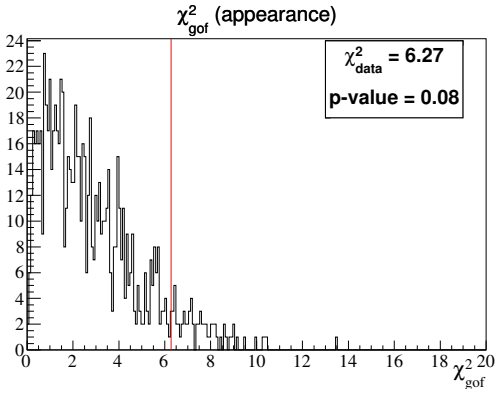

Figure 220: Distribution of χ^2_{gof} from 1k toy MC experiments generated at the dataset #11 stand-alone 3-flavour ν_e appearance analysis best-fit oscillation point. The χ^2_{gof} value for the dataset #11 (χ^2_{data}) is highlighted. All χ^2_{gof} values were computed using the 3 (single e-like ring) reconstructed energy binning scheme as described in Sec. 6.2.

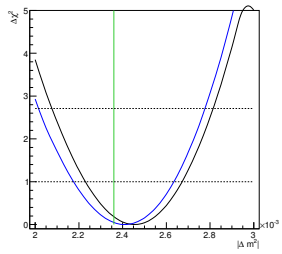

Figure 221: $\Delta\chi^2$ as function of $|\Delta m^2|$ for fake dataset #11. At each point, χ^2 was minimized with respect to $\sin^2\theta_{23}$, $\sin^2\theta_{13}$, δ_{CP} and all relevant nuisance parameters for the joint analysis (black) and with respect to $\sin^2\theta_{23}$ and all relevant nuisance parameters for the disappearance analysis (blue).

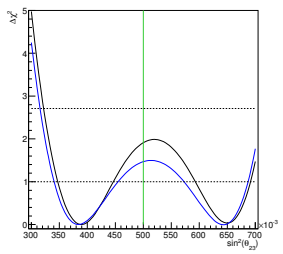

Figure 222: $\Delta\chi^2$ as function of $sin^2\theta_{23}$ for fake dataset #11. At each point, χ^2 was minimized with respect to $|\Delta m^2|$, $\sin^2\theta_{13}$, δ_{CP} and all relevant nuisance parameters for the joint analysis (black) and with respect to $\sin^2\theta_{23}$ and all relevant nuisance parameters for the disappearance analysis (blue).

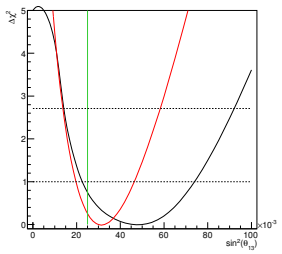

Figure 223: $\Delta\chi^2$ as function of $sin^2\theta_{13}$ for fake dataset #11. At each point, χ^2 was minimized with respect to $\sin^2\theta_{23}$, $\sin^2\theta_{13}$, δ_{CP} and all relevant nuisance parameters for the joint analysis (black) and with respect to all relevant nuisance parameters (δ_{CP} is fixed to 0) for the appearance analysis (red).

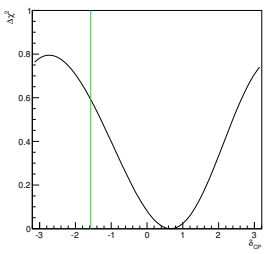

Figure 224: $\Delta\chi^2$ as function of δ_{CP} for fake dataset #11. At each point, χ^2 was minimized with respect to all oscillation parameters not shown (and not considered to be fixed) and all relevant nuisance parameters.

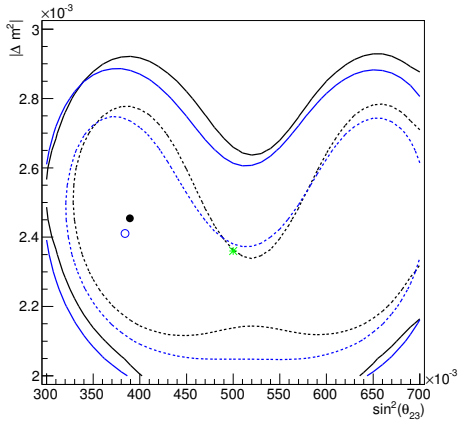

Figure 225: 68% and 90% CL regions in ($sin^2\theta_{23}$, $|\Delta m^2|$) space for fake dataset #11. At each point, χ^2 was minimized with respect to $\sin^2\theta_{13}$, δ_{CP} and all relevant nuisance parameters for the joint analysis (black) and with respect to all relevant nuisance parameters for the disappearance analysis (blue).

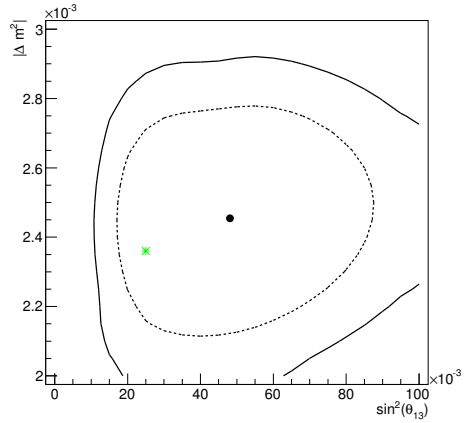

Figure 226: 68% and 90% CL regions in ($sin^2\theta_{13}$, $|\Delta m^2|$) space for fake dataset #11. At each point, χ^2 was minimized with respect to all oscillation parameters not shown (and not considered to be fixed) and all relevant nuisance parameters.

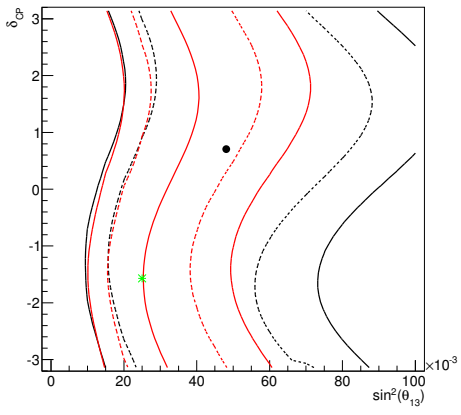

Figure 227: 68% and 90% CL regions in ($sin^2\theta_{13}$, δ_{CP}) space for fake dataset #11. At each point, χ^2 was minimized with respect to $|\Delta m^2|$, $\sin^2\theta_{23}$ and all relevant nuisance parameters for the joint analysis (black) and with respect to all relevant nuisance parameters for the appearance analysis (red). Notice that different methods are used to construct confidence regions for the joint analysis (global minimum) and for the stand-alone appearance analysis (raster scan).

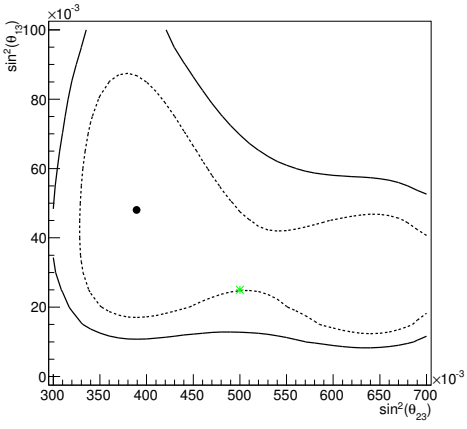

Figure 228: 68% and 90% CL regions in ($sin^2\theta_{23}$, $sin^2\theta_{13}$) space for fake dataset #11. At each point, χ^2 was minimized with respect to all oscillation parameters not shown (and not considered to be fixed) and all relevant nuisance parameters.

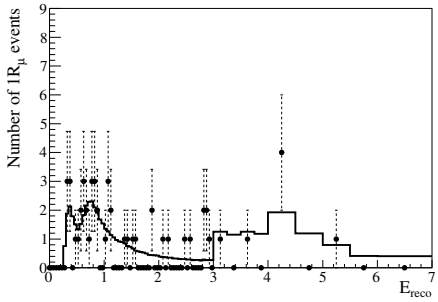

Figure 229: Single μ-like ring event best-fit reconstructed energy spectrum to fake dataset #12.

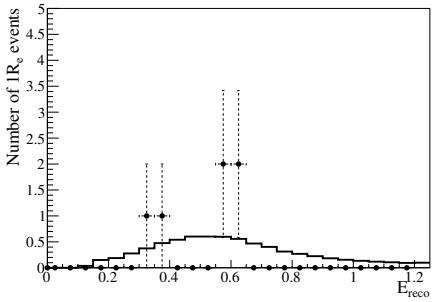

Figure 230: Single e-like ring event best-fit reconstructed energy spectrum to fake dataset #12.

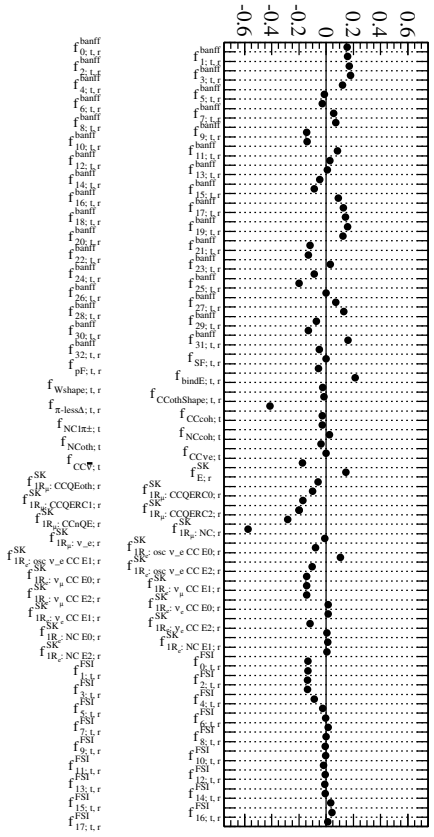

Figure 231: Systematic parameter pulls for the oscillation fit to fake dataset #12.

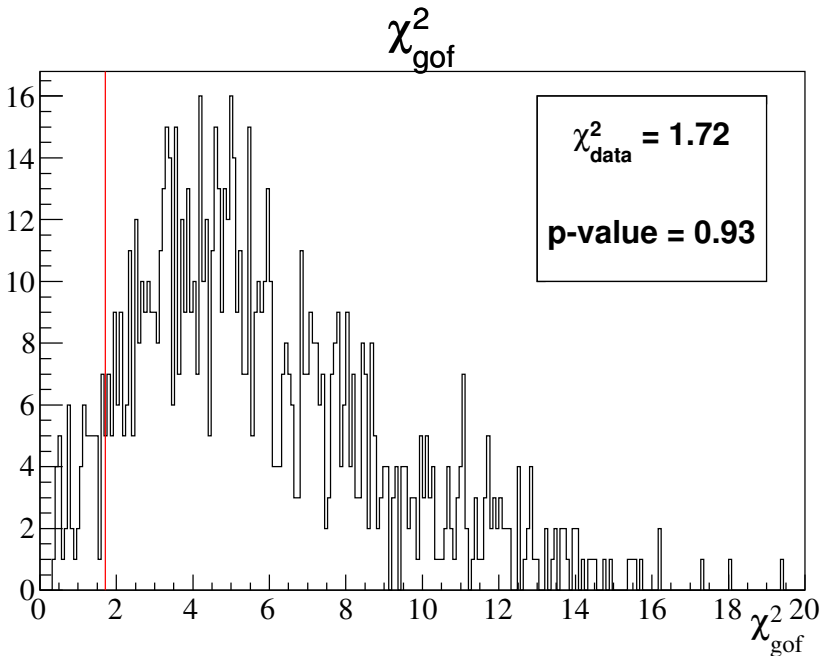

Figure 232: Distribution of χ^2_{gof}, the goodness-of-fit (gof) χ^2, from 1k toy MC experiments generated at dataset #12 joint 3-flavour analysis best-fit oscillation point. The χ^2_{gof} value for the dataset #12 (χ^2_{data}) is highlighted. All χ^2_{gof} values were computed using the 5 (single μ-like ring) + 3 (single e-like ring) reconstructed energy binning scheme described in Sec. 6.2.

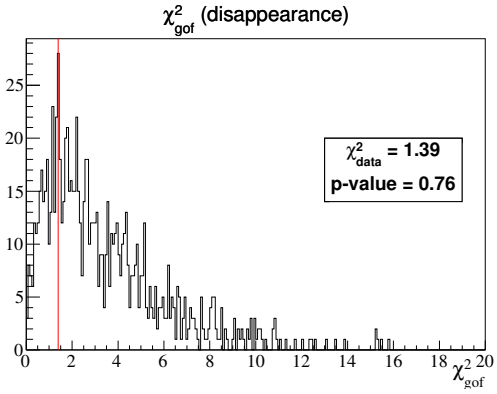

Figure 233: Distribution of χ^2_{gof} from 1k toy MC experiments generated at the dataset #12 stand-alone 3-flavour ν_μ disappearance analysis best-fit oscillation point. The χ^2_{gof} value for the dataset #12 (χ^2_{data}) is highlighted. All χ^2_{gof} values were computed using the 5 (single μ-like ring) reconstructed energy binning scheme described in Sec. 6.2.

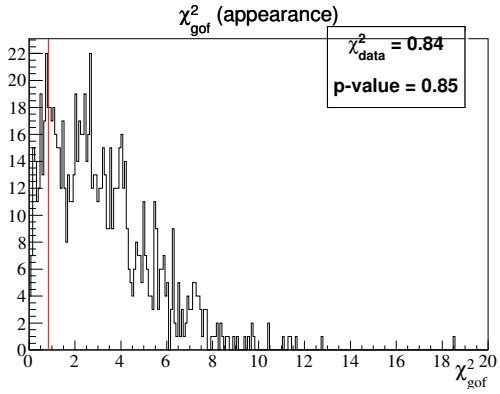

Figure 234: Distribution of χ^2_{gof} from 1k toy MC experiments generated at the dataset #12 stand-alone 3-flavour ν_e appearance analysis best-fit oscillation point. The χ^2_{gof} value for the dataset #12 (χ^2_{data}) is highlighted. All χ^2_{gof} values were computed using the 3 (single e-like ring) reconstructed energy binning scheme as described in Sec. 6.2.

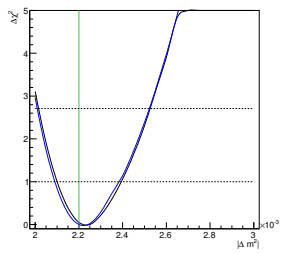

Figure 235: $\Delta\chi^2$ as function of $|\Delta m^2|$ for fake dataset #12. At each point, χ^2 was minimized with respect to $\sin^2\theta_{23}$, $\sin^2\theta_{13}$, δ_{CP} and all relevant nuisance parameters for the joint analysis (black) and with respect to $\sin^2\theta_{23}$ and all relevant nuisance parameters for the disappearance analysis (blue).

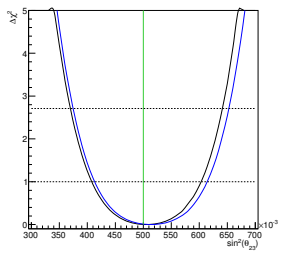

Figure 236: $\Delta\chi^2$ as function of $sin^2\theta_{23}$ for fake dataset #12. At each point, χ^2 was minimized with respect to $|\Delta m^2|$, $\sin^2\theta_{13}$, δ_{CP} and all relevant nuisance parameters for the joint analysis (black) and with respect to $\sin^2\theta_{23}$ and all relevant nuisance parameters for the disappearance analysis (blue).

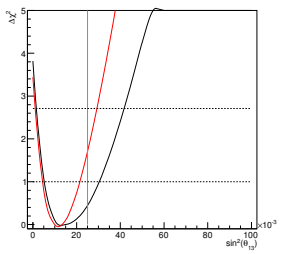

Figure 237: $\Delta\chi^2$ as function of $sin^2\theta_{13}$ for fake dataset #12. At each point, χ^2 was minimized with respect to $\sin^2\theta_{23}$, $\sin^2\theta_{13}$, δ_{CP} and all relevant nuisance parameters for the joint analysis (black) and with respect to all relevant nuisance parameters (δ_{CP} is fixed to 0) for the appearance analysis (red).

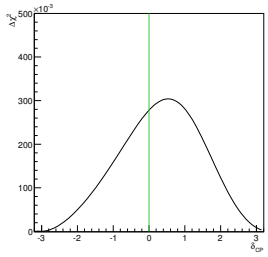

Figure 238: $\Delta\chi^2$ as function of δ_{CP} for fake dataset #12. At each point, χ^2 was minimized with respect to all oscillation parameters not shown (and not considered to be fixed) and all relevant nuisance parameters.

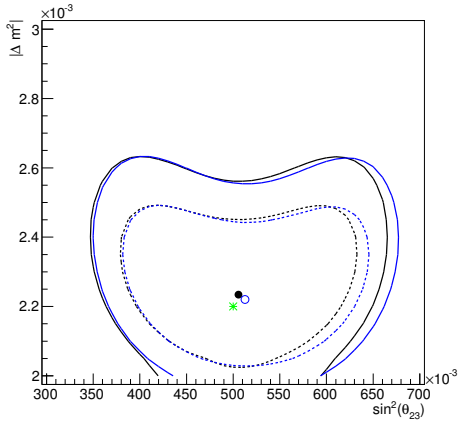

Figure 239: 68% and 90% CL regions in ($sin^2\theta_{23}$, $|\Delta m^2|$) space for fake dataset #12. At each point, χ^2 was minimized with respect to $\sin^2\theta_{13}$, δ_{CP} and all relevant nuisance parameters for the joint analysis (black) and with respect to all relevant nuisance parameters for the disappearance analysis (blue).

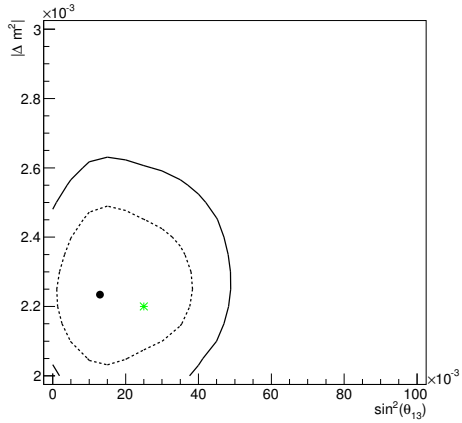

Figure 240: 68% and 90% CL regions in ($sin^2\theta_{13}$, $|\Delta m^2|$) space for fake dataset #12. At each point, χ^2 was minimized with respect to all oscillation parameters not shown (and not considered to be fixed) and all relevant nuisance parameters.

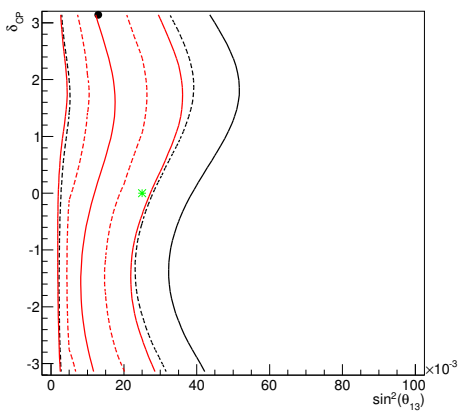

Figure 241: 68% and 90% CL regions in ($sin^2\theta_{13}$, δ_{CP}) space for fake dataset #12. At each point, χ^2 was minimized with respect to $|\Delta m^2|$, $\sin^2\theta_{23}$ and all relevant nuisance parameters for the joint analysis (black) and with respect to all relevant nuisance parameters for the appearance analysis (red). Notice that different methods are used to construct confidence regions for the joint analysis (global minimum) and for the stand-alone appearance analysis (raster scan).

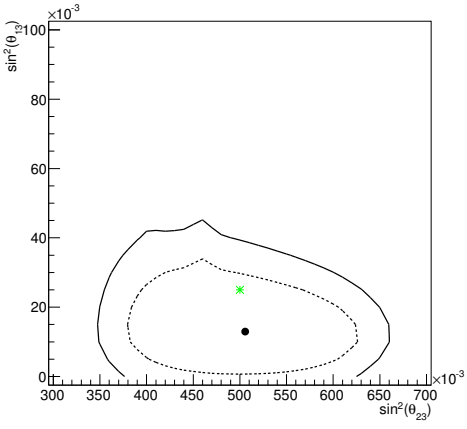

Figure 242: 68% and 90% CL regions in ($sin^2\theta_{23}$, $sin^2\theta_{13}$) space for fake dataset #12. At each point, χ^2 was minimized with respect to all oscillation parameters not shown (and not considered to be fixed) and all relevant nuisance parameters.

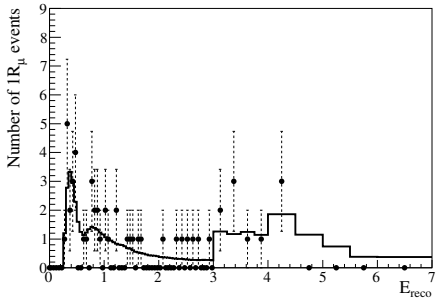

Figure 243: Single μ-like ring event best-fit reconstructed energy spectrum to fake dataset #13.

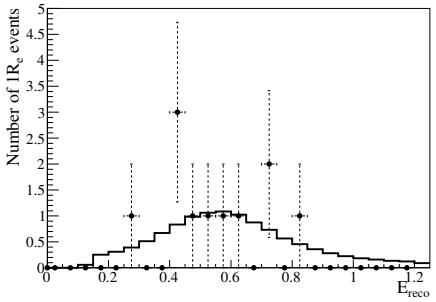

Figure 244: Single e-like ring event best-fit reconstructed energy spectrum to fake dataset #13.

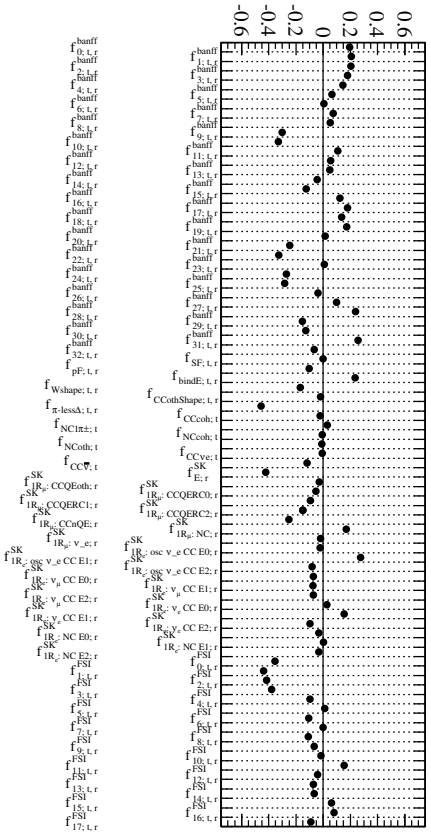

Figure 245: Systematic parameter pulls for the oscillation fit to fake dataset #13.

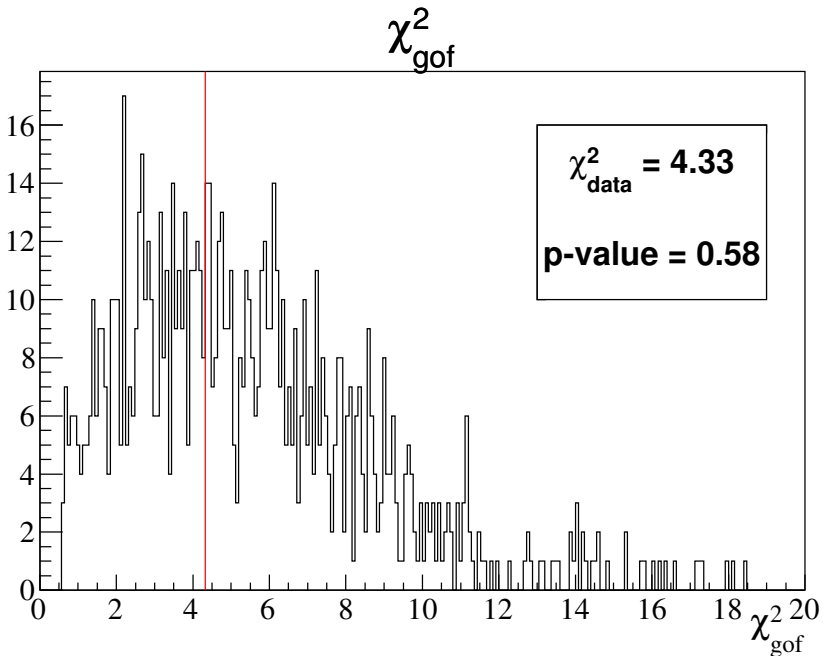

Figure 246: Distribution of χ^2_{gof}, the goodness-of-fit (gof) χ^2, from 1k toy MC experiments generated at dataset #13 joint 3-flavour analysis best-fit oscillation point. The χ^2_{gof} value for the dataset #13 (χ^2_{data}) is highlighted. All χ^2_{gof} values were computed using the 5 (single μ-like ring) + 3 (single e-like ring) reconstructed energy binning scheme described in Sec. 6.2.

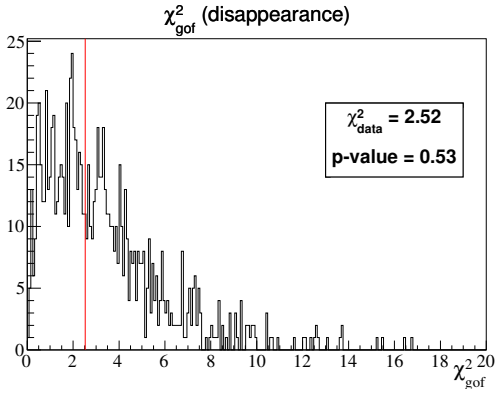

Figure 247: Distribution of χ^2_{gof} from 1k toy MC experiments generated at the dataset #13 stand-alone 3-flavour ν_μ disappearance analysis best-fit oscillation point. The χ^2_{gof} value for the dataset #13 (χ^2_{data}) is highlighted. All χ^2_{gof} values were computed using the 5 (single μ-like ring) reconstructed energy binning scheme described in Sec. 6.2.

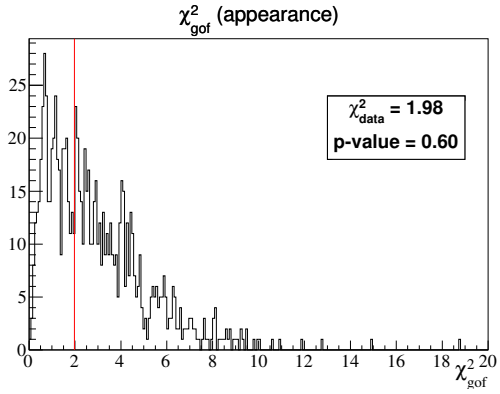

Figure 248: Distribution of χ^2_{gof} from 1k toy MC experiments generated at the dataset #13 stand-alone 3-flavour ν_e appearance analysis best-fit oscillation point. The χ^2_{gof} value for the dataset #13 (χ^2_{data}) is highlighted. All χ^2_{gof} values were computed using the 3 (single e-like ring) reconstructed energy binning scheme as described in Sec. 6.2.

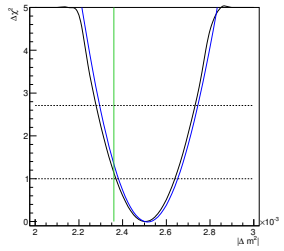

Figure 249: $\Delta\chi^2$ as function of $|\Delta m^2|$ for fake dataset #13. At each point, χ^2 was minimized with respect to $\sin^2\theta_{23}$, $\sin^2\theta_{13}$, δ_{CP} and all relevant nuisance parameters for the joint analysis (black) and with respect to $\sin^2\theta_{23}$ and all relevant nuisance parameters for the disappearance analysis (blue).

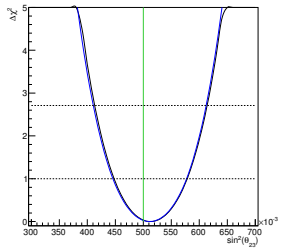

Figure 250: $\Delta\chi^2$ as function of $sin^2\theta_{23}$ for fake dataset #13. At each point, χ^2 was minimized with respect to $|\Delta m^2|$, $\sin^2\theta_{13}$, δ_{CP} and all relevant nuisance parameters for the joint analysis (black) and with respect to $\sin^2\theta_{23}$ and all relevant nuisance parameters for the disappearance analysis (blue).

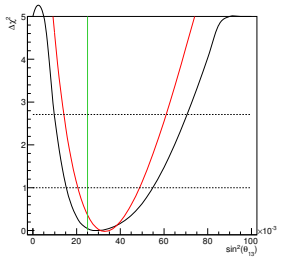

Figure 251: $\Delta\chi^2$ as function of $sin^2\theta_{13}$ for fake dataset #13. At each point, χ^2 was minimized with respect to $\sin^2\theta_{23}$, $\sin^2\theta_{13}$, δ_{CP} and all relevant nuisance parameters for the joint analysis (black) and with respect to all relevant nuisance parameters (δ_{CP} is fixed to 0) for the appearance analysis (red).

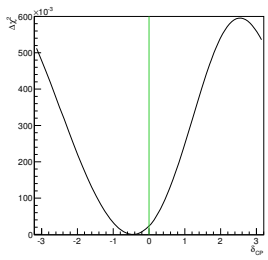

Figure 252: $\Delta\chi^2$ as function of δ_{CP} for fake dataset #13. At each point, χ^2 was minimized with respect to all oscillation parameters not shown (and not considered to be fixed) and all relevant nuisance parameters.

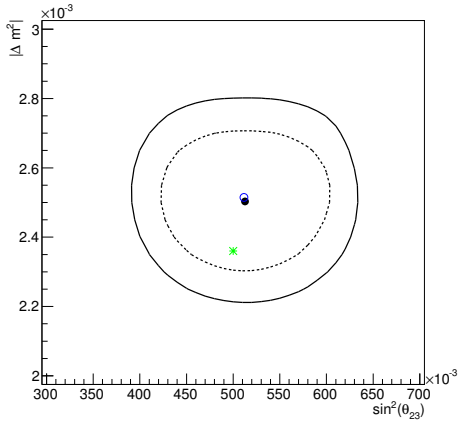

Figure 253: 68% and 90% CL regions in ($sin^2\theta_{23}$, $|\Delta m^2|$) space for fake dataset #13. At each point, χ^2 was minimized with respect to $\sin^2\theta_{13}$, δ_{CP} and all relevant nuisance parameters for the joint analysis (black) and with respect to all relevant nuisance parameters for the disappearance analysis (blue).

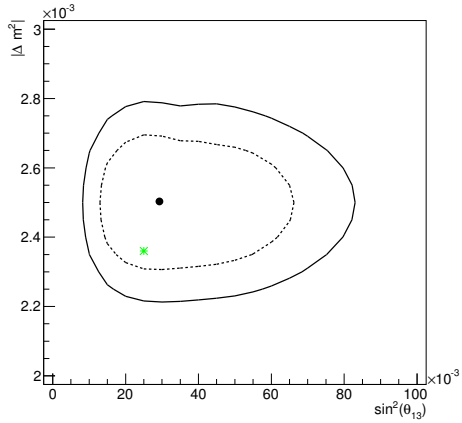

Figure 254: 68% and 90% CL regions in ($sin^2\theta_{13}$, $|\Delta m^2|$) space for fake dataset #13. At each point, χ^2 was minimized with respect to all oscillation parameters not shown (and not considered to be fixed) and all relevant nuisance parameters.

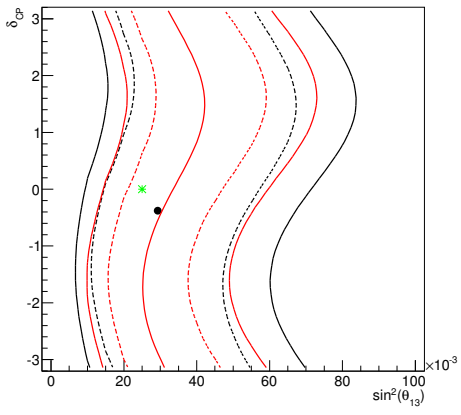

Figure 255: 68% and 90% CL regions in ($sin^2\theta_{13}$, δ_{CP}) space for fake dataset #13. At each point, χ^2 was minimized with respect to $|\Delta m^2|$, $\sin^2\theta_{23}$ and all relevant nuisance parameters for the joint analysis (black) and with respect to all relevant nuisance parameters for the appearance analysis (red). Notice that different methods are used to construct confidence regions for the joint analysis (global minimum) and for the stand-alone appearance analysis (raster scan).

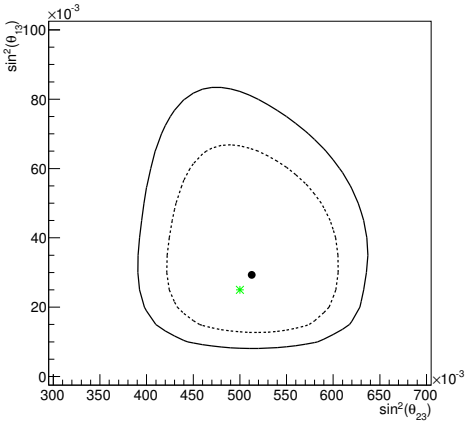

Figure 256: 68% and 90% CL regions in ($sin^2\theta_{23}$, $sin^2\theta_{13}$) space for fake dataset #13. At each point, χ^2 was minimized with respect to all oscillation parameters not shown (and not considered to be fixed) and all relevant nuisance parameters.

D. 3.010×10^20 POT sensitivity studies

A sensitivity study was performed at each of the true oscillation parameter points shown in Tab. 21. For each point the profile $\Delta\chi^2$ distribution is shown as a function of each of the oscillation parameters $|\Delta m^2|$, $\sin^2\theta_{23}$, $\sin^2\theta_{13}$ and δ_{CP}.

In addition, a sensitivity study was performed at the best fit point found for the Run1+2+3 data fit in both hierarchies (Sec. 7). For these best-fit points, the 90% CL regions are also presented in the following four 2-dimensional oscillation parameter spaces: ($\sin^2\theta_{23}$, $|\Delta m^2|$), ($\sin^2\theta_{13}$, $|\Delta m^2|$), ($\sin^2\theta_{13}$, δ_{CP}) and ($\sin^2\theta_{23}$, $\sin^2\theta_{13}$).

To generate each one of the 1-dimensional plots, an average χ^2 was calculated as a function of the oscillation parameters shown on the plot, using fits to an ensemble of several hundreds of toy MC experiments with statistical and systematic fluctuations. In the joint 3-flavour analysis plots, for each toy experiment the χ^2 was minimized with respect to all 83 nuisance parameters and the other oscillation parameters not shown on the plot (as explained in Sec. F, $\sin^2\theta_{12}$ and δm^2 have a negligible effect and they were fixed to 0.311 and 7.5×10^{-5} eV^2/c^4 respectively throughout this analysis). In the stand-alone ν_e-appearance analysis plots, $\sin^2\theta_{23}$ and $|\Delta m^2|$ were also fixed, and the χ^2 was minimized with respect to all 69 nuisance parameters relevant to that analysis, while in the stand-alone ν_μ-disappearance plots $\sin^2\theta_{13}$ and δ_{CP} were fixed, and the χ^2 was minimized with respect to all 57 nuisance parameters relevant to that analysis. This is identical to the method used for the T2K published results. In the plots showing the 90% CL regions in the four 2-dimensional oscillation parameter spaces for the best-fit points found for the Run1+2+3 data fit in both hierarchies, the sensitivity contours were computed by averaging the contours of the ensemble of toy MC experiments generated with statistical fluctuations and all systematic parameters randomized.

The following color scheme is used for all plots:

- green → true,
- black → VaLOR joint 3-flavour oscillation analysis,
- red → VaLOR stand-alone ν_e appearance analysis,
- blue → VaLOR stand-alone ν_μ disappearance analysis, and
- orange → VaLOR joint 3-flavour oscillation analysis, result of the sensitivity study, when compared with data fit.

Sensitivities for true oscillation parameter points in table 21 are shown in Figs. 257 - 280. The sensitivity studies done for true oscillation parameters corresponding to the Run1+2+3 data best-fit point are shown compared with the result from the Run1+2+3 data fit in Figs. 281 - 288 (1-dimensional) and in Figs. 297 - 300 (2-dimensional) for Normal Hierarchy. For Inverted Hierarchy the same study is presented in Figs. 285 - 288 (1-dimensional) and in Figs. 301 - 304 (2-dimensional). Notice that no smoothing was applied to the contours result of the sensitivity studies in Figs. 297 - 304.

The results from these sensitivity studies are consistent with the ones obtained in the study of residuals presented in Sec. B. As an example, in Figs. 257 - 260 sensitivity studies for point #0 in table 21 are presented. It is clear that in Fig. 258 the distribution of averaged $\Delta\chi^2$ got smoothed centered at the center of symmetry of the P($\nu_\mu \to \nu_\mu$) curve (maximal disappearance), whose value, slightly different to the true input value for $\sin^2\theta_{23}$, depends on the true input value of $\sin^2\theta_{13}$ (see Sec. E). Due to this feature, a small bias appears for $|\Delta m^2|$ in Fig. 257, exactly the same that was found in Figs. 57 or 68.

No unexpected features were found.

Point	$\|\Delta m^2\|$ (eV^2/c^4)	$\sin^2\theta_{23}$	$\sin^2\theta_{13}$	δ_{CP}	Hierarchy
0	2.36×10^{-3}	0.5	0.025	0	Normal
1	2.36×10^{-3}	0.38	0.025	0	Normal
2	2.36×10^{-3}	0.5	0.015	0	Normal
3	2.36×10^{-3}	0.5	0.025	$-\pi/2$	Normal
4	2.2×10^{-3}	0.5	0.025	0	Normal
5	2.36×10^{-3}	0.5	0.025	0	Inverted

Table 21: True oscillation parameter points used in the sensitivity study. $\sin^2\theta_{12}$ and δm^2 were fixed to 0.857 and 7.5×10^{-5} eV^2/c^4 respectively (2012 PDG values).

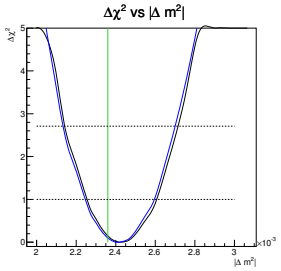

Figure 257: $\Delta\chi^2$ as a function of $|\Delta m^2|$ for true oscillation parameter point #0. χ^2 was averaged over hundreds of toy-MC experiments and, for each experiment, it was minimized with respect to $\sin^2\theta_{23}$, $\sin^2\theta_{13}$, δ_{CP} and all relevant nuisance parameters for the joint analysis (black) and with respect to $\sin^2\theta_{23}$ and all relevant nuisance parameters for the disappearance analysis (blue).

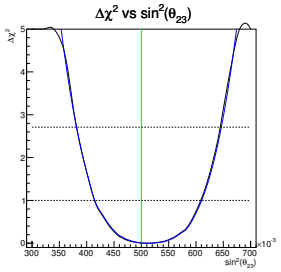

Figure 258: $\Delta\chi^2$ as function of $\sin^2\theta_{23}$ for true oscillation parameter point #0. χ^2 was averaged over hundreds of toy-MC experiments and, for each experiment, it was minimized with respect to $\sin^2\theta_{23}$, $\sin^2\theta_{13}$, δ_{CP} and all relevant nuisance parameters for the joint analysis (black) and with respect to $\sin^2\theta_{23}$ and all relevant nuisance parameters for the disappearance analysis (blue).

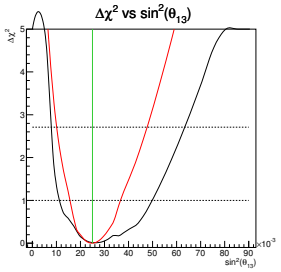

Figure 259: $\Delta\chi^2$ as function of $\sin^2\theta_{13}$ for true oscillation parameter point #0. χ^2 was averaged over hundreds of toy-MC experiments and, for each experiment, it was minimized with respect to $\sin^2\theta_{23}$, $\sin^2\theta_{13}$, δ_{CP} and all relevant nuisance parameters for the joint analysis (black) and with respect to all relevant nuisance parameters (δ_{CP} is fixed to 0) for the appearance analysis (red).

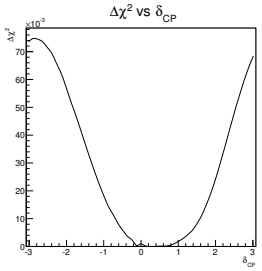

Figure 260: $\Delta\chi^2$ as function of δ_{CP} for true oscillation parameter point #0. χ^2 was averaged over hundreds of toy-MC experiments and, for each experiment, it was minimized with respect to $|\Delta m^2|$, $\sin^2\theta_{23}$, $\sin^2\theta_{13}$ and all relevant nuisance parameters.

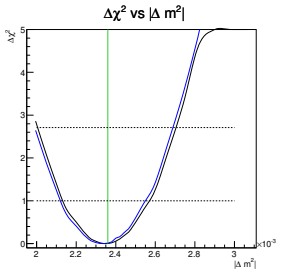

Figure 261: $\Delta\chi^2$ as function of $|\Delta m^2|$ for true oscillation parameter point #1. χ^2 was averaged over hundreds of toy-MC experiments and, for each experiment, it was minimized with respect to $\sin^2\theta_{23}$, $\sin^2\theta_{13}$, δ_{CP} and all relevant nuisance parameters for the joint analysis (black) and with respect to $\sin^2\theta_{23}$ and all relevant nuisance parameters for the disappearance analysis (blue).

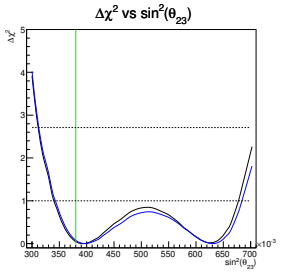

Figure 262: $\Delta\chi^2$ as function of $\sin^2\theta_{23}$ for true oscillation parameter point #1. χ^2 was averaged over hundreds of toy-MC experiments and, for each experiment, it was minimized with respect to $|\Delta m^2|$, $\sin^2\theta_{13}$, δ_{CP} and all relevant nuisance parameters for the joint analysis (black) and with respect to $\sin^2\theta_{23}$ and all relevant nuisance parameters for the disappearance analysis (blue).

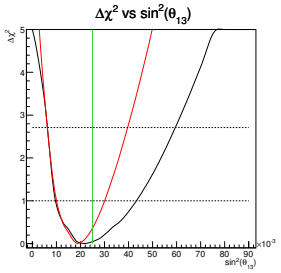

Figure 263: $\Delta\chi^2$ as function of $\sin^2\theta_{13}$ for true oscillation parameter point #1. χ^2 was averaged over hundreds of toy-MC experiments and, for each experiment, it was minimized with respect to $\sin^2\theta_{23}$, $\sin^2\theta_{13}$, δ_{CP} and all relevant nuisance parameters for the joint analysis (black) and with respect to all relevant nuisance parameters (δ_{CP} is fixed to 0) for the appearance analysis (red).

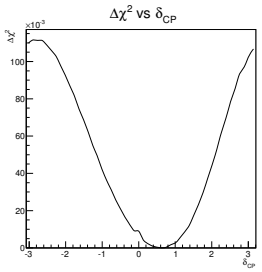

Figure 264: $\Delta\chi^2$ as function of δ_{CP} for true oscillation parameter point #1. χ^2 was averaged over hundreds of toy-MC experiments and, for each experiment, it was minimized with respect to $|\Delta m^2|$, $\sin^2\theta_{23}$, $\sin^2\theta_{13}$ and all relevant nuisance parameters.

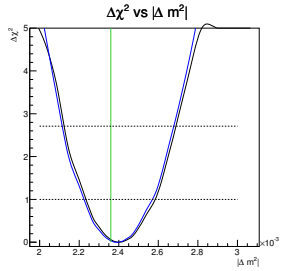

Figure 265: $\Delta\chi^2$ as function of $|\Delta m^2|$ for true oscillation parameter point #2. χ^2 was averaged over hundreds of toy-MC experiments and, for each experiment, it was minimized with respect to $\sin^2\theta_{23}$, $\sin^2\theta_{13}$, δ_{CP} and all relevant nuisance parameters for the joint analysis (black) and with respect to $\sin^2\theta_{23}$ and all relevant nuisance parameters for the disappearance analysis (blue).

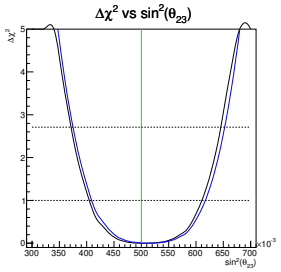

Figure 266: $\Delta\chi^2$ as function of $\sin^2\theta_{23}$ for true oscillation parameter point #2. χ^2 was averaged over hundreds of toy-MC experiments and, for each experiment, it was minimized with respect to $|\Delta m^2|$, $\sin^2\theta_{13}$, δ_{CP} and all relevant nuisance parameters for the joint analysis (black) and with respect to $\sin^2\theta_{23}$ and all relevant nuisance parameters for the disappearance analysis (blue).

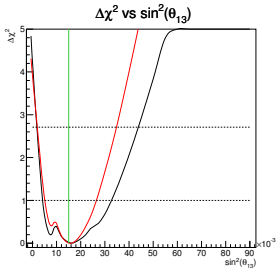

Figure 267: $\Delta\chi^2$ as function of $\sin^2\theta_{13}$ for true oscillation parameter point #2. χ^2 was averaged over hundreds of toy-MC experiments and, for each experiment, it was minimized with respect to $\sin^2\theta_{23}$, $\sin^2\theta_{13}$, δ_{CP} and all relevant nuisance parameters for the joint analysis (black) and with respect to all relevant nuisance parameters (δ_{CP} is fixed to 0) for the appearance analysis (red).

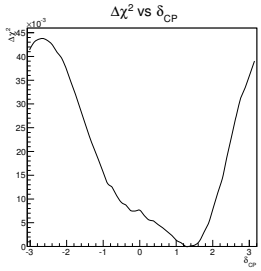

Figure 268: $\Delta\chi^2$ as function of δ_{CP} for true oscillation parameter point #2. χ^2 was averaged over hundreds of toy-MC experiments and, for each experiment, it was minimized with respect to $|\Delta m^2|$, $\sin^2\theta_{23}$, $\sin^2\theta_{13}$ and all relevant nuisance parameters.

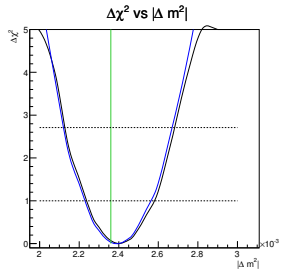

Figure 269: $\Delta\chi^2$ as function of $|\Delta m^2|$ for true oscillation parameter point #3. χ^2 was averaged over hundreds of toy-MC experiments and, for each experiment, it was minimized with respect to $\sin^2\theta_{23}$, $\sin^2\theta_{13}$, δ_{CP} and all relevant nuisance parameters for the joint analysis (black) and with respect to $\sin^2\theta_{23}$ and all relevant nuisance parameters for the disappearance analysis (blue).

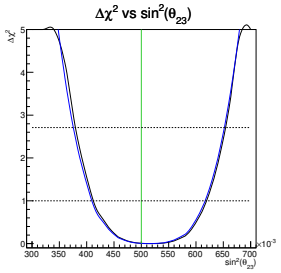

Figure 270: $\Delta\chi^2$ as function of $\sin^2\theta_{23}$ for true oscillation parameter point #3. χ^2 was averaged over hundreds of toy-MC experiments and, for each experiment, it was minimized with respect to $|\Delta m^2|$, $\sin^2\theta_{13}$, δ_{CP} and all relevant nuisance parameters for the joint analysis (black) and with respect to $\sin^2\theta_{23}$ and all relevant nuisance parameters for the disappearance analysis (blue).

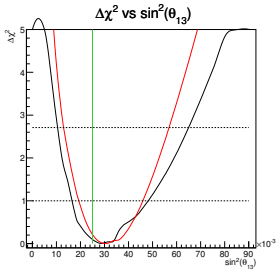

Figure 271: $\Delta\chi^2$ as function of $\sin^2\theta_{13}$ for true oscillation parameter point #3. χ^2 was averaged over hundreds of toy-MC experiments and, for each experiment, it was minimized with respect to $\sin^2\theta_{23}$, $\sin^2\theta_{13}$, δ_{CP} and all relevant nuisance parameters for the joint analysis (black) and with respect to all relevant nuisance parameters (δ_{CP} is fixed to 0) for the appearance analysis (red).

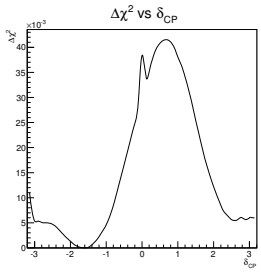

Figure 272: $\Delta\chi^2$ as function of δ_{CP} for true oscillation parameter point #3. χ^2 was averaged over hundreds of toy-MC experiments and, for each experiment, it was minimized with respect to $|\Delta m^2|$, $\sin^2\theta_{23}$, $\sin^2\theta_{13}$ and all relevant nuisance parameters.

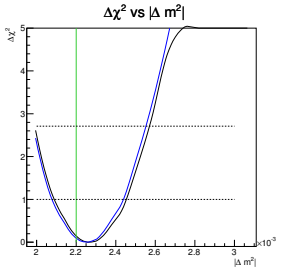

Figure 273: $\Delta\chi^2$ as function of $|\Delta m^2|$ for true oscillation parameter point #4. χ^2 was averaged over hundreds of toy-MC experiments and, for each experiment, it was minimized with respect to $\sin^2\theta_{23}$, $\sin^2\theta_{13}$, δ_{CP} and all relevant nuisance parameters for the joint analysis (black) and with respect to $\sin^2\theta_{23}$ and all relevant nuisance parameters for the disappearance analysis (blue).

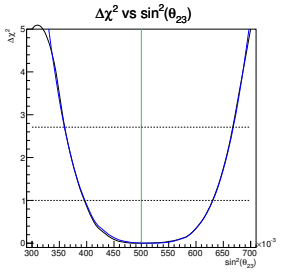

Figure 274: $\Delta\chi^2$ as function of $\sin^2\theta_{23}$ for true oscillation parameter point #4. χ^2 was averaged over hundreds of toy-MC experiments and, for each experiment, it was minimized with respect to $|\Delta m^2|$, $\sin^2\theta_{13}$, δ_{CP} and all relevant nuisance parameters for the joint analysis (black) and with respect to $\sin^2\theta_{23}$ and all relevant nuisance parameters for the disappearance analysis (blue).

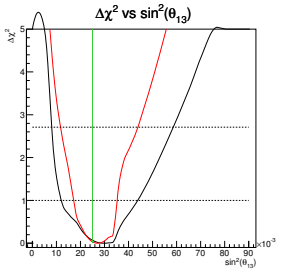

Figure 275: $\Delta\chi^2$ as function of $\sin^2\theta_{13}$ for true oscillation parameter point #4. χ^2 was averaged over hundreds of toy-MC experiments and, for each experiment, it was minimized with respect to $\sin^2\theta_{23}$, $\sin^2\theta_{13}$, δ_{CP} and all relevant nuisance parameters for the joint analysis (black) and with respect to all relevant nuisance parameters (δ_{CP} is fixed to 0) for the appearance analysis (red).

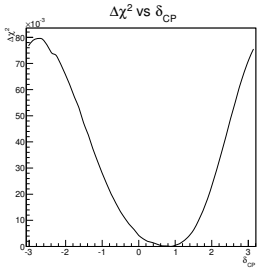

Figure 276: $\Delta\chi^2$ as function of δ_{CP} for true oscillation parameter point #4. χ^2 was averaged over hundreds of toy-MC experiments and, for each experiment, it was minimized with respect to $|\Delta m^2|$, $\sin^2\theta_{23}$, $\sin^2\theta_{13}$ and all relevant nuisance parameters.

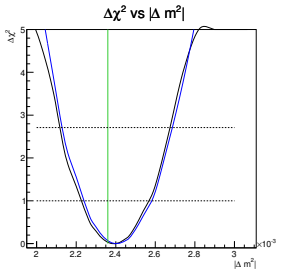

Figure 277: $\Delta\chi^2$ as function of $|\Delta m^2|$ for true oscillation parameter point #5. χ^2 was averaged over hundreds of toy-MC experiments and, for each experiment, it was minimized with respect to $\sin^2\theta_{23}$, $\sin^2\theta_{13}$, δ_{CP} and all relevant nuisance parameters for the joint analysis (black) and with respect to $\sin^2\theta_{23}$ and all relevant nuisance parameters for the disappearance analysis (blue).

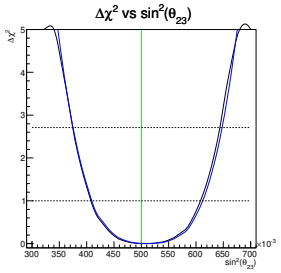

Figure 278: $\Delta\chi^2$ as function of $\sin^2\theta_{23}$ for true oscillation parameter point #5. χ^2 was averaged over hundreds of toy-MC experiments and, for each experiment, it was minimized with respect to $|\Delta m^2|$, $\sin^2\theta_{13}$, δ_{CP} and all relevant nuisance parameters for the joint analysis (black) and with respect to $\sin^2\theta_{23}$ and all relevant nuisance parameters for the disappearance analysis (blue).

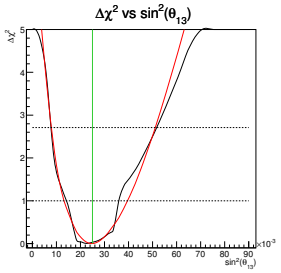

Figure 279: $\Delta\chi^2$ as function of $\sin^2\theta_{13}$ for true oscillation parameter point #5. χ^2 was averaged over hundreds of toy-MC experiments and, for each experiment, it was minimized with respect to $\sin^2\theta_{23}$, $\sin^2\theta_{13}$, δ_{CP} and all relevant nuisance parameters for the joint analysis (black) and with respect to all relevant nuisance parameters (δ_{CP} is fixed to 0) for the appearance analysis (red).

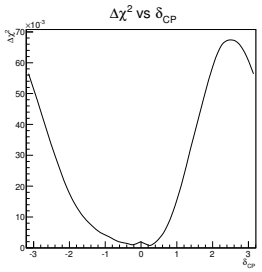

Figure 280: $\Delta\chi^2$ as function of δ_{CP} for true oscillation parameter point #5. χ^2 was averaged over hundreds of toy-MC experiments and, for each experiment, it was minimized with respect to $|\Delta m^2|$, $\sin^2\theta_{23}$, $\sin^2\theta_{13}$ and all relevant nuisance parameters.

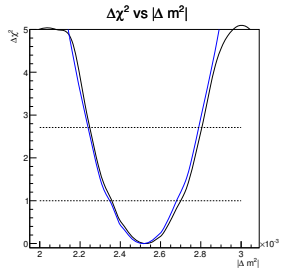

Figure 281: $\Delta\chi^2$ as function of $|\Delta m^2|$ for the best fit point found for Run1+2+3 with Normal Hierarchy. χ^2 was averaged over hundreds of toy-MC experiments and, for each experiment, it was minimized with respect to $\sin^2\theta_{23}$, $\sin^2\theta_{13}$, δ_{CP} and all relevant nuisance parameters for the joint analysis (black) and with respect to $\sin^2\theta_{23}$ and all relevant nuisance parameters for the disappearance analysis (blue).

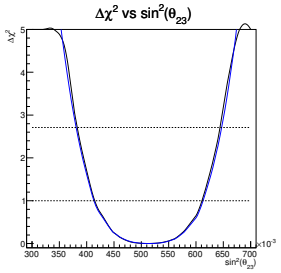

Figure 282: $\Delta\chi^2$ as function of $\sin^2\theta_{23}$ for the best fit point found for Run1+2+3 with Normal Hierarchy. χ^2 was averaged over hundreds of toy-MC experiments and, for each experiment, it was minimized with respect to $\sin^2\theta_{23}$, $\sin^2\theta_{13}$, δ_{CP} and all relevant nuisance parameters for the joint analysis (black) and with respect to $\sin^2\theta_{23}$ and all relevant nuisance parameters for the disappearance analysis (blue).

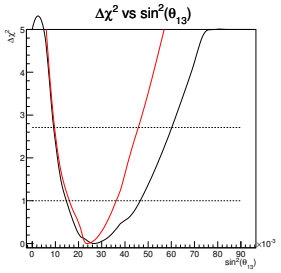

Figure 283: $\Delta\chi^2$ as function of $\sin^2\theta_{13}$ for the best fit point found for Run1+2+3 with Normal Hierarchy. χ^2 was averaged over hundreds of toy-MC experiments and, for each experiment, it was minimized with respect to $\sin^2\theta_{23}$, $\sin^2\theta_{13}$, δ_{CP} and all relevant nuisance parameters for the joint analysis (black) and with respect to all relevant nuisance parameters (δ_{CP} is fixed to 0) for the appearance analysis (red).

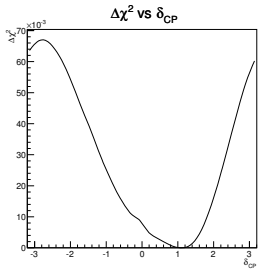

Figure 284: $\Delta\chi^2$ as function of δ_{CP} for the best fit point found for Run1+2+3 with Normal Hierarchy. χ^2 was averaged over hundreds of toy-MC experiments and, for each experiment, it was minimized with respect to $|\Delta m^2|$, $\sin^2\theta_{23}$, $\sin^2\theta_{13}$ and all relevant nuisance parameters.

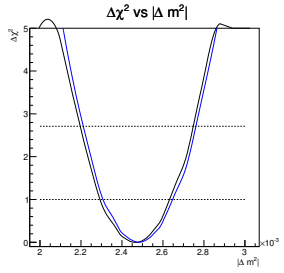

Figure 285: $\Delta\chi^2$ as function of $|\Delta m^2|$ for the best fit point found for Run1+2+3 with Inverted Hierarchy. χ^2 was averaged over hundreds of toy-MC experiments and, for each experiment, it was minimized with respect to $\sin^2\theta_{23}$, $\sin^2\theta_{13}$, δ_{CP} and all relevant nuisance parameters for the joint analysis (black) and with respect to $\sin^2\theta_{23}$ and all relevant nuisance parameters for the disappearance analysis (blue).

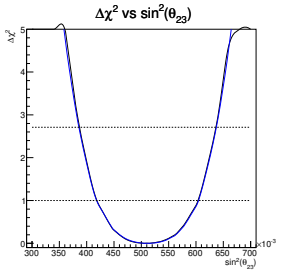

Figure 286: $\Delta\chi^2$ as function of $\sin^2\theta_{23}$ ffor the best fit point found for Run1+2+3 with Inverted Hierarchy. χ^2 was averaged over hundreds of toy-MC experiments and, for each experiment, it was minimized with respect to $\sin^2\theta_{23}$, $\sin^2\theta_{13}$, δ_{CP} and all relevant nuisance parameters for the joint analysis (black) and with respect to $\sin^2\theta_{23}$ and all relevant nuisance parameters for the disappearance analysis (blue).

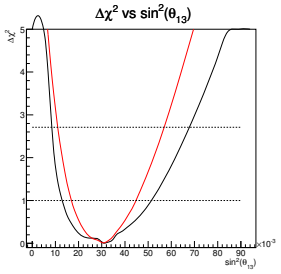

Figure 287: $\Delta\chi^2$ as function of $\sin^2\theta_{13}$ for the best fit point found for Run1+2+3 with Inverted Hierarchy. χ^2 was averaged over hundreds of toy-MC experiments and, for each experiment, it was minimized with respect to $\sin^2\theta_{23}$, $\sin^2\theta_{13}$, δ_{CP} and all relevant nuisance parameters for the joint analysis (black) and with respect to all relevant nuisance parameters (δ_{CP} is fixed to 0) for the appearance analysis (red).

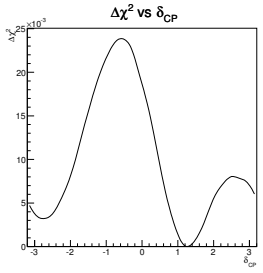

Figure 288: $\Delta\chi^2$ as function of δ_{CP} for the best fit point found for Run1+2+3 with Inverted Hierarchy. χ^2 was averaged over hundreds of toy-MC experiments and, for each experiment, it was minimized with respect to $|\Delta m^2|$, $\sin^2\theta_{23}$, $\sin^2\theta_{13}$ and all relevant nuisance parameters.

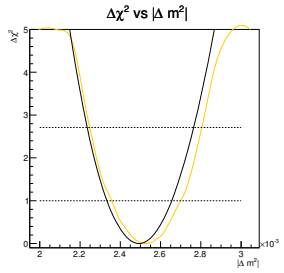

Figure 289: $\Delta\chi^2$ as function of $|\Delta m^2|$ for the best fit point found for Run1+2+3 with Normal Hierarchy. Oranged line is the result of the sensitivity study, where χ^2 was averaged over hundreds of toy-MC experiments and black line is the result of the Run1+2+3 dataset fit.

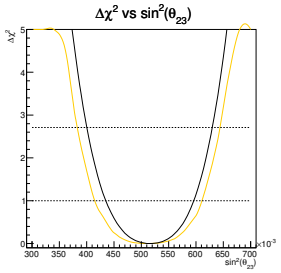

Figure 290: $\Delta\chi^2$ as function of $\sin^2\theta_{23}$ for the best fit point found for Run1+2+3 with Normal Hierarchy. Orange line is the result of the sensitivity study, where χ^2 was averaged over hundreds of toy-MC experiments and black line is the result of the Run1+2+3 dataset fit.

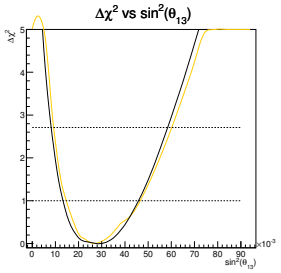

Figure 291: $\Delta\chi^2$ as function of $\sin^2\theta_{13}$ for the best fit point found for Run1+2+3 with Normal Hierarchy. Orange line is the result of the sensitivity study, where χ^2 was averaged over hundreds of toy-MC experiments and black line is the result of the Run1+2+3 dataset fit.

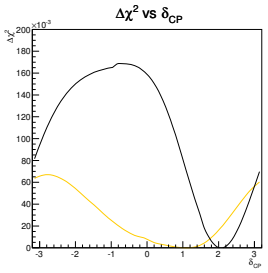

Figure 292: $\Delta\chi^2$ as function of δ_{CP} for the best fit point found for Run1+2+3 with Normal Hierarchy. Orange line is the result of the sensitivity study, where χ^2 was averaged over hundreds of toy-MC experiments and black line is the result of the Run1+2+3 dataset fit.

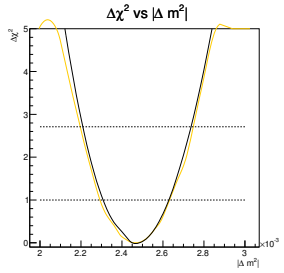

Figure 293: $\Delta\chi^2$ as function of $|\Delta m^2|$ for the best fit point found for Run1+2+3 with Inverted Hierarchy. Orange line is the result of the sensitivity study, where χ^2 was averaged over hundreds of toy-MC experiments and black line is the result of the Run1+2+3 dataset fit.

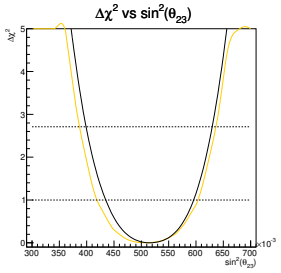

Figure 294: $\Delta\chi^2$ as function of $\sin^2\theta_{23}$ for the best fit point found for Run1+2+3 with Inverted Hierarchy. Orange line is the result of the sensitivity study, where χ^2 was averaged over hundreds of toy-MC experiments and black line is the result of the Run1+2+3 dataset fit.

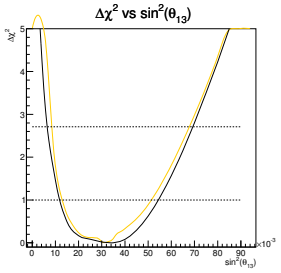

Figure 295: $\Delta\chi^2$ as function of $\sin^2\theta_{13}$ for the best fit point found for Run1+2+3 with Inverted Hierarchy. Orange line is the result of the sensitivity study, where χ^2 was averaged over hundreds of toy-MC experiments and black line is the result of the Run1+2+3 dataset fit.

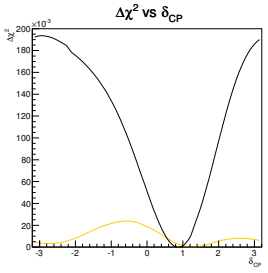

Figure 296: $\Delta\chi^2$ as function of δ_{CP} for the best fit point found for Run1+2+3 with Inverted Hierarchy. Orange line is the result of the sensitivity study, where χ^2 was averaged over hundreds of toy-MC experiments and black line is the result of the Run1+2+3 dataset fit.

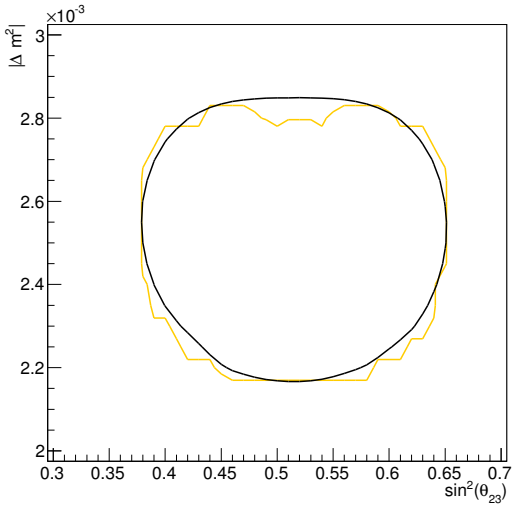

Figure 297: 90% CL region in ($\sin^2\theta_{23}$, $|\Delta m^2|$) space for the best fit point found for Run1+2+3 with Normal Hierarchy. Orange line is the sensitivity contour that was computed by averaging the contours of the ensemble of hundreds of toy MC experiments and, for each experiment, it was minimized with respect to $\sin^2\theta_{13}$, δ_{CP} and all relevant nuisance parameters for the joint analysis. Black line is the result of the Run1+2+3 dataset fit.

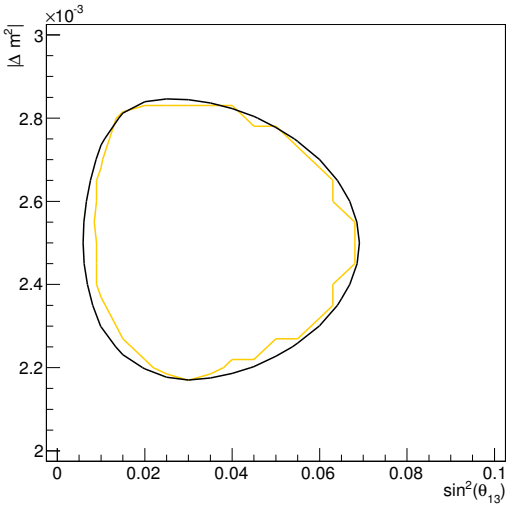

Figure 298: 90% CL region in ($\sin^2\theta_{13}$, $|\Delta m^2|$) space for the best fit point found for Run1+2+3 with Normal Hierarchy. Orange line is the sensitivity contour that was computed by averaging the contours of the ensemble of hundreds of toy MC experiments and, for each experiment, it was minimized with respect to $\sin^2\theta_{13}$, δ_{CP} and all relevant nuisance parameters for the joint analysis. Black line is the result of the Run1+2+3 dataset fit.

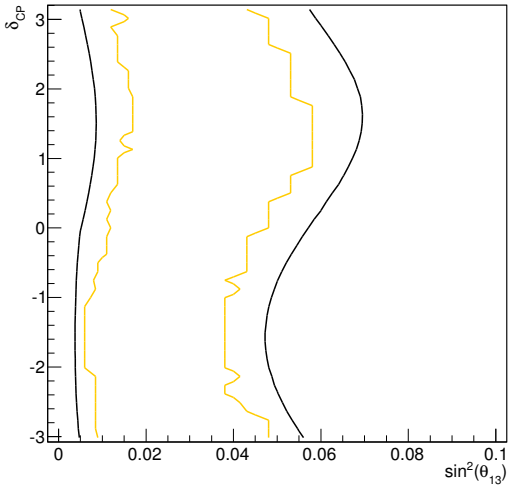

Figure 299: 90% CL region in ($\sin^2\theta_{23}$, δ_{CP}) space for the best fit point found for Run1+2+3 with Normal Hierarchy. Orange line is the sensitivity contour that was computed by averaging the contours of the ensemble of hundreds of toy MC experiments and, for each experiment, it was minimized with respect to $\sin^2\theta_{13}$, δ_{CP} and all relevant nuisance parameters for the joint analysis. Black line is the result of the Run1+2+3 dataset fit.

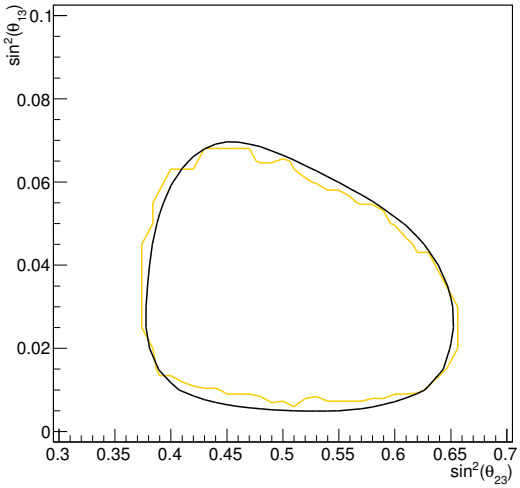

Figure 300: 90% CL region in ($\sin^2\theta_{23}$, $\sin^2\theta_{13}$) space for the best fit point found for Run1+2+3 with Normal Hierarchy. Orange line is the sensitivity contour that was computed by averaging the contours of the ensemble of hundreds of toy MC experiments and, for each experiment, it was minimized with respect to $\sin^2\theta_{13}$, δ_{CP} and all relevant nuisance parameters for the joint analysis. Black line is the result of the Run1+2+3 dataset fit.

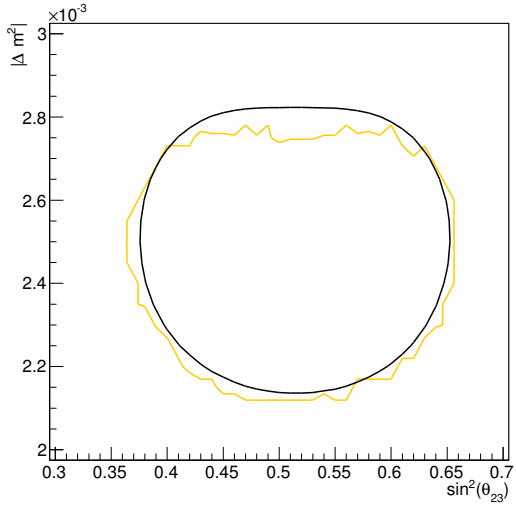

Figure 301: 90% CL region in ($\sin^2\theta_{23}$, $|\Delta m^2|$) space for the best fit point found for Run1+2+3 with Inverted Hierarchy. Orange line is the sensitivity contour that was computed by averaging the contours of the ensemble of hundreds of toy MC experiments and, for each experiment, it was minimized with respect to $\sin^2\theta_{13}$, δ_{CP} and all relevant nuisance parameters for the joint analysis. Black line is the result of the Run1+2+3 dataset fit.

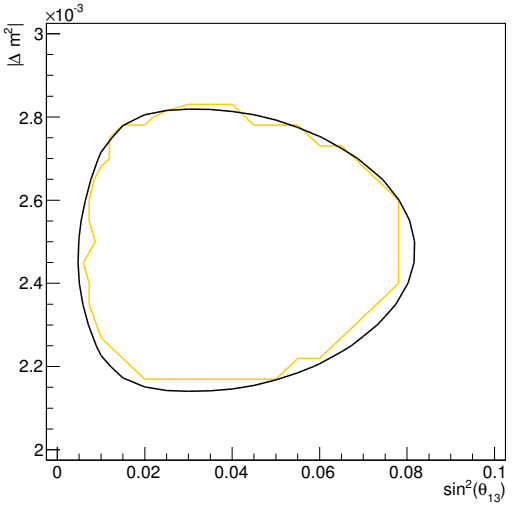

Figure 302: 90% CL region in ($\sin^2\theta_{13}$, $|\Delta m^2|$) space for the best fit point found for Run1+2+3 with Inverted Hierarchy. Orange line is the sensitivity contour that was computed by averaging the contours of the ensemble of hundreds of toy MC experiments and, for each experiment, it was minimized with respect to $\sin^2\theta_{13}$, δ_{CP} and all relevant nuisance parameters for the joint analysis. Black line is the result of the Run1+2+3 dataset fit.

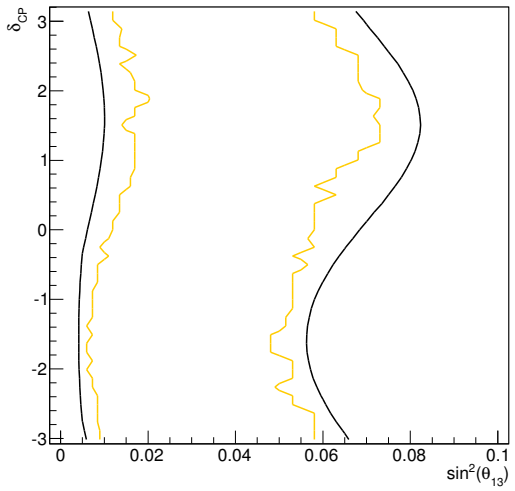

Figure 303: 90% CL region in ($\sin^2\theta_{13}$, δ_{CP}) space for the best fit point found for Run1+2+3 with Normal Hierarchy. Orange line is the sensitivity contour that was computed by averaging the contours of the ensemble of hundreds of toy MC experiments and, for each experiment, it was minimized with respect to $\sin^2\theta_{13}$, δ_{CP} and all relevant nuisance parameters for the joint analysis. Black line is the result of the Run1+2+3 dataset fit.

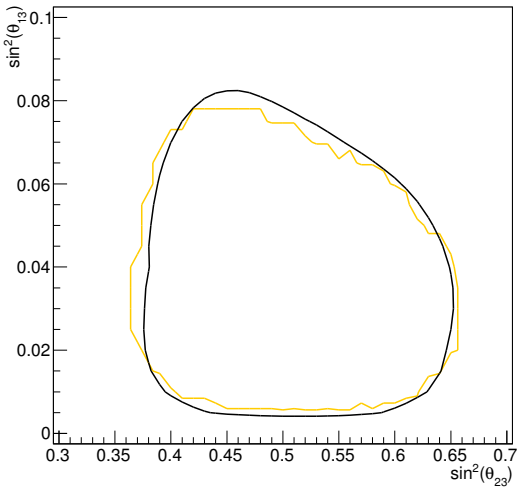

Figure 304: 90% CL region in ($\sin^2\theta_{23}$, $\sin^2\theta_{13}$) space for the best fit point found for Run1+2+3 with Normal Hierarchy. Orange line is the sensitivity contour that was computed by averaging the contours of the ensemble of hundreds of toy MC experiments and, for each experiment, it was minimized with respect to $\sin^2\theta_{13}$, δ_{CP} and all relevant nuisance parameters for the joint analysis. Black line is the result of the Run1+2+3 dataset fit.

E. Difference between $\sin^2\theta_{23}$ values for maximal mixing and maximal disappearance.

As it has been already shown in this note, $\Delta\chi^2$ is not always symmetric with respect to $\sin^2\theta_{23} = 0.5$. The reason for this behaviour will be explained in this section.

The distribution of $\Delta\chi^2$ vs $\sin^2\theta_{23}$ has two minima which are at values of $\sin^2\theta_{23}$ that are symmetric with respect to a center of symmetry (see, for example, figure 106). It seems natural to think that this center of symmetry must be at exactly $\sin^2\theta_{23} = 0.5$ since the value of $\sin^2 2\theta_{23}$ is exactly identical for θ_{23} and $\pi/2 - \theta_{23}$. However it will be shown in this section that the position of the center of symmetry depends on the value of $\sin^2\theta_{13}$ and that it is at 0.5 only if $\sin^2\theta_{13} = 0$.

All the results in this technical note include matter effects, but the following calculation is made using the 3-flavour vacuum oscillation probabilities so that the algebra is manageable:

$$P(\nu_\alpha \to \nu_\beta) = \delta_{\alpha\beta} - 4\sum_{i>j} \mathcal{R}e\left[U^*_{\alpha i}U_{\beta i}U_{\alpha j}U^*_{\beta j}\right] sin^2\left(\frac{\Delta m^2_{ij}L}{4E}\right) + 2\sum_{i>j} \mathcal{I}m\left[U^*_{\alpha i}U_{\beta i}U_{\alpha j}U^*_{\beta j}\right] sin\left(\frac{\Delta m^2_{ij}L}{2E}\right) \quad (7)$$

where U_{ab} represents the ab element of the PMNS matrix:

$$U = \begin{pmatrix} c_{12}c_{13} & c_{13}s_{12} & s_{13}e^{-i\delta} \\ -c_{23}s_{12} - s_{13}s_{23}c_{12}e^{i\delta} & c_{12}c_{23} - s_{12}s_{13}s_{23}e^{i\delta} & c_{13}s_{23} \\ s_{12}s_{23} - s_{13}c_{12}c_{23}e^{i\delta} & -s_{23}c_{12} - s_{12}c_{23}s_{13}e^{i\delta} & c_{13}c_{23} \end{pmatrix} \quad (8)$$

with $s_{12} = \sin(\theta_{12})$, $c_{12} = \cos(\theta_{12})$, etc.

The ν_μ-survival probability is plotted as a function of $\sin^2(\theta_{23})$ in figure 305 for different values of $\sin^2(\theta_{13})$. From this figure, it can be seen that the center of symmetry is only at $\sin^2(\theta_{23}) = 0.5$ for $\sin^2(\theta_{13}) = 0$ and that it moves to higher values of $\sin^2(\theta_{23})$ as $\sin^2(\theta_{13})$ increases, for both mass hierarchies. The center of symmetry of the $P(\nu_\mu \to \nu_\mu)$ curve corresponds to its minimum and therefore to the maximal disappearance, so both terms, center of symmetry of the $P(\nu_\mu \to \nu_\mu)$ curve and maximal disappearance are equivalent.

The 3-flavour ν_μ-survival probability is

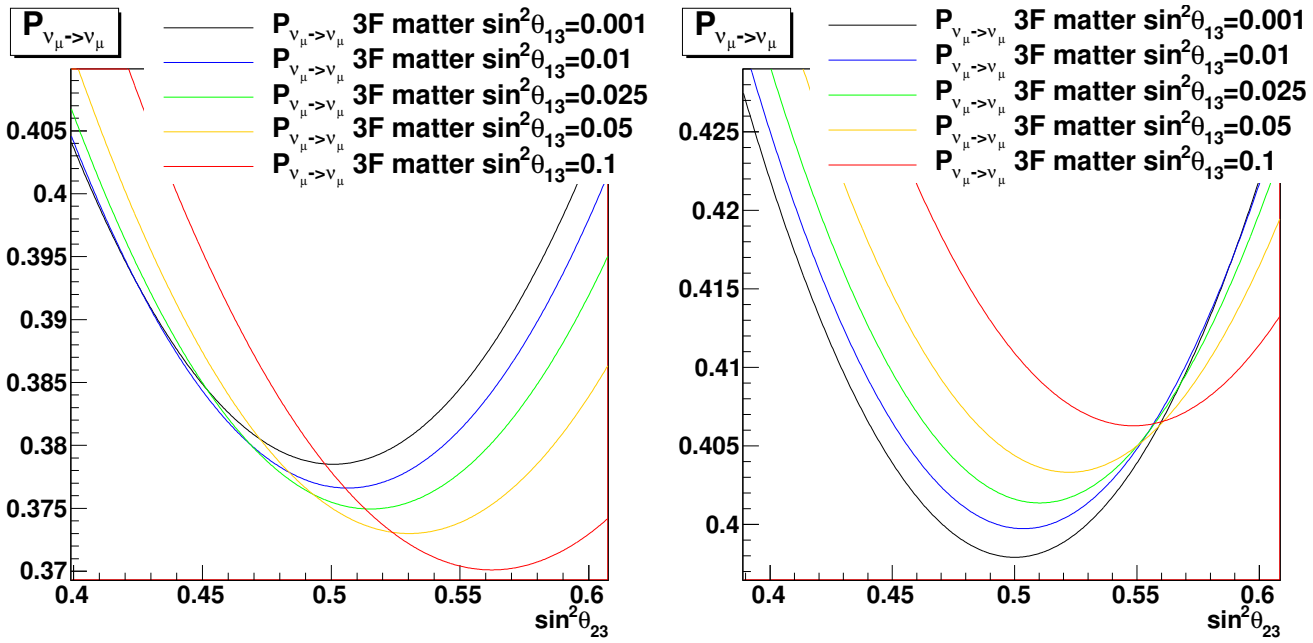

Figure 305: The 3-flavour $P(\nu_\mu \to \nu_\mu)$ with matter effects as a function of $\sin^2\theta_{23}$ for different values of $\sin^2\theta_{13}$ for the normal mass hierarchy (left) and the inverted mass hierarchy (right); $|\Delta m^2_{32}|$ is fixed to 2.4×10^{-3} eV^2/c^4 and δ_{CP} is fixed to 0.

$$
\begin{aligned}
P(\nu_\mu \to \nu_\mu) = 1 &- 4|U_{\mu 2}|^2|U_{\mu 1}|^2 sin^2\left(\tfrac{\Delta m^2_{21} L}{4E}\right) \\
&- 4|U_{\mu 3}|^2|U_{\mu 1}|^2 sin^2\left(\tfrac{\Delta m^2_{31} L}{4E}\right) \\
&- 4|U_{\mu 3}|^2|U_{\mu 2}|^2 sin^2\left(\tfrac{\Delta m^2_{32} L}{4E}\right)
\end{aligned} \tag{9}
$$

where from equation 8 the PMNS matrix elements are

$$
\begin{aligned}
|U_{\mu 1}|^2 &= s^2_{12}c^2_{23} + s^2_{13}s^2_{23}c^2_{12} + 2s_{12}s_{13}s_{23}c_{12}c_{23}cos(\delta) \\
|U_{\mu 2}|^2 &= c^2_{12}c^2_{23} + s^2_{13}s^2_{23}s^2_{12} - 2s_{12}s_{13}s_{23}c_{12}c_{23}cos(\delta) \\
|U_{\mu 3}|^2 &= s^2_{23}c^2_{13}
\end{aligned} \tag{10}
$$

The movement of the center of symmetry can be explained mathematically by making some approximations to the 3-flavour P($\nu_\mu \to \nu_\mu$) in equation 9. Neglecting Δm^2_{21}, and therefore setting $\Delta m^2_{32} \approx \Delta m^2_{31}$, the third terms in $|U_{\mu 1}|^2$ and $|U_{\mu 2}|^2$ cancel each other,

$$
\begin{aligned}
P(\nu_\mu \to \nu_\mu) &\approx 1 - 4\sin^2\left(\frac{\Delta m^2_{31} L}{4E}\right) c^2_{13}s^2_{23}\left[s^2_{12}c^2_{23} + c^2_{12}s^2_{13}s^2_{23} + c^2_{12}c^2_{23} + s^2_{12}s^2_{13}s^2_{23}\right] \\
&= 1 - 4\sin^2\left(\frac{\Delta m^2_{31} L}{4E}\right) c^2_{13}s^2_{23}\left(s^2_{12} + c^2_{12}\right)\left[c^2_{23} + s^2_{13}s^2_{23}\right] \\
&= 1 - 4\sin^2\left(\frac{\Delta m^2_{31} L}{4E}\right) c^2_{13}s^2_{23}\left[c^2_{23} + s^2_{13}s^2_{23}\right]
\end{aligned} \tag{11}
$$

Equation 11 can be written as

$$
y \approx 1 - 4Ax(1-k)\left[(1-x) + kx\right] = 1 - 4Ax(1-k) + 4Ax^2(1-k)^2 \tag{12}
$$

where A = $\sin^2\left(\frac{\Delta m^2_{31} L}{4E}\right)$, x = s^2_{23} = $\sin^2(\theta_{23})$ and k = s^2_{13} = $\sin^2(\theta_{13})$. The minimum of this equation can be found setting the first derivative to zero:

$$
\frac{dy}{dx} = -4A(1-k) + 8Ax(1-k)^2 \tag{13}
$$

Since A $\neq 0$ and (1-k) $\neq 0$ (for an angle $\theta_{13} < \pi/2$), the value of x at which the oscillation probability is at a minimum is

$$
x_{min} = \frac{1}{2(1-k)} \tag{14}
$$

It is clear from equation 14 that x_{min} is at $\frac{1}{2}$ when $\sin^2(\theta_{13})$ = 0. Also the only physically-allowed values of $\sin^2(\theta_{13})$ are ≥ 0, and this means that x_{min} is at $\sin^2(\theta_{23}) > \frac{1}{2}$ when $\sin^2(\theta_{13})$ is non-zero. This simple result explains the dependence on $\sin^2(\theta_{13})$ of the center of symmetry of the P($\nu_\mu \to \nu_\mu$) curve, and therefore the dependence on $\sin^2(\theta_{13})$ of the center of symmetry between the two minima of the $\Delta\chi^2$ distribution when plotted against $\sin^2(\theta_{23})$.

As the true value of $\sin^2(\theta_{23})$ approaches the center of symmetry, the two minima become more difficult to separate. If the true value of $\sin^2(\theta_{23})$ is exactly at the center of symmetry, there is only a single minimum in the distribution of $\Delta\chi^2$ against $\sin^2(\theta_{23})$. For a value of $\sin^2(\theta_{23})$ close to the center of symmetry, the χ^2 distribution becomes smoothed around the center of symmetry when statistical fluctuations are added, and the two minima disappear ending up in a single larger minimum combination of both (see for example Fig. 258). This is the explanation of the bias observed in the distribution of residuals for $\sin^2(\theta_{23})$ for any oscillation point with true input value $\sin^2(\theta_{23}) = 0.5$ in Sec. B.

Usually one of the minima is in each octant, but it is also possible that both minima could be in the second octant. For example, the center of symmetry is at $\sin^2(\theta_{23}) \approx 0.513$ if $\sin^2(\theta_{13}) \approx 0.025$ (from reactor experiments). If the best fit is very close to this center of symmetry, say at $\sin^2(\theta_{23})$ = 0.505, the second minimum is at $\sin^2(\theta_{23})$ = 0.521, i.e. both minima are in the second octant.

As observed in Tab. 13, the best-fit value for $\sin^2\theta_{23}$ is the same in both hierarchies although the best-fit values for the other oscillation parameters are different. Already in Fig. 305 one can see that the bias in $\sin^2\theta_{23}$ with respect to 0.5 at the center of symmetry of the P($\nu_\mu \to \nu_\mu$) curve is different for same values of $\sin^2\theta_{13}$ depending on the mass hierarchy selected (being the difference with 0.5 smaller for Inverted Hierarchy). Figure 306 shows the 3-flavour P($\nu_\mu \to \nu_\mu$) oscillation probability with matter effects as a function of $\sin^2\theta_{23}$ for the best-fit value found for Run1+2+3 dataset with Normal (left) and Inverted (right) Hierarchy. In this figure it is clear that the minimum is found at the best-fit value $\sin^2\theta_{23} = 0.516$ (indicated with a green line) in both hierarchies.

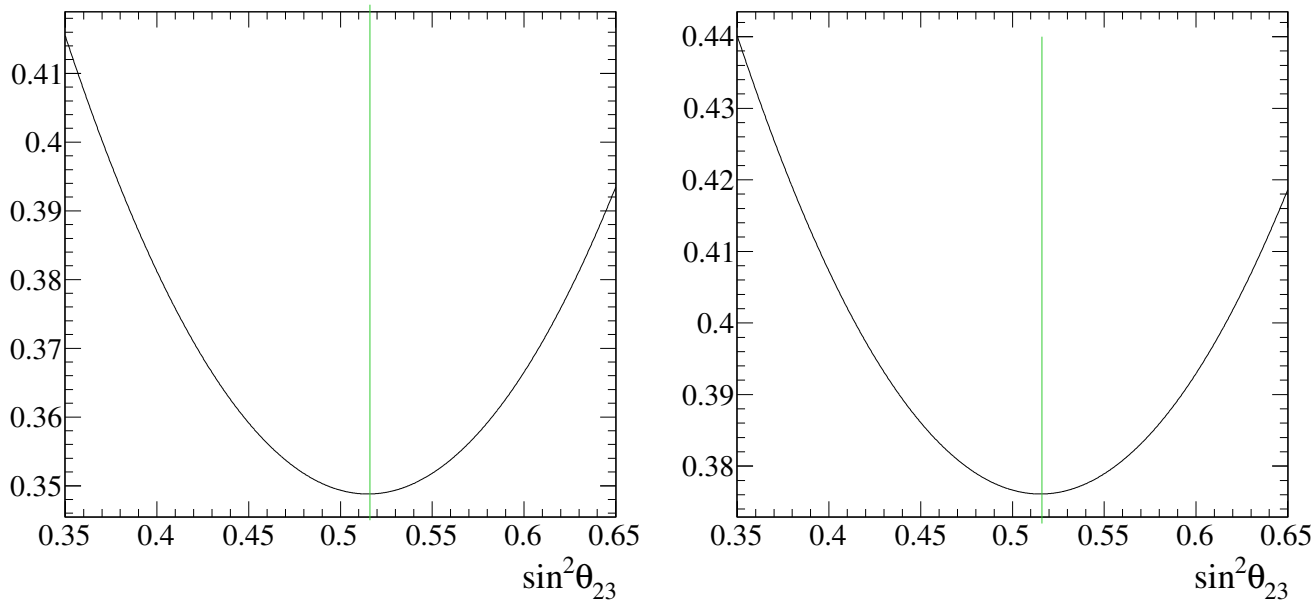

Figure 306: The 3-flavour P($\nu_\mu \rightarrow \nu_\mu$) with matter effects as a function of $\sin^2\theta_{23}$ for the best fit value found for Run1+2+3 dataset fit with Normal Hierarchy (left) and Inverted Hierarchy (right). The values for the left plot are: $\sin^2\theta_{13} = 0.029$, $|\Delta m^2_{32}| = 2.494\times10^{-3}$ eV^2/c^4 and $\delta_{CP} = 2.086$. The values for the right plot are: $\sin^2\theta_{13} = 0.034$, $|\Delta m^2_{32}| = 2.468\times10^{-3}$ eV^2/c^4 and $\delta_{CP} = 0.921$. In both hierarchies the minimum is found at the best-fit value $\sin^2\theta_{23} = 0.516$ (indicated with a green line).

F. Study of the effect of 12-sector (solar) oscillation parameters in the joint oscillation analysis

The effect of including solar parameters, $\sin^2 2\theta_{12}$ and Δm^2_{21}, in the joint fit has been studied. These parameters were allowed to vary in the fit and were marginalized. As shown in Fig. 307, confidence contours became larger when solar parameters are included in the fit. The best fit point for those parameters is at their extreme values allowed in the fit (see Fig. 308), demonstrating that the joint analysis is unable to fit them, even for the estimated final POT.

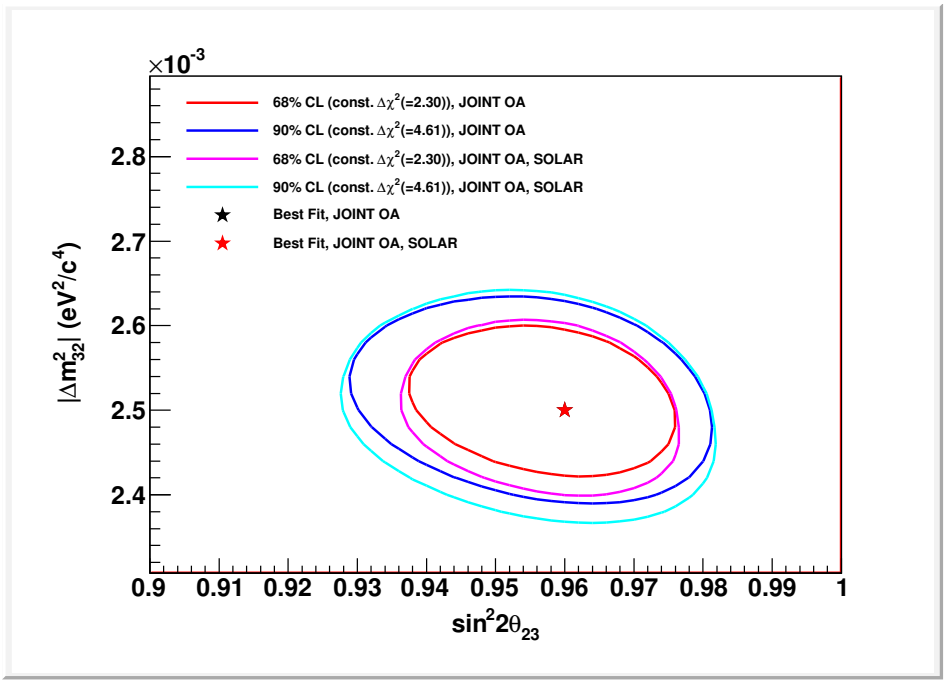

Figure 307: $\sin^2 2\theta_{23}$ versus Δm^2_{32} confidence regions for the estimated final POT (7×10^{21}). Dark colors for the fit with fixed solar parameters and light colors for the fit with marginalized solar parameters.

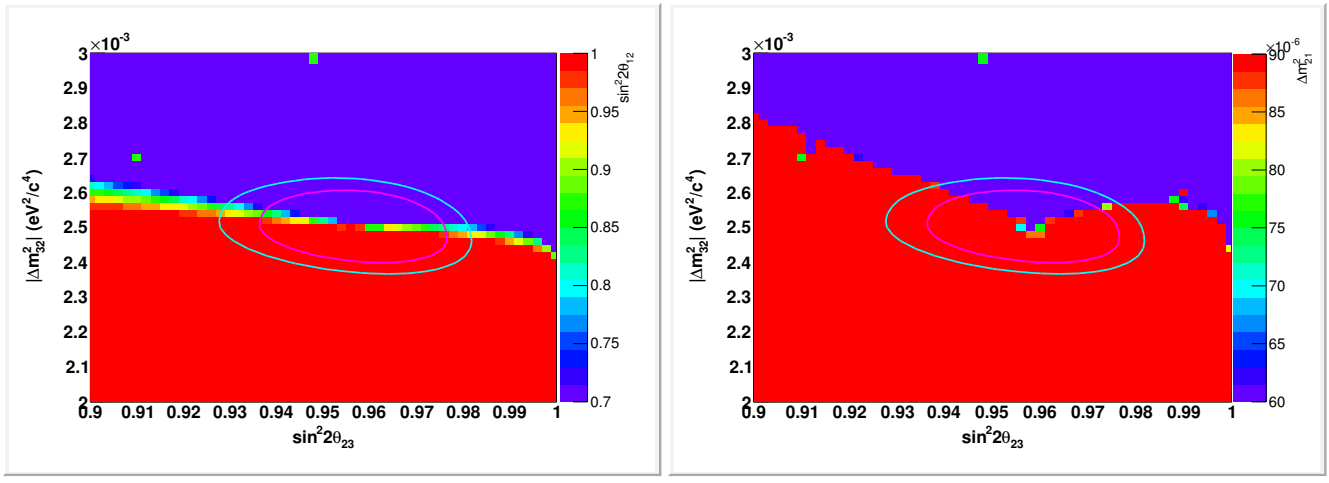

Figure 308: Fitted values of $\sin^2 2\theta_{12}$ (left) and Δm^2_{21} (right) for the joint fit with marginalized solar parameters, for the estimated final POT (7×10^{21}).

G. Further studies for δ_{CP}

Further studies were performed in order to understand the results for δ_{CP} in Sec. B. The residuals (fitted value - true input value) for δ_{CP} in figures 57-77 show that the fitter tends to return 0 or $\pm\pi$ irrespective of the true input value. This behaviour is due to the correlations between $\sin^2\theta_{13}$ and δ_{CP} as it will be explained in this section.

To see how the correlation between $\sin^2\theta_{13}$ and δ_{CP} explains the distribution of residuals, the following test was performed:

1. For one toy experiment with the same true input values as in Fig.57 and no fluctuations, the true χ^2 surface in ($\sin^2\theta_{13}$,δ_{CP}) space (fixing $\sin^2\theta_{23}$ and $|\Delta m^2|$ to their input values) was built. The true χ^2 surface can be found in Fig. 309. Notice that when zooming the true χ^2 surface around a value of $\sin^2\theta_{13}$ (Fig. 309, right plot) the difference in χ^2 for different values of δ_{CP} is very small at current POT.
2. For a selected value of $\sin^2\theta_{13}$, the values of δ_{CP} in the true χ^2 surface with a value of χ^2 in a minimal band defined (with χ^2 smaller than a certain value) are found and a histogram is filled with them.
3. Different values of $\sin^2\theta_{23}$ are selected following a Gaussian distribution around the true input value to reproduce the effect of the distribution of residuals for this parameter in Fig. 57.

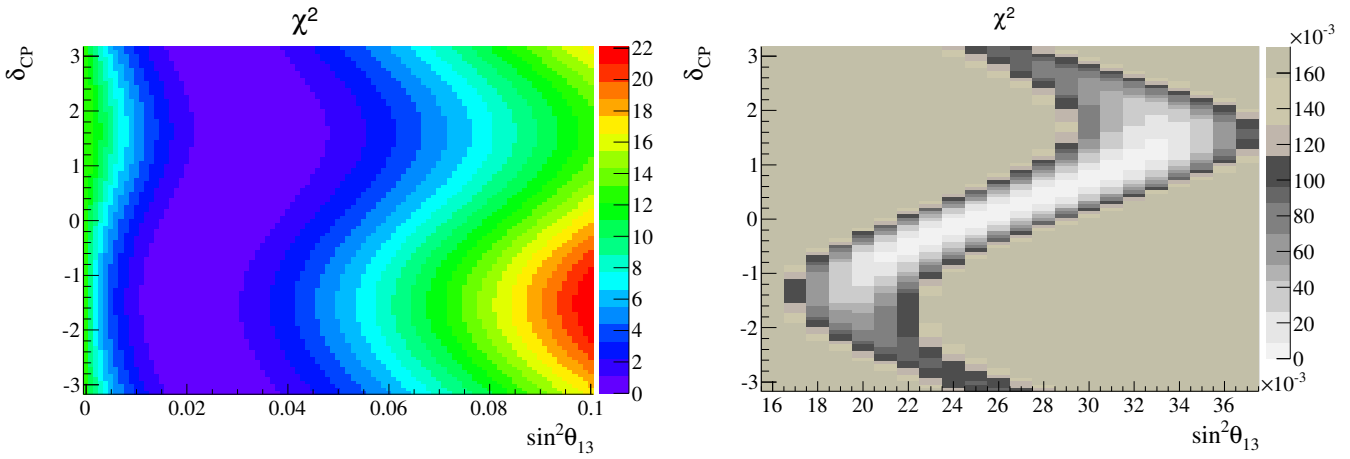

Figure 309: True χ^2 surface in ($\sin^2\theta_{13}$,δ_{CP}) space for a toy experiment with true input values $\sin^2\theta_{23} = 0.5$, $|\Delta m^2| = 2.36 \times 10^{-3}(eV^2/c^4)$, $\sin^2\theta_{13} = 0.025$ and δ_{CP}=0 and no fluctuations, fixing $\sin^2\theta_{23}$ and $|\Delta m^2|$ to their input values. Right, same true χ^2 surface zoomed around true input value for $\sin^2\theta_{13}$.

Figure 310 explains graphically the test made. Figure 311 complements this explanation showing in left top plot the density of points in the true χ^2 minimal band.

The result of the test (Fig. 312, left plot) presents three peaks in the values of $\delta_{CP} = 0$ and $\delta_{CP} = \pm\pi$. The fact that the $P_{\nu_\mu\to\nu_e}$ oscillation probability is almost identical for those values (see Fig. 313) explains these three peaks as well as the S-shape observed in the true χ^2 surface in Fig. 309.

A more realistic result can be obtained if the test is repeated including the deviations in $\sin^2\theta_{23}$ and $\sin^2\theta_{13}$ from Fig. 57. This is done fixing $\sin^2\theta_{23}$ in the construction of the true χ^2 surface to a value slightly different to the one used to create the toy experiment and centering the Gaussian distribution of selected values of $\sin^2\theta_{13}$ slightly biased with respect to its true input value. In this case the central peak is not centered at 0 but biased as can be observed in Fig. 312, right plot, in good agreement with the distribution of residuals for δ_{CP} in Fig. 57.

Now the test was performed again using as true input values $\delta_{CP} = \pm\pi/2$. Figures 314 and 315 show the true χ^2 surface in ($\sin^2\theta_{13}$,δ_{CP}) space for a toy experiment without fluctuations with true input value $\delta_{CP} = \pi/2$ and $\delta_{CP} = -\pi/2$ respectively and a zoom around the true input value for $\sin^2\theta_{13}$. The rest of input values are the same as for Fig. 309. From the zoom of the true χ^2 surface (right plots in 314 and 315) it is clear that selecting values of $\sin^2\theta_{13}$ around its true input value is only going to intersect with the minimum band in one area, giving then a single peak in the distribution for δ_{CP}. The results of the test for these two toy experiments are shown in Fig. 316 ($\delta_{CP} = \pi/2$ left plot, $\delta_{CP} = -\pi/2$ right plot). Those results do not show three peaks as the test for $\delta_{CP} = 0$ but a single peak around the true input value, because no other values of δ_{CP} give the same value of $P_{\nu_\mu\to\nu_e}$ as that for either $\delta_{CP} = \pi/2$ or $\delta_{CP} = -\pi/2$.

However, to reproduce the results observed in Figs. 63 and 64 is necessary to include the biases in $\sin^2\theta_{23}$ and $\sin^2\theta_{13}$ which are much more important now. The result is presented in Fig. 317. Notice that Figs.63 and 64 show the distribution of

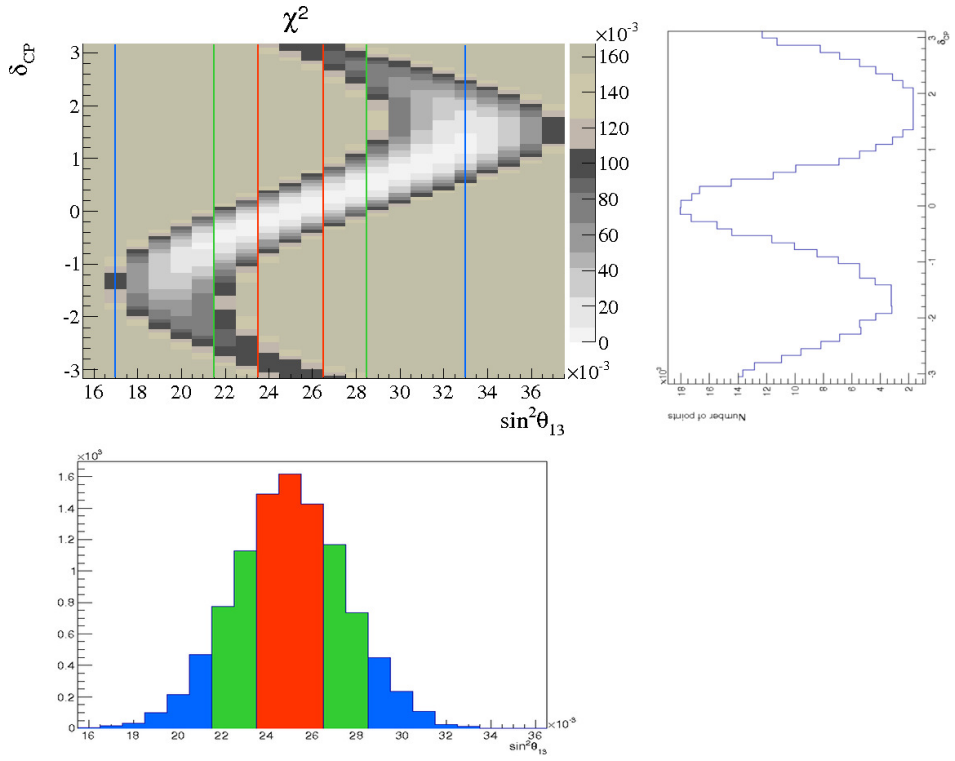

Figure 310: Graphical explanation of the test made to understand the distribution of residuals for δ_{CP}. For the Gaussian distribution of selected values of $\sin^2\theta_{13}$ (left bottom plot) the values of δ_{CP} in the true χ^2 minimal band are found (left top plot) and a histogram is filled with them (right plot).

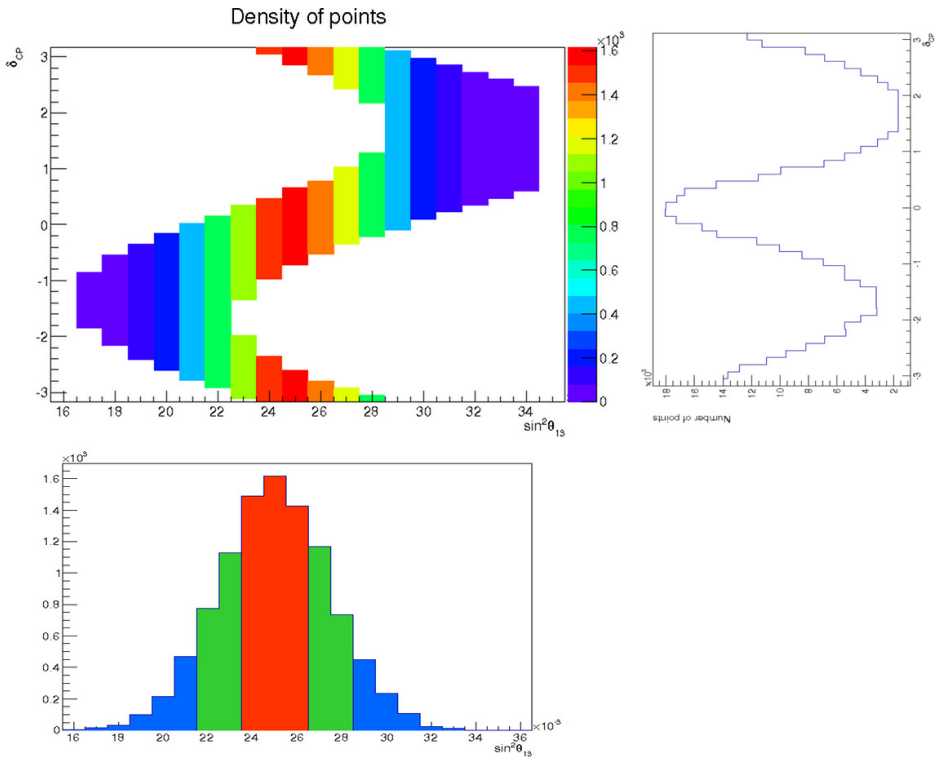

Figure 311: Graphical explanation of the test made to understand the distribution of residuals for δ_{CP}. Same as in figure 311 but replacing left top plot with the density of points in the true χ^2 minimal band.

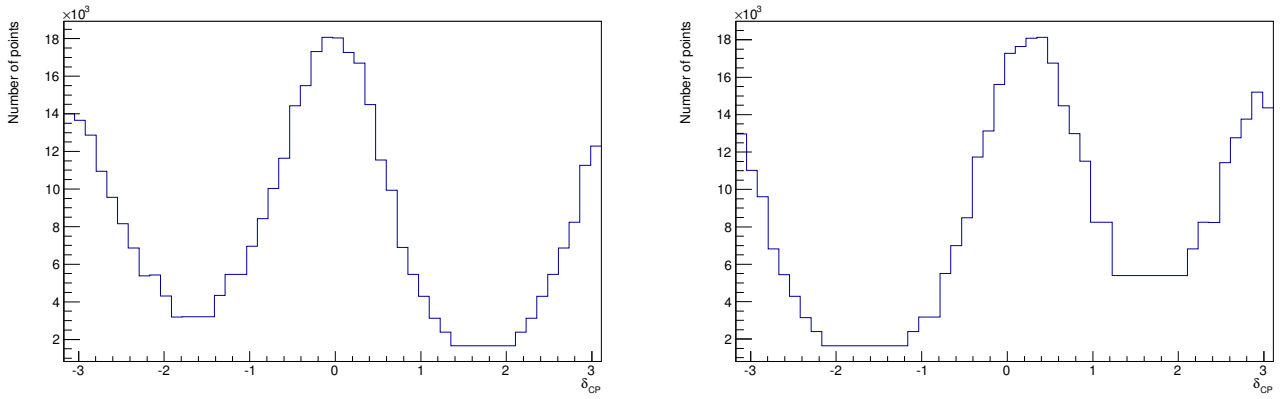

Figure 312: Result of the test explained in figure 310, i.e. the distribution of selected points vs δ_{CP}. On the left, perfect case. On the right, realistic case including the deviations in $\sin^2\theta_{23}$ and $\sin^2\theta_{13}$ from Fig. 57.

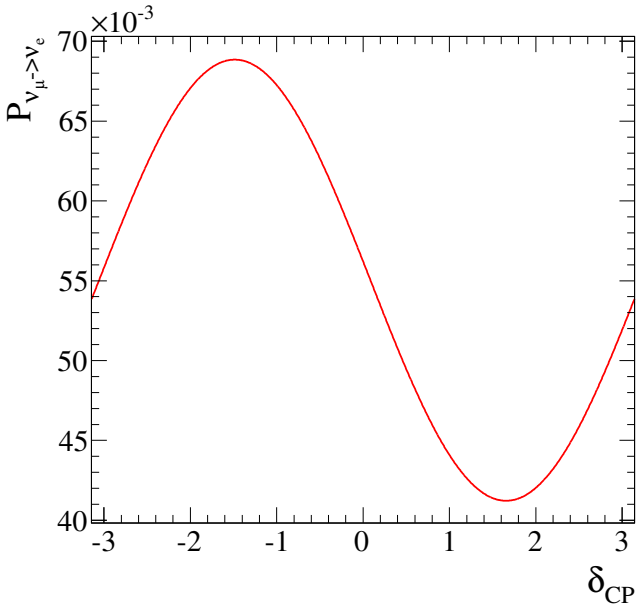

Figure 313: $P_{\nu_\mu \to \nu_e}$ oscillation probability vs δ_{CP} with values $\sin^2\theta_{23} = 0.5$, $|\Delta m^2| = 2.36 \times 10^{-3}(eV^2/c^4)$ and $\sin^2\theta_{13} = 0.025$.

residuals (bestfit - input value) and the result of this test in Fig.317 shows a distribution comparable to bestfit values (not (bestfit - input value)).

The same test was repeated for $\delta_{CP} = \pm\pi/2$ including the biases in $\sin^2\theta_{23}$ and $\sin^2\theta_{13}$ from Figs.63 and 64. Notice that the bias in $\sin^2\theta_{13}$ is much larger than in the case of $\delta_{CP} = 0$ and with opposite senses (mean in $\sin^2\theta_{13} \approx -0.005$ for $\delta_{CP} = \pi/2$ and mean in $\sin^2\theta_{13} \approx 0.006$ for $\delta_{CP} = -\pi/2$, while mean in $\sin^2\theta_{13} \approx 0.0007$ for $\delta_{CP} = 0$). The result of this new test is shown in Fig. 317. As expected, even for those true input values of $\delta_{CP} = \pm\pi/2$ the distribution vs δ_{CP} presents three peaks at $\delta_{CP} = 0$ and $\delta_{CP} = \pm\pi$ when including the corresponding biases in $\sin^2\theta_{23}$ and $\sin^2\theta_{13}$.

An attempt was made to improve the sensitivity to δ_{CP} by constraining the fitted values of the other oscillation parameters. It was found that the sensitivity was improved if $\sin^2\theta_{13}$ was constrained at larger POT (at current POT the constraint in $\sin^2\theta_{13}$ is not efficient due to the small sensitivity): the bias in fitting δ_{CP} was removed if $\sin^2\theta_{13}$ was constrained through the penalty term in equation 5 with an error of 10%, and this is shown in figure 318.

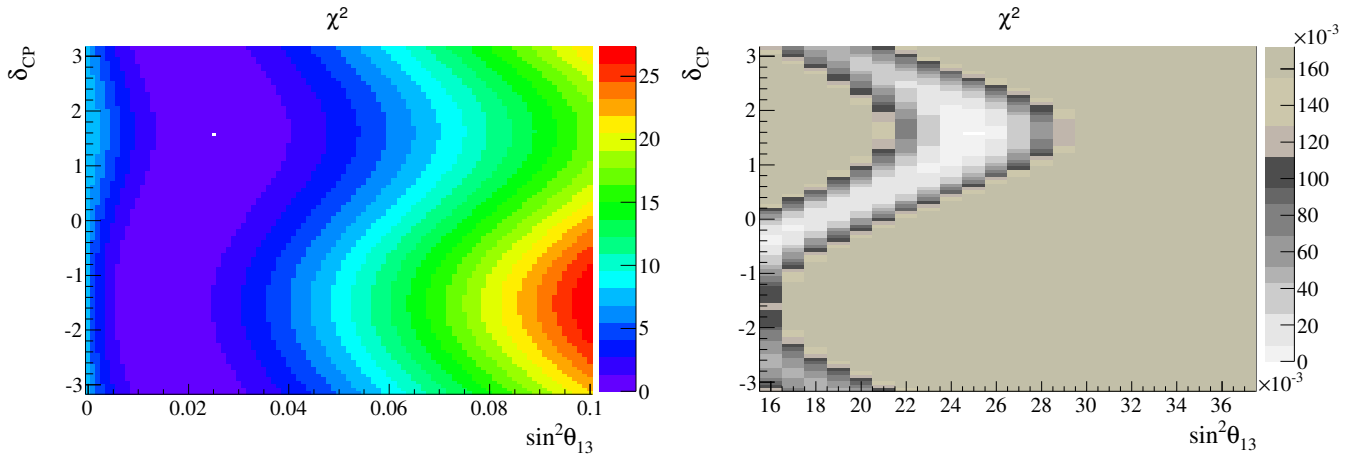

Figure 314: True χ^2 surface in $\sin^2\theta_{13}$,δ_{CP}) space for a toy experiment without fluctuations and with true input values $\sin^2\theta_{23} = 0.5$, $|\Delta m^2| = 2.36 \times 10^{-3}(eV^2/c^4)$, $\sin^2\theta_{13} = 0.025$ and $\delta_{CP} = \pi/2$, fixing $\sin^2\theta_{23}$ and $|\Delta m^2|$ to their input values. Right, same true χ^2 surface zoomed around true input value for $\sin^2\theta_{13}$.

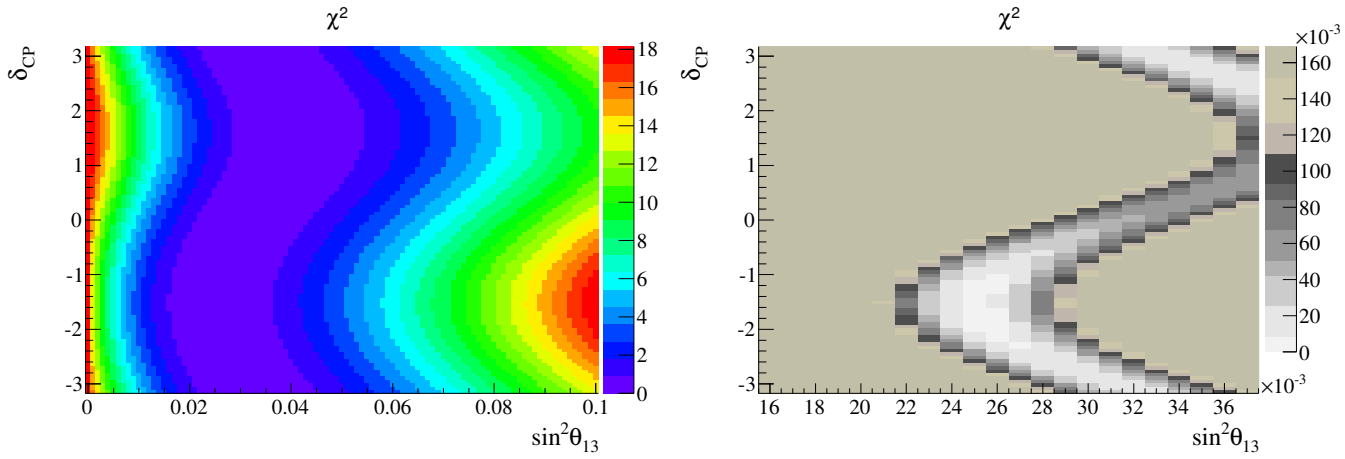

Figure 315: True χ^2 surface in $\sin^2\theta_{13}$,δ_{CP}) space for a toy experiment without fluctuations and with true input values $\sin^2\theta_{23} = 0.5$, $|\Delta m^2| = 2.36 \times 10^{-3}(eV^2/c^4)$, $\sin^2\theta_{13} = 0.025$ and $\delta_{CP} = -\pi/2$, fixing $\sin^2\theta_{23}$ and $|\Delta m^2|$ to their input values. Right, same true χ^2 surface zoomed around true input value for $\sin^2\theta_{13}$.

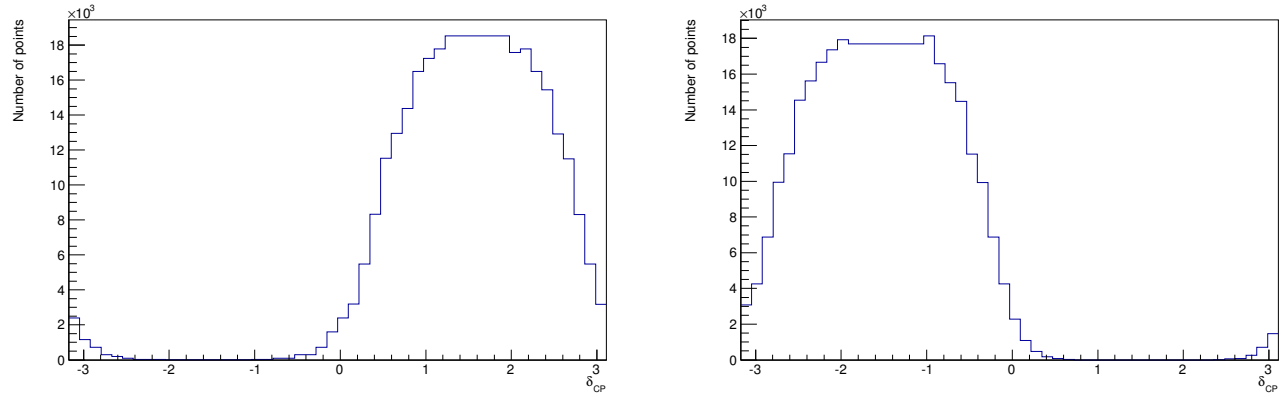

Figure 316: Result of the test explained in figure 310, i.e. the distribution of selected points vs δ_{CP}. Left plot is for $\delta_{CP} = \pi/2$ and right plot is for $\delta_{CP} = -\pi/2$.

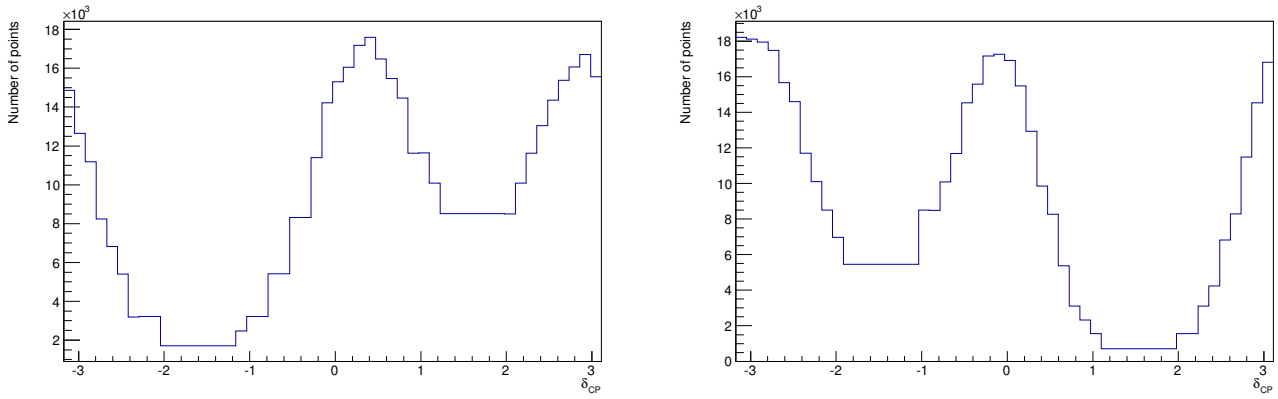

Figure 317: Result of the test explained in figure 310, i.e. the distribution of selected points vs δ_{CP} when including the corresponding biases in $\sin^2\theta_{23}$ and $\sin^2\theta_{13}$ from Figs. 63 and 64. Left plot is for $\delta_{CP} = \pi/2$ and right plot is for $\delta_{CP} = -\pi/2$.

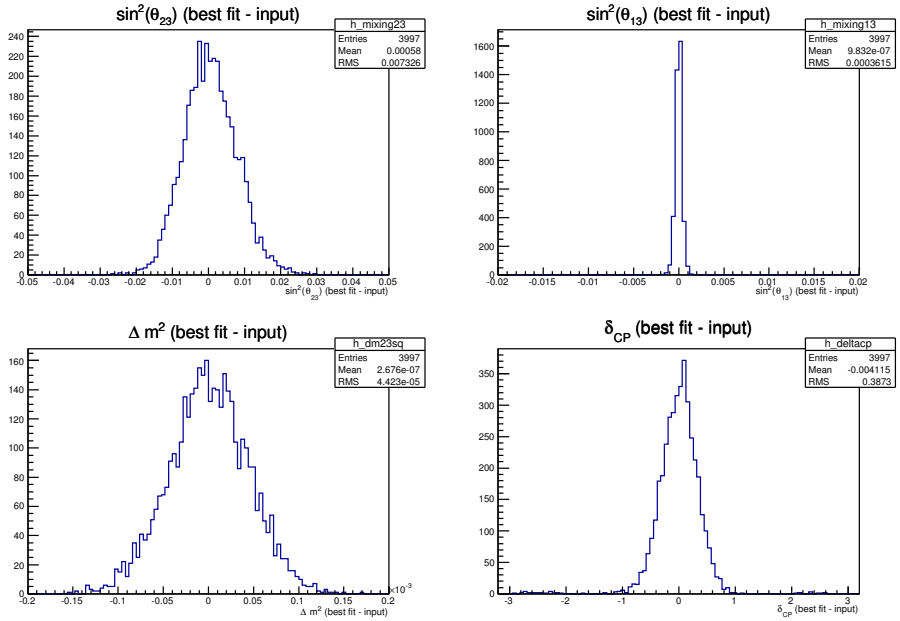

Figure 318: Distribution of residuals of the four oscillation parameters in the '4 + 0' fit for oscillation point with values $\sin^2\theta_{23} = 0.34$, $|\Delta m^2| = 2.4 \times 10^{-3}(eV^2/c^4)$, $\sin^2\theta_{13} = 0.025$ and $\delta_{CP} = 0$ at the T2K goal POT (7.8×10^{21}) constraining $\sin^2\theta_{13}$ with an error of 10%.

The sensitivity improves when constraining θ_{13} since δ_{CP} is always found in combination with $\sin\theta_{13}$ in the PMNS matrix:

$$U = \begin{pmatrix} 1 & 0 & 0 \\ 0 & c_{23} & s_{23} \\ 0 & -s_{23} & c_{23} \end{pmatrix} \times \begin{pmatrix} c_{13} & 0 & s_{13}e^{-i\delta} \\ 0 & 1 & 0 \\ -s_{13}e^{\ i\delta} & 0 & c_{13} \end{pmatrix} \times \begin{pmatrix} c_{12} & s_{12} & 0 \\ -s_{12} & c_{12} & 0 \\ 0 & 0 & 1 \end{pmatrix} \tag{15}$$

The test presented in Fig. 318 shows that the distribution of residuals is well behaved and centered at the true value also for δ_{CP} at larger POT, discarding any intrinsic problems in the fitter. It can be repeated for different true input values of δ_{CP}. Figures 319 and 320 shows the same study of residuals for a true input value of $\delta_{CP} = \pi/2$ and $\delta_{CP} = -\pi/2$ respectively. The asymmetry in the residuals for $\sin^2\theta_{13}$ in Figs. 319 and 320 can be explained with the shape of $P_{\nu_\mu \to \nu_e}$ in Fig. 313. When the true input value is $\delta_{CP} = \pi/2$ then $P_{\nu_\mu \to \nu_e}$ is at a minimum, and any different value of δ_{CP} gives a larger $P_{\nu_\mu \to \nu_e}$ so that the fitter tends to compensate this decreasing the fitted value of $\sin^2\theta_{13}$, creating a negative bias. The opposite happens when the true input value is $\delta_{CP} = -\pi/2$: in this case $P_{\nu_\mu \to \nu_e}$ is at a maximum and any other value of δ_{CP} makes $P_{\nu_\mu \to \nu_e}$ to be smaller so that the fitter tries to compensate increasing the fitted value of $\sin^2\theta_{13}$, creating a positive bias.

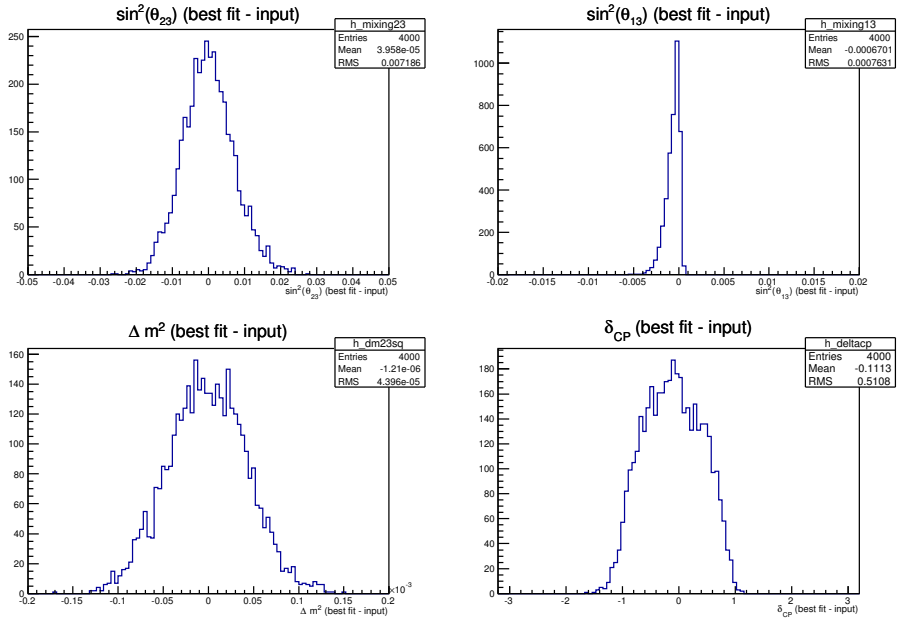

Figure 319: Distribution of residuals of the four oscillation parameters in the '4 + 0' fit for oscillation point with values $\sin^2\theta_{23} = 0.34$, $|\Delta m^2| = 2.4 \times 10^{-3}(eV^2/c^4)$, $\sin^2\theta_{13} = 0.025$ and $\delta_{CP} = \pi/2$ at the T2K goal POT (7.8×10^{21}) constraining $\sin^2\theta_{13}$ with an error of 10%.

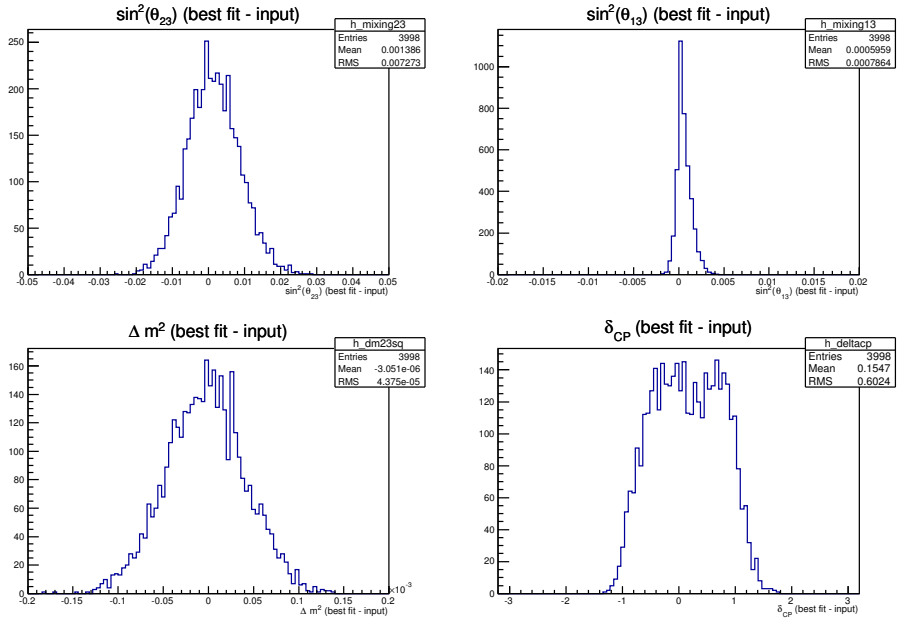

Figure 320: Distribution of residuals of the four oscillation parameters in the '4 + 0' fit for oscillation point with values $\sin^2\theta_{23} = 0.34$, $|\Delta m^2| = 2.4 \times 10^{-3}(eV^2/c^4)$, $\sin^2\theta_{13} = 0.025$ and $\delta_{CP} = -\pi/2$ at the T2K goal POT (7.8×10^{21}).

From the results presented in this appendix it can be concluded that the distributions of residuals for δ_{CP} in figures 57-77 make sense.

H. Comparison between results in the two mass hierarchies using the Fogli and Lisi convention $\left(|\Delta m^2|, \delta m^2\right)$ and the $\left(|\Delta m^2_{32}|, \Delta m^2_{21}\right)$ convention.

As discussed in Sec. 3, the VaLOR joint oscillation analysis uses the scheme defined by Fogli and Lisi in [21] [25] in which $\left(|\Delta m^2_{32}|, \Delta m^2_{21}\right)$ are replaced by $\left(|\Delta m^2|, \delta m^2\right)$. This change was adopted in order to compare results with Normal and Inverted mass hierarchies. It is not possible to compare the two hierarchies if the atmospheric mass-squared difference is input as $|\Delta m^2_{32}|$, because in that convention $|\Delta m^2_{31}|$ is the largest mass-squared splitting in the NH, whereas $|\Delta m^2_{32}|$ is the largest in the IH. Then, when comparing results in the two mass hierarchies using $|\Delta m^2_{32}|$, an artificial difference appears between the two results simply because the quantity compared, $|\Delta m^2_{32}|$, has a different meaning in each hierarchy. This fact will be illustrated in this section.

Figure 321 shows the P($\nu_\mu \rightarrow \nu_\mu$) survival probability in the 2-dimensional oscillation parameter spaces ($\sin^2\theta_{23}$, $|\Delta m^2|$) (left) and ($\sin^2\theta_{23}$, $|\Delta m^2_{32}|$) (right) for a fixed value of P($\nu_\mu \rightarrow \nu_\mu$) = 0.05. Clearly, the results for NH (solid line) and IH (dashed line) in the plot on the left (using Fogli and Lisi convention) are almost identical since the quantity compared, $|\Delta m^2|$, is the same in both hierarchies. However, in the plot on the right a clear difference appears between the oscillation probability in NH and IH, due to the fact that the quantity compared, $|\Delta m^2_{32}|$, has a different meaning in each hierarchy.

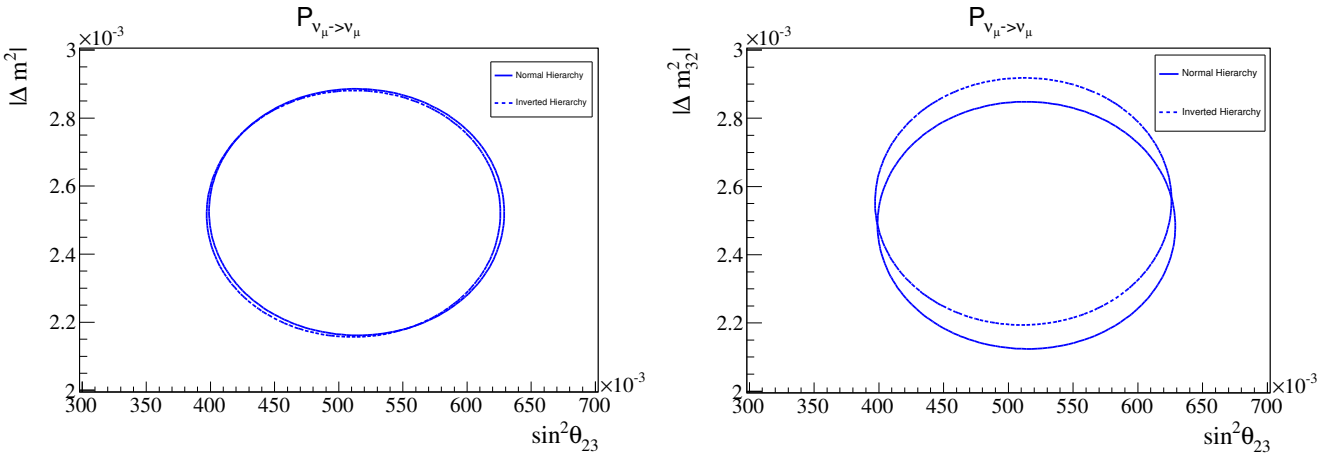

Figure 321: P($\nu_\mu \rightarrow \nu_\mu$) survival probability in the 2-dimensional oscillation parameter spaces ($\sin^2\theta_{23}$, $|\Delta m^2|$) (left) and ($\sin^2\theta_{23}$, $|\Delta m^2_{32}|$) (right) for a fixed value of P($\nu_\mu \rightarrow \nu_\mu$) = 0.05.

Figure 322 shows the true χ^2 surface for the single ring μ-like sample of the Run1+2+3 dataset in the 2-dimensional oscillation parameter spaces ($\sin^2\theta_{23}$, $|\Delta m^2|$) (left) and ($\sin^2\theta_{23}$, $|\Delta m^2_{32}|$) (right). A contour is drawn in this figure for a fixed value of true $\chi^2 = 60$ in order to compare a line of points with the same vale of true χ^2 in both mass hierarchies. The behaviour in the plots in Figure 322 is exactly the same as observed in Figure 321.

Figure 323 shows the 90% CL for the Run1+2+3 dataset in the 2-dimensional oscillation parameter spaces ($\sin^2\theta_{23}$, $|\Delta m^2|$) (left) and ($\sin^2\theta_{23}$, $|\Delta m^2_{32}|$) (right) for the stand-alone ν_μ disappearance analysis with Normal Hierarchy (solid line) and Inverted Hierarchy (dashed line) with the constant $\Delta\chi^2$ method. As shown in this figure, an artificial difference between the contours in both hierarchies appears when using ($\sin^2\theta_{23}$, $|\Delta m^2_{32}|$) because the quantity $|\Delta m^2_{32}|$ has a different meaning in each mass hierarchy (it is the largest mass-squared splitting in IH whereas the second largest in NH). There is almost no difference between the contours in both hierarchies when using the Fogli and Lisi convention ($\sin^2\theta_{23}$, $|\Delta m^2|$) .

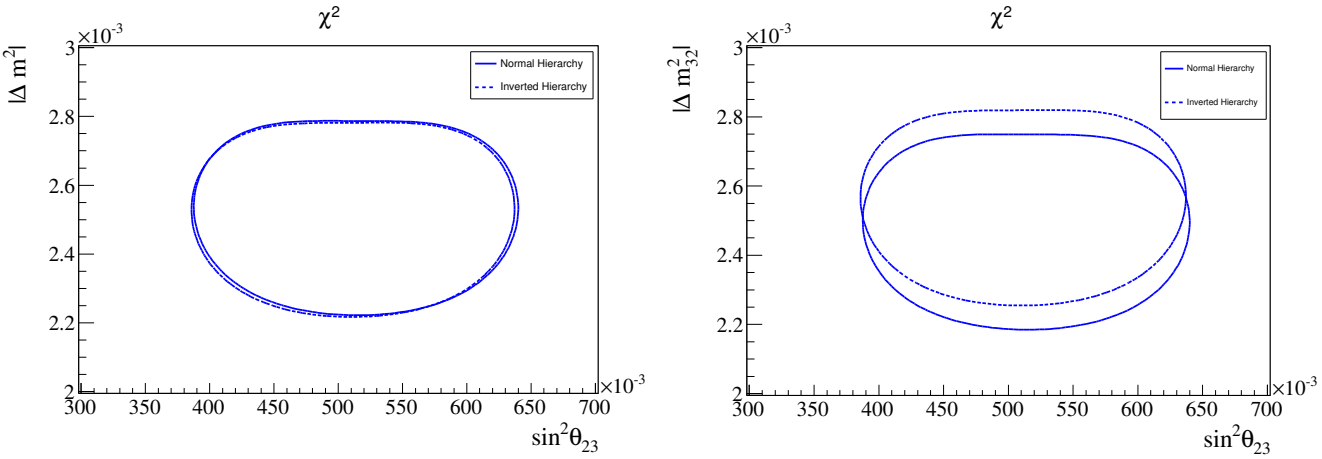

Figure 322: True χ^2 surface for the single ring μ-like sample of the Run1+2+3 dataset in the 2-dimensional oscillation parameter spaces ($\sin^2\theta_{23}$, $|\Delta m^2|$) (left) and ($\sin^2\theta_{23}$, $|\Delta m^2_{32}|$) (right) for a fixed value of true $\chi^2 = 60$.

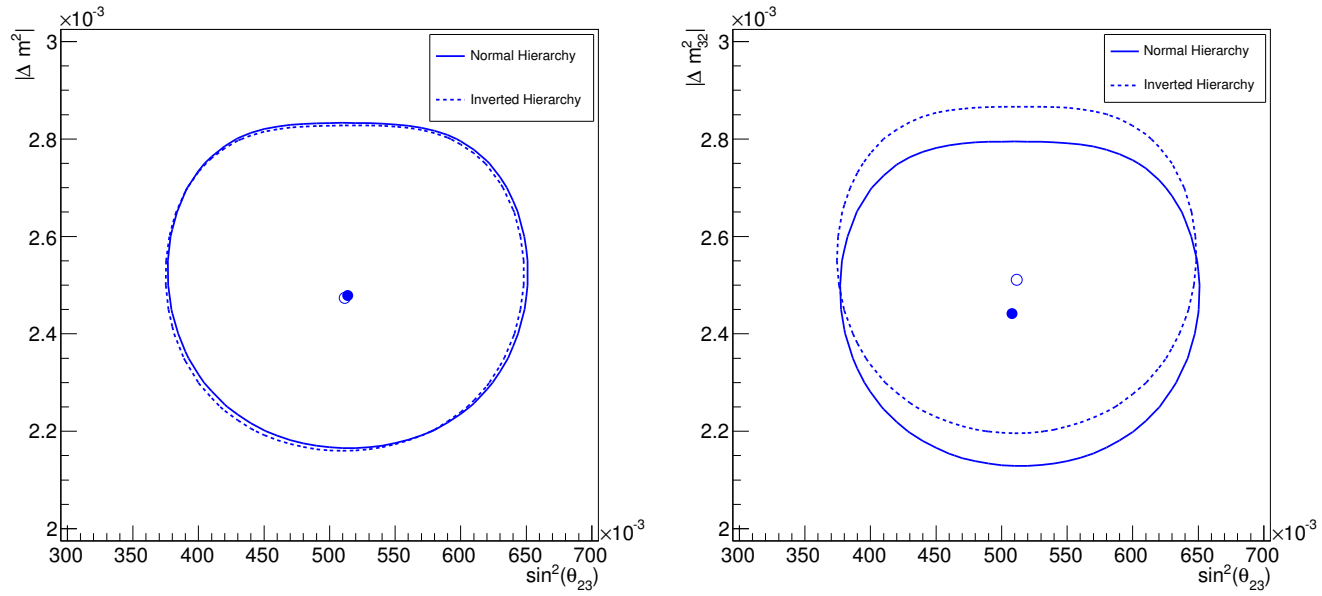

Figure 323: 90% CL for the Run1+2+3 dataset in the 2-dimensional oscillation parameter spaces ($\sin^2\theta_{23}$, $|\Delta m^2|$) (left) and ($\sin^2\theta_{23}$, $|\Delta m^2_{32}|$) (right) for the stand-alone ν_μ disappearance analysis with Normal Hierarchy (solid line) and Inverted Hierarchy (dashed line) with the constant $\Delta\chi^2$ method.

I. Coverage studies

The studies presented in this section are intended to check if the coverage of the confidence intervals obtained with the constant $\Delta\chi^2$ method used in this technical note is correct.

For these studies, sets of toy MC experiments at different oscillation points were produced, using an ensemble of 1000 toy MC experiments at each oscillation point considered. For those toy experiments, critical values of $\Delta\chi^2$ have been calculated and compared with the canonical $\Delta\chi^2$ values for different confidence levels.

At least two effects can produce differences between the critical values of $\Delta\chi^2$ in the toy experiments and the canonical values: physical boundaries and systematic variations. Other reasons as stated in [27] are not considered in this study since they refer to extreme values of $|\Delta m^2|$, out of the range of our analysis. In order to produce the closest possible scenario to the actual fit in the results of the joint analysis, the oscillation parameters that are not under study in each 2D parameter space must be fitted. The results of these tests are in Sec.I.2. But first other simpler studies were done in order to separate the two effects mentioned. Thus, in Sec. I.1 checks with toy experiments with statistical fluctuations only are presented and in Sec.I.2 checks were made including systematic fluctuations too, in both cases fixing the other oscillation parameters not studied to their true input values. Now the three different kinds of coverage checks are described.

Firstly, for the coverage checks with statistical fluctuations only presented in Sec. I.1, the procedure is as follows:

- At a certain oscillation point, 1k toy experiments were created with statistical fluctuations.
- The true value of χ^2 (χ^2_{true}) was computed for each toy experiment fixing the oscillation parameters to the true input values used to calculate the toy experiment.
- A fit was performed for each toy experiment fitting oscillation parameters only, the ones corresponding to the parameter space under study. For instance, when studying the 1D $sin^2\theta_{23}$ parameter space, only $sin^2\theta_{23}$ was included in the fit, when studying the $sin^2\theta_{23}$,$|\Delta m^2|$) parameter space both ($sin^2\theta_{23}$ and $|\Delta m^2|$ were fitted. The other oscillation parameters were fixed to their true input values.
- The value of $\Delta\chi^2$ was calculated for each toy experiment as the difference between the true χ^2 and the value of χ^2 at the best-fit point.

$$\Delta\chi^2 = \chi^2_{true} - \chi^2_{bf}$$

- Finally the critical $\Delta\chi^2$ value for a given confidence interval N% was obtained as the value of $\Delta\chi^2$ for which N% of the toy experiments had a $\Delta\chi^2$ smaller than that critical value.

These studies were produced for different scenarios in 1D (I.1.1) and 2D (I.1.2). In the 2D parameter spaces several oscillation points were selected varying those oscillation parameters where a physical boundary is present. For instance, in the ($sin^2\theta_{23}$,$|\Delta m^2|$) parameter space, grid points were studied for different values of $sin^2\theta_{23}$.

Secondly, studies including systematic variations were done in Sec.I.2 These studies were produced for 2D parameter spaces, considering the same oscillation points as in Sec. I.1.2. The procedure in these studies is the following:

- At a certain oscillation point, 1k toy experiments were created with statistical fluctuations and random systematic variations.
- A first value of χ^2 (χ^2_{init}) was obtained for each toy experiment fixing the oscillation parameters to the true input values and fitting the systematic parameters.
- A second fit was performed for each toy experiment fitting oscillation parameters and systematic errors, obtaining χ^2_{bf}. Like in the case with only statistical fluctuations, the oscillation parameters included in the fit were the ones corresponding to the parameter space under study.
- The value of $\Delta\chi^2$ was calculated for each toy experiment as the difference $\Delta\chi^2 = \chi^2_{init} - \chi^2_{bf}$, and the critical $\Delta\chi^2$ value for a given confidence interval N% was obtained as explained for the tests with statistical fluctuations only.

Finally, the effect of fitting the rest of oscillation parameters was incorporated in a third set of checks in Sec. I.3, considering the same oscillation points as in Sec.I.2. The procedure in these studies is the following:

- At a certain oscillation point, 1k toy experiments were created with statistical fluctuations and random systematic variations.

- A first value of χ^2 (χ^2_{init}) was obtained for each toy experiment fixing the oscillation parameters under study to the true input values and fitting the systematic parameters and the other two oscillation parameters.
- A second fit was performed for each toy experiment fitting the four oscillation parameters and systematic errors, obtaining χ^2_{bf}.
- The value of $\Delta\chi^2$ was calculated for each toy experiment as the difference $\Delta\chi^2 = \chi^2_{init} - \chi^2_{bf}$, and the critical $\Delta\chi^2$ value for a given confidence interval N% was obtained as explained for the tests with statistical fluctuations only.

In every study, the values of the oscillation parameters that remain fixed are the following:

Parameter	Value
$\sin^2\theta_{12}$	0.311
$\sin^2\theta_{13}$	0.025
$\sin^2\theta_{23}$	0.5
δm^2	7.5×10^{-5} eV^2/c^4
$\lvert\Delta m^2\rvert$	2.36×10^{-5} eV^2/c^4
δ_{CP}	0

Table 22: True input values of the oscillation parameters when not varied used for the coverage checks.

Conclusions

From the studies presented in next pages the following conclusions can be extracted:

- There is a good agreement between $\Delta\chi^2$ vs coverage distributions and the canonical $\Delta\chi^2$ pdf for 1 degree and 2 degrees of freedom when away from the physical boundaries, that means when $|sin^2\theta_{23} - 0.5| \geq 0.1$ and $sin^2\theta_{13} \geq 0.005$, with statistical and systematic fluctuations and fixing the other oscillation parameters to their true input values.
- There is overcoverage for intervals close to a physical boundary, i.e. when $|sin^2\theta_{23} - 0.5| < 0.1$ or $sin^2\theta_{13} < 0.005$.This overcoverage is due to the pile-up of best fits at the physical boundary, where they have a smaller $\Delta\chi^2$ than in an unconstrained fit.
- The parameter δ_{CP} is acting like a nuisance parameter, not like a real degree of freedom in the fits, due to the limited sensitivity to this parameter at current POT. So when δ_{CP} is a fitted parameter in Secs. I.2 and I.1, the plots clearly show that the coverage is similar to the canonical value for one degree of freedom less than the number of fitted parameters.
- There is a general overcoverage for intervals when the check is done not fixing the other oscillation parameters to their true values but including them in the fit as shown in Sec.I.3. This behaviour is independent of the addition of systematic fluctuations, appearing the same overcoverage with statistical fluctuations only, as can be clearly observed when comparing both kind of plots (for instance 397 vs 398).
- Compared with the same studies done fixing the other oscillation parameters, the overcoverage found when fitting them is more significant in the 2D parameter spaces ($sin^2\theta_{13}$,$|\Delta m^2|$) and ($sin^2\theta_{13}$,$sin^2\theta_{23}$). After several checks made at the end of the section, seems clear that the extra overcoverage appears when $sin^2\theta_{13}$ and δ_{CP} are both fitted at the same time.
- The parameter δ_{CP} is producing overcoverage in two ways: firstly, as explained in a previous bullet, it is not acting as a real degree of freedom itself, and secondly, due to the correlation existing between δ_{CP} and $sin^2\theta_{13}$, these two parameters are not independent degrees of freedom and overcoverage is appearing when both are fitted together.

I.1. Coverage studies with statistical fluctuations only

I.1.1. Coverage studies in 1D

The checks presented in this subsection were done following this procedure:

- At a certain oscillation point, 1k toy experiments were created with statistical fluctuations.
- The true value of χ^2 (χ^2_{true}) was computed for each toy experiment fixing the oscillation parameters to the true input values used to calculate the toy experiment.
- A fit was performed for each toy experiment fitting oscillation parameters only, the ones corresponding to the parameter space under study. For instance, when studying the 1D $sin^2\theta_{23}$ parameter space, only $sin^2\theta_{23}$ was included in the fit, when studying the $sin^2\theta_{23}$,$|\Delta m^2|$) parameter space both ($sin^2\theta_{23}$ and $|\Delta m^2|$ were fitted. The other oscillation parameters were fixed to their true input values.
- The value of $\Delta\chi^2$ was calculated for each toy experiment as the difference between the true χ^2 and the value of χ^2 at the best-fit point.

$$\Delta\chi^2 = \chi^2_{true} - \chi^2_{bf}$$

- Finally the critical $\Delta\chi^2$ value for a given confidence interval N% was obtained as the value of $\Delta\chi^2$ for which N% of the toy experiments had a $\Delta\chi^2$ smaller than that critical value.

The following figures in this subsection show the distribution of $\Delta\chi^2$ vs coverage (black lines) for different oscillation points in 1D parameter spaces, overlaying the canonical $\Delta\chi^2$ pdf for 1 degree of freedom (red lines). Figures 324-327 show the distribution of $\Delta\chi^2$ vs coverage for different values of $|\Delta m^2|$, calculated with 1k toy experiments with statistical fluctuations and fitting for $|\Delta m^2|$ only (as it is a 1D test the other three oscillation parameters are fixed). In Fig. 328 a summary of the previous plots is presented, showing the value of $\Delta\chi^2$ at 99%, 90% and 68% confidence intervals vs the value of $|\Delta m^2|$. Similarly for $sin^2\theta_{23}$ in Figs. 329-333 and $sin^2\theta_{13}$ in Figs. 334-339

For δ_{CP} the distributions can be observed in Figs. 340-344. From those figures, there is already a sense that this parameter is not acting as a real degree of freedom like the rest of oscillation parameters, but more like a nuisance parameter instead.

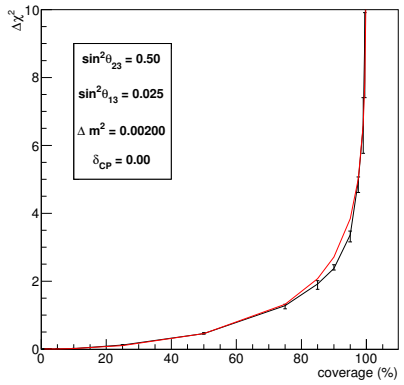

Figure 324: Distribution of $\Delta\chi^2$ vs coverage in the $|\Delta m^2|$ parameter space from 1k toy MC experiments generated with the Run 1+2+3 POT with statistical fluctuations at the oscillation point indicated in the legend.

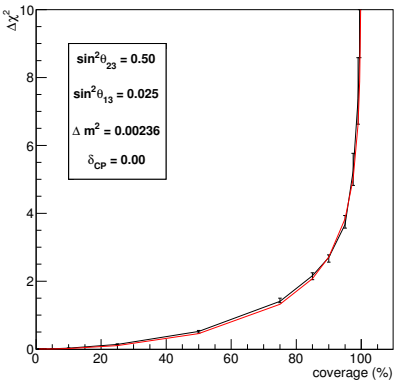

Figure 325: Distribution of $\Delta\chi^2$ vs coverage in the $|\Delta m^2|$ parameter space from 1k toy MC experiments generated with the Run 1+2+3 POT with statistical fluctuations at the oscillation point indicated in the legend.

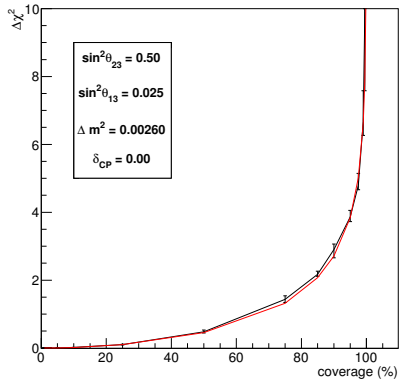

Figure 326: Distribution of $\Delta\chi^2$ vs coverage in the $|\Delta m^2|$ parameter space from 1k toy MC experiments generated with the Run 1+2+3 POT with statistical fluctuations at the oscillation point indicated in the legend.

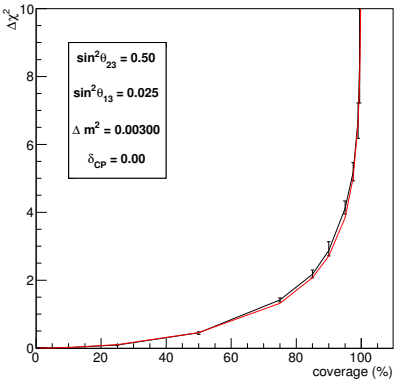

Figure 327: Distribution of $\Delta\chi^2$ vs coverage in the $|\Delta m^2|$ parameter space from 1k toy MC experiments generated with the Run 1+2+3 POT with statistical fluctuations at the oscillation point indicated in the legend.

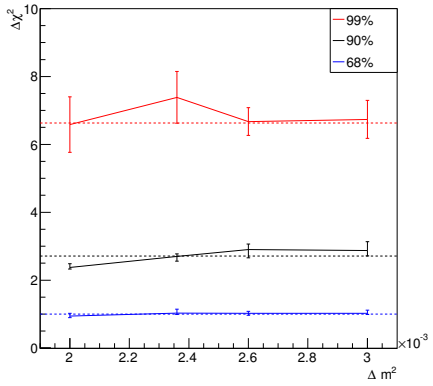

Figure 328: Summary of figures 324-327 showing the value of $\Delta\chi^2$ at 99%, 90% and 68% confidence intervals vs the value of $|\Delta m^2|$. Horizontal dashed lines show the canonical $\Delta\chi^2$ value for 1 degree of freedom.

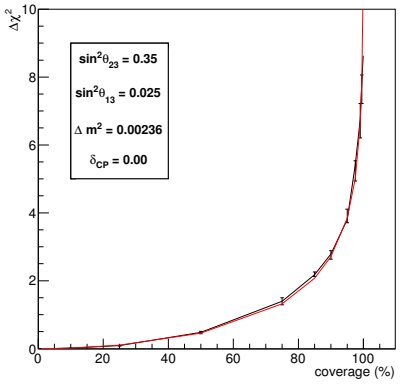

Figure 329: Distribution of $\Delta\chi^2$ vs coverage in the $sin^2\theta_{23}$ parameter space from 1k toy MC experiments generated with the Run 1+2+3 POT with statistical fluctuations at the oscillation point indicated in the legend.

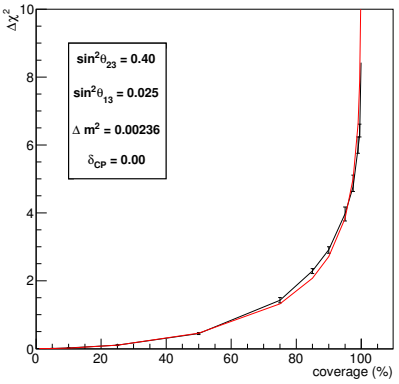

Figure 330: Distribution of $\Delta\chi^2$ vs coverage in the $sin^2\theta_{23}$ parameter space from 1k toy MC experiments generated with the Run 1+2+3 POT with statistical fluctuations at the oscillation point indicated in the legend.

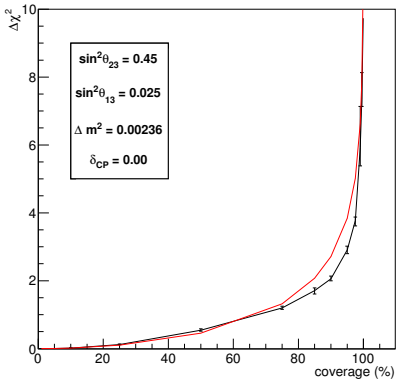

Figure 331: Distribution of $\Delta\chi^2$ vs coverage in the $sin^2\theta_{23}$ parameter space from 1k toy MC experiments generated with the Run 1+2+3 POT with statistical fluctuations at the oscillation point indicated in the legend.

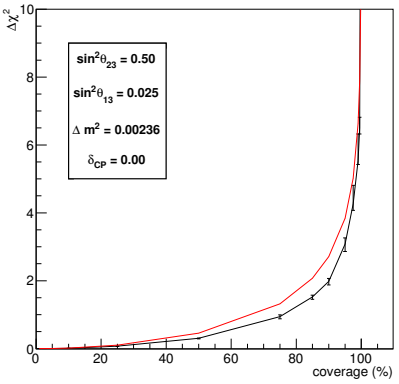

Figure 332: Distribution of $\Delta\chi^2$ vs coverage in the $sin^2\theta_{23}$ parameter space from 1k toy MC experiments generated with the Run 1+2+3 POT with statistical fluctuations at the oscillation point indicated in the legend.

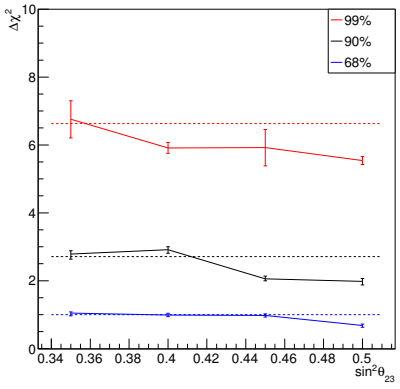

Figure 333: Summary of figures 329-332 showing the value of $\Delta\chi^2$ at 99%, 90% and 68% confidence intervals vs the value of $sin^2\theta_{23}$. Horizontal dashed lines show the canonical $\Delta\chi^2$ value for 1 degree of freedom.

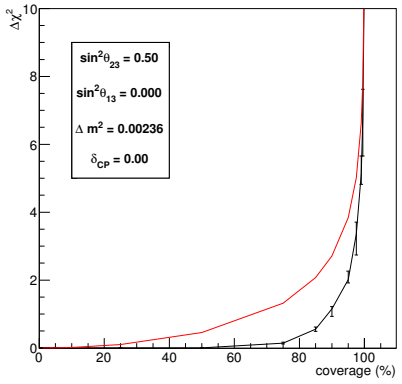

Figure 334: Distribution of $\Delta\chi^2$ vs coverage in the $sin^2\theta_{13}$ parameter space from 1k toy MC experiments generated with the Run 1+2+3 POT with statistical fluctuations at the oscillation point indicated in the legend.

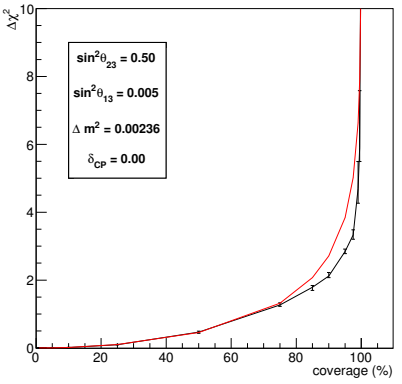

Figure 335: Distribution of $\Delta\chi^2$ vs coverage in the $sin^2\theta_{13}$ parameter space from 1k toy MC experiments generated with the Run 1+2+3 POT with statistical fluctuations at the oscillation point indicated in the legend.

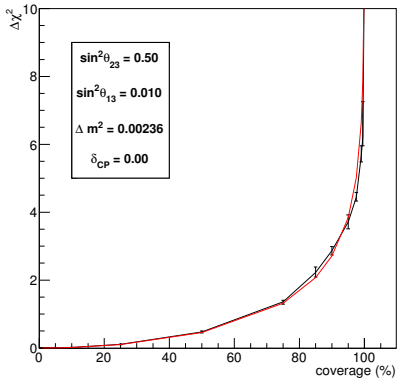

Figure 336: Distribution of $\Delta\chi^2$ vs coverage in the $sin^2\theta_{13}$ parameter space from 1k toy MC experiments generated with the Run 1+2+3 POT with statistical fluctuations at the oscillation point indicated in the legend.

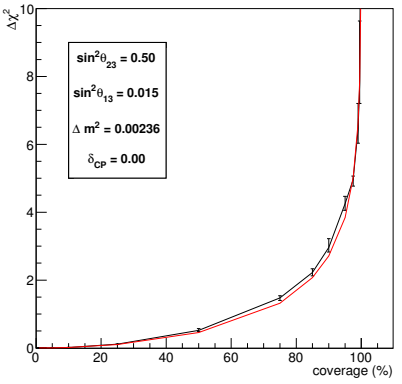

Figure 337: Distribution of $\Delta\chi^2$ vs coverage in the $sin^2\theta_{13}$ parameter space from 1k toy MC experiments generated with the Run 1+2+3 POT with statistical fluctuations at the oscillation point indicated in the legend.

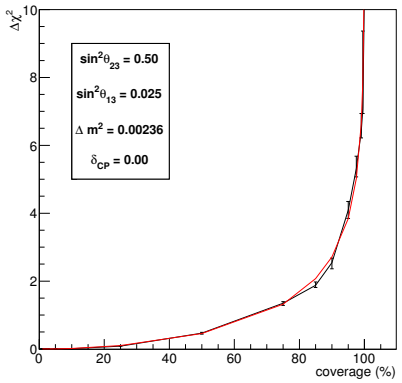

Figure 338: Distribution of $\Delta\chi^2$ vs coverage in the $sin^2\theta_{13}$ parameter space from 1k toy MC experiments generated with the Run 1+2+3 POT with statistical fluctuations at the oscillation point indicated in the legend.

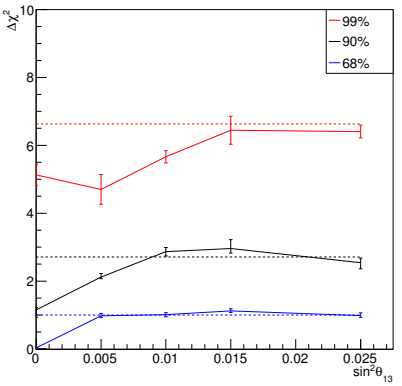

Figure 339: Summary of figures 334-338 showing the value of $\Delta\chi^2$ at 99%, 90% and 68% confidence intervals vs the value of $sin^2\theta_{13}$. Horizontal dashed lines show the canonical $\Delta\chi^2$ value for 1 degree of freedom.

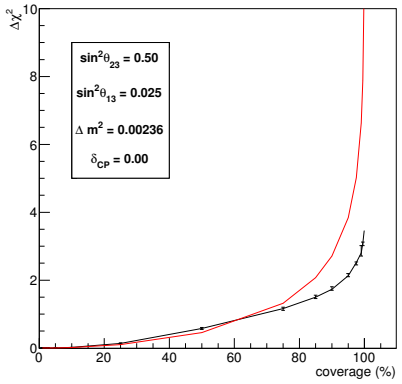

Figure 340: Distribution of $\Delta\chi^2$ vs coverage in the δ_{CP} parameter space from 1k toy MC experiments generated with the Run 1+2+3 POT with statistical fluctuations at the oscillation point indicated in the legend.

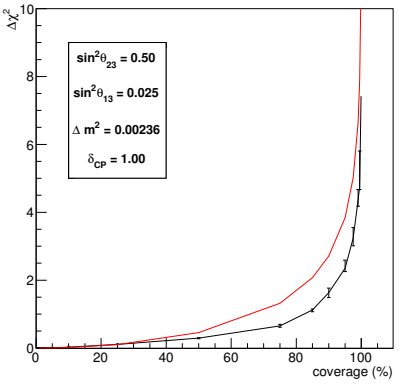

Figure 341: Distribution of $\Delta\chi^2$ vs coverage in the δ_{CP} parameter space from 1k toy MC experiments generated with the Run 1+2+3 POT with statistical fluctuations at the oscillation point indicated in the legend.

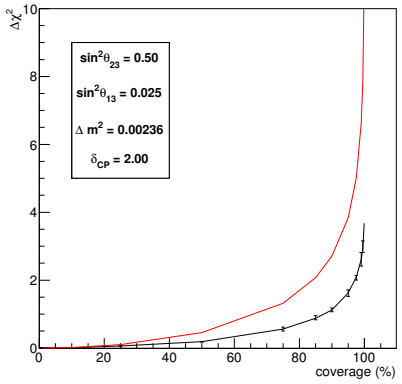

Figure 342: Distribution of $\Delta\chi^2$ vs coverage in the δ_{CP} parameter space from 1k toy MC experiments generated with the Run 1+2+3 POT with statistical fluctuations at the oscillation point indicated in the legend.

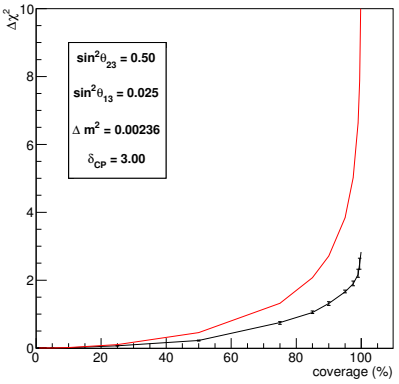

Figure 343: Distribution of $\Delta\chi^2$ vs coverage in the δ_{CP} parameter space from 1k toy MC experiments generated with the Run 1+2+3 POT with statistical fluctuations at the oscillation point indicated in the legend.

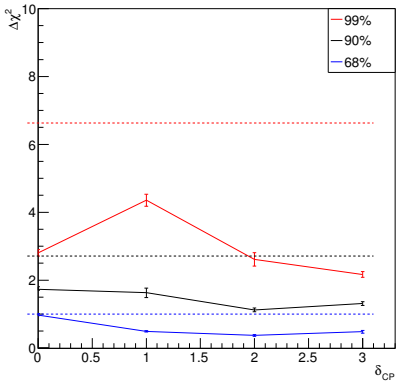

Figure 344: Summary of figures 340-343 showing the value of $\Delta\chi^2$ at 99%, 90% and 68% confidence intervals vs the value of δ_{CP}. Horizontal dashed lines show the canonical $\Delta\chi^2$ value for 1 degree of freedom.

I.1.2. Coverage studies in 2D

In this subsection the distribution of $\Delta\chi^2$ vs coverage is presented for different oscillation points in the 2D parameter spaces where our results are presented, overlaying the canonical $\Delta\chi^2$ pdf for 2 degrees of freedom (red lines). The procedure is the same described in previous subsection.

Figures 345-348 show the distribution of $\Delta\chi^2$ vs coverage in the 2D parameter space ($sin^2\theta_{23}$,$|\Delta m^2|$), calculated with 1k toy experiments with statistical fluctuations and fitting for $sin^2\theta_{23}$ and $|\Delta m^2|$, for different values of $sin^2\theta_{23}$ (to investigate the physical boundary concerning this parameter). In Fig. 349 a summary of the previous plots is presented, showing the value of $\Delta\chi^2$ at 99%, 90% and 68% confidence intervals vs the value of $sin^2\theta_{23}$. Similarly for the 2D parameter space ($sin^2\theta_{13}$,$|\Delta m^2|$) in Figs. 350-355.

The distributions for the parameter space ($sin^2\theta_{13}$,δ_{CP}) are plotted differently, including in Figs. 356-359 the canonical $\Delta\chi^2$ pdf both for 2 degrees of freedom (red solid lines) and 1 degree of freedom (red dashed lines). In Fig. 361 the lines with the canonical values of $\Delta\chi^2$ are also shown with different colors for 2 and 1 degrees of freedom (see legend). It is clear than in this special parameter space the distributions are closer to the ones corresponding to 1 degree of freedom than the ones for the 2 degrees of freedom, indicating again than the behaviour of δ_{CP} is similar to a nuisance parameter's one.

Finally in the distributions for the parameter space ($sin^2\theta_{13}$,$sin^2\theta_{23}$), physical boundaries are present in both oscillation parameters so more grid points are to be studied with the combination of the selected values in the other 2D parameter spaces. Those distributions are presented in Figs. 362-381 and a summary vs $sin^2\theta_{23}$ in Fig. 382 and vs $sin^2\theta_{13}$ in Fig. 383. Then a summary is presented with the value of $\Delta\chi^2$ in Z axis (color) vs $sin^2\theta_{23}$ in X axis and $sin^2\theta_{13}$ in Y axis at 68% confidence interval in Fig.384, at 90% confidence interval in Fig. 385 and at 99% confidence interval in Fig. 386.

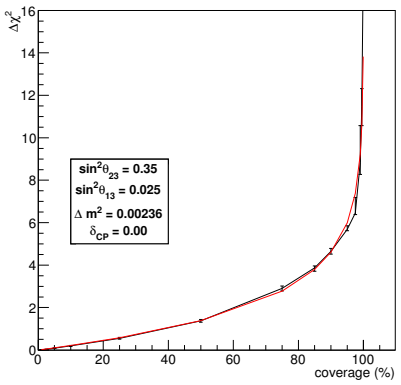

Figure 345: Distribution of $\Delta\chi^2$ vs coverage in the ($sin^2\theta_{23}$,$|\Delta m^2|$) parameter space from 1k toy MC experiments generated with the Run 1+2+3 POT with statistical fluctuations at the oscillation point indicated in the legend.

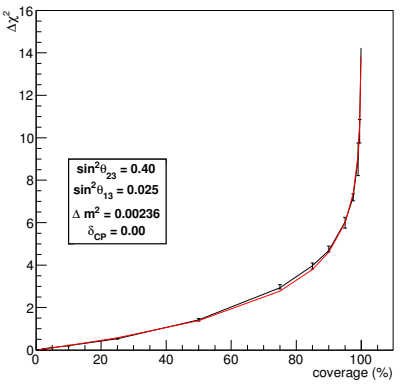

Figure 346: Distribution of $\Delta\chi^2$ vs coverage in the ($sin^2\theta_{23}$,$|\Delta m^2|$) parameter space from 1k toy MC experiments generated with the Run 1+2+3 POT with statistical fluctuations at the oscillation point indicated in the legend.

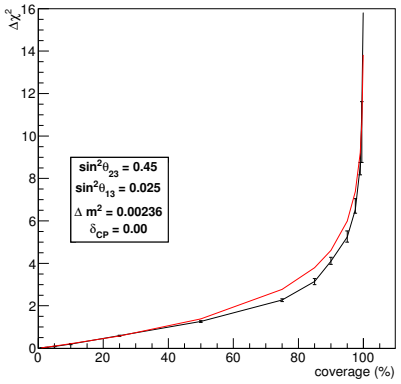

Figure 347: Distribution of $\Delta\chi^2$ vs coverage in the ($sin^2\theta_{23}$,$|\Delta m^2|$) parameter space from 1k toy MC experiments generated with the Run 1+2+3 POT with statistical fluctuations at the oscillation point indicated in the legend.

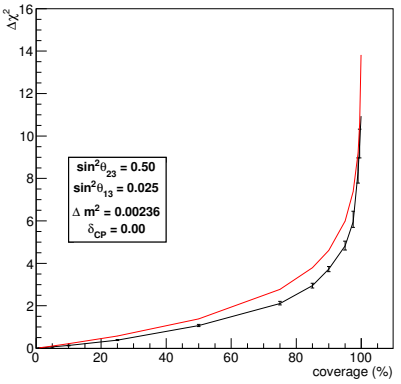

Figure 348: Distribution of $\Delta\chi^2$ vs coverage in the ($sin^2\theta_{23}$,$|\Delta m^2|$) parameter space from 1k toy MC experiments generated with the Run 1+2+3 POT with statistical fluctuations at the oscillation point indicated in the legend.

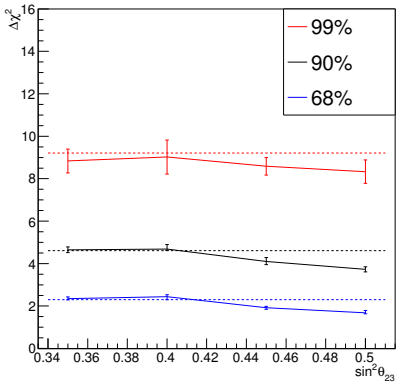

Figure 349: Summary of figures 345-348 showing the value of $\Delta\chi^2$ at 99%, 90% and 68% confidence intervals vs the value of $sin^2\theta_{23}$. Horizontal dashed lines show the canonical $\Delta\chi^2$ value for 2 degrees of freedom.

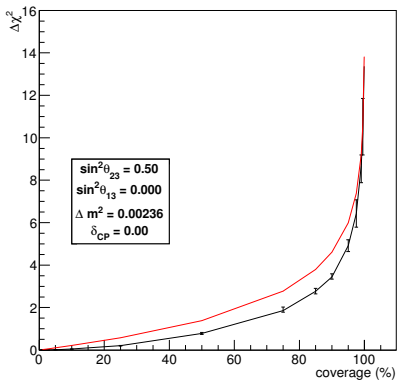

Figure 350: Distribution of $\Delta\chi^2$ vs coverage in the ($sin^2\theta_{13}$,$|\Delta m^2|$) parameter space from 1k toy MC experiments generated with the Run 1+2+3 POT with statistical fluctuations at the oscillation point indicated in the legend.

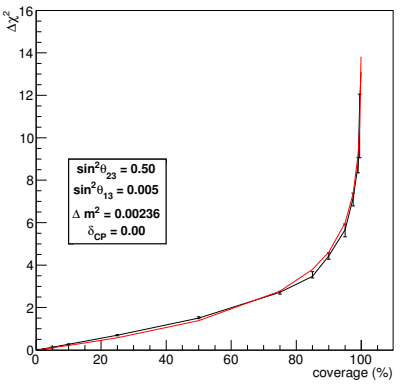

Figure 351: Distribution of $\Delta\chi^2$ vs coverage in the ($sin^2\theta_{13}$,$|\Delta m^2|$) parameter space from 1k toy MC experiments generated with the Run 1+2+3 POT with statistical fluctuations at the oscillation point indicated in the legend.

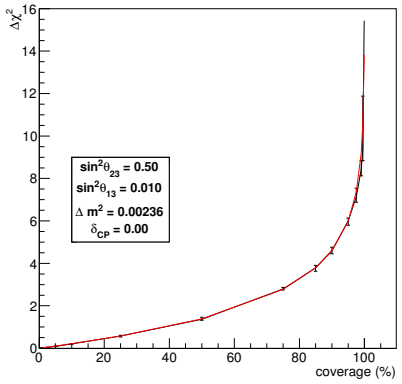

Figure 352: Distribution of $\Delta\chi^2$ vs coverage in the ($sin^2\theta_{13}$,$|\Delta m^2|$) parameter space from 1k toy MC experiments generated with the Run 1+2+3 POT with statistical fluctuations at the oscillation point indicated in the legend.

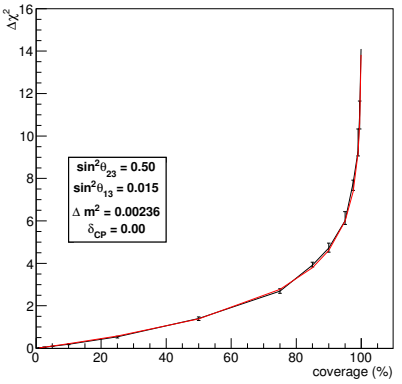

Figure 353: Distribution of $\Delta\chi^2$ vs coverage in the ($sin^2\theta_{13}$,$|\Delta m^2|$) parameter space from 1k toy MC experiments generated with the Run 1+2+3 POT with statistical fluctuations at the oscillation point indicated in the legend.

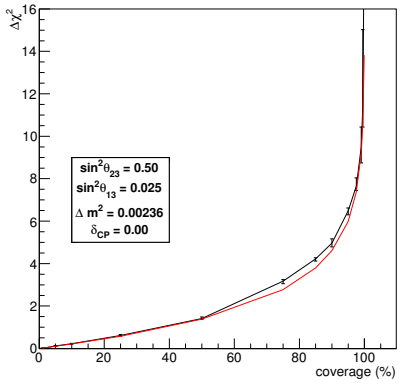

Figure 354: Distribution of $\Delta\chi^2$ vs coverage in the ($sin^2\theta_{13}$,$|\Delta m^2|$) parameter space from 1k toy MC experiments generated with the Run 1+2+3 POT with statistical fluctuations at the oscillation point indicated in the legend.

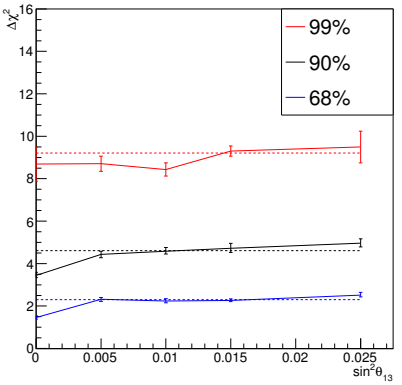

Figure 355: Summary of figures 350-354 showing the value of $\Delta\chi^2$ at 99%, 90% and 68% confidence intervals vs the value of $sin^2\theta_{13}$. Horizontal dashed lines show the canonical $\Delta\chi^2$ value for 2 degrees of freedom.

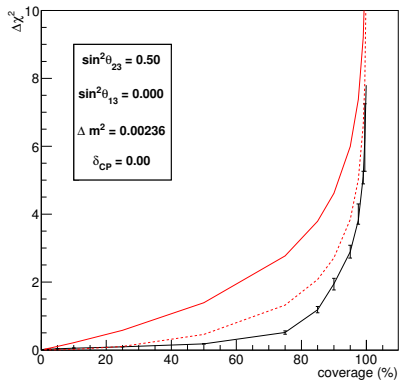

Figure 356: Distribution of $\Delta\chi^2$ vs coverage in the $(sin^2\theta_{13},\delta_{CP})$ parameter space from 1k toy MC experiments generated with the Run 1+2+3 POT with statistical fluctuations at the oscillation point indicated in the legend. The solid red line shows the canonical $\Delta\chi^2$ pdf for 2 degrees of freedom and the dashed red line shows the canonical $\Delta\chi^2$ pdf for 1 degree of freedom.

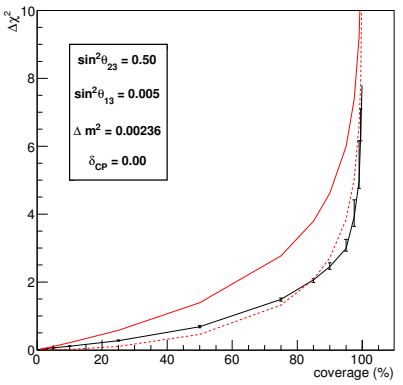

Figure 357: Distribution of $\Delta\chi^2$ vs coverage in the $(sin^2\theta_{13},\delta_{CP})$ parameter space from 1k toy MC experiments generated with the Run 1+2+3 POT with statistical fluctuations at the oscillation point indicated in the legend. The solid red line shows the canonical $\Delta\chi^2$ pdf for 2 degrees of freedom and the dashed red line shows the canonical $\Delta\chi^2$ pdf for 1 degree of freedom.

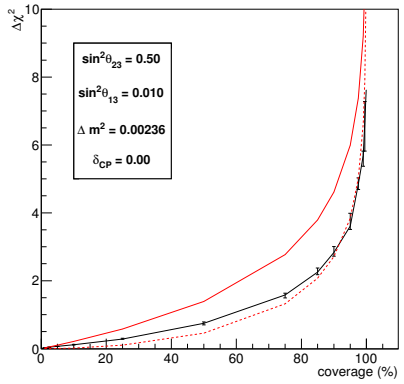

Figure 358: Distribution of $\Delta\chi^2$ vs coverage in the $(sin^2\theta_{13},\delta_{CP})$ parameter space from 1k toy MC experiments generated with the Run 1+2+3 POT with statistical fluctuations at the oscillation point indicated in the legend. The solid red line shows the canonical $\Delta\chi^2$ pdf for 2 degrees of freedom and the dashed red line shows the canonical $\Delta\chi^2$ pdf for 1 degree of freedom.

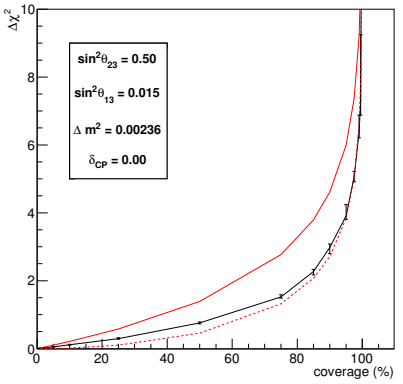

Figure 359: Distribution of $\Delta\chi^2$ vs coverage in the $(sin^2\theta_{13},\delta_{CP})$ parameter space from 1k toy MC experiments generated with the Run 1+2+3 POT with statistical fluctuations at the oscillation point indicated in the legend. The solid red line shows the canonical $\Delta\chi^2$ pdf for 2 degrees of freedom and the dashed red line shows the canonical $\Delta\chi^2$ pdf for 1 degree of freedom.

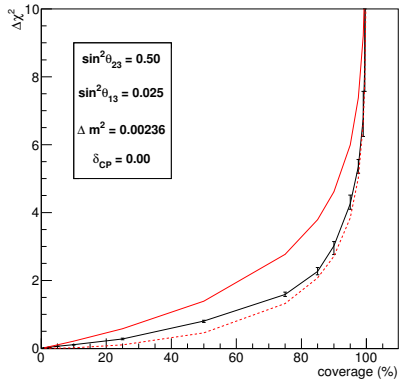

Figure 360: Distribution of $\Delta\chi^2$ vs coverage in the $(sin^2\theta_{13},\delta_{CP})$ parameter space from 1k toy MC experiments generated with the Run 1+2+3 POT with statistical fluctuations at the oscillation point indicated in the legend. The solid red line shows the canonical $\Delta\chi^2$ pdf for 2 degrees of freedom and the dashed red line shows the canonical $\Delta\chi^2$ pdf for 1 degree of freedom.

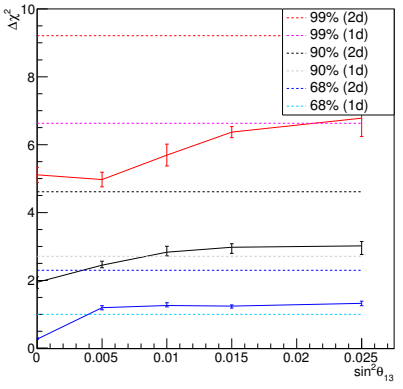

Figure 361: Summary of figures 356-360 showing the value of $\Delta\chi^2$ at 99%, 90% and 68% confidence intervals vs the value of $sin^2\theta_{13}$. Horizontal dashed lines show the canonical $\Delta\chi^2$ value for 2 degrees of freedom and 1 degree of freedom (see legend).

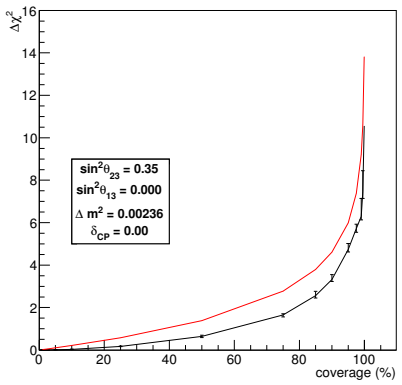

Figure 362: Distribution of $\Delta\chi^2$ vs coverage in the ($sin^2\theta_{13}$,$sin^2\theta_{23}$) parameter space from 1k toy MC experiments generated with the Run 1+2+3 POT with statistical fluctuations at the oscillation point indicated in the legend.

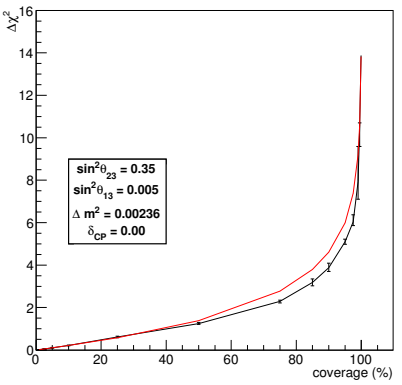

Figure 363: Distribution of $\Delta\chi^2$ vs coverage in the ($sin^2\theta_{13}$,$sin^2\theta_{23}$) parameter space from 1k toy MC experiments generated with the Run 1+2+3 POT with statistical fluctuations at the oscillation point indicated in the legend.

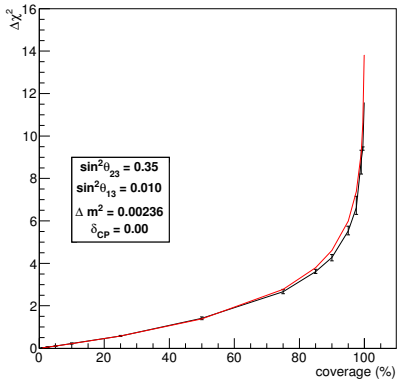

Figure 364: Distribution of $\Delta\chi^2$ vs coverage in the ($sin^2\theta_{13}$,$sin^2\theta_{23}$) parameter space from 1k toy MC experiments generated with the Run 1+2+3 POT with statistical fluctuations at the oscillation point indicated in the legend.

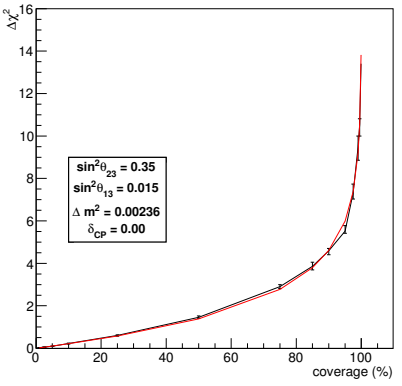

Figure 365: Distribution of $\Delta\chi^2$ vs coverage in the ($sin^2\theta_{13}$,$sin^2\theta_{23}$) parameter space from 1k toy MC experiments generated with the Run 1+2+3 POT with statistical fluctuations at the oscillation point indicated in the legend.

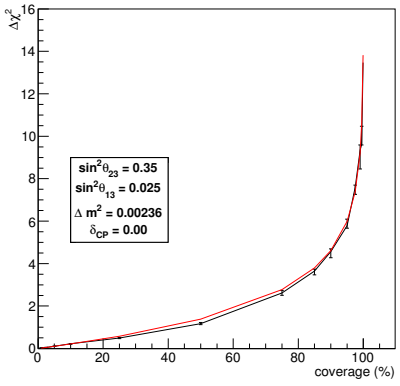

Figure 366: Distribution of $\Delta\chi^2$ vs coverage in the ($sin^2\theta_{13}$,$sin^2\theta_{23}$) parameter space from 1k toy MC experiments generated with the Run 1+2+3 POT with statistical fluctuations at the oscillation point indicated in the legend.

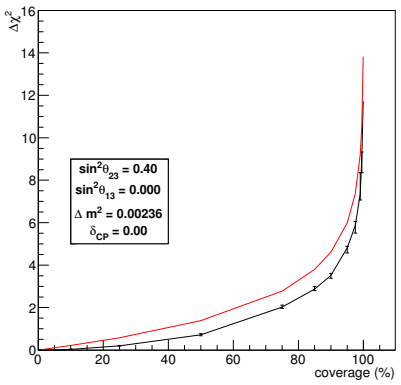

Figure 367: Distribution of $\Delta\chi^2$ vs coverage in the ($sin^2\theta_{13}$,$sin^2\theta_{23}$) parameter space from 1k toy MC experiments generated with the Run 1+2+3 POT with statistical fluctuations at the oscillation point indicated in the legend.

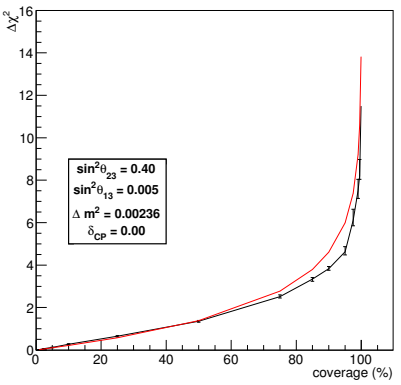

Figure 368: Distribution of $\Delta\chi^2$ vs coverage in the ($sin^2\theta_{13}$,$sin^2\theta_{23}$) parameter space from 1k toy MC experiments generated with the Run 1+2+3 POT with statistical fluctuations at the oscillation point indicated in the legend.

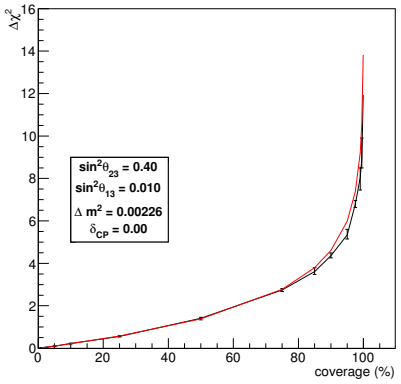

Figure 369: Distribution of $\Delta\chi^2$ vs coverage in the ($sin^2\theta_{13}$,$sin^2\theta_{23}$) parameter space from 1k toy MC experiments generated with the Run 1+2+3 POT with statistical fluctuations at the oscillation point indicated in the legend.

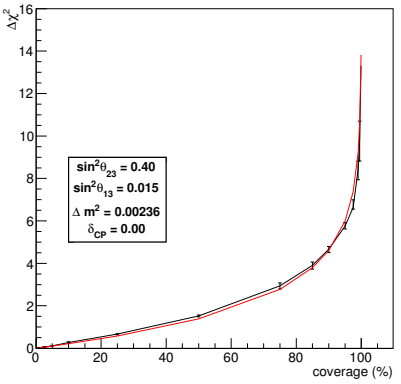

Figure 370: Distribution of $\Delta\chi^2$ vs coverage in the ($sin^2\theta_{13}$,$sin^2\theta_{23}$) parameter space from 1k toy MC experiments generated with the Run 1+2+3 POT with statistical fluctuations at the oscillation point indicated in the legend.

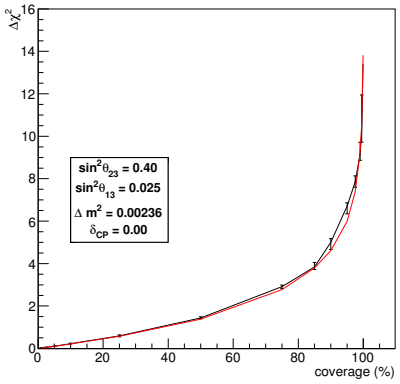

Figure 371: Distribution of $\Delta\chi^2$ vs coverage in the ($sin^2\theta_{13}$,$sin^2\theta_{23}$) parameter space from 1k toy MC experiments generated with the Run 1+2+3 POT with statistical fluctuations at the oscillation point indicated in the legend.

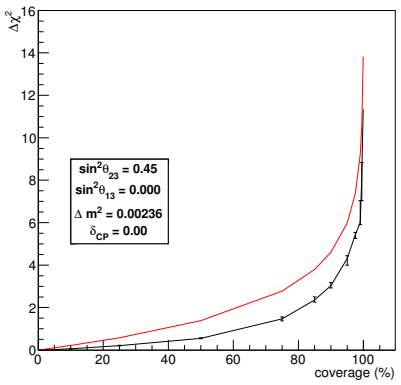

Figure 372: Distribution of $\Delta\chi^2$ vs coverage in the ($sin^2\theta_{13}$,$sin^2\theta_{23}$) parameter space from 1k toy MC experiments generated with the Run 1+2+3 POT with statistical fluctuations at the oscillation point indicated in the legend.

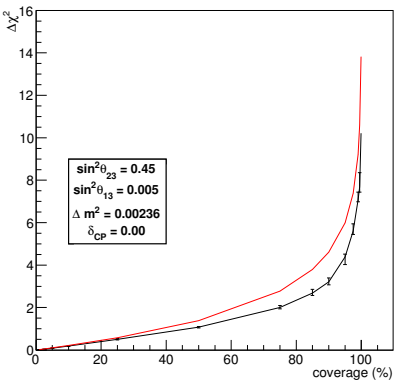

Figure 373: Distribution of $\Delta\chi^2$ vs coverage in the ($sin^2\theta_{13}$,$sin^2\theta_{23}$) parameter space from 1k toy MC experiments generated with the Run 1+2+3 POT with statistical fluctuations at the oscillation point indicated in the legend.

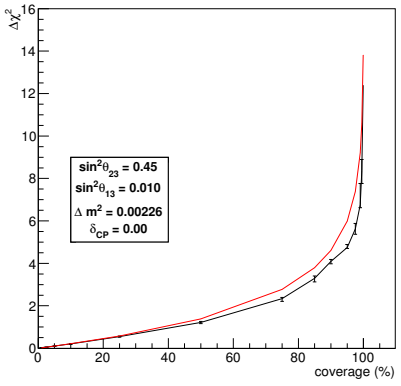

Figure 374: Distribution of $\Delta\chi^2$ vs coverage in the ($sin^2\theta_{13}$,$sin^2\theta_{23}$) parameter space from 1k toy MC experiments generated with the Run 1+2+3 POT with statistical fluctuations at the oscillation point indicated in the legend.

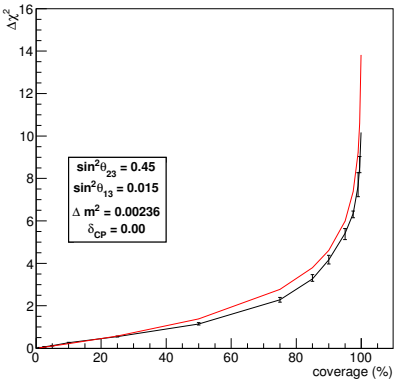

Figure 375: Distribution of $\Delta\chi^2$ vs coverage in the ($sin^2\theta_{13}$,$sin^2\theta_{23}$) parameter space from 1k toy MC experiments generated with the Run 1+2+3 POT with statistical fluctuations at the oscillation point indicated in the legend.

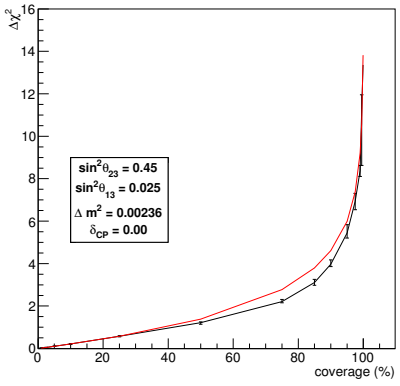

Figure 376: Distribution of $\Delta\chi^2$ vs coverage in the ($sin^2\theta_{13}$,$sin^2\theta_{23}$) parameter space from 1k toy MC experiments generated with the Run 1+2+3 POT with statistical fluctuations at the oscillation point indicated in the legend.

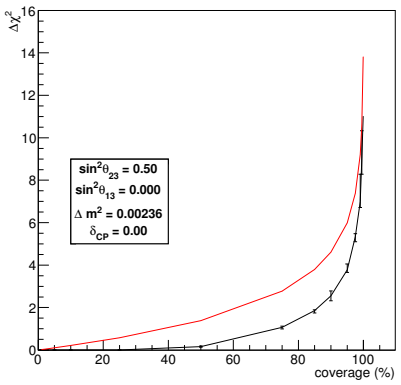

Figure 377: Distribution of $\Delta\chi^2$ vs coverage in the ($sin^2\theta_{13}$,$sin^2\theta_{23}$) parameter space from 1k toy MC experiments generated with the Run 1+2+3 POT with statistical fluctuations at the oscillation point indicated in the legend.

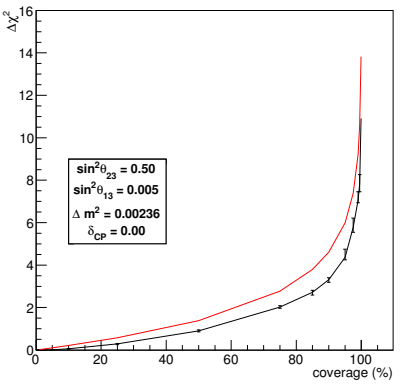

Figure 378: Distribution of $\Delta\chi^2$ vs coverage in the ($sin^2\theta_{13}$,$sin^2\theta_{23}$) parameter space from 1k toy MC experiments generated with the Run 1+2+3 POT with statistical fluctuations at the oscillation point indicated in the legend.

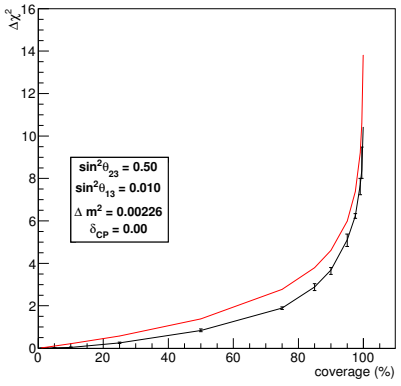

Figure 379: Distribution of $\Delta\chi^2$ vs coverage in the ($sin^2\theta_{13}$,$sin^2\theta_{23}$) parameter space from 1k toy MC experiments generated with the Run 1+2+3 POT with statistical fluctuations at the oscillation point indicated in the legend.

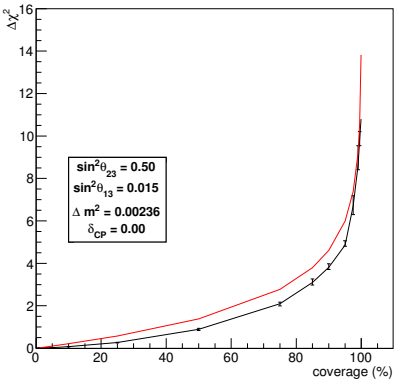

Figure 380: Distribution of $\Delta\chi^2$ vs coverage in the ($sin^2\theta_{13}$,$sin^2\theta_{23}$) parameter space from 1k toy MC experiments generated with the Run 1+2+3 POT with statistical fluctuations at the oscillation point indicated in the legend.

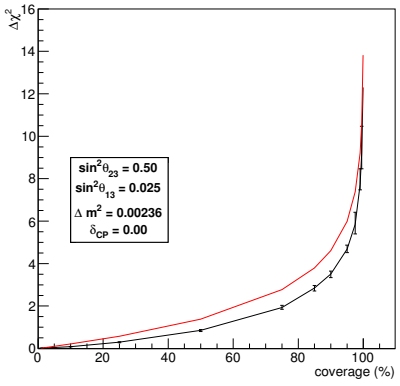

Figure 381: Distribution of $\Delta\chi^2$ vs coverage in the ($sin^2\theta_{13}$,$sin^2\theta_{23}$) parameter space from 1k toy MC experiments generated with the Run 1+2+3 POT with statistical fluctuations at the oscillation point indicated in the legend.

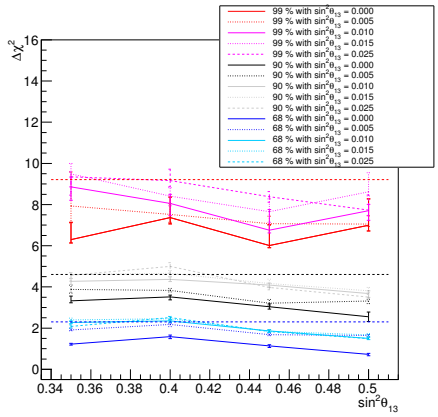

Figure 382: Summary of figures 362-381 showing the value of $\Delta\chi^2$ at 99%, 90% and 68% confidence intervals vs the value of $sin^2\theta_{23}$. Horizontal dashed lines show the canonical $\Delta\chi^2$ value for 2 degrees of freedom.

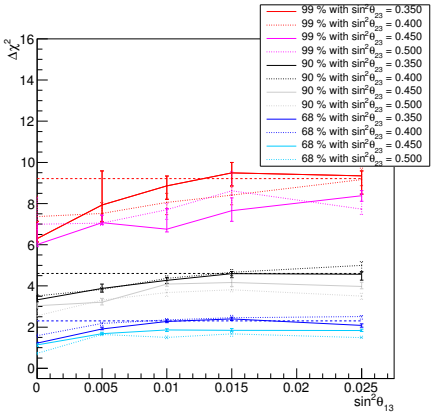

Figure 383: Summary of figures 362-381 showing the value of $\Delta\chi^2$ at 99%, 90% and 68% confidence intervals vs the value of $sin^2\theta_{13}$. Horizontal dashed lines show the canonical $\Delta\chi^2$ value for 2 degrees of freedom.

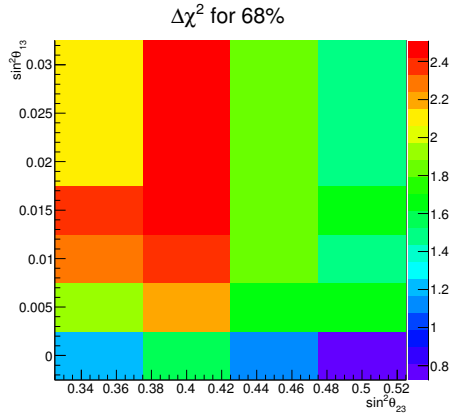

Figure 384: Summary of figures 362-381 showing the value of $\Delta\chi^2$ at 68% confidence intervals in Z axis (color) vs the value of $sin^2\theta_{23}$ in X axis and $sin^2\theta_{13}$ in Y axis.

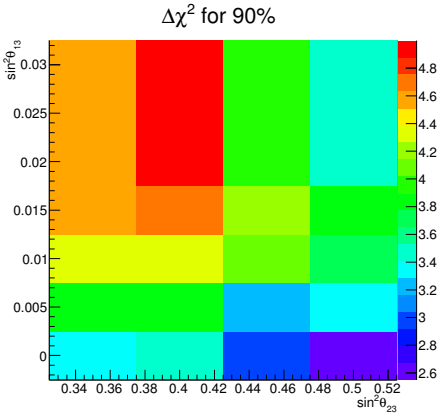

Figure 385: Summary of figures 362-381 showing the value of $\Delta\chi^2$ at 90% confidence intervals in Z axis (color) vs the value of $sin^2\theta_{23}$ in X axis and $sin^2\theta_{13}$ in Y axis.

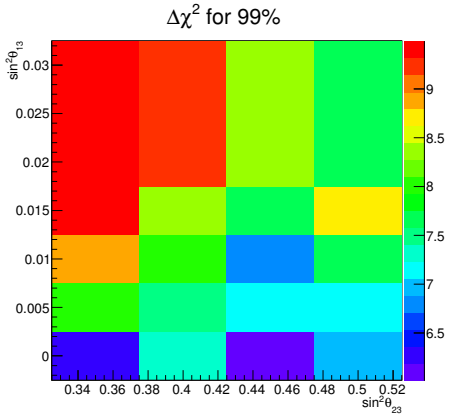

Figure 386: Summary of figures 362-381 showing the value of $\Delta\chi^2$ at 99% confidence intervals in Z axis (color) vs the value of $sin^2\theta_{23}$ in X axis and $sin^2\theta_{13}$ in Y axis.

I.2. Coverage studies in 2D including systematic variations

The coverage studies in this subsection are presented for the same oscillation points in the 2D parameter spaces seen previously, now applying systematic variations to the toy MC experiments and fitting for systematics along with the corresponding oscillation parameters. The procedure is the following:

- At a certain oscillation point, 1k toy experiments were created with statistical fluctuations and random systematic variations.
- A first value of χ^2 (χ^2_{init}) was obtained for each toy experiment fixing the oscillation parameters to the true input values and fitting the systematic parameters.
- A second fit was performed for each toy experiment fitting oscillation parameters and systematic errors, obtaining χ^2_{bf}. Like in the case with only statistical fluctuations, the oscillation parameters included in the fit were the ones corresponding to the parameter space under study.
- The value of $\Delta\chi^2$ was calculated for each toy experiment as the difference $\Delta\chi^2 = \chi^2_{init} - \chi^2_{bf}$, and the critical $\Delta\chi^2$ value for a given confidence interval N% was obtained as explained for the tests with statistical fluctuations only.

In this subsection only summary plots like Fig. 349 in previous subsection are presented. They are built in the same way, first plotting the distribution of $\Delta\chi^2$ vs coverage like in Figs. 345-348, but those plots were omitted now. Thus, Fig.387 is the summary plot for the 2D parameter space ($sin^2\theta_{23}$,$|\Delta m^2|$), Fig. 388 for the 2D parameter space ($sin^2\theta_{13}$,$|\Delta m^2|$) and Fig. 389 for the 2D parameter space ($sin^2\theta_{13}$,δ_{CP}).

For the 2D parameter space ($sin^2\theta_{13}$,$sin^2\theta_{23}$) summaries are presented in Fig. 390 and in Fig. 391 showing the values of $\Delta\chi^2$ vs $sin^2\theta_{23}$ and $sin^2\theta_{13}$ respectively and then a summary is presented with the value of $\Delta\chi^2$ in Z axis (color) vs $sin^2\theta_{23}$ in X axis and $sin^2\theta_{13}$ in Y axis at 68% confidence interval in Fig.392, at 90% confidence interval in Fig. 393 and at 99% confidence interval in Fig. 394.

Results obtained in this section including systematic variations are similar to the ones with statistical fluctuations only.

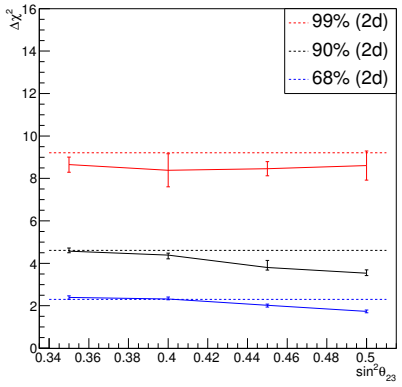

Figure 387: Summary of values of $\Delta\chi^2$ at 99%, 90% and 68% confidence intervals in the 2D parameter space ($sin^2\theta_{23}$,$|\Delta m^2|$) vs the value of $sin^2\theta_{23}$. True input values for the other oscillation parameters: $|\Delta m^2| = 2.36 \times 10^{-3}$, $sin^2\theta_{13} = 0.025$ and δ_{CP} = 0.

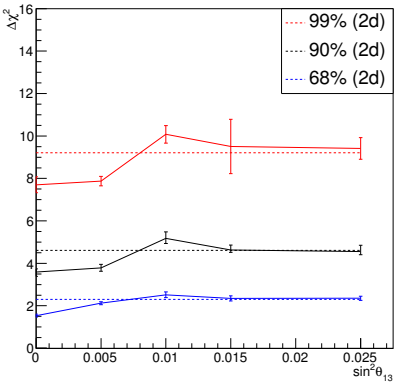

Figure 388: Summary of values of $\Delta\chi^2$ at 99%, 90% and 68% confidence intervals in the 2D parameter space ($sin^2\theta_{13}$,$|\Delta m^2|$) vs the value of $sin^2\theta_{13}$. True input values for the other oscillation parameters: $|\Delta m^2| = 2.36 \times 10^{-3}$, $sin^2\theta_{23} = 0.5$ and δ_{CP} = 0.

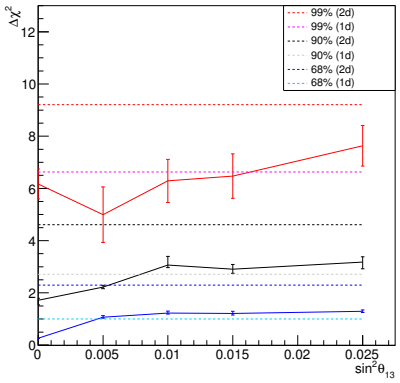

Figure 389: Summary of values of $\Delta\chi^2$ at 99%, 90% and 68% confidence intervals in the 2D parameter space ($sin^2\theta_{13}$,$|\delta_{CP}|$) vs the value of $sin^2\theta_{13}$. True input values for the other oscillation parameters: $|\Delta m^2| = 2.36 \times 10^{-3}$, $sin^2\theta_{23} = 0.5$ and δ_{CP} = 0.

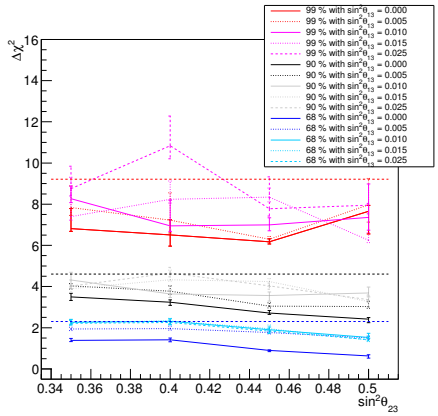

Figure 390: Summary of values of $\Delta\chi^2$ at 99%, 90% and 68% confidence intervals in the 2D parameter space ($sin^2\theta_{13}$,$sin^2\theta_{23}$) vs the value of $sin^2\theta_{23}$. True input values for the other oscillation parameters: $|\Delta m^2| = 2.36 \times 10^{-3}$ and $\delta_{CP} = 0$.

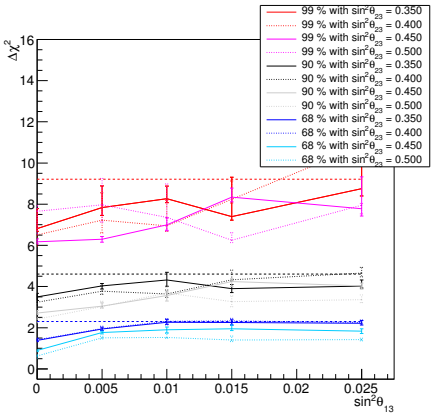

Figure 391: Summary of values of $\Delta\chi^2$ at 99%, 90% and 68% confidence intervals in the 2D parameter space ($sin^2\theta_{13}$,$sin^2\theta_{23}$) vs the value of $sin^2\theta_{13}$. True input values for the other oscillation parameters: $|\Delta m^2| = 2.36 \times 10^{-3}$ and $\delta_{CP} = 0$.

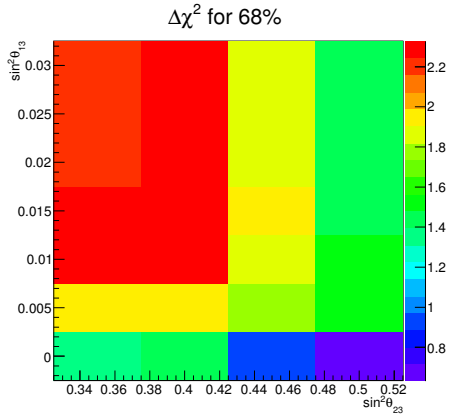

Figure 392: Summary of values of $\Delta\chi^2$ at 68% confidence intervals in Z axis (color) in the 2D parameter space ($sin^2\theta_{13}$,$sin^2\theta_{23}$) vs the value of $sin^2\theta_{23}$ in X axis and $sin^2\theta_{13}$ in Y axis. True input values for the other oscillation parameters: $|\Delta m^2| = 2.36 \times 10^{-3}$ and $\delta_{CP} = 0$.

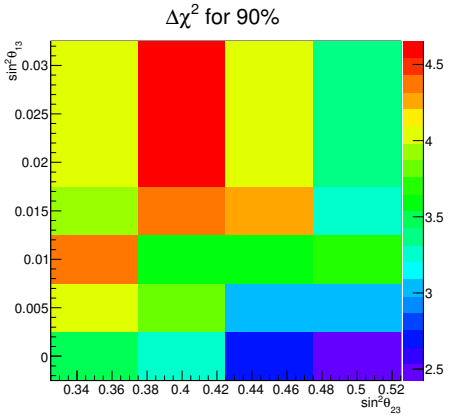

Figure 393: Summary of values of $\Delta\chi^2$ at 90% confidence intervals in Z axis (color) in the 2D parameter space ($sin^2\theta_{13}$,$sin^2\theta_{23}$) vs the value of $sin^2\theta_{23}$ in X axis and $sin^2\theta_{13}$ in Y axis. True input values for the other oscillation parameters: $|\Delta m^2| = 2.36 \times 10^{-3}$ and $\delta_{CP} = 0$.

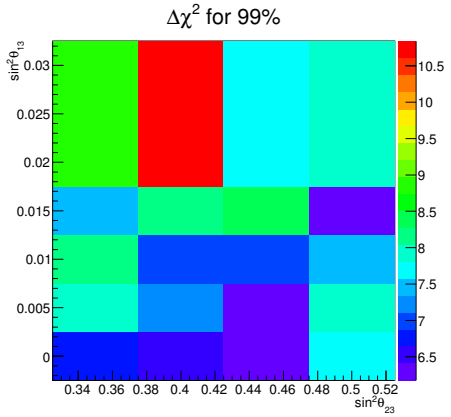

Figure 394: Summary of values of $\Delta\chi^2$ at 99% confidence intervals in Z axis (color) in the 2D parameter space ($sin^2\theta_{13}$,$sin^2\theta_{23}$) vs the value of $sin^2\theta_{23}$ in X axis and $sin^2\theta_{13}$ in Y axis. True input values for the other oscillation parameters: $|\Delta m^2| = 2.36 \times 10^{-3}$ and $\delta_{CP} = 0$.

I.3. Coverage studies in 2D including the other oscillation parameters in the fit

In this subsection the studies are done for the same oscillation points in the 2D parameter spaces seen previously, but including the other two oscillation parameters in the fit in order to reproduce the same scenario as the fits done for the results in this analysis. The studies will be presented with statistical fluctuations only and with systematic variations added. In both cases none of the oscillation parameters remains fixed to its true value now: those that are not under study are now fitted in both fits as explained at the beginning of the section. So the procedure is as follows (similarly for statistical fluctuations only, removing systematics from both fits):

- At a certain oscillation point, 1k toy experiments were created with statistical fluctuations and random systematic variations.
- A first value of χ^2 (χ^2_{init}) was obtained for each toy experiment fixing the oscillation parameters under study to the true input values and fitting the systematic parameters and the other two oscillation parameters.
- A second fit was performed for each toy experiment fitting the four oscillation parameters and systematic errors, obtaining χ^2_{bf}.
- The value of $\Delta\chi^2$ was calculated for each toy experiment as the difference $\Delta\chi^2 = \chi^2_{init} - \chi^2_{bf}$, and the critical $\Delta\chi^2$ value for a given confidence interval N% was obtained as explained for the tests with statistical fluctuations only.

In this subsection only summary plots are presented. For the 2D parameter space ($sin^2\theta_{23}$,$|\Delta m^2|$), Figures 395 and 396 are the summary plots with statistical fluctuations only and including systematic variations respectively. The same for the 2D parameter space ($sin^2\theta_{13}$,$|\Delta m^2|$) in Figs. 397 and 398 and Figs. 399 and400 for the 2D parameter space ($sin^2\theta_{13}$,δ_{CP}).

For the 2D parameter space ($sin^2\theta_{13}$,$sin^2\theta_{23}$) summaries are presented in Figs. 401 and 403 with statistical fluctuations only and in Figs. 402 and 404 with systematic variations, showing the values of $\Delta\chi^2$ vs $sin^2\theta_{23}$ and $sin^2\theta_{13}$. Then a summary is presented with the value of $\Delta\chi^2$ in Z axis (color) vs $sin^2\theta_{23}$ in X axis and $sin^2\theta_{13}$ in Y axis at 68% confidence interval in Figs.405 and 406, at 90% confidence interval in Figs. 407 and 408 and at 99% confidence interval in Figs. 409 and 410.

Results obtained in this section present a general overcoverage. This behaviour seems to be independent of the addition of systematic fluctuations, appearing the same overcoverage with statistical fluctuations only, as can be clearly observed when comparing both kind of plots (for instance 395 vs 396). On the other hand, compared with the same studies done fixing the other oscillation parameters, the overcoverage found when fitting them is more significant in the 2D parameter space ($sin^2\theta_{23}$,$|\Delta m^2|$).

To investigate the reduction of the critical value of $\Delta\chi^2$ when the other oscillation parameters are fitted in the study, an additional set of plots was done with true input value $sin^2\theta_{23} = 0.35$ to minimize boundary effects related to this parameter. The additional checks were made trying to separate different effects, and therefore they introduce new parameters in the fit one by one: Fig.411 presents the distribution with statistical fluctuations only and fixing $sin^2\theta_{23}$ and δ_{CP} to their true input values, then Fig. 412 presents the distribution with statistical fluctuations only, fitting $sin^2\theta_{23}$ and fixing δ_{CP}. Until this step results are in good agreement with the critical values for 2 degrees of freedom. However, when now δ_{CP} is included in the fit, results present the extra overcoverage observed in the studies in this subsection. This overcoverage is now almost identical when fitting δ_{CP} fixing $sin^2\theta_{23}$ in Fig. 413 and when fitting both parameters without (Fig 414) and with systematic variations (Fig. 415). So clearly the extra overcoverage found is due to some pathological behaviour of the parameter δ_{CP}.

Looking deeper, this overcoverage does not appear due to simply adding δ_{CP} in the fit, but it is related to the correlation between δ_{CP} and $sin^2\theta_{13}$. This can be seen in the following tests done (made with only 200 toy experiments). Fig 416 presents the 1D distribution for different values of $sin^2\theta_{23}$ with statistical fluctuations only where two fits were done: the first one is fitting only δ_{CP}, fixing the other three oscillation parameters to their true input value, and the second one is fitting δ_{CP} and $sin^2\theta_{23}$, keeping $sin^2\theta_{13}$ and $|\Delta m^2|$ fixed to their true input values. If Fig 416 is compared with 333, there is no extra overcoverage appearing due to the addition of δ_{CP} in the fit. Similarly with $|\Delta m^2|$, comparing Fig. 417 with Fig. 328 . It is however when the fit is including $sin^2\theta_{13}$ that the overcoverage appears as can be seen in Fig. 418 with critical values clearly smaller than the ones obtained in Fig. 339.

In order to discard that the fit could be giving as result a local minimum in the ($sin^2\theta_{13}$,δ_{CP}) space, the following test was done: for 100 toy experiments with statistical fluctuations, the values of $sin^2\theta_{13}$ and δ_{CP} were scanned and the values giving the minimum true χ^2 were compared with the best-fit values result from the fit. The values found scanning agree very well within the step sizes used ($\delta sin^2\theta_{13}$ = 0.001 and δ_{CP} = 0.02) with the ones given by the fitter as it is presented in Fig.419 and Fig.420, so it indicates that the fitter is giving the real global minimum.

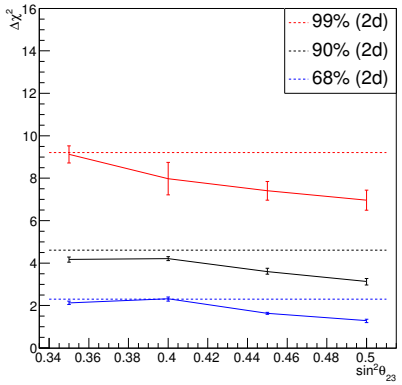

Figure 395: Summary of the values of $\Delta\chi^2$ at 99%, 90% and 68% confidence intervals in the 2D parameter space ($sin^2\theta_{23}$,$|\Delta m^2|$) vs the value of $sin^2\theta_{23}$ with statistical fluctuations only and fitting $sin^2\theta_{13}$ and δ_{CP}. True input values for the other oscillation parameters: $|\Delta m^2| = 2.36 \times 10^{-3}$, $sin^2\theta_{13} = 0.025$ and $\delta_{CP} = 0$.

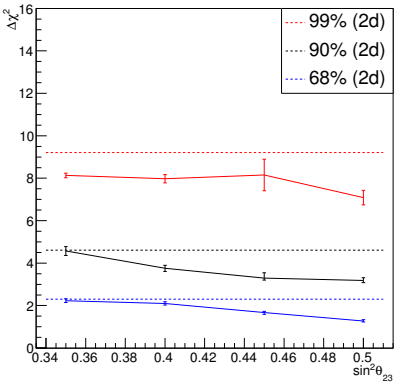

Figure 396: Summary of the values of $\Delta\chi^2$ at 99%, 90% and 68% confidence intervals in the 2D parameter space ($sin^2\theta_{23}$,$|\Delta m^2|$) vs the value of $sin^2\theta_{23}$ with statistical fluctuations and systematic variations and fitting $sin^2\theta_{13}$ and δ_{CP}. True input values for the other oscillation parameters: $|\Delta m^2| = 2.36 \times 10^{-3}$, $sin^2\theta_{13} = 0.025$ and $\delta_{CP} = 0$.

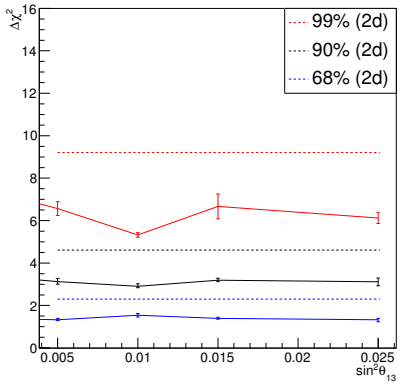

Figure 397: Summary of the values of $\Delta\chi^2$ at 99%, 90% and 68% confidence intervals in the 2D parameter space ($sin^2\theta_{13}$,$|\Delta m^2|$) vs the value of $sin^2\theta_{13}$ with statistical fluctuations only and fitting $sin^2\theta_{23}$ and δ_{CP}. True input values for the other oscillation parameters: $|\Delta m^2| = 2.36 \times 10^{-3}$, $sin^2\theta_{23} = 0.5$ and $\delta_{CP} = 0$.

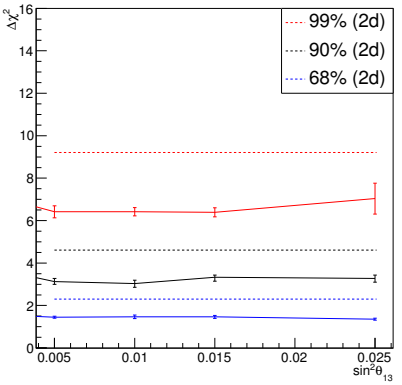

Figure 398: Summary of the values of $\Delta\chi^2$ at 99%, 90% and 68% confidence intervals in the 2D parameter space ($sin^2\theta_{13}$,$|\Delta m^2|$) vs the value of $sin^2\theta_{13}$ with statistical fluctuations and systematic variations and fitting $sin^2\theta_{23}$ and δ_{CP}. True input values for the other oscillation parameters: $|\Delta m^2| = 2.36 \times 10^{-3}$, $sin^2\theta_{23} = 0.5$ and $\delta_{CP} = 0$.

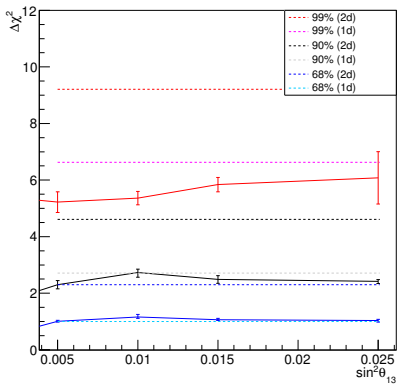

Figure 399: Summary of the values of $\Delta\chi^2$ at 99%, 90% and 68% confidence intervals in the 2D parameter space ($sin^2\theta_{13}$,δ_{CP}) vs the value of $sin^2\theta_{13}$ with statistical fluctuations only and fitting $sin^2\theta_{23}$ and $|\Delta m^2|$. True input values for the other oscillation parameters: $|\Delta m^2| = 2.36 \times 10^{-3}$, $sin^2\theta_{23} = 0.5$ and $\delta_{CP} = 0$.

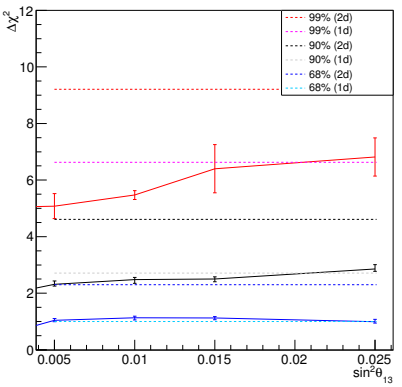

Figure 400: Summary of the values of $\Delta\chi^2$ at 99%, 90% and 68% confidence intervals in the 2D parameter space ($sin^2\theta_{13}$,δ_{CP}) vs the value of $sin^2\theta_{13}$ with statistical fluctuations and systematic variations and fitting $sin^2\theta_{23}$ and $|\Delta m_2|$. True input values for the other oscillation parameters: $|\Delta m^2| = 2.36 \times 10^{-3}$, $sin^2\theta_{23} = 0.5$ and $\delta_{CP} = 0$.

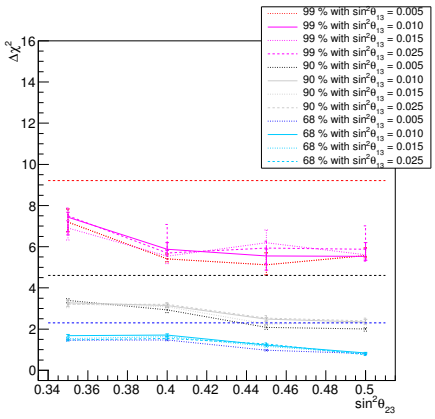

Figure 401: Summary of the values of $\Delta\chi^2$ at 99%, 90% and 68% confidence intervals in the 2D parameter space ($sin^2\theta_{13}$,$sin^2\theta_{23}$) vs the value of $sin^2\theta_{23}$ with statistical fluctuations only and fitting $|\Delta m^2|$ and δ_{CP}. True input values for the other oscillation parameters: $|\Delta m^2| = 2.36 \times 10^{-3}$ and δ_{CP} = 0.

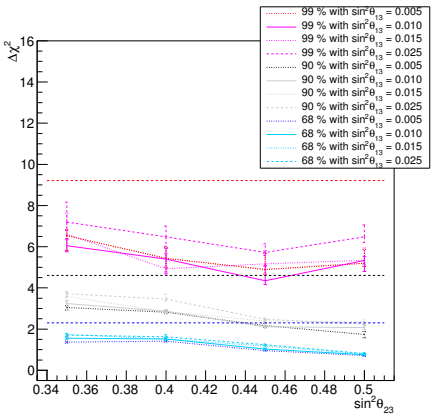

Figure 402: Summary of the values of $\Delta\chi^2$ at 99%, 90% and 68% confidence intervals in the 2D parameter space ($sin^2\theta_{13}$,$sin^2\theta_{23}$) vs the value of $sin^2\theta_{23}$ with statistical fluctuations and systematic variations and fitting $|\Delta m^2|$ and δ_{CP}. True input values for the other oscillation parameters: $|\Delta m^2| = 2.36 \times 10^{-3}$ and δ_{CP} = 0.

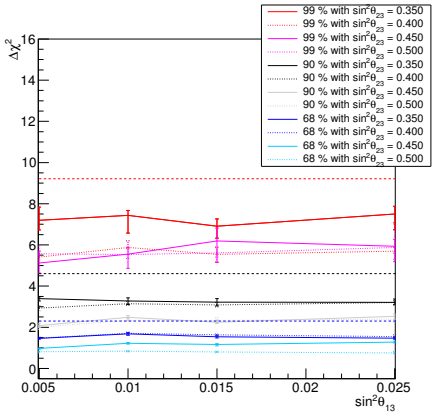

Figure 403: Summary of the values of $\Delta\chi^2$ at 99%, 90% and 68% confidence intervals in the 2D parameter space ($sin^2\theta_{13}$,$sin^2\theta_{23}$) vs the value of $sin^2\theta_{13}$ with statistical fluctuations only and fitting $|\Delta m^2|$ and δ_{CP}. True input values for the other oscillation parameters: $|\Delta m^2| = 2.36 \times 10^{-3}$ and δ_{CP} = 0.

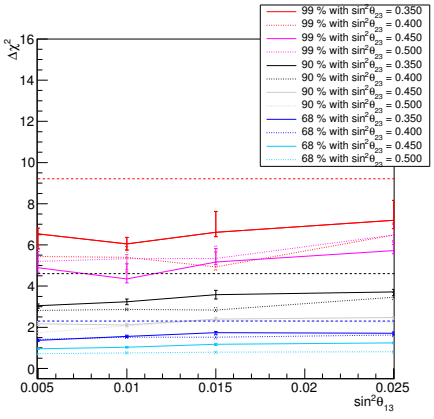

Figure 404: Summary of the values of $\Delta\chi^2$ at 99%, 90% and 68% confidence intervals in the 2D parameter space ($sin^2\theta_{13}$,$sin^2\theta_{23}$) vs the value of $sin^2\theta_{13}$ with statistical fluctuations and systematic variations and fitting $|\Delta m^2|$ and δ_{CP}. True input values for the other oscillation parameters: $|\Delta m^2| = 2.36 \times 10^{-3}$ and δ_{CP} = 0.

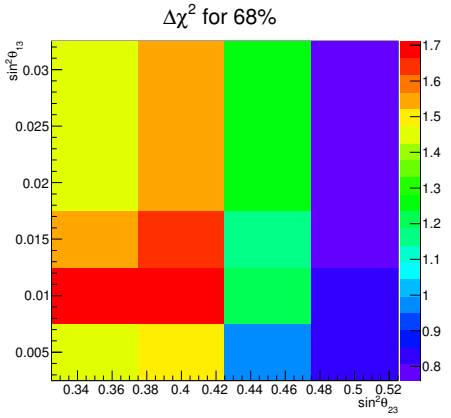

Figure 405: Summary of values of $\Delta\chi^2$ at 68% confidence intervals in Z axis (color) in the 2D parameter space ($sin^2\theta_{13}$,$sin^2\theta_{23}$) vs the value of $sin^2\theta_{23}$ in X axis and $sin^2\theta_{13}$ in Y axis for toy experiments with statistical fluctuations only and fitting $|\Delta m^2|$ and δ_{CP}. True input values for the other oscillation parameters: $|\Delta m^2| = 2.36 \times 10^{-3}$ and $\delta_{CP} = 0$.

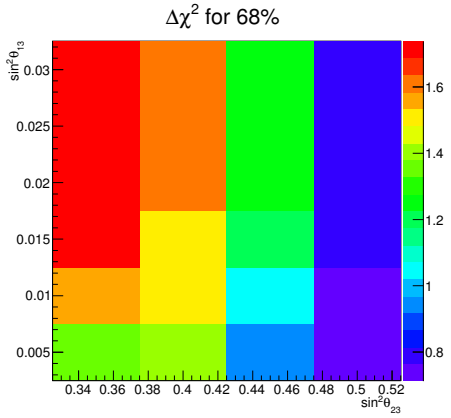

Figure 406: Summary of values of $\Delta\chi^2$ at 68% confidence intervals in Z axis (color) in the 2D parameter space ($sin^2\theta_{13}$,$sin^2\theta_{23}$) vs the value of $sin^2\theta_{23}$ in X axis and $sin^2\theta_{13}$ in Y axis for toy experiments with statistical fluctuations and systematic fluctuations and fitting $|\Delta m^2|$ and δ_{CP}. True input values for the other oscillation parameters: $|\Delta m^2| = 2.36 \times 10^{-3}$ and $\delta_{CP} = 0$.

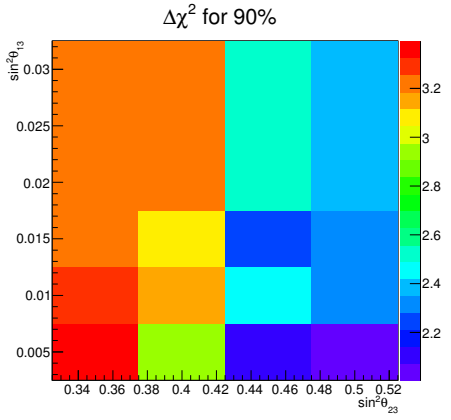

Figure 407: Summary of values of $\Delta\chi^2$ at 90% confidence intervals in Z axis (color) in the 2D parameter space ($sin^2\theta_{13}$,$sin^2\theta_{23}$) vs the value of $sin^2\theta_{23}$ in X axis and $sin^2\theta_{13}$ in Y axis for toy experiments with statistical fluctuations only and fitting $|\Delta m^2|$ and δ_{CP}. True input values for the other oscillation parameters: $|\Delta m^2| = 2.36 \times 10^{-3}$ and $\delta_{CP} = 0$.

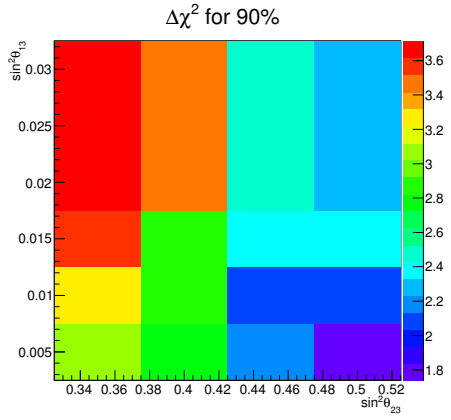

Figure 408: Summary of values of $\Delta\chi^2$ at 90% confidence intervals in Z axis (color) in the 2D parameter space ($sin^2\theta_{13}$,$sin^2\theta_{23}$) vs the value of $sin^2\theta_{23}$ in X axis and $sin^2\theta_{13}$ in Y axis for toy experiments with statistical fluctuations and systematic fluctuations and fitting $|\Delta m^2|$ and δ_{CP}. True input values for the other oscillation parameters: $|\Delta m^2| = 2.36 \times 10^{-3}$ and $\delta_{CP} = 0$.

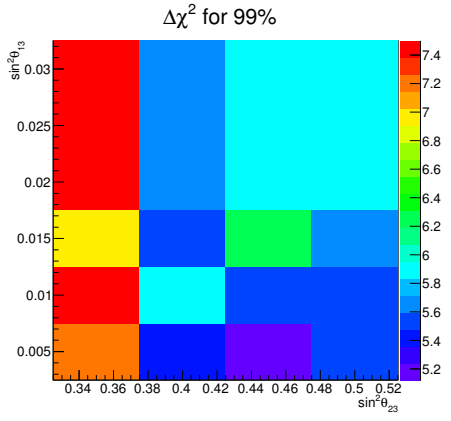

Figure 409: Summary of values of $\Delta\chi^2$ at 99% confidence intervals in Z axis (color) in the 2D parameter space ($sin^2\theta_{13}$,$sin^2\theta_{23}$) vs the value of $sin^2\theta_{23}$ in X axis and $sin^2\theta_{13}$ in Y axis for toy experiments with statistical fluctuations only and fitting $|\Delta m^2|$ and δ_{CP}. True input values for the other oscillation parameters: $|\Delta m^2| = 2.36 \times 10^{-3}$ and $\delta_{CP} = 0$.

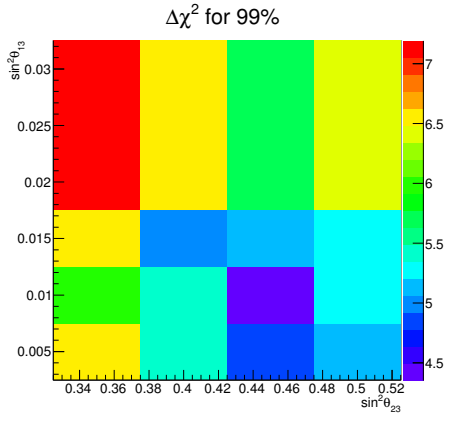

Figure 410: Summary of values of $\Delta\chi^2$ at 99% confidence intervals in Z axis (color) in the 2D parameter space ($sin^2\theta_{13}$,$sin^2\theta_{23}$) vs the value of $sin^2\theta_{23}$ in X axis and $sin^2\theta_{13}$ in Y axis for toy experiments with statistical fluctuations and systematic fluctuations and fitting $|\Delta m^2|$ and δ_{CP}. True input values for the other oscillation parameters: $|\Delta m^2| = 2.36 \times 10^{-3}$ and $\delta_{CP} = 0$.

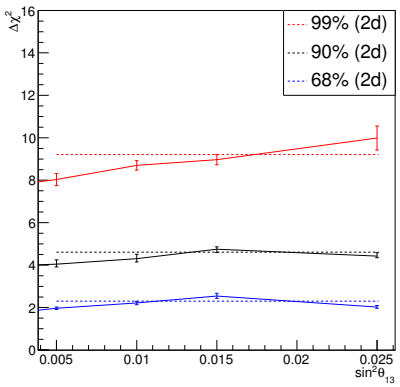

Figure 411: Summary of the values of $\Delta\chi^2$ at 99%, 90% and 68% confidence intervals in the 2D parameter space ($sin^2\theta_{13}$,$|\Delta m^2|$) vs the value of $sin^2\theta_{13}$ with statistical fluctuations only and **fixing** $sin^2\theta_{23}$ **and** δ_{CP}. True input values for the other oscillation parameters: $|\Delta m^2| = 2.36 \times 10^{-3}$, $sin^2\theta_{23} = 0.35$ and $\delta_{CP} = 0$.

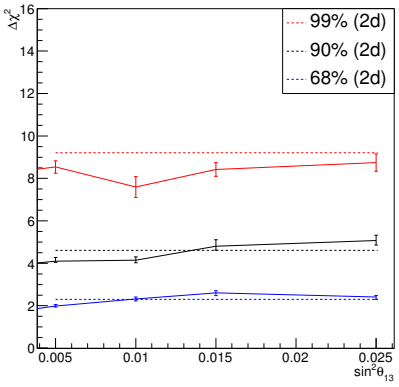

Figure 412: Summary of the values of $\Delta\chi^2$ at 99%, 90% and 68% confidence intervals in the 2D parameter space ($sin^2\theta_{13}$,$|\Delta m^2|$) vs the value of $sin^2\theta_{13}$ with statistical fluctuations only and **fitting** $sin^2\theta_{23}$ **and fixing** δ_{CP}. True input values for the other oscillation parameters: $|\Delta m^2| = 2.36 \times 10^{-3}$, $sin^2\theta_{23} = 0.35$ and $\delta_{CP} = 0$.

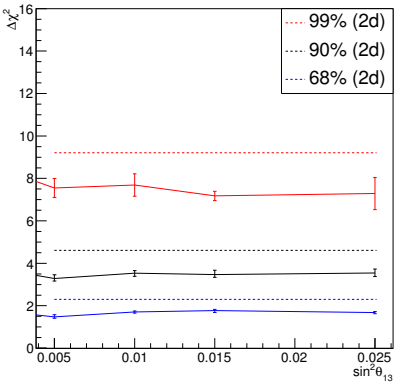

Figure 413: Summary of the values of $\Delta\chi^2$ at 99%, 90% and 68% confidence intervals in the 2D parameter space ($sin^2\theta_{13}$,$|\Delta m^2|$) vs the value of $sin^2\theta_{13}$ with statistical fluctuations only and **fitting** δ_{CP} **and fixing** $sin^2\theta_{23}$. True input values for the other oscillation parameters: $|\Delta m^2| = 2.36 \times 10^{-3}$, $sin^2\theta_{23} = 0.35$ and $\delta_{CP} = 0$.

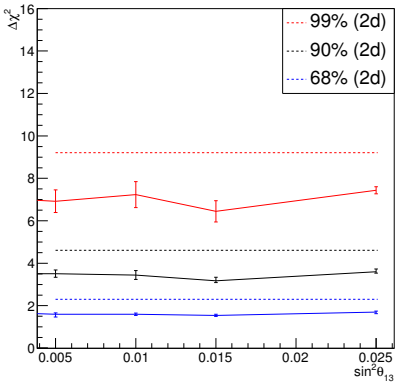

Figure 414: Summary of the values of $\Delta\chi^2$ at 99%, 90% and 68% confidence intervals in the 2D parameter space ($sin^2\theta_{13}$,$|\Delta m^2|$) vs the value of $sin^2\theta_{13}$ with statistical fluctuations only and **fitting** $sin^2\theta_{23}$ **and** δ_{CP}. True input values for the other oscillation parameters: $|\Delta m^2| = 2.36 \times 10^{-3}$, $sin^2\theta_{23} = 0.35$ and $\delta_{CP} = 0$.

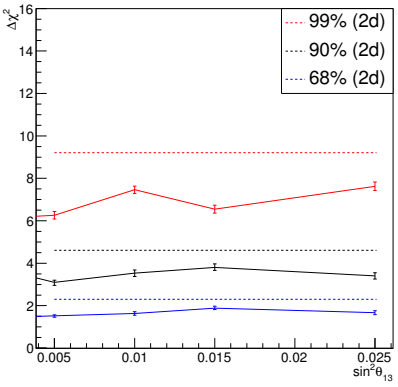

Figure 415: Summary of the values of $\Delta\chi^2$ at 99%, 90% and 68% confidence intervals in the 2D parameter space ($sin^2\theta_{13}$,$|\Delta m^2|$) vs the value of $sin^2\theta_{13}$ with statistical fluctuations and systematic variations and **fitting** $sin^2\theta_{23}$ **and** δ_{CP}. True input values for the other oscillation parameters: $|\Delta m^2| = 2.36 \times 10^{-3}$, $sin^2\theta_{23} = 0.35$ and $\delta_{CP} = 0$.

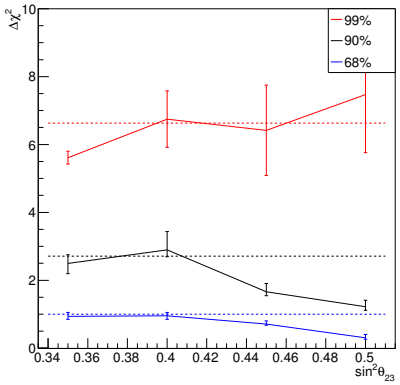

Figure 416: Summary of the values of $\Delta\chi^2$ at 99%, 90% and 68% confidence intervals in the 1D parameter space $sin^2\theta_{23}$ vs the value of $sin^2\theta_{23}$ with statistical fluctuations only where $\Delta\chi^2$ was calculated as folllows: a first fit was done fitting only δ_{CP}, fixing the other three oscillation parameters to their true input value, and χ^2_{init} was obtained; then a second fit was done fitting δ_{CP} and $sin^2\theta_{23}$, keeping $sin^2\theta_{13}$ and $|\Delta m^2|$ fixed to their true input values and χ^2_{bf} was obtained, computing finally $\Delta\chi^2 = \chi^2_{init} - \chi^2_{bf}$. True input values for the other oscillation parameters: $|\Delta m^2| = 2.36 \times 10^{-3}$, $sin^2\theta_{13} = 0.025$ and $\delta_{CP} = 0$.

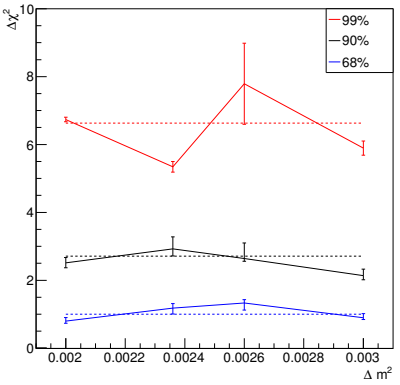

Figure 417: Summary of the values of $\Delta\chi^2$ at 99%, 90% and 68% confidence intervals in the 1D parameter space $|\Delta m^2|$ vs the value of $|\Delta m^2|$ with statistical fluctuations only where $\Delta\chi^2$ was calculated as folllows: a first fit was done fitting only δ_{CP}, fixing the other three oscillation parameters to their true input value, and χ^2_{init} was obtained; then a second fit was done fitting δ_{CP} and $|\Delta m^2|$, keeping $sin^2\theta_{13}$ and $sin^2\theta_{23}$ fixed to their true input values and χ^2_{bf} was obtained, computing finally $\Delta\chi^2 = \chi^2_{init} - \chi^2_{bf}$. True input values for the other oscillation parameters: $sin^2\theta_{23} = 0.5$, $sin^2\theta_{13} = 0.025$ and $\delta_{CP} = 0$.

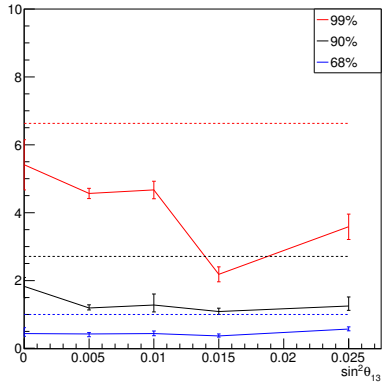

Figure 418: Summary of the values of $\Delta\chi^2$ at 99%, 90% and 68% confidence intervals in the 1D parameter space $sin^2\theta_{13}$ vs the value of $sin^2\theta_{13}$ with statistical fluctuations only where $\Delta\chi^2$ was calculated as folllows: a first fit was done fitting only δ_{CP}, fixing the other three oscillation parameters to their true input value, and χ^2_{init} was obtained; then a second fit was done fitting δ_{CP} and $sin^2\theta_{13}$, keeping $sin^2\theta_{23}$ and $|\Delta m^2|$ fixed to their true input values and χ^2_{bf} was obtained, computing finally $\Delta\chi^2 = \chi^2_{init} - \chi^2_{bf}$. True input values for the other oscillation parameters: $|\Delta m^2| = 2.36 \times 10^{-3}$, $sin^2\theta_{23} = 0.5$ and $\delta_{CP} = 0$.

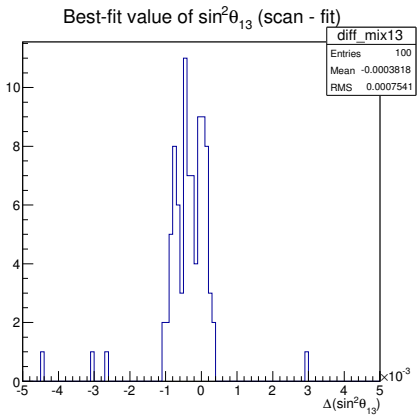

Figure 419: Comparison between the value of $sin^2\theta_{13}$ giving the true minimum χ^2 found scanning the ($sin^2\theta_{13}$, δ_{CP}) parameter space with the best-fit value result from the fit over 100 toy experiments created at true input values: $|\Delta m^2| = 2.36 \times 10^{-3}$, $sin^2\theta_{23} = 0.5$, $sin^2\theta_{13} = 0.025$ and δ_{CP} = 0. Results present a good agreement within the step sizes used ($\delta sin^2\theta_{13}$ = 0.001 and δ_{CP} = 0.02).

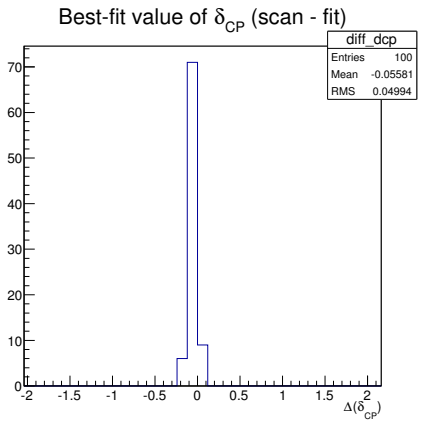

Figure 420: Comparison between the value of δ_{CP} giving the true minimum χ^2 found scanning the ($sin^2\theta_{13}$, δ_{CP}) parameter space with the best-fit value result from the fit over 100 toy experiments created at true input values: $|\Delta m^2| = 2.36 \times 10^{-3}$, $sin^2\theta_{23} = 0.5$, $sin^2\theta_{13} = 0.025$ and δ_{CP} = 0. Results present a good agreement within the step sizes used ($\delta sin^2\theta_{13}$ = 0.001 and δ_{CP} = 0.02).